The effect of chronic hypoxia and low dose-rate β-irradiation on the MCF-7 human cancer cell

by *in vitro* cellular protein incorporation of ^{3}H-valine in 8% O_2

Emil Knut Stenersen Espe

Department of Physics
University of Oslo

Master Thesis in Physics

October 2009

I en gassboks med trettisju grader
Der grodde det celler i monn
Helt fritatt fra G_1-blokader
Med oksygenmåling på bånn

For ^3H til cellene søkte
Med O_2-nivå sub-normalt
Og respirasjonen den økte
Skulle tro disse celler ble kvalt

Men de tålte jo lavt oksygen
Så hvorfor sa syklusen stopp?
For boksen, den var ikke ren
Og cellene hadde fått sopp

For med oksygen-proben i flasken
Var korken blitt tatt av tildels
En dag gikk forsøket i vasken
Da flasken en dag hadde pels

Moralen fra dette må bli
Når forsøk som dette man får
For sporer må man være fri
Celler skal ikke ha hår!

Preface

The work on this thesis is done at the Biophysics and medical physics group, Institute of P*h*ysics, University of Oslo.

My supervisor has been professor dr.philos Erik Olai Pettersen, and my co-supervisor has been scientist dr.scient Nina F. J. Edin. Thank you both very much for helping me in all phases of the work with this thesis, for encouraging words throughout and a knowledge beyond grasp. Thank you for letting me be a part of such an interesting and challenging research field!

Also thanks to Joe Alexander Sandvik and Siri Fenne for invaluable help in the lab, no experiments would be possible without you.

In addition, I want to thank and all my co-students and employees at the Biophysics and medical physics group for a great social environment and interesting discussions, especially Erlend, for your interest, help and valuable suggestions.

I will also thank DREAM THEATER for helping me getting through (manually) counting close to 150.000 cells.

Thank **you** for reading at least the preface!

Last but not least I want to thank my lovely and supporting wife Sigrun for her support and encouraging spirit throughout the process of writing this thesis. I could not have done this without you!

This thesis is written in TeXnicCenter 7.01 and typeset with LaTeXby using MikTeX 2.7. Graphics has been treated and converted to `*.eps` in either GIMP 2.6.7, Adobe Photoshop CS2 or Adobe Illustrator CS2. Vector graphics are made in Adobe Illustrator CS2. Matlab R2008a was used for data analysis and data presentation.

Some words about thesis structure

The current thesis is is divided into four main chapters; *Theory*, containing the theoretical background needed in the experiments and calculations presented in later chapters; *Methods*, containing descriptions of the methodical procedures, analytic tools and experimental equipment used; *Results and analysis*, containing all the experimental results and calculations performed as well as analysis of the main experiments and *Discussion*, containing a discussion of the main results.

Throughout in this thesis, a distinction between *oxygen concentration* (% O_2) and *gas phase oxygen concentration* (% O_2^{gp}) is made, as the latter refers to the maintained oxygen concentration in the gas phase surrounding the cell flask. It does not, however, represent the actual oxygen concentration experienced by the cells (due to limited diffusion through the medium). In addition, % O_2^{gp} is used to identify the hypoxia experiments.

The unit of quantity q is $[q]$, and its unitless value is $\{q\}$. Quantities with uncertainty are given on the form $q \pm se_q$, where se_q are the calculated standard error of the quantity. Some supplementary statistical comments are found in section 2.8 on page 49.

Abstract

Hypoxic cells exposed to acute irradiation are found, in general, to be more radioresistant than the equivalent well-oxygenized counterpart due to various cellular responses to low oxygen availability. However, previous studies have indicated that chronic hypoxic cells are less tolerable to *low dose-rate irradiation* than well-oxygenized cells.

In the present study the MCF-7 human breast cancer cell was exposed to various oxygen concentrations and thus varying levels of chronic hypoxia, and the associated cellular respiration and proliferation were investigated.

In addition, ^{3}H-valine, a radioactive version of the essential amino acid valine, was used to irradiate the cells with low dose-rate β-irradiation. A fraction of ^{3}H-valine was added to the growth medium of the cells, and as the valine was incorporated into the cellular proteins, the radioactive decay irradiated the cell from within. The microdosimetry of this system was performed.

Finally, some respirational effects of cells simultaneously exposed to both hypoxia and low dose-rate irradiation were investigated.

The following was observed in the experiments and associated analysis:

- The initial medium specific activity of 1.67 μCi/ml yielded a dose-rate to the MCF-7 nucleus of $\dot{D} = 0.0270 \pm 0.0030$ Gy/h. Furthermore, a medium specific activity of 0.735 μCi/ml was used to achieve a lower dose-rate of $\dot{D} = 0.0119 \pm 0.0013$ Gy/h, more comparable to the dose-rates used in earlier studies.

- A gas phase oxygen concentration of 8% O_2^{gp} was found to meet the two requirements of not killing the cells by asphyxy, while still providing sufficient low oxygen availability, making the observation of hypoxia effects possible.

- In a gas phase oxygen concentration of 8% O_2, the maximum measured cellular respiration was

  - 642.7 fmol/h·cell for the unirradiated cells
  - 812.1 fmol/h·cell for cells irradiated with 0.027 Gy/h
  - 530.3 fmol/h·cell for cells irradiated with 0.012 Gy/h

  However, the 0.012 Gy/h experiment was not run long enough to exclude any further increase in respiration.

- The irradiated cells seemed to accumulate lower pericellular oxygen concentrations than unirradiated cells. Furthermore, a dose-rate of 0.012 Gy/h seemed to yield even lower POC values than 0.027 Gy/h.

- The pericellular oxygen concentration at which the cellular respiration was at its maximum was

  - 2.55 ± 0.28 % O_2 for the unirradiated cells
  - 3.31 ± 0.99 % O_2 for cells exposed to 0.027 Gy/h
  - 0.750 ± 0.029 % O_2 for cells exposed to 0.012 Gy/h

  These results indicated that a dose-rate of 0.012 Gy/h (i.e. a specific medium activity of 0.735 μCi/ml) yielded a significantly decreased lower threshold for maximum respiration compared to the unirradiatad cells. They also indicate that a dose-rate of 0.012 Gy/h yields a greater cellular response than a dose-rate of 0.027 Gy/h with respect to lowered POC values.

Sammendrag

Hypoksiske celler som eksponeres for akutt bestråling vil, som hovedregel, være mer strålingsresistente enn veloksygenerte celler. Tidligere studier har derimot vist at kronisk hypoksiske celler tåler ståling med *lav doserate* dårligere enn enn veloksygenerte celler.

I denne oppgaven ble den humane brystkreftcellen MCF-7 eksponert for varierende oksygenkonsentrasjoner og dermed varierende grad av kronisk hypoksi, og cellenes oksygenforbruk (respirasjon) og formeringsevne (proliferasjon) ble undersøkt.

I tillegg har ^{3}H-valin, en radioaktiv versjon av den essensielle aminosyren valin, blitt brukt til å bestråle cellene med lav-doserate β-stråling. En andel ^{3}H-valin ble tilsatt cellenes vekstmedium, og når cellene inkorporerte valin i sine proteiner bestrålte de radioaaktive atomene cellen innenfra. Mikrodosimetriske beregninger på dette systemet ble utført.

Til slutt ble respirasjonen til celler eksponert for både hypoksi og lav-doserate bestråling studert.

Det følgende ble observert i eksperimentene og tilhørende analyse:

- En spesifikk mediumaktivitet på 1.67 μCi/ml resulterte i en doserate på $\dot{D} = 0.0270 \pm 0.0030$ Gy/t til MCF-7-kjernen. Videre ble en spesifikk mediumaktivitet på 0.735 μCi/ml brukt til å oppnå en doserate på $\dot{D} = 0.0119 \pm 0.0013$ Gy/t, sammenliknbar med doseratene brukt i tidligere studier.
- En oksygenkonsentrasjon i atmosfæren på 8% O_2^{gp} ble funnet til å oppfylle kravene om at cellene ikke skulle dø av oksygenmangel, mens de samtidig opplevde tilstrekkelig lav oksygentilgjengelighet til å utvise hypoksiske effekter.
- Den målte maksimale cellerespirasjonen for celler som grodde i en en atmosfære med 8% O_2 var
  - 642.7 fmol/h·cell for ubestrålte celler
  - 812.1 fmol/h·cell for celler bestrålt med 0.027 Gy/t

  - 530.3 fmol/h·cell for celler bestrålt med 0.012 Gy/t

  Imidlertid ble ikke eksperimentet med 0.012 Gy/t kjørt lenge nok til å kunne ekskludere noen eventuell videre økning i respirasjon.

- Cellene under bestråling opparbeidet en lavere pericellulær oksygenkonsentrasjon (POC) enn ubestrålte celler. Videre så en doserate på 0.012 Gy/t ut til å resultere i enda lavere POC enn en doserate på 0.027 Gy/t.

- Den pericellulære oksygenkonsentrasjonen når cellenes respirasjonsmaksimum ble målt var

  - 2.55 ± 0.28 % O_2 for ubestrålte celler
  - 3.31 ± 0.99 % O_2 for celler bestrålt med 0.0270 Gy/t
  - 0.750 ± 0.029 % O_2 for celler bestrålt med 0.012 Gy/t

  Disse resultatene indikerer at en doserate på 0.012 Gy/t (dvs en spesifikk mediumaktivitet på 0.735 μCi/ml) resulterte i en betydlig redusering i nedre terskelverdi for maksimal respirasjon, sammenliknet med ikke-bestrålte celler. Dette ble derimot ikke observert i cellene bestrålt med 0.027 Gy/t, noe som kan indikere at den lavere doseraten på 0.012 Gy/h resulterer i en større cellulær effekt enn doseraten på 0.027 Gy/h.

Contents

1 Introduction **1**

2 Theory **5**

2.1 Radioactivity 5

2.1.1 Radioactive decay 6

2.1.2 Tritium 6

2.2 Radiation physics 7

2.2.1 Ionizing radiation 7

2.2.2 Charged particle interaction processes 8

2.3 Dosimetry 10

2.3.1 Describing radiation fields 10

2.3.2 Stopping power 11

2.3.3 Linear energy transfer 12

2.3.4 Classical dose calculation 13

2.3.5 Radiation and charged-particle equilibria 14

2.3.6 Cellular tritium micro dosimetry 15

2.4 Cell biology 17

2.4.1 The cell cycle 18

2.4.2 Cell growth and colony growth phases 21

2.4.3 Biological effects of tritium substitution 22

2.4.4 DNA 22

2.5 Radiation biology 24

2.5.1 Cell irradiation 24

2.5.2 Poisson function in cancer treatment by radiation . . 25

2.5.3 Radiation damage 25

2.5.4 Cellular countermeasures to stress 26

2.5.5 The p53 factor 28

2.5.6 Cell survival curves 30

2.5.7 Direct and indirect effect of radiation 32

2.5.8 Radiosensitivity and the cell cycle 34

2.5.9 The oxygen effect 36

2.5.10 Oxygen enhancement radio . . . 37
2.5.11 The dose-rate effect . . . 37
2.5.12 Relative biological effect . . . 42
2.6 Cellular hypoxia . . . 43
2.6.1 Chronic and acute hypoxia . . . 44
2.6.2 Hypoxia-mediated cell cycle arrest . . . 45
2.6.3 Hypoxia-mediated apoptosis . . . 45
2.6.4 Other consequences of cellular hypoxia . . . 45
2.7 Oxygen diffusion and cellular respiration . . . 47
2.7.1 Oxygen solubility in the RPMI medium . . . 48
2.7.2 Oxygen consumption calculation . . . 48
2.7.3 The stabilizing phase . . . 49
2.8 Some statistical considerations . . . 49
2.8.1 Error propagation . . . 50

3 Methods **51**
3.1 Cell cultivation and maintenance . . . 51
3.1.1 The MCF-7 human breast cancer cell line . . . 51
3.1.2 Laboratory equipment . . . 51
3.1.3 The RPMI medium . . . 52
3.1.4 Trypsin . . . 52
3.1.5 The cell recultivation process . . . 53
3.1.6 Medium change . . . 53
3.2 Phase-contrast microscopy . . . 54
3.2.1 Microscope resolution . . . 54
3.3 Cell and nucleus size determination . . . 56
3.4 Cell counting . . . 56
3.5 Cell irradiation . . . 58
3.5.1 Production of radioactive medium . . . 58
3.6 Dosimetry . . . 60
3.6.1 Measure of cell and nucleus size . . . 60
3.6.2 Cell preparation for scintillation counting . . . 60
3.6.3 Nucleus preparation for scintillation counting . . . 61
3.6.4 Liquid scintillation counting . . . 61
3.7 Cellular response to hypoxia . . . 62
3.7.1 O_2 concentration profile acquirement . . . 63
3.7.2 Experimental set-up in the cabinet . . . 67
3.8 Analyzing the respirational data . . . 68
3.8.1 Sensor calibration . . . 69
3.8.2 Data input . . . 70
3.8.3 Timing . . . 71
3.8.4 Cell count . . . 71

3.8.5 Truncating the data . . . 71
3.8.6 Medium level detection . . . 72
3.8.7 Profile plotting (2D and 3D) . . . 72
3.8.8 Gas phase and flask bottom oxygen concentration . . . 72
3.8.9 Slope calculation . . . 72
3.8.10 Plotting of experiment data . . . 73
3.9 Cellular survival experiments . . . 76
3.9.1 Cell survival calculation . . . 76

4 Results and analysis **79**
4.1 Microscope resolution . . . 79
4.1.1 Determining pictures per flask (set-up 1) . . . 79
4.1.2 Determining pictures per flask (set-up 2) . . . 81
4.2 Cell and nucleus size measurement . . . 82
4.3 Dosimetry . . . 83
4.3.1 Cellular and nuclear activity . . . 83
4.3.2 Determining the f values . . . 85
4.3.3 Determining the cellular S values . . . 86
4.3.4 Dose-rate to the nucleus . . . 87
4.3.5 Dose-rate as a function of medium specific activity . . . 87
4.3.6 Accumulated activity and dose to the nucleus . . . 88
4.3.7 Radioactive medium activity measurement . . . 89
4.3.8 The extracellular and intracellular specific activities . . . 91
4.3.9 Control of the T-47D dose-rate . . . 91
4.4 Overview: Hypoxia experiments . . . 93
4.5 Hypoxia experiments w/o irr. . . . 94
4.5.1 Data from experiment 081103 . . . 94
4.5.2 Experiment 081103 summary . . . 102
4.5.3 Data from experiment 081118 . . . 107
4.5.4 Experiment 081118 summary . . . 119
4.5.5 Data from experiment 081212 . . . 124
4.5.6 Experiment 081212 summary . . . 128
4.6 Hypoxia experiments with irr. . . . 130
4.6.1 Data from experiment 090608 . . . 131
4.6.2 Experiment 090608 summary . . . 137
4.6.3 Data from experiment 090622 . . . 140
4.6.4 Experiment 090622 summary . . . 145
4.7 Confluence experiment . . . 145
4.7.1 Data from experiment 081020 . . . 147
4.7.2 Experiment 081020 summary . . . 148
4.8 Comparison: Cellular proliferation . . . 150
4.9 Comparison: POC . . . 151

4.10 Comparison: Cellular respiration 154
4.11 Cellular survival experiments 155
4.12 The degrading of scintillation samples 155
4.12.1 ^{3}H and ^{3}Hn samples 155
4.12.2 ^{3}H-RPMI samples 158
4.12.3 KV samples 158

5 Discussion **159**
5.1 Cell cultivation and maintenance 159
5.2 Microscopic resolution 159
5.2.1 Cell counting 160
5.2.2 Cell and nucleus size determination 161
5.3 Cell irradiation 163
5.3.1 Radioactive medium activity 163
5.3.2 Electron versus gamma irradiation 163
5.4 Dosimetry 164
5.4.1 Problems with cellular tritium microdosimetry . . . 164
5.4.2 Scintillation counting and specific activity 166
5.4.3 Dose-rate and accumulated dose 167
5.4.4 Comparison to earlier studies of the T-47D cell line . 167
5.5 Cell survival experiments 170
5.6 Hypoxia experiment set-up and analysis 171
5.6.1 O_2 concentration control 171
5.6.2 Oxygen measurement 172
5.6.3 Software issues 177
5.7 Cellular effects of hypoxia and irradiation 178
5.7.1 Determining the appropriate gas phase oxygen concentration 178
5.7.2 Effects of medium evaporation 178
5.7.3 Effects of medium change and cell counting 179
5.7.4 Cellular proliferation 180
5.7.5 O_2 consumption slope and associated POCs 181
5.7.6 Comparative respirational trends 184
5.7.7 Possible effects due to non-constant dose-rate 184
5.7.8 Respiration and proliferation relationship 186
5.7.9 Comparison to earlier studies 186
5.8 Cellular effects of hypoxia and confluency 187
5.9 Suggestions for further investigations 187

6 Conclusion **189**

References **197**

A Analysis and plotting software **207**

B Respiration versus cell number plots **219**

C Cell pictures **225**

D Cell counts **239**

E Geometric red. factors and e. ranges **243**
E.1 Geometric reduction factors 243
E.2 Electron stopping power as function of energy 244

F Cellular S values **245**

G Recipies **247**

H Chemical list **249**

Dictionary

Anoxia The state of no available oxygen (see *Hypoxia*)

Cellular respiration The total respiration of a group of cells divided by the cell number, resulting in the (mean) oxygen consumption of a single cell

Confluency A state in which the cells have grown to a certain level of density

CPE Charged particle equilibrium

Flask respiration The total oxygen consumption of a cell culture in a flask

Hypoxia The state of low oxygen availability, see *Anoxia*. In Cummins and Taylor (2005), cellular hypoxia is defined as a state occurring when the demand for oxygen necessary to generate ATP in the cell is greater than the molecular oxygen supply

In vitro Lit. in glass, as opposed to *in situ* (in place) or *in vivo* (in tissue)

LD Lethal radiation damage, a radiation damage on a cell that inevitably leads to cell death

LET Linear energy transfer

% O_2^{gp} Gas phase oxygen concentration, as opposed to *POC*

OER Oxygen enhancement ratio

POC Pericellular oxygen concentration, i.e. the oxygen concentration in the close vicinity of the cells

PLD Potential lethal radiation damage, a radiation damage on a cell that may or may not leads to cell death, depending on e.g. the available repair time before mitosis.

RBE Relative biological efficiency

RE Radiation equilibrium

Reparation Cellular mechanisms fixing DNA damage

Restitution Spontaneous chemical reparation

Sublethal radiation damage (SLD) A radiation damage on a cell that by itself does not kill the cell, but may contribute to a lethal damage in combination with other sublethal damages

Valine An essential amino acid

Mathematical definitions

A	Activity
C'	Oxygen concentration
C	Cell count (cells per flask)
C_p	Cells per picture
$\mathcal{D}$	The diffusion coefficient
D	Dose
$\dot{D}$	Dose rate
$D(r_t \rightarrow r_s)$	Mean absorbed dose from region r_s to region r_t
Δ	Mean energy released per decay
E	Energy
E_k	Kinetic energy
E_n	Energy transport scenario n (see figure 2.4)
ϵ	Energy imparted in a volume V
P_f	Pictures per flask
Φ	Fluence
φ	Fluence rate
$\phi(R_t \leftarrow R_s)$	The fraction of energy released in region R_s absorbed in region R_t
Ψ	Energy fluence
ψ	Energy fluence rate
$\Psi_{r_t \leftarrow r_s}$	The geometric reduction factor
R	(Mean) cellular respiration [fmol/h·cell]
R_f	Total cellular respiration [fmol/h·flask]
$\mathcal{R}$	Range of a particle
$\mathcal{R}_{\text{CSDA}}$	CSDA estimate range of a particle
r_c	Cell radius
r_n	Nucleus radius
S	Signal from microsensor
S	Stopping power
t	Time
T_2	Cellular doubling time
$\bar{T}_2$	Mean cellular doubling time
V	Theoretical volume
X	Depth in medium

Chapter 1

Introduction

Cancer is a horrible disease. Cancerous cells are characterized by two properties—the ability to proliferate regardless of external or internal control mechanisms, and the ability to invade and colonize other (possibly distant) tissues (Alberts et al., 2008). Most cancer cases originate from a single aberrant cell (see figure 1.1).

Several factors may increase the risk of development of cancer—such as chemicals (e.g. smoking), bacteria, virus and ionizing radiation. In 2007, 25.943 patients were diagnosed with cancer in Norway (Kreftforeningen, 2009). The four most frequent forms of cancer are prostate, breast, colon and lung cancer. More than 183.000 persons are currently living with a cancer diagnosis in Norway (Kreftforeningen, 2009).

Ionizing radiation has been used to treat cancer since 1897 (only two years after Röntgen's initial discovery of the x-ray), and its ability to kill cancerous cells is well established (Hall and Giaccia, 2006). Radiation therapy is still used extentively in cancer treatment.

In a tumor, the blood vessel network is often poor and unstable, resulting in a highly varying oxygen supply to the tumor cells (Mayles et al., 2007). This will often lead to areas of cellular hypoxia within the tumor, a state where the demand for oxygen necessary to generate ATP and thus maintain normal metabolism in a cell is greater than the molecular oxygen supply (Cummins and Taylor, 2005). The hypoxic cancer cell will typically have increased radioresistance, and thus pose a problem in cancer therapy. This is referred to as the *oxygen effect* (Hall and Giaccia, 2006; Mayles et al., 2007). Due to the fact that viable hypoxic cells thus may survive traditional radiation treatment and continue to proliferate, this effect is a major challenge, in reducing the efficiency of the treatment (Mayles et al., 2007). In addition, other cellular responses to hypoxia (treated in section 2.6) will emerge, resulting in the fact that tumors with extensive hypoxia

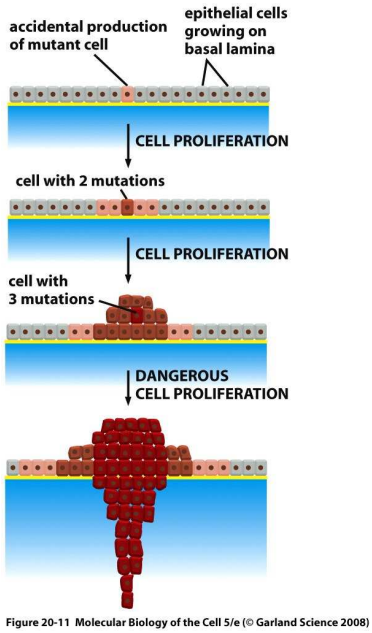

Figure 1.1: *An illustration showing the process of tumor development from a single deviating cell (from Alberts et al., 2008). Each step involves mutations either promoting proliferation or impede cell death, making the daughter cells more malignant.*

often are associated with poor patient prognosis (Guppy et al., 2005).

Today, radiation therapy usually involves fractionation (see section 2.5.11), i.e. the daily delivery of discrete dose fractions (typically 2 Gy) over a course of several weeks (Mayles et al., 2007), thereby, in a way, simulating a decrease in dose-rate. This reduces the impact of the oxygen effect (by allowing reoxygenation) in addition to exploiting the intrinsic difference between late and early responding tissues (described in section 2.5.6) to increase treatment efficiency.

Studies have, on the other hand, shown that cells exposed to low dose-rate irradiation are more sensitive in a hypoxic state than in a well-oxygenized state, indicating a *reverse oxygen effect* (Pettersen et al., 2007; Storhaug, 2008).

In this thesis, the human breast cancer cell line MCF-7 has been studied. The main aims of this study have been the following:

1. To develop software to analyze and present the respirational data acquired in the experiments

2. To perform a dosimetric method described by Søvik (2002) to calculate the dose-rate to the nucleus of the MCF-7 cell

3. To investigate the respirational and proliferative response of the MCF-7 cell line to varying degrees of hypoxia, and its respirational response of simultaneous exposure to hypoxia and low dose-rate electron irradiation.

The cells were cultivated in a hypoxia cabinet where the gas phase oxygen concentration was monitored and controlled by the user. The cells were seeded into cell flasks along with growth medium, supplying the cells with a.o. nutrients, vitamins and antibiotics. The medium layer was about 1.8 mm thick. The cellular oxygen availability was based on the diffusion of molecular oxygen from the gas phase through the medium to the flask floor, resulting in a stable oxygen concentration gradient whose slope was proportional with the total respiration in the flask. An oxygen sensor was used to acquire these gradients (called oxygen profiles) at certain intervals. This way, both oxygen availability and consumption could be monitored on a dynamic scale.

The irradiation was performed by allowing the cell to incorporate a radioactive amino acid into its proteins, and thereby irradiating itself from within. The microdosimetry used to calculate the resulting dose-rate is described by Søvik (2002).

When the data was acquired on a dedicated computer, the analysis was performed in a custom-made software reading the raw data from the oxygen sensor and performing analysis and plotting of both the raw and the processed data.

Chapter 2

Theory

2.1 Radioactivity

The known configuration of the nucleus of a stable atom can seem to contradict common sense, having multiple positive particles[1] clung together in the nucleus mutually expressing huge repulsive Coulomb forces.

The standard model of physics explains this apparent paradox with the existence of the strong nuclear force, ensuring the cohesion of a nucleus (Mayles et al., 2007).

However, as Henri Bequerel discovered in 1896, some atoms show a unstable property and may disintegrate by emitting radiation—energetic photons or particles.

Being governed by fundamental physical laws, the occurrence of these decays can only be described by probabilities. This leads to the definition of the *activity* A

$$A = \frac{dN}{dt} \tag{2.1}$$

where dN is the expectation value of the number of spontaneous disintegrations during time interval dt. A is defined for a specified nucleus at a particular energy state (Mayles et al., 2007).

The unit of activity is becquerel (Bq) where

$$1 \text{ Bq} \equiv 1 \text{ s}^{-1}.$$

representing one disintegration (on average) per second.

In addition, the *specific activity* A^S, i.e. the total activity in a volume dV, is defined as

$$A^S = \frac{A}{dV}. \tag{2.2}$$

[1] Except for the hydrogen atom.

2.1.1 Radioactive decay

The law concerning radioactive decay was experimentally established by Rutherford and Soddy in 1902 (Mayles et al., 2007). It expressed the proportionality

$$dN = -\lambda N \, dt \tag{2.3}$$

defining the decay constant λ. From the above definition an expression for the number of atoms at time t, N_t, can be derived, given the initial number of atoms N_0:

$$N_t = N_0 e^{-\lambda t}. \tag{2.4}$$

From (2.3) the activity can also be expressed as

$$A = \lambda N$$

resulting in

$$A_t = A_0 e^{-\lambda t}.$$

Furthermore, the *half life* $t_{1/2}$ of a radioactive nuclide is given from

$$\frac{N}{N_0} \stackrel{!}{=} 0.5 = e^{-\lambda t_{1/2}}$$

$$t_{1/2} = \frac{\ln 2}{\lambda}.$$

2.1.2 Tritium

Tritium, ^{3}H or T, is a radioactive isotope of hydrogen with a half-life of about 12.4 years (Rowberg, 2001; Dworschak, 1993). Its nucleus consists of one proton and two neutrons, in contrast to protium ("normal" hydrogen), ^{1}H, having only one proton and no neutrons. The atomic mass of tritium is 3.016 u (as compared to protium, having an atomic mass of 1.008 u and being the lightest element).

At standard pressure and temperature, tritium is a gas, $(^3\text{H})_2$. Reacting with oxygen it can form $(^3\text{H})_2\text{O}$ (tritiated water) or $(^3\text{H})\text{HO}$ (partially tritiated water).

Tritium decays to ^{3}He by emitting an electron and an electron-antineutrino, following the reaction

$$^3\text{H} \rightarrow {}^3\text{He} + e^- + \bar{\nu}_e. \tag{2.5}$$

The total amount of energy released in the decay is 18.6 keV. As a result, tritium has the lowest decay energy of all known β-emitters (Dworschak, 1993).

Studying the escaping electron from the tritium decay, scientists were (and still are) puzzled to find a continuous spectrum of energies, leading to the idea of a nearly undetectable particle carrying away a part of the energy released. This was later shown to be due to the existence of an antineutrino, having a very small interaction cross section. The energy released in the tritium decay (18.6 keV) is distributed between the electron and the antineutrino, explaining the observed energy spectrum.

Our use of tritium will be shown to exploit the effect of the emitted electron, having an average kinetic energy of 5.6 keV (Chen, 2006). In addition, the antineutrino carries away 12.9 keV of energy on average, but can be neglected in our context as its interaction cross section is, as mentioned above, extremely low.

The maximum range $\mathcal{R}$ of the tritium β-particle in air is about 6 mm, and the average range is 0.5 mm (Dworschak, 1993). In water the maximum range is about 6 μm, and the average range is 0.56 μm (Chen, 2006).

2.2 Radiation physics

2.2.1 Ionizing radiation

Radiation in this context refers to either electromagnetic waves (mass $m = 0$) or particles with nonzero kinetic energy ($m \neq 0$).

We define radiation as *ionizing* if it has enough energy to ionize atoms or molecules it meets along its path (Podgorsak, 2005). The required energy for an ionization of a valence electron varies is in the order of 4-25 eV, and thus the radiation must carry energy (kinetic or quantum) of this magnitude to be called ionizing (Attix, 2004). In terms of wavelength of electromagnetic radiation this corresponds to values up to about 320 nm (Attix, 2004).

In addition it is useful to distinguish between *directly ionizing* and *indirectly ionizing* radiation (Podgorsak, 2005). Uncharged particles (n) and electromagnetic radiation (γ) are considered indirectly ionizing, while charged particles (α, β) are directly ionizing radiation.

The radiation administered in the present experiments will be delivered by the means of electron radiation, and therefore we will focus on the theory of particle radiation and dosimetry.

Particle radiation

Particle radiation can be both indirectly ionizing (n) and directly ionizing (α, β).

Particles show, as well as photons, wave-particle-dualism, but in contrast to the massless photons particles always have nonzero (rest) mass.

Our main interest is describing the energy of the electron, given by

$$E = \gamma m_0 c^2 \tag{2.6}$$

where $m_0 \approx 9.109 \times 10^{-31}$ kg is the rest mass of the electron, $c \approx 2.998 \times 10^8$ m/s is the speed of light in vacuum and

$$\gamma = \frac{1}{\sqrt{1 - \left(\frac{v^2}{c^2}\right)}}$$

where v is the velocity of the electron.

In the context of this thesis it is only the kinetic energy E_k of the electron that needs to be considered

$$E_k = (\gamma - 1) m_0 c^2 \tag{2.7}$$

from which, given a value for E_k, the actual speed of an electron can be calculated.

2.2.2 Charged particle interaction processes

The understanding of radiation interaction with matter is essentially the core of dosimetry, where the main goal is to calculate the energy transferred from radiation to matter. A satisfying understanding of these processes is therefore of vast importance.

The interaction processes of particle radiation is fundamentally different from photon interaction processes. The photon has in principle, when traveling through a finite slab of matter, a non-zero probability of never interacting. Consequently it may, in principle, carry with it all of its energy out of our region of interest (Attix, 2004), regardless of the size of the region. In other words, a photon can travel through the Great Wall of China without losing any energy.

On the other hand, a charged particle will, because of its surrounding Coulomb electric force field, interact with nearly every atom (typically its electron cloud) it passes. A charged particle traveling through matter will therefore experience a much more friction-like process than a photon—the charged particle in a vast number of interactions with little or no energy loss, and the photon in few events where a significant chunk or all of the energy is transferred to the surroundings in each event (Attix, 2004).

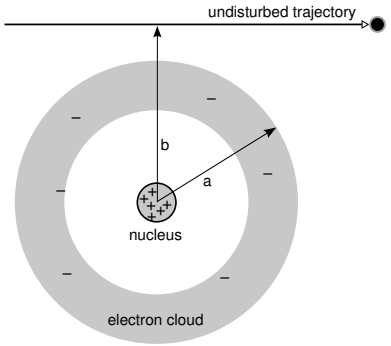

Figure 2.1: *Impact parameters a and b used to describing charged particle interaction processes (Illustration from Attix (2004), modified). Parameter a represents the size of the atom, and parameter b the distance from the atomic core to the undisturbed trajectory of the traveling particle.*

The impact parameters a and b

On a more theoretical level we differentiate between two main types of particle interaction: soft and hard collisions. We define the difference with help from the classical impact parameters a and b, shown in figure 2.1.

When impact parameters $b \gg a$, i.e. the distance from the particle to the atom is very large, the net effect is the transfer of a very small amount of energy and a small deflection of the particle (Attix, 2004). The atom may experience either an excitation, an ionization or a spatial displacement.

The soft collision is dominating over hard collisions in occurrence, but contributes only to about half of the total transferred energy.

When $b \approx a$, we have a so-called direct hit process where the incident particle interacts primarily with a single atomic electron.

The secondary electron may gain enough energy to travel a considerable distance from the interaction point (see δ-rays, section 2.3.2).

Characteristic radiation and/or Auger electrons may also be emitted as an inner-shell electron of the atom may be ejected by the hit process (Attix, 2004).

The incident particle may also penetrate the electron cloud of the atom and interact directly with the atomic nucleus. In terms of impact parameters, this is a $b \ll a$ direct hit process.

In the majority (97-98%) of these interactions the result is an elastic scattering of the incident particle with insignificant energy losses. This accounts for the unruly behaviour of electron radiation in matter, especially in high-Z media (Attix, 2004).

In the other 2-3% of the cases, an inelastic scatter process occurs. The result is an emission of a photon (recieving most of the incident particle's

kinetic energy), namely *bremsstrahlung*, which is of great importance in e.g. x-ray production (Attix, 2004).

2.3 Dosimetry

Dosimetry is the theories concerning estimation of the energy imparted ϵ to a matter of mass m.

The dosimetry for directly and indirectly ionizing radiation is somewhat different, both share many of the same principles and are equally important and interesting. However, as the radiation quality used in the experiments treated in this thesis are electron (i.e. directly ionizing) we will in this thesis mainly focus on the dosimetry of directly ionizing radiation.

2.3.1 Describing radiation fields

A number of quantities can be assigned to a general (both directly and indirectly ionizing) radiation field.

The *fluence* Φ at an arbritary point P is defined as

$$\Phi = \frac{dN_e}{da}$$

where N_e is the expectation value of *rays* (that is, photons or particles) striking a sphere, surrounding point P with a infinitesimal great-circle area da, during a specified time interval (Attix, 2004).

The *fluence rate* φ is then defined as

$$\varphi = \frac{d\Phi}{dt} = \frac{d}{dt}\frac{dN_e}{da}.$$

Attix (2004) emphasises that Φ and φ only expresses the sum of rays, not taking in to account their quantum or kinetic energy. These quantities provide thereby little useful information of the incident radiation field.

One of the main goals in describing a radiation field is therefore to gain information of the energy carried with it and therefore potentially transferred. The simplest field-descriptive quantity taking energy into account is the *energy fluence* Ψ

$$\Psi = \frac{dR}{da}$$

where R is the expectation value of total energy (minus rest-mass energy) carried by the N_e rays striking the previously mentioned sphere with a great-circle area da within a time window Δt (Attix, 2004).

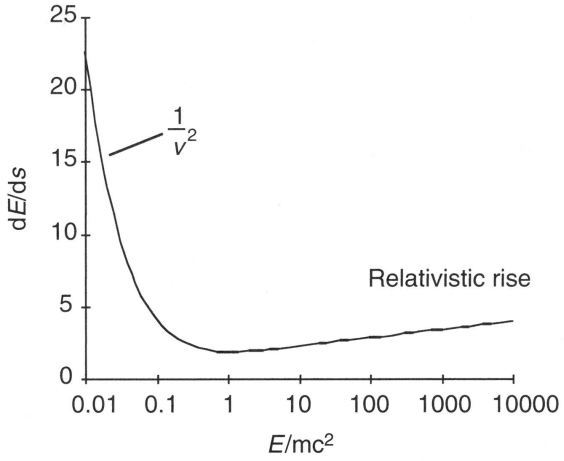

Figure 2.2: *The collision stopping power of the electron as a function of the particle energy on a log scale (from Mayles et al., 2007).*

As with fluence we define the *energy fluence rate* as

$$\psi = \frac{d\Psi}{dt} = \frac{d}{dt}\frac{dR}{da}.$$

2.3.2 Stopping power

We now want to get to business describing the energy exchange of a charged-particle interaction in a more detailed and quantitative form.

One appealing way is to look at energy transferred from the incident charged particle to its transient surroundings per distance traveled (note that this is *not* the same as depth in matter), namely $\Delta E/\Delta x$. From there the way seems short to determining the energy absorbed in the matter of interest.

Stopping power is therefore, at first glance, a rather simple and intuitive quantity. It simply expresses expected energy transferred per distance traveled:

$$S = -\frac{dT}{dx}, \tag{2.8}$$

where T is kinetic energy. The equation has a negative sign because, from the particle's point of view, it loses energy to its surroundings.

We will also see that it can be useful to define the quantity *mass stopping power*, being the stopping power divided by the density ρ of the absorbing medium:

$$S^m = -\frac{dT}{\rho dx}. \tag{2.9}$$

Intuitively, we expect the (mass) stopping power to be a function of a number of variables, such as the velocity (and thereby kinetic energy) and charge of the incident particle, in addition to atomic configuration of the matter of interest.

From section 2.2.2, we know that a charged particle interaction with energy exchange has two possible classes of outcome—the energy can either be transferred to secondary particles (collision losses), or energy can constitute to creating photons (radiative losses). Consequently, we divide the mass stopping power S^m in *mass collision stopping power* S_c^m and *mass radiative stopping power* S_r^m:

$$\frac{dT}{\rho dx} = \left(\frac{dT}{\rho dx}\right)_c + \left(\frac{dT}{\rho dx}\right)_r. \tag{2.10}$$

Completely without consideration of derivation, an expression for the mass collision stopping power is (Attix, 2004)

$$\left(\frac{dT}{\rho dx}\right)_c \propto \frac{Zz^2}{A\beta^2}\left[13.8373 + \ln\left(\frac{\beta^2}{1-\beta^2}\right) - \beta^2 - \ln I\right]. \tag{2.11}$$

It is important to note that the (non-relative) mass collision stopping power is inversely proportional to the square of the velocity of the particle.

The mass collision stopping power, derived from the theory of soft and hard collisions (section 2.2.2), gives us a tool to estimating the energy loss of the particle and thus the energy imparted.

Continuous slowing down approximation range

As a consequence of the almost continuous energy loss of a charged particle, a somewhat reasonable approximation called *continuous slowing down approximation* (CSDA) can be used to estimate the range $\mathcal{R}$ of a particle:

$$\mathcal{R}_{\text{CSDA}} = \int_0^{T_0} \left(\frac{dT}{\rho dx}\right)^{-1} dT \tag{2.12}$$

where T_0 is the initial energy of the particle (Attix, 2004).

However, as a consequence of the discrete energy loss of the particle, the CSDA range will underestimate the penetrating ability of the particle, especially for heavier particles (Attix, 2004).

2.3.3 Linear energy transfer

Because there, in general, is a difference between transferred energy and absorbed energy, it is useful to introduce the quantity *linear energy transfer* (LET) L_Δ, also known as *restricted stopping power*.

Table 2.1: *Typical LET (linear energy transfer) values for a selection of radiation qualities different from photon radiation (Hall and Giaccia, 2006).*

Radiation quality	LET (keV/μm)
10 MeV protons	4.7
150 MeV protons	0.5
2.5 MeV α-particles	166
2 GeV Fe ions	1000

LET takes into account the possibility that the secondary particle (receiving energy from the primary particle) gains enough energy to travel a significant distance from the interaction point (Attix, 2004). This is for historical reasons called a δ-ray[2]. The neglection of the difference between stopping power and LET (i.e. transferred and absorbed energy) tends to overestimate the dose in the interaction point.

Linear energy transfer is therefore nothing more than the fraction of the collision stopping power that includes both soft and hard collisions resulting in δ-rays with energies less than the cutoff value Δ (Attix, 2004). The specific value for Δ is determined based on what one defines as a "local" energy deposition.

As an extension of this, the *unrestricted linear energy transfer* L_∞ is the case where $\Delta = \infty$.

LET can be used as a mean to describe radiation quality, see table 2.1 for some examples other than electron. As we shall see, LET has important implications in radiation biology and thus in radiation protection.

2.3.4 Classical dose calculation

Having quantities describing the incident radiation field and its energy, our next goal is to be able to define quantities concerning the energy transferred in interaction processes.

In this section classical dose calculations are treated, and is a part of the motivation of our next section (2.3.6) concerning micro dosimetry.

The *dose* D is defined as the energy $d\epsilon$ imparted in an infinitesimal volume dV of mass dm during a specified time interval (Attix, 2004):

$$D = \frac{d\epsilon}{dm}. \tag{2.13}$$

[2]Scientists believed initially that these rays were a new kind of radiation different from α-, β- and γ-rays, hence the name δ-rays.

The *dose-rate* is thus defined as

$$\dot{D} = \frac{dD}{dt} = \frac{d}{dt}\left(\frac{d\epsilon}{dm}\right) \tag{2.14}$$

Dose is measured in the unit grey (Gy), where

$$1 \text{ Gy} \equiv 1 \text{ J/kg}. \tag{2.15}$$

The equivalent dose is typically defined as

$$H = w \times D \tag{2.16}$$

where w is the weighting factor. For photons and electrons, $w = 1$ and the absorbed and equivalent dose is equal. For neutrons, protons and heavier nuclei $w = 2 - 20$.

In the experiments performed with the work of this thesis, electron irradiation is used and $H = D$.

2.3.5 Radiation and charged-particle equilibria

Two of the simplest and most appealing approximations used in dosimetry is the concepts of *radiation equilibrium* (RE) and *charged particle equilibrium* (CPE).

If RE exists in a volume V, it simply means that for every joule of energy entering V by the means of any radiation fluence, an exact equal amount of energy is leaving V. In other words—the dose D equals only the net rest mass converted to energy per unit mass in our volume of interest, e.g. from a radioactive source (Attix, 2004):

$$D \overset{RE}{=} \frac{d(\Sigma Q)}{dm}$$

CPE is the special case where the general definition of RE is applied valid for charged particles only. That is, any energy transported into our volume by charged particles is compensated by an equal amount of energy transported out by identical particles. This simplifies the dose calculations considerably. If RE exists in a volume, then CPE also exists by definition.

By assuming that the density and atomic composition in V is homogeneous, there are no pertubating magnetic or electric fields and the internal radioactive source (if any) is uniformly distributed within a volume surrounding V by at least the maximum range of the radiation, RE (and thus CPE) exists in V (Attix, 2004).

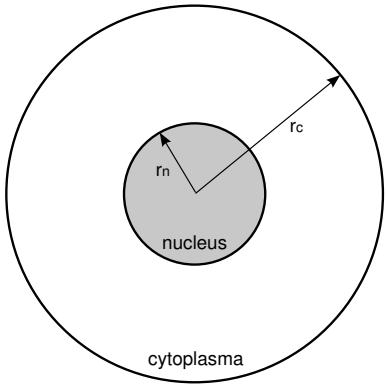

Figure 2.3: *The simplified cell model used in tritium micro dosimetry, with two concentric spheres with radii r_C and r_N (from Søvik, 2002, modified).*

2.3.6 Cellular tritium micro dosimetry

In a cell the condition for RE listed is *not* met. The radioactive source can not be said to be uniformly distributed, resulting in a radiation non-equilibrium where high-activity regions have a net loss of energy, and low-activity regions have a net energy gain (Søvik, 2002). In addition, the electron stopping power is, as we already know, dependent on the kinetic energy of the particle and will therefore vary along its path. This, in addition to electron scatter, will complicate the dosimetry calculations considerably (Søvik, 2002).

Søvik (2002) derives the following model for cellular tritium micro dosimetry, originally from the publication *MIRD Cellular S-values*[3] (Goddu et al., 1997).

Figure 2.4 shows six possible energy transport scenarios. E_1 and E_4 resulting from decay within the nucleus, E_2, E_3, E_5 and E_6 from decay within the cytoplasm. Decays from the extracellular space and neighboring cells are omitted. Furthermore, E_2 and E_4 are resulting in an energy deposit within the nucleus, and the rest are not[4].

The following model is used to estimate the imparted energy from radio nucleides such as tritium in a relatively simple way by the means of so-called *S*-values. The *S*-values, given as absorbed dose per unit activity, in combination with knowledge of the cell and nucleus size and mutual activity distribution, can be used to calculate an estimate of absorbed dose

[3]The full name of the publication is *MIRD cellular S-values: Self-absorbed dose per unit accumulated activity for selected radionuclides and monoenergetic electron and alpha particle emitters incorporated into different cell compartments*.

[4]This is given that all the energy is deposited at the arrow head, which we know is, in fact, not the case. However, we shall justify this approximation.

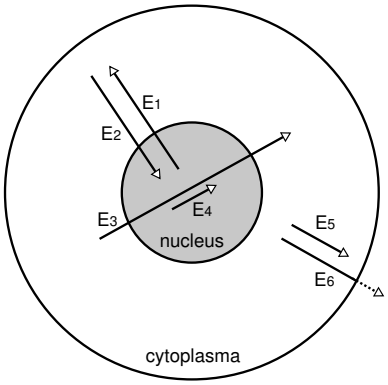

Figure 2.4: *Six possible energy transport scenarios in a concentric spherical cell (as in figure 2.3) (from Søvik, 2002, modified). Two scenarios, E_2 and E_4, contributes directly to the dose in the cell nucleus.*

to the cell's nucleus.

Figure 2.3 shows the basic idea of this model: the cell is modeled as two concentric spheres with cell radius r_C and nucleus radius r_N. The activity (i.e. the tritium) is considered homogeneously distributed within the cytoplasm and the nucleus, hence the simplicity of the model.

The mean absorbed dose $D(R_t \leftarrow R_s)$ from source region R_s to target region R_t is then (Goddu et al., 1994)

$$D(R_t \leftarrow R_s) = A_s S(R_t \leftarrow R_s) \tag{2.17}$$

where A_s is the activity in the source region. The S-value is defined as

$$S(R_t \leftarrow R_s) \equiv \Delta \cdot \frac{\phi(R_t \leftarrow R_s)}{m_t} \tag{2.18}$$

where Δ is mean energy released per decay, m_t is the target region mass and $\phi(R_t \leftarrow R_s)$ is the fraction of energy released in region R_s absorbed in region R_t (Goddu et al., 1994). This fraction can be estimated from

$$\phi(R_t \leftarrow R_s) = \int_0^\infty \Psi_{R_t \leftarrow R_s}(x) \frac{1}{E} \left(\frac{dE}{dx}\right)_{R(E)-x} dx \tag{2.19}$$

where E is the initial energy of the ejected electron, $\Psi_{R_t \leftarrow R_s}$ is the geometric reduction factor and $\left(\frac{dE}{dx}\right)_{\mathcal{R}(E)-x}$ is the electron stopping power evaluated in point $\mathcal{R}(E) - x$, that is, the remaining mean range (see section 2.3.2) of an electron of energy E reaching x (Goddu et al., 1994).

Given a vector $\vec{x}$ with length $|\vec{x}| = x$ starting in an arbitrary point in R_s, the geometric reduction factor is the mean probability of $\vec{x}$ ending in R_s. $\Psi_{R_t \leftarrow R_s}$ as a function of x and radii r_t and r_s is given in appendix E, as well

as the functions used to estimate the range of the electron as a function of it's energy.

The cellular S values as a function of cell and nucleus radii from Goddu et al. (1994) are given in appendix F.

The mean dose-rate to the nucleus, $\dot{D}_N$, is

$$\dot{D}_N = A_C \left[f_N S(R_N \leftarrow R_N) + f_{Cy} S(R_N \leftarrow R_{Cy}) \right] \tag{2.20}$$

where A_C is the intracellular activity, $S(R_N \leftarrow R_N)$ is the dose to the cell nucleus per unit activity in the nucleus itself, $S(R_N \leftarrow R_{Cy})$ is the dose to the cell nucleus per unit activity in the cytoplasm. f_N and f_{Cy} is the fraction of the intracellular activity in the nucleus and the cytoplasm, respectively. The standard error of the dose-rate is

$$se_{\dot{D}} = \sqrt{\left(\frac{\partial \dot{D}}{\partial A_C} \cdot se_{A_C} \right)^2 + \left(\frac{\partial \dot{D}}{\partial f_N} \cdot se_{f_N} \right)^2 + \left(\frac{\partial \dot{D}}{\partial f_{Cy}} \cdot se_{f_{Cy}} \right)^2}. \tag{2.21}$$

The mean absorbed dose in the nucleus is

$$D_N = \tilde{A}_C \left[f_N S(R_N \leftarrow R_N) + f_{Cy} S(R_N \leftarrow R_{Cy}) \right] \tag{2.22}$$

where $\tilde{A}_C$ is the activity integrated over the radiation period (i.e. the total number of disintegration events during the irradiation). The standard error of the mean absorbed dose is

$$se_D = \sqrt{\left(\frac{\partial D}{\partial \tilde{A}_C} \cdot se_{\tilde{A}_C} \right)^2 + \left(\frac{\partial D}{\partial f_N} \cdot se_{f_N} \right)^2 + \left(\frac{\partial D}{\partial f_{Cy}} \cdot se_{f_{Cy}} \right)^2}. \tag{2.23}$$

In section 5.4.1 in the *Discussion* chapter, some challenges and problems with cellular tritium microdosimetry is addressed.

2.4 Cell biology

All living things are made up of protoplasm, consisting of both small molecules such as amino acids and monosaccharides and macromolecules such as lipids, proteins and polysaccharides, all suspended or dissolved in water.

A cell is the smallest protoplasm (surrounded by a plasma membrane) capable to sustain life on its own (Podgorsak, 2005).

The cell are the building blocks of life as we know it, and an understanding of human biology depends on an understanding of cell biology.

This section deals with cell biology in general, in addition to some considerations concerning the MCF-7 cell (presented in section 3.1.1 on page 51), being the cell used in the experiments performed.

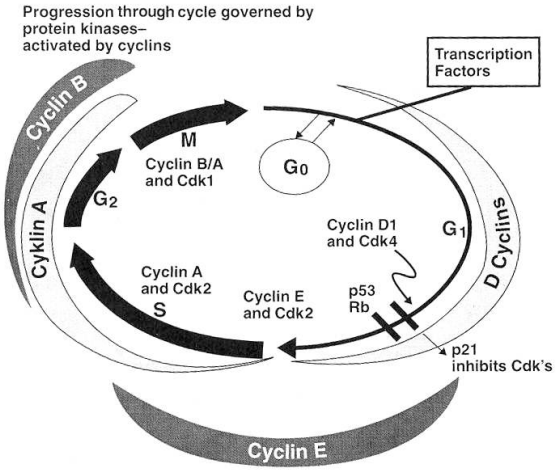

Figure 2.5: *The cell cycle with some of its central control mechanisms (from Hall and Giaccia, 2006).*
The figure also illustrates the checkpoints at which p53 and pRb have central roles (see section 2.5.5).

2.4.1 The cell cycle

This section is largely based on Hall and Giaccia (2006), Alberts et al. (2008) and Davis (1996).

Every single cell is a copy of an already existing cell, where the new cell (ideally) is identical to its predecessor. This duplication is a result of the *cell cycle*, the most basic and important property of a proliferating cell.

The cell cycle is the lifespan and associated control mechanisms of a single cell—from its creation to its own division where two new cells are created[5] (Alberts et al., 2008).

Observed through a light microscope, the only cellular event that can be directly observed is the mitosis—the cell division itself (Hall and Giaccia, 2006). The study of the cell cycle has therefore been difficult, as the mechanisms behind cell proliferation is complex and involves a large numbers of different molecules.

The cell cycle for most cultured animal cells is 15-25 hours (Davis, 1996), but the most rapidly proliferating mammalian cells have cell cycles as short as about 9 hours[6]. In contrast, brain and nervous cells can have doubling time too long to be experimentally measured ($\bar{T}_2 \to \infty$).

[5]This is only correct for *somatic* cells. Germ cells, on the other hand, undergo meiosis (Podgorsak, 2005). Although important, the meiosis will not be addressed further in this thesis.

[6]Often, it is the mean doubling time $\bar{T}_2$ in a population that is of interest, as the individual diversity of cell cycle times T_2s may be large and difficult to monitor.

The duration of the mitosis (M phase) is somewhat independent of cell type, usually lasting 0.5-1 hour (Hall and Giaccia, 2006; Alberts et al., 2008; Davis, 1996).

The remaining cell cycle is called the interphase, which is further divided into the G_1, S and G_2 phases. The S and G_2 phases have, in addition to M phase, a duration that does not vary much in length in mammalian cells, almost regardless of total cell cycle time. S phase typically lasts 7-8 hours, and G_2 phase 2-4 hours (Davis, 1996).

The G_1 phase, however, is held responsible for most of the variation in cell cycle times between cell types. Its duration is usually in the range of 6-15 hours (Davis, 1996). However, G_1 may not exist in the most rapidly dividing cells (Davis, 1996).

A non-cycling cell is said to be in G0 phase.

The S phase is the stage at which DNA is duplicated, in a complicated process known as DNA synthesis.

The complex cell division (M phase), begins with a chromosome condensation. Then, each pair of sister chromatides is attached to the mitotic spindle, and travels to opposite poles. The chromosomes decondense and the cytokinesis (the cytoplasmic division) takes effect.

The cell cycle control system

Being a fundamental property of cell proliferation, the cell cycle is strictly controlled and monitored, and is regulated by activation and inactivation of certain molecules within the cell (Hall and Giaccia, 2006; Alberts et al., 2008).

The *cell cycle control system* operates somewhat like a conductor of an orchestra—cueing the different parts in a symphony and making sure everything happens in the correct order, and tries to conduct appropriate measures to correct any errors or abnormalities.

As with the orchestra, the cell cycle is a feedback-system where information received during the process is controlling the process itself.

Cellular checkpoints

The control system consists of several *checkpoints*, where intra- and extracellular properties are monitored and, in case of abnormalities, proper actions are taken.

A cell cycle checkpoint may induce a pause in the cell cycle allowing time for environmental changes or repair processes, command the cell into G0 (resting phase) or simply kill it. With regard to the musical conductor

analogy, the maestro may indeed suggest a break if the performance is not to his satisfaction (but he usually does not end up killing the orchestra).

A very important checkpoint is the *restriction point* before the S phase. Here, the cell cycle control system determines if the cell is ready to begin DNA replication. If the system allows passage toward S phase, DNA replication is initiated no matter what (Alberts et al., 2008).

In addition, checkpoints plays an extremely important role in the field of radiation biology, as a pause in the cell cycle may provide time for cellular repair processes (see section 2.5.4).

A cell may proliferate even if the checkpoints are disabled, as the cellular checkpoints are not vital to the cell cycle. In fact, cancer cells often have a corrupt control system. In fact, control systems in cell cycle progression is often found to be abnormal in cancer cells, leading to unrestricted cell proliferation (Alberts et al., 2008). Oncogenic HPVs (human papillomavirus) has been shown to transcribe proteins leading to G_1 checkpoint abrogation in low dose-rate exposed cells (DeWeese et al., 1997)[7].

To maintain a healthy cell and organism an intact cell checkpoint system is thus of great importance.

Cyclin and the cyclin dependent kinases

The cell cycle control system is regulated by molecules called *cyclin dependent kinases (Cdk)* and their respective *cyclins*. The control system uses negative feedback to control the events, because in the incredibly complex process a cell cycle is, it yields less room for errors. This is due to the fact that it is much easier to check for the absence of any STOP messages than it is to control if there exists a sufficient number of GO messages.

The cyclin-Cdk-complexes may trigger cell cycle events, and are therefore of great importance in regulating the cell cycle (see figure 2.5).

The concentration of Cdks are somewhat constant during a cell cycle, it is rather the cycline concentration that varies and thus control the cell cycle progress.

Cyclin-Cdk-complexes may in turn be inhibited by phosphorylation by proteins known as Cdk inhibitor proteins (CKIs).

Cell cycle blocking

The cell cycle checkpoints may result in *cell cycle blocking*.

The *retinoblastoma protein* pRB may bind to the *gene regulatory protein* E2F and block passage to S phase by obstructing transcription of S phase

[7] However, the cited article notes that no consistent difference in cellular survival was found when compared to cells with functional G_1 checkpoint (DeWeese et al., 1997).

genes. Loss of both RB gene copies has been shown to cause eye cancer (retinoblastoma) in children, hence the name. Thus, pRB plays an important role in the cell cycle control mechanism.

There are at least two checkpoints that react to DNA damage, one in late G_1 and one in late G_2, regulating entry to S phase and M phase, respectively.

In addition, stress factors such as hypoxia have been shown to arrest the cell cycle in the S phase (Seim et al., 2003). Cellular hypoxia is treated in section 2.6.

2.4.2 Cell growth and colony growth phases

The cyclic behavior of the cells results in an exponential increase in cell number as the cells are allowed to proliferate. The time a group of cells use to double its number is called the cellular doubling time, T_2.

Given a simple exponential increase in cell number, the cell number at any time t is

$$C(t) = C_0 e^{bt} \tag{2.24}$$

where C_0 is the cell number at time $t = 0$. The doubling time is thus

$$T_2 = \frac{\ln 2}{b}. \tag{2.25}$$

In this thesis the mean doubling time $\bar{T}_2$ (also called population doubling time, PDT) is used, as it applies to a whole population of cells. $\bar{T}_2$ are given as (Davis, 1996)

$$\bar{T}_2 = \frac{\text{Total time elapsed}}{\text{Number of generations}} \tag{2.26}$$

Studying the cell proliferation *in vitro* in a freshly recultivated cell flask, cell proliferation phases will be seen in which the increase in cell number is *not* exponential.

The initial phase, called the *lag phase*, is due to the stress the cells have been exposed to from cultivation and trypsination, and represents a certain amount of time the cells need to compose themselves. The duration of the lag phase is dependent on, among other factor, cell seeding density (Davis, 1996). Sparsely seeded cells will exhibit a longer lag phase.

After the log phase, a exponential growth phase is (ideally) observed. This is when the cells are considered "healthiest" (Davis, 1996), and a cell fraction as high as 0.9-1 may be in active cell cycle.

In addition, if the cells grow to the limits of confluency, a *plateau phase* will be seen. This phase is due to a reduction in the cellular growth as the

growth area becomes cramped, in addition to an accumulation of cellular waste products (if the medium is not changed) (Davis, 1996). When a culture is in the plateau phase, only a fraction of 0-0.1 of the cells are in active cell cycle. Cell death may be balanced by cell division (Davis, 1996), with no net increase in living cells. In addition, daughter cells may be released into the medium (Davis, 1996), causing artifacts in the measurement of oxygen profiles (see section 3.7.1).

If no maintenance are performed to the cells, the culture will reach a *decline phase* where cell death is uncompensated (Davis, 1996) and the number of (living) cells are decreasing.

2.4.3 Biological effects of tritium substitution

The biological effect of tritium itself, in addition to the energy deposit due to its decay, has not yet been considered. The incorporated ^{3}H results in different chemical and physical properties of tritiated valine compared to cold valine, resulting in an isotope effect.

When ^{3}H decays, $^3He^+$ is formed (see equation 2.5), giving rise to a change in the chemical property of the associated molecule (in this case, valine). However, the concentration of tritiated valine required to produce any significant biological disturbance due to changed chemical (and thus biological) properties are higher than the concentration used in the present experiments (Feinenegen, 1967).

The recoil energy of the helium atom is in the order of 3 eV, an energy considered too low to cause any further ionizing damage (Attix, 2004).

The biological effect of the tritium substitution can therefore be considered to primarily be due to the energy deposition discussed in section 2.1.2.

2.4.4 DNA

The *DNA* (*deoxyribonucleic acid*) is the blueprint of life. All genetic information is carried in a linear sequence of base pairs. Chadwick and Leenhouts published in 1973 their important discovery that the DNA strands were whirled up in a double helix shape, as shown in figure 2.6 (Chadwick and Leenhouts, 1973).

The DNA molecule consists of two complimentary strands of nucleotides linked together in a chain of alternating sugar and phosphates. The strands are held together by hydrogen bonds between the linear arrangement of base pairs that constitutes the code for every gene the organism will ever need to synthesize (Alberts et al., 2008).

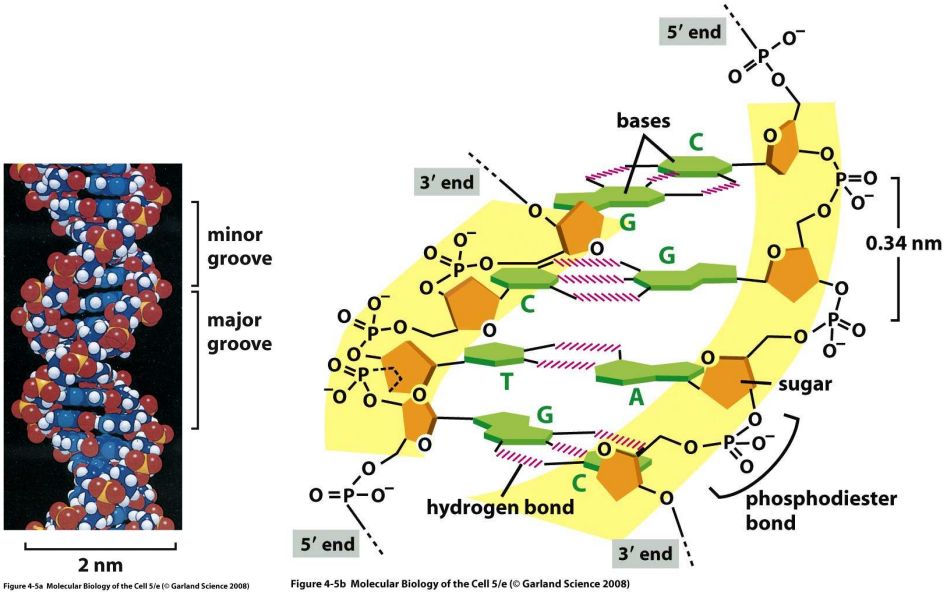

Figure 2.6: *The double helix of the deoxyribonucleic acid DNA (from Alberts et al., 2008).*

Figure 2.7: *Pierre Curie is said to have used a radiation tube to induce a radiation ulcer on himself, illustrating an observable damage of radiation (from Hall and Giaccia, 2006).*

2.5 Radiation biology

As the name suggests, the term *radiation biology* includes a combination of the disciplines of radiation physics and biology.

First, the physical principles of radiation interaction theory, energy impartion theory and dosimetry treated in section 2.2, *Radiation physics* and 2.3, *Dosimetry* are very important. Second, the biological principles treated in section 2.4, *Cell biology* gives us the foundation to understand the effects of irradiation of biological systems.

Historically, soon after the discovery of x-rays in 1895 by Röntgen, several immediate biological effects such as skin burns and eye irritation were described (see figure 2.7), and already in 1897 x-rays was used to treat cancer. In 1902, however, it was reported that cancer had occurred in a x-ray ulcer (Hall and Giaccia, 2006).

The field of radiation biology has since then grown, increasing the understanding of the effect on biological system by ionizing radiation. In this section, a somewhat brief summary of the most important concepts are presented.

2.5.1 Cell irradiation

What is the possible consequences of radiation to a cell? Podgorsak (2005) classifies the fate, in general, of an irradiated cell into nine possible outcomes:

No effect

Division delay The mitosis is delayed, but no sustaining damage is induced

Apoptosis Programmed cell death—the cell dies and disintegrates before division and is neatly packaged before being digested by neighboring cells

Reproductive failure The cell dies attempting to divide

Genomic instability A delayed form of reproductive failure

Mutation The cell survives, but changes in the DNA is induced by the radiation

Transformation The cell survives, but the mutation leads to transformation and possible carcinogenesis

Bystander effects Unirradiated cells can be damaged by signals from irradiated neighboring cells

Adaptive responses The cell reacts to irradiation by becoming more resistant to subsequent irradiation (Podgorsak, 2005)

2.5.2 Poisson function in cancer treatment by radiation

Radiation can be very effective in killing cancer cells in patients, and thus stagnate the tumor growth[8].

The Poisson distribution gives us the probability of a succesfull treatment (Mayles et al., 2007). The probability P_n of n surviving cells are given as

$$P_n = \frac{\mu^n}{n!} e^{-\mu}$$

where μ is the theoretical mean cell survival (see section 2.5.6). The probability P_0 for a succesfull treatment (i.e. zero surviving cancer cells) is

$$P_0 = e^{-\mu}.$$

2.5.3 Radiation damage

Hall and Giaccia (2006) points out that there are strong circumstantial evidence that DNA damage is fundamentally linked to cellular radiation responses.

[8]The tumor growth rate for the MCF-7 cell is indeed inhibited by irradiation, and does not fully recover after irradiation. The growth rate recovery decreases with increased dose (Guirado et al., 2003).

As seen in section 2.4.4, a functional DNA molecule is vital to the cell. Unrepaired damage in the cell's blueprint can therefore be critical for the cell, and may lead to cell death or, often worse, cell mutation.

Before beginning to discuss the different kind of damage radiation can induce in a cell, a precise definition of the term cell death must be established. With regard to cancer cells, Hall and Giaccia (2006) define cell death as the loss of clonogenic properties, that is, a cancer cell is per definition dead when it has lost its ability to divide and therefore proliferate. A cell may however, as a result of radiation induced damage, continue to grow without dividing. This is sometime referred to as a fried egg. Such a living (but not clonogenic) cancer cell is therefore, in our context, regarded as dead.

Radiation damage to a cell and its DNA is divided into three categories:

Lethal damage is, per definition, a cell damage that inevitably leads to its death regardless of any repair processes.

Potential lethal damage is damage that, if not repaired, will lead to cell death. It only differs from lethal damage in being possible for the cell to repair if given enough time for repair processes.

Sublethal damage is damage that by itself is not lethal. However, a combination of multiple sublethal damages can be lethal if not separated by sufficient space and time.

Furthermore, the actual damage to the DNA molecule is typically classified into either single or double strand breaks:

Single stand break (SSB) is a sublethal damage, as it *by itself* cannot induce lethal chromatid abbretions since only one DNA strand is affected. In general, a SSB is repairable due to the fact that one strand is intact and may thus be used as a template to regenerate the other, destroyed strand.

Double stand break (DSB) is potentially lethal, as repair processes becomes considerably more complex since both DNA stands are damaged. If two or more SSBs occur sufficient close in time and space, they can result in a DSB, which may lead to cell death if not repaired.

2.5.4 Cellular countermeasures to stress

Cells are constantly exposed to different kinds of stress, many of which resulting in some form of DNA damage (section 2.5.1). This may, if the

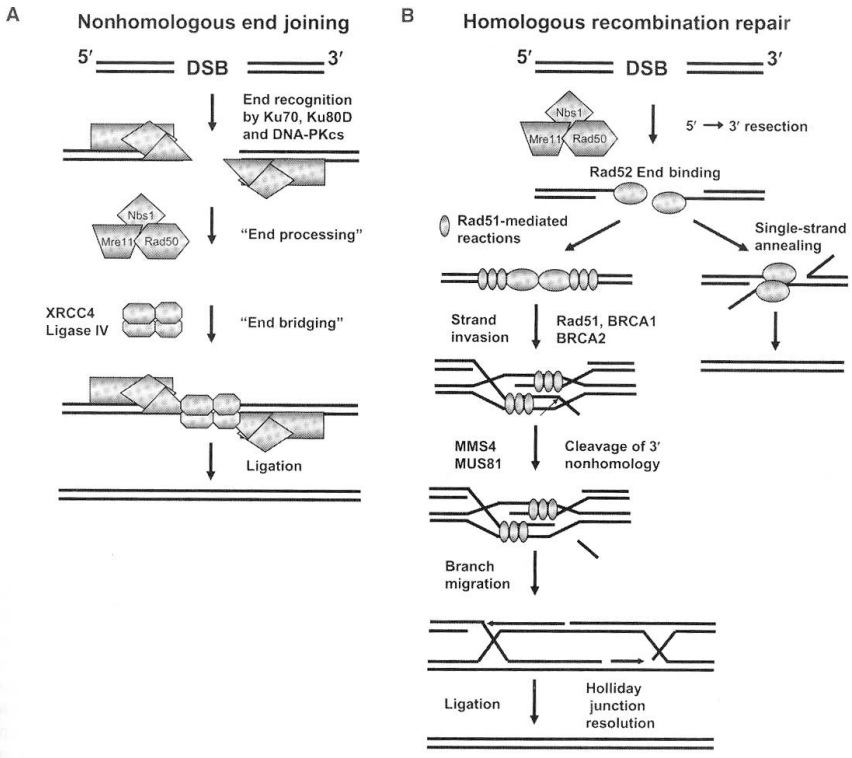

Figure 2.8: *Cellular repair processes (from Hall and Giaccia, 2006). Illustrating the basic principles of both nonhomologous end joining and homologous recombination repair.*

damage is not repaired, lead to chromosome and/or chomatid aberrations (Hall and Giaccia, 2006). To avoid cell death, or worse, mutations or transformations that may lead to carcinogenesis, cellular repair processes are vital to the well-being of the organism. As the DNA damage may be more or less complex, more or less complex repair processes are required.

The role of the checkpoints

In the cell cycle there are two DNA damage checkpoints (see section 2.4.1); one in late G_1 monitoring entry into S-phase, and one in late G_2 controlling that the cell is ready to proceed into mitosis (Alberts et al., 2008). Each of these checkpoints strive to assure that the cell has sufficient time to conduct necessary repair processes.

In late G_2, damaged DNA signals to the activation of *Cdc25*, blocking activation of M-Cdk and thus entry into mitosis (Alberts et al., 2008). If the damage is repaired, M-Cdk is unblocked and M-phase entry is allowed.

The repair processes

SSBs are simply repaired by using the intact strand as a template. DNA damages such as DSBs, however, need more complex repair mechanisms.

Homologous recombination repair (HRR), a process illustrated in figure 2.8 b), taking place in the G_2-phase uses the double set of chromosomes to acquire information from the copy of a damaged DNA section (Pettersen, 2007). This way, intact copies of the damaged genes are used as templates (Hall and Giaccia, 2006).

There are other repair mechanisms, such as *non-homologous end joining* (NHEJ), illustrated in figure 2.8 a), that merely removes the damaged section of the DNA and "glues" the two resulting ends together. This leads, however, to changes in the DNA, but may be the lesser of two evils due to the fact that only a small fraction of the DNA represent genes (Hall and Giaccia, 2006; Pettersen, 2007).

The state of hypoxia has been shown to affect the cellular ability to perform certain repair processes, as well as the ability to undergo apoptosis (see section 2.6) (Bindra et al., 2004).

2.5.5 The p53 factor

In late G_1, damaged DNA may lead to the activation of the very important tumor suppression factor *p53*, playing a key role in cellular stress responses by inducing or repressing several genes involved in a.o. cell cycle arrest, apoptosis, DNA repair and angiogenesis (Lacroix et al., 2006;

Young et al., 2005; Zhao et al., 2009). It acts as a tumor suppressor by binding and regulating its target genes (Zhao et al., 2009). p53 may, as a response to stress such as ionizing radiation, e.g. promote the transcription of genes inhibiting the G_1/S-Cdk and S-Cdk and thus preventing entry into S-phase (Lin and Chang, 1996; Alberts et al., 2008; Lacroix et al., 2006; Essmann et al., 2004).

p53 was discovered in 1979, and was defined as an oncogene until 1989 (Zhao et al., 2009).

Normally, p53 is highly unstable (by its interaction with the *Mdm2* protein) and thus only present in the cell in very small concentrations. Cellular stress such as DNA damage propagates phosphorylation of p53 through proteins such as the *ataxia telangiectasia-mutated (ATM)* protein which reduces the binding of p53 to Mdm2, making it possible to increase p53 concentration within the cell (Alberts et al., 2008; Zhao et al., 2009). Different pathways to stabilizing p53 exist in response to different forms of stress (Ashcroft et al., 2000).

Mutations in the p53 gene are found in at least half of all human cancers (Pettersen, 2007), and is in fact the most frequently mutated gene in human cancers (Zhao et al., 2009), illustrating its importance as a tumor suppressor. During radiation treatment of cancer, radio modifying chemicals such as D7 (diospyrin diethylether) has been shown to upregulate the p53 and thus sensitize the cells to increase effectiveness of the treatment (Kumar et al., 2007).

The MCF-7 cell line does, however, have a normal p53 function (Fan et al., 1995) and a strong p53 mediated G_1-phase arrest expressed as a result of ionizing radiation (Hain et al., 1996). Increased levels of p53 has been observed in the MCF-7 cell line for up to 30 hours after irradiation (Hain et al., 1996). Studies has also shown an increased concentration of p53 in the MCF-7 cell as a result of hypoxia (Chandel et al., 2000).

Apoptosis

If a cell is no longer needed or wanted, it may be beneficial to the organism that it is eliminated peacefully and neatly. *Apoptosis*, or programmed cell death, is a process in which the cell commits suicide. This is a very important property of the cell, apoptosis is for example in an embryo important in the process of separating the fingers (Alberts et al., 2008).

In addition, apoptosis is an important countermeasure to carcinogenesis, and may be a result of e.g. severe DNA damage. The previously mentioned p53 protein are known to have the ability to induce apoptosis (Pettersen, 2007; Lacroix et al., 2006), as a dysfunctional p53 has been shown to disrupt apoptosis and promote tumor growth (Lacroix et al.,

2006).

However, the MCF-7 cell line, being a tumor cell type with a normal p53 expression, does *not* willingly undergo p53-mediated apoptosis (Fan et al., 1995). In fact, MCF-7 has been considered especially resistant to apoptosis induced by ionizing radiation (Essmann et al., 2004). This has been linked to the fact that MCF-7 lack *caspase-3*, a proteolytic enzyme in the caspase family[9] (Essmann et al., 2004).

It has been shown that apoptosis in the MCF-7 cells relies on sufficient energy and oxygen availability, and that cells with sub-optimal energy levels may become aponecrotic (a state in which the cells shows signs of both apoptosis and necrosis) as a result of an incomplete apoptosis execution (Formigli et al., 2002).

On the other hand, an inhibition of the p53 function in the MCF-7 cells has shown to have a sensitizing effect on certain DNA-damaging agents other than ionizing radiation (Fan et al., 1995).

In addition, chemicals such as β-lapachone[10], a naturally occurring compound found in the bark of the Lapacho tree, may induce apoptosis without p53 activation (Wuerzberger et al., 1998).

Apoptosis is an "all-or-nothing" process, meaning that if apoptosis is initiated, it is bound to be completed (Alberts et al., 2008).

2.5.6 Cell survival curves

By plotting the fraction of surviving irradiated cells as a function of radiation dose, a survival curve can be produced. Typically, it is plotted in a semilogarithmic[11] plot.

The slope of the curve reveals several important properties of the cell line in question. Chadwick and Leenhouts presented in 1973 a theory fitting the survival curve with an equation on the form (Chadwick and Leenhouts, 1973)

$$S = e^{-(\alpha D + \beta D^2)}. \tag{2.27}$$

In this model, often referred to as the *LQ (linear-quadratic) model*, the α component represents the linear part of the cell killing mechanism, and the β component represents the quadratic part[12] (see figure 2.9).

[9] Caspases are responsible for cleaving intracellular proteins and thus help killing the cell (Alberts et al., 2008).

[10] 3,4-dihydro-2,2-dimethyl-2H-naphtol[1,2-b] pyran-5,6-dione (Wuerzberger et al., 1998)

[11] A semilogarithmic plot has one linear axis (in this case, the abscissa) and one logarithmic axis (the ordinate).

[12] In reality, it is the linear and quadratic part of the exponent. But as the data typically is plotted on semilogarithmic axis, the equation becomes $\ln S = -(\alpha D + \beta D^2)$.

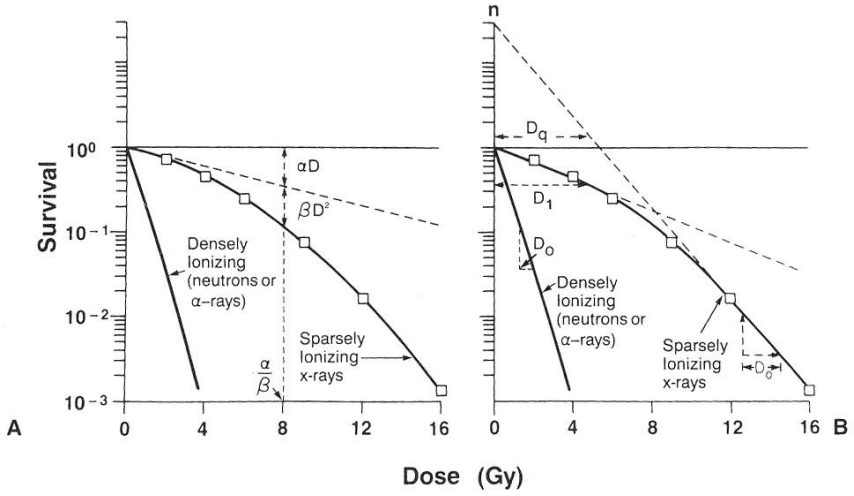

Figure 2.9: *A quantitative cellular survival curve for irradiated mammalian cells (from Hall and Giaccia, 2006). Densely ionizing radiation (i.e. α particles and heavy ions) produces a straight line in this semi-logarithmic plot, while sparsely ionizing x-rays produce a curve with a noticeable shoulder.*
A: the linear quadratic model (α-β model).
B: the multitarget model (not addressed in this thesis).

Equation 2.27 can be seen as a product of two independent Poisson probability functions, describing single- (α) and double-hit (β) dose kinetics Chapman (2003). The surviving fraction S is in this picture the product of the individual probabilities of lethal damage given by exponentials αD (mean lethal damage from the linear process) and βD^2 (mean lethal damage from the quadratic process).

It has been proposed that α and β correspond to the concepts of double and single DNA strand breaks. The linear component αD represents the probability of DSBs (that are somewhat difficult to repair), and the quadratic component βD^2 represents the probability for two or more independent SSBs to occur close enough in space and time to become a DSB (Hall and Giaccia, 2006).

A relatively linear survival curve (in a semi-logarithmic plot) is represented by a strong linear component with no shoulder (i.e. large α/β ratio) and is typically seen in early responding tissues (such as skin and intestinal epithelium, mucosa and tumor tissue). On the contrary, a weak linear component with a large shoulder (i.e. a low α/β ratio) is typically seen in late responding tissues (such as kidney, lung and nervous tissue.).

With high-LET radiation, the single-hit α-mechanism dominates (Chapman, 2003), indicating severe radiation induced damages leaving repair processes limited successfully. It also yields a larger indirect hydroxyl ef-

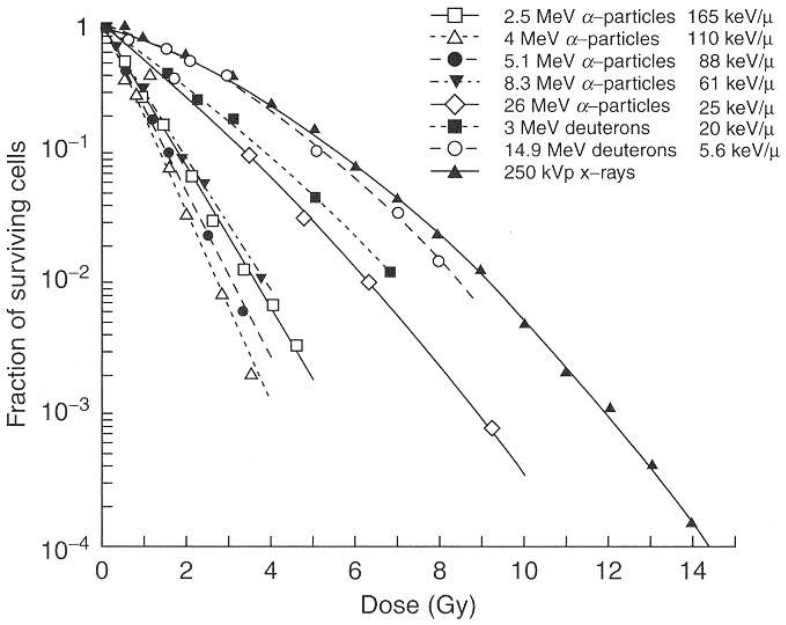

Figure 2.10: *Dose-response plots for human kidney cells exposed to different radiation qualities (mean LET values are listed) (from Mayles et al., 2007).*

fect (section 2.5.7) and smaller OER (section 2.5.10). See figure 2.10. LET are discussed in section 2.3.3.

2.5.7 Direct and indirect effect of radiation

We have until now steered clear of the physics (and chemistry) behind radiation damage. We shall now see the two main processes of how radiation may create damage in DNA, and see how the environment of the cell affect its sensitivity to radiation.

Initially it is natural to picture the energy imparted directly in DNA as a main contributing process leading to cell damage and possibly death. As we shall se, however, this is not the whole story.

Dertinger and Jung (1970) refers to an example indicating the relevance of the environment of the target molecule. Referring to an experiment where the inactivation of an enzyme is studied by exposing it to a selection of doses, the result clearly shows a radiation sensitizing effect when irradiated in a aquatious environment, relative to irradiation in a dry environment.

This motivates the definition of two main types of effects of cell irradiation:

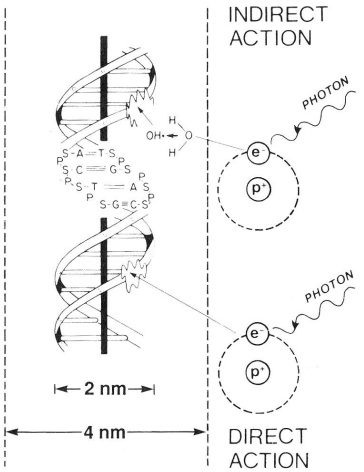

Figure 2.11: *The direct and indirect effect of radiation (from Hall and Giaccia, 2006). The indirect effect is illustrated to show the importance of a nearby water molecule produce radicals, as described in the text. As shown, it is estimated that it is water molecules within a cylinder of twice the DNA helix diameter that can induce DNA damages (Hall and Giaccia, 2006).*

The direct effect represent the fraction of damages that origin directly from primary ionizations or excitations in the target molecule (Pettersen, 2007). In other words—the direct effect is the effect of energy deposited directly in DNA. The direct effect is the dominant process regarding high-LET radiation (see section 2.3.3) (Dertinger and Jung, 1970).

The indirect effect is due to unstable radicals (typically that of water) created by radiation in the cell's environment which induce damage in DNA. In the present context, the indirect effect is mostly due to the presence of water molecules.

It is important to remember that the direct and indirect effect of ionizing radiation does *not* correspond to the concepts of directly and indirectly ionizing radiation (see section 2.2.1).

The chemistry of the indirect effect

The production of water radicals $H^\bullet$ and $OH^\bullet$ starts with the ionization or excitation of water (Dertinger and Jung, 1970; Pettersen, 2007):

$$\begin{aligned} H_2O + \epsilon &\rightarrow H_2O^+ + e^- \\ H_2O + \epsilon &\rightarrow H_2O^*. \end{aligned}$$

The initial ions have an extremely short life span (in order of 10^{-10} s), but will participate in reactions with water to form stable free radicals (Attix, 2004):

$$\begin{aligned} H_2O^+ &\rightarrow H^+ + OH^\bullet \\ e^- + H_2O &\rightarrow OH^- + H^\bullet \\ H_2O^* &\rightarrow H^\bullet + OH^\bullet. \end{aligned}$$

A free radical, marked with a $^\bullet$, is uncharged and therefore electrically stable, but has an unpaired electron in the outer shell which makes it chemically highly reactive (Attix, 2004). The free radicals have a life span in the order of 10^{-5}. Compared to the initial ions, the secondary radicals experience a life time ten thousand times longer.

In addition to the radicals $H^\bullet$ and $OH^\bullet$ the free electron e^- may polarize a water molecule and make a stable configuration known as a hydratized electron e^-_{aq} (Dertinger and Jung, 1970).

The two $H^\bullet$ and $OH^\bullet$ radical may recombine and form H_2 and H_2O_2 which, from a biological point of view, has little or no damaging effect (Pettersen, 2007). It is therefore interesting to note that high LET radiation, densely producing water radicals, suffer more from recombination and therefore have a less important indirect effect (Pettersen, 2007).

2.5.8 Radiosensitivity and the cell cycle

As mentioned, the radiosensitivity of a cell is closely related to the possibility the cell has to repair radiation induced damages. In general, cells in M- and G_2-phase are most radiosensitive, having a steep and shoulderless survival curve (Hall and Giaccia, 2006). In late S-phase the cell is typically most resistant, having a less steep survival curve with a very broad shoulder (Hall and Giaccia, 2006). In terms of the LQ-model (see section 2.5.6), the α and β coefficients are thus clearly independent functions of cell cycle phase (Chapman, 2003).

The radioresistance in late S-phase is thought to be due to the fact that homologous recombination repair (see section 2.5.4) is more likely to occur after DNA replication (Hall and Giaccia, 2006).

Just before entry into M-phase, the chromosome material are condensed in to discrete entities, correlating with the phase in the cell cycle where radiosensitivity is at its maximum (Hall and Giaccia, 2006). In addition, G_2 is subject to the G_2 block effect for low dose-rate irradiation mentioned in section 2.5.11.

An absent p53 function (and thus reduced control mechanisms in G_1) has been suggested to leave cancer cells more vulnerable to G_2 checkpoint

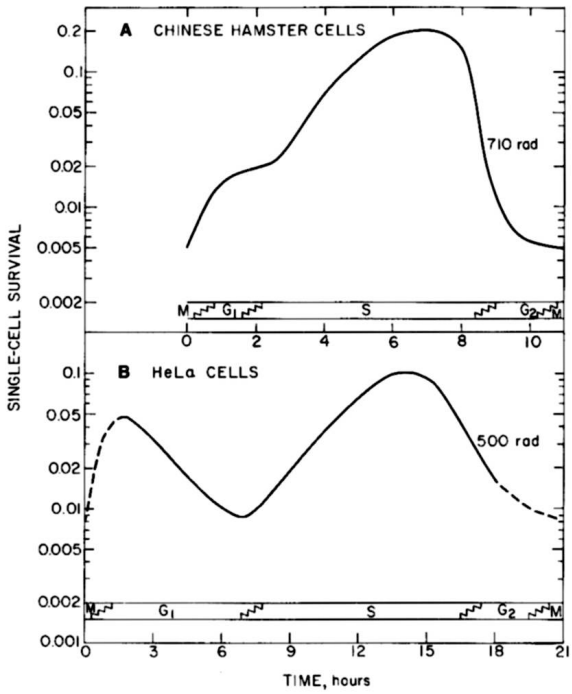

Figure 2.12: *Radiosensitivity (age-response curves) in the cell cycle . Two different cell lines are shown, with varying G_1 duration. Curve A is Chinese hamster cells and B is HeLa cells (taken from Hall and Giaccia, 2006, originally from Sinclair, W.K.: Dependence of radiosensitivity upon cell age in* Proceedings of the Carmel Conference on Time and Dose Relationships in Radiation Biology as Applied to Radiotherapy*, 97-107, 1969).*

abrogation (Fan et al., 1995). However, if the dose is delivered with a lower rate (i.e. lower dose-rate), cells has been shown to respond differently, as treated in section 2.5.11.

High-LET radiation, however, yields an cell cycle phase-response function that is nearly flat, indicating an independence on radiosensitivity and cell cycle phase (Hall and Giaccia, 2006).

2.5.9 The oxygen effect

In 1912, Swartz discovered that that the skin reaction on his arm was reduced if the apparatus was pressed hard onto the skin, but it was not until 1923 a correlation between molecular oxygen presence and radiosensitivity was published by E. Petry (Hall and Giaccia, 2006).

The *oxygen effect* in which a presence of oxygen increases the biological effect is now a well-known mechanism in cellular radiobiology. As mentioned in section 2.5.7, the damage in the cellular DNA may be due to both a direct and an indirect action. From a molecular point of view, the oxygen effect is also divided into the *direct* and the *indirect oxygen effect*.

In general, the biomolecular radicals is created from radiation by

$$MH + \gamma \rightarrow {}^{+}MH^{-} \rightarrow M^{\bullet} + H^{\bullet} \tag{2.28}$$

where MH is an intact biomolecule and $M^{\bullet}$ is the remaining molecule radical after loosing the hydrogen, $H^{\bullet}$ (Dertinger and Jung, 1970; Pettersen, 2007).

The *oxygen effect* is the effect where oxygen interfere in the process of repairing the reactive $M^{\bullet}$ radical. The distinction between the direct and the indirect oxygen effect is described below.

The direct oxygen effect

The polarized biomolecule ${}^{+}MH^{-}$ created following equation 2.28 may spontaneous restitute

$${}^{+}MH^{-} \rightarrow MH \tag{2.29}$$

as the polarization is a highly reversible state (Pettersen, 2007). The oxygen may, however, interfere with this restitution by abducting an electron following

$${}^{+}MH^{-} + \mathrm{O}_2 \rightarrow MH^{+} + \mathrm{O}_2^{-} \rightarrow M^{\bullet} + H^{+} + \mathrm{O}_2^{-} \tag{2.30}$$

due to the great electron affinity of the oxygen. The spontaneous restitution is thus made impossible. This is the *direct oxygen effect*, in which the oxygen has a sensitizing effect.

The indirect oxygen effect

In addition to the direct oxygen effect, the oxygen may react directly with the bioradical created in equation 2.28:

$$M^{\bullet} + O_2 \rightarrow MO_2 \tag{2.31}$$

This fixes the damage done and compromises the repair mechanisms.

In addition to the spontaneous restitution in equation 2.29, the damage (that is, the biomolecule radical) may restitute reacting with the so-called water radicals e^-_{aq} and $H^{\bullet}$. The indirect oxygen effect, however, also involves the oxygen reacting with the water radicals, thereby reducing the possibility of this restitution.

Both these actions sensitize the biological system, and oxygen thus has a sensitizing effect. In dry systems, where water radicals are absent, the dominant effect is equation 2.31 (Pettersen, 2007).

2.5.10 Oxygen enhancement radio

The *oxygen enhancement ratio* (OER) is a measure of the difference in radiosensitivity between cells in the presence of molecular oxygen and hypoxic cells. OER is defined as the ratio of the doses under hypoxic and aerated conditions necessary to produce the same level of cell killing (Hall and Giaccia, 2006). The principle is illustrated in figure 2.14. An OER of 2.8, as seen in figure 2.13, means that the dose must be 2.8 higher to produce the same fraction cells killed when oxygen is absent from the system, as compared to well-oxygenated cells.

As seen in figure 2.18 on page 43, OER is a function of LET. In addition, OER varies throughout the cell cycle (Hall and Giaccia, 2006).

Although cellular hypoxia traditionally is associated with a decreased radiosensitivity, experiments have indicated that cells experiencing *chronic* hypoxia (see section 2.6.1) has increased radiosentitivity to both acute (Zölzer and Streffer, 2002) and low dose-rate (Pettersen et al., 2007) irradiation compared to well-oxygenized cells.

2.5.11 The dose-rate effect

What happens if the energy impartion rate (i.e. the dose-rate $\dot{D}$ as defined in equation 2.14) is varied? The standard survival curves (as discussed in section 2.5.6) concerns acute irradiation only, where $\dot{D}$ is very high (that is, all energy is delivered at once). Where in the theories does time effects enter?

In section 2.5.4, when discussing cellular repair mechanisms, the repair of sublethal damage (SLD) was presented. *Low dose-rate irradiation* (LDR)

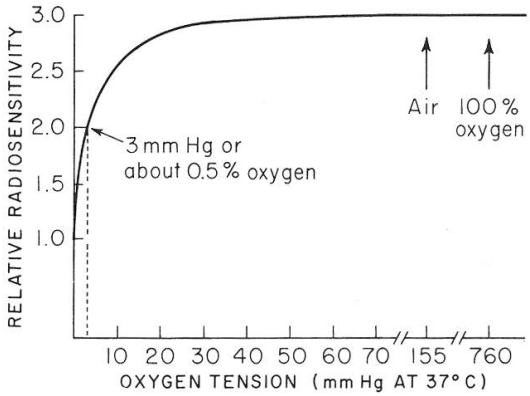

Figure 2.13: *A graph showing the relative radiosensitivity as a function of oxygen tension (from Hall and Giaccia, 2006). As seen, most of the change in radiosensitivity occurs at oxygen tensions below 30 mmHg (or about 4% O_2), indicating that the oxygen effect is present even at relatively low oxygen concentrations $>$ 4% O_2.*

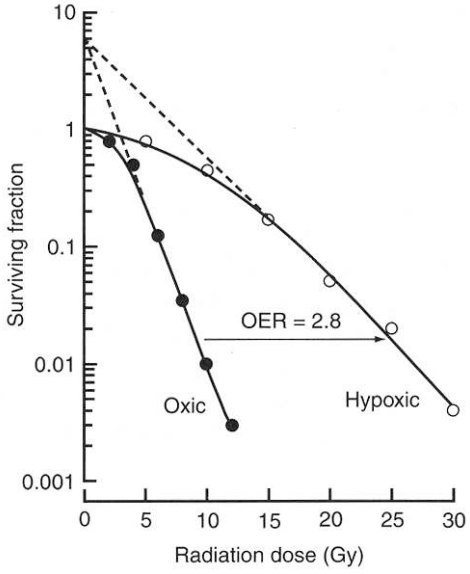

Figure 2.14: *The oxygen enhancement ratio (OER) (from Hall and Giaccia, 2006). In this system, a dose 2.8 times higher must be used to produce the same biological effect in the hypoxic cells, relative the oxic cells.*

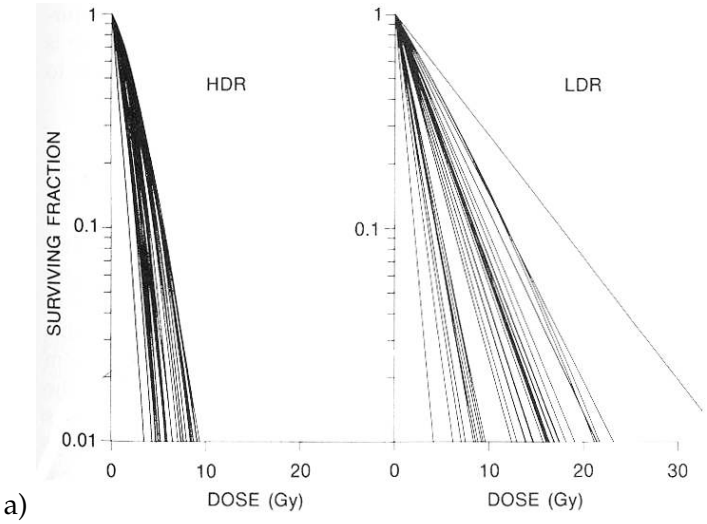

a)

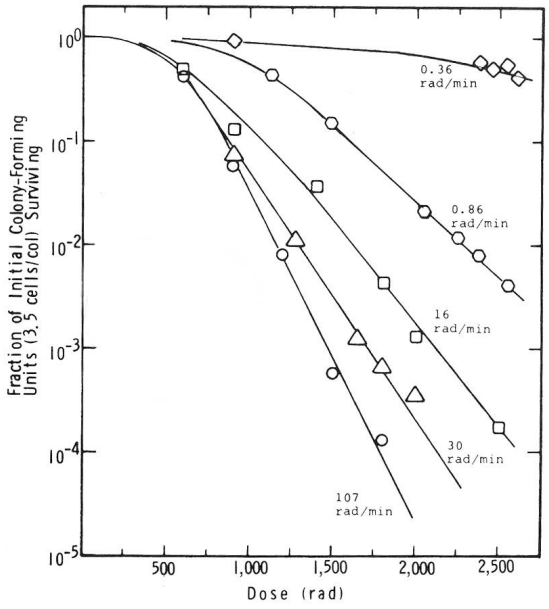

b)

Figure 2.15: *The difference between survival curves for different dose-rates demonstrating the dose-rate effect. Note the more expressed shoulder (i.e. lower α/β ratio) in the HDR (high dose-rate) curves as the repair of sublethal damage is less expressed. a) shows a variety of different cells lines cultured* in vitro *of human origin (from Hall and Giaccia, 2006).*
b) shows Chinese hamster cells (CHL-F) exposed to ^{60}Co radiation (taken from Hall and Giaccia, 2006, originally from Bedford, J.S.: Dose-rate effects in synchronous mammalian cells in culture in Radiation Research, *54:316-327, 1973).*

will increase the available time for SLD repair, and thus it is to be expected that the abundance of double strand breaks and thus chromosome damage will decrease as a response to lower dose-rate.

This is, in general, indeed the case, a decrease in dose-rate will result in a increase in cell survival[13].

LDR in the LQ-model

From a more theoretical point of view, the increased available time for sublethal damage repair (section 2.5.4) results in a higher α/β ratio (see section 2.5.6) and thus a straighter curve (because the linear α component becomes dominant). This is clearly seen in figures 2.15 a), where the same cell lines has been exposed to both low and high dose-rate irradiation.

As mentioned in section 2.5.6, the survival curve can be treated as a plot of two independent Poisson probabilities. A lowered dose-rate and thus a higher α/β ratio represents in this picture a decreased probability of the quadratic process to cause lethal damage. This is consistent with the theory of LDR resulting in increased time available for DNA repair processes.

Different tissues responds differently to decreased dose-rate, both because of survival curve shape (section 2.5.6) and because LDR radiosensitivity is genotype dependent (Williams et al., 2008).

Fractionated treatment

In cancer treatment, a radiotherapy plan typically consists of several *fractions* (see figure 2.17). As discussed in section 2.5.6, early- and late responding tissues have different shaped survival curves. This difference is exploited and enhanced in fractionated therapy, as tissue with low α/β ratio (that is, late responding tissue) has a more expressed shoulder and will benefit[14] from fractionation (as illustrated in figure 2.17) compared to tissue with high α/β ratio (that is, early responding tissue). Typically, cancerous cells are early responding which makes fractionation beneficial by increasing the biological effect (i.e. DNA damage) on these cells.

The inverse dose-rate effect

The *inverse dose-rate effect* (illustrated in figure 2.16) is seen when the dose-rate is further reduced. This has been associated with a radiation-induced

[13] An important exception to this is the *inverse dose-rate effect*, soon to be addressed.

[14] In this context "'benefit"' refers to being more radioresistant, as late responding tissue typically is to be spared in radiotherapy. Examples of late responding tissue are spine, kidney, lung and bladder.

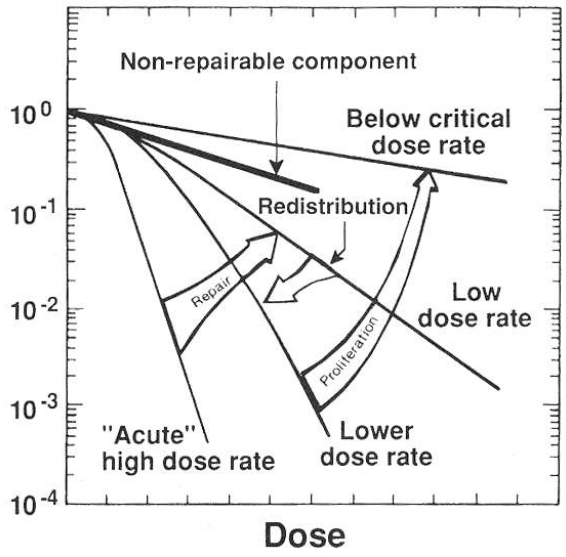

Figure 2.16: *The effect of varying dose-rate on the survival curve. Notice the difference in the initial shoulder (i.e. varying α/β ratio) (from Hall and Giaccia, 2006). Acute irradiation is recognized by a broad shoulder. Lowered dose-rate allows more time for sublethal damage repair, and the curve becomes shallower and parallel to the initial slope of the shoulder (i.e. α-dominant). If the dose-rate is reduced further, the inverse dose-rate increases the slope of the curve. Finally, if the dose-rate is low enough, cell proliferation will compensate cell death and the slope will again decrease.*

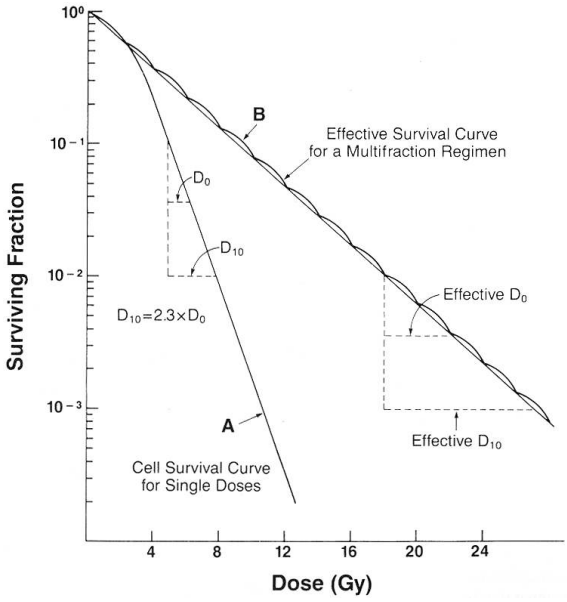

Figure 2.17: *Theoretical survival curves of the same cells without and with fractionated irradiation (from Hall and Giaccia, 2006). The effect is similar to the lowered dose-rate effect discussed in the text and seen in figure 2.15 and 2.16.*

cell cycle arrest in the sensitive G_2-phase.

However, as mentioned in section 2.4.1, cells with disabled G_1 checkpoint (and thus allowed to be arrested in the sensitive G_2 phase) was found *not* to be more radiosensitive than cells with functional G_1 checkpoint, when treated with low dose-rate irradiation (DeWeese et al., 1997). This suggests that cells allowed to arrest in G_1 are as sensitive to low dose-rate irradiation as cells that are arrested only in G_2, in a phase traditionally considered to be exquisitely radiosensitive (DeWeese et al., 1997).

2.5.12 Relative biological effect

The *relative biological effect* (RBE) is a way of describing the effect of varying factors to cell survival, usually different radiation qualities. Being relative (as is OER), it is only useful when comparing two different factors, such as radiation with different LET.

RBE comparable to OER (see section 2.5.10), being a ratio of doses needed to produce the same fraction of cells killed. RBE of some test radiation is in general defined as (Hall and Giaccia, 2006)

$$\text{RBE} = \frac{D_{250}}{D_r} \tag{2.32}$$

where D_{250} and D_r are the doses of 250 kV X-rays and the test radiation required to induce the same biological effect (Hall and Giaccia, 2006).

RBE as a function of LET

The RBE as a function of LET is due to the differences in energy deposition patterns on a microscopic level (Hall and Giaccia, 2006). As seen in figure 2.18, radiation with LET in the order of 100 keV/μm has the highest RBE. This curve is not unambiguous, as RBE varies with different tissue[15] and dose level (Hall and Giaccia, 2006).

RBE of sparsely ionizing radiation (such as γ-radiation) is a function of dose-rate, and will increase with decreased dose-rate. This is no surprise, as the dose-response curve tends to flatten out (that is, the linear α dominates) when the dose-rate is decreased (Hall and Giaccia, 2006).

RBE of densely ionizing radiation is, however, not does-rate dependent (Hall and Giaccia, 2006).

Figure 2.18 also shows the OER and the RBE as a function of LET. In this plot, the RBE is as in equation 2.32 defined relative to 250 kV X-rays, having RBE = 1) (Hall and Giaccia, 2006).

[15] In fact, RBE tends to be higher in tissue that has significant SLD repair (Hall and Giaccia, 2006).

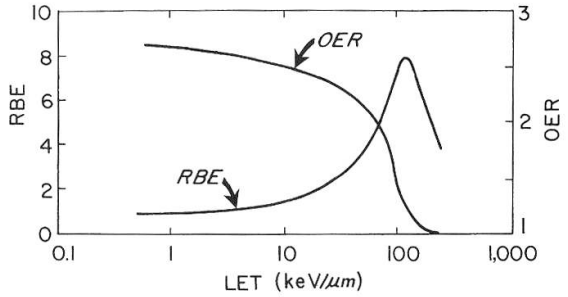

Figure 2.18: *Oxygen enhancement ratio (OER) and relative biological effect (RBE) as a function of LET (taken from Hall and Giaccia, 2006, originally from Barendsen, G. W.: Proceedings of the Conference on Particle Accelerators in Radiation Therapy in* US Atomic Energy Commission, Technical Information Center*, 120-125, 1972).*

The tritium β-particle is more efficient in producing complex DSBs than gamma irradiation, having a complex-DSB-RBE estimated to 1.3 relative to ^{137}Cs γ-radiation (Moiseenko et al., 2001). The overall RBE for tritium β-radiation has been measured to be 2-3 relative gamma radiation from ^{137}Cs and ^{60}Co decay (Straume and Carsten, 1993). This is most likely due to the fact that the tritium decay electron deposits its energy highly clustered (Moiseenko et al., 2001).

2.6 Cellular hypoxia

Cellular hypoxia is a state occurring when the demand for oxygen necessary to generate ATP in the cell is greater than the molecular oxygen supply (Cummins and Taylor, 2005). As oxygen is the primary source of metabolic energy for eucaryotes, mechanisms to handle oxygen deprivation is of great importance to cells (Cummins and Taylor, 2005). But severe and prolonged oxygen deprivation will inevitably result in cell death by asphyxiation.

In tumors, angiogenesis (the creation of blood vessels) is typically primitive in nature and insufficient to supply all tumor cells with oxygen (Mayles et al., 2007). As a result of a highly varying blood supply to the cells, states of hypoxia may occur within the tumor.

Most solid tumors contain hypoxic parts of varying scale (Bando et al., 2003; Hockel and Vaupel, 2001), and tumors with severe states of hypoxia are considered to be aggressive and have high metastatic potential, and therefore provide poor prognosis (Guppy et al., 2005).

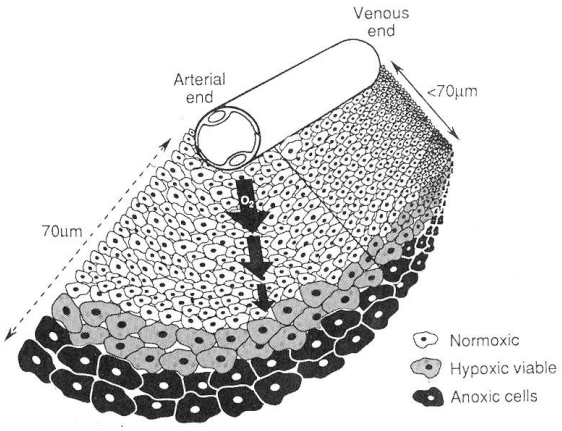

Figure 2.19: *Figure showing the effect of limited diffusion of oxygen (from Hall and Giaccia, 2006). This may, as a result of sub-optimal angiogenesis, lead to hypoxic and anoxic cells. The thin layer of hypoxic cells shown in the figure represents the cells where oxygen aviliability is high enough to keep the cell viable, but low enough so that the cell experience increased radioresistance due to hypoxia.*

2.6.1 Chronic and acute hypoxia

Tumor hypoxia can arise from two different mechanisms:

Chronic hypoxia is a state in which the cells experience low oxygen supply over a prolonged period of time due to limited oxygen diffusion (Dewhirst et al., 1996). In the vicinity of a blood vessel, a cylindrical layer of cells may be formed a certain distance from the vessel (typically $< 70\mu$m) where the oxygen concentration is high enough to keep the cells viable but low enough for the cell to experience hypoxia-induced effects (Hall and Giaccia, 2006). The principle is illustrated in figure 2.19.

Acute hypoxia, however, occurs as a result of changes in perfusion (Dewhirst et al., 1996). It may arise in tumors due to temporary blockage or closing of a blood vessel (Hall and Giaccia, 2006). This means that a part of the tumor may be hypoxic at the time a dose is delivered, but be reoxygenated soon after. At least two types of fluctant flow have been described; short (typically a few seconds) reductions in flow (usually in single vessels) and cyclic fluctations lasting 20-60 minutes (observed in vessel groups) (Dewhirst et al., 1996).

2.6.2 Hypoxia-mediated cell cycle arrest

Studies have shown that extreme hypoxia arrest the cell cycle in the S phase. This has been associated with a down-regulation of cyclin A (Seim et al., 2003) (see figure 2.5). In the T-47D breast cancer cell, this process is irreversible upon reoxygenation. However, in the NHIK 3025 cancer cell this process is shown to be reversible. This is associated with the fact that pRB (section 2.4.1) is non-functional in the NHIK 3025 cell, indicating an important role of pRB in the permanent S phase arrest and cyclin A down-regulation (Seim et al., 2003).

2.6.3 Hypoxia-mediated apoptosis

Hypoxia (up to 5000 ppm) has been found to induce apoptosis in the MCF-7 cell line (having an intact p53 expression), but not in cells with either mutated (T-47D) or abrogated (NHIK 3025) p53 expression (Åmellem et al., 1997). However, regardless of p53 status, hypoxia does not *change* the expression of p53, even under extreme conditions (< 4 ppm O_2) (Åmellem et al., 1997). Experiments have indicated that p53 status and cell survival following extreme hypoxia are uncorrelated (Åmellem et al., 1997), in the sense that p53 may indeed induce apoptosis as a result of hypoxia, but it is probably not the only factor of importance (Åmellem et al., 1997).

On the other hand, *erythropoietin* (Epo), being induced by hypoxia, has been shown to decrease the apoptotic potential of the MCF-7 cell, suggesting that this is another mechanism resulting in increased tumor aggressivity and resistance to therapy (Acs et al., 2004).

The on-set of hypoxia-mediated apoptosis was limited to 10 to 24 hours after exposure to extreme hypoxia (Åmellem et al., 1997).

2.6.4 Other consequences of cellular hypoxia

It has been proposed that the aggressiveness of hypoxic tumors is partly due to the fact that hypoxic parts of the tumor may generate signals resulting in increased angiogenesis, providing more oxygen and nutrients to the tumor allowing it to grow further (Guppy et al., 2005). In addition, hypoxia may induce apoptosis in some cells while decreasing the apoptotic potential in other cells, thus provide a mechanism for developing a more aggressive phenotype (Acs et al., 2004). Furthermore, the fact that hypoxic cells generally are found to be more resistant than well-oxygenated cells poses a problem in both endocrine therapy (Liu et al., 2004), cytotoxic drug therapy (Acs et al., 2004) and radiation therapy (Hall and Giaccia, 2006).

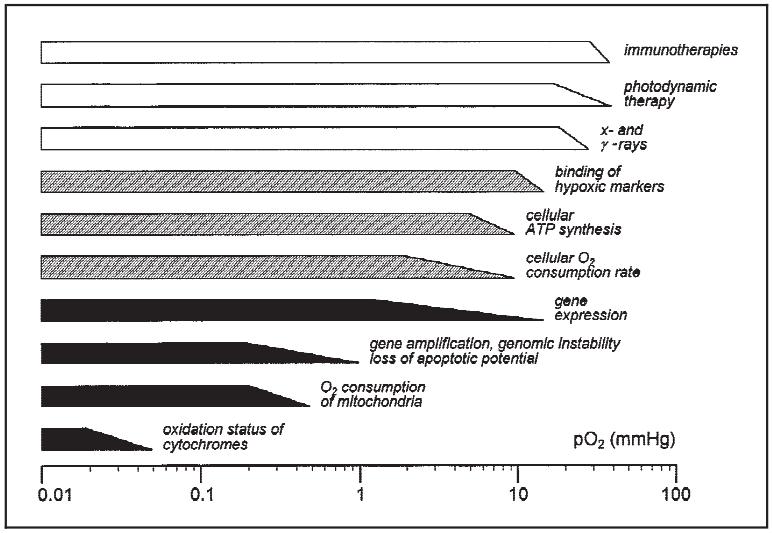

Figure 2.20: *A figure showing hypoxia induced changes in processes as a function of level of hypoxia (from Hockel and Vaupel, 2001).*
Open bars: therapy forms
Hatched bars: cellular functions
Solid bars: sub-cellular and molecular mechanisms.

Genetic effects

Hypoxia induce other cellular alterations and gene instability (Bando et al., 2003). Figure 2.20 is a graph taken from Hockel and Vaupel (2001) showing hypoxia levels and a selection of processes that are changed.

Hypoxia also affects the regulation of genes, and 26 of over 12 000 genes studied are found to be upregulated in hypoxic MCF-7 cells (Scherbakov et al., 2009; Bando et al., 2003). In addition, genes such as *RAD51*, a key mediator of homologous recombination (see section 2.5.4), has been shown to be down-regulated in hypoxic cells (Bindra et al., 2004). This probably has important functional consequences in DNA repair, and reduced levels of homologous recombination is indeed observed in hypoxic (as well as in posthypoxic) cells (Bindra et al., 2004). The protein synthesis in the MCF-7 cell has also been found to be down-regulated by hypoxia (Guppy et al., 2005).

Hypoxia-inducible factor 1

Hypoxia-inducible factor 1 (HIF-1) is a key transcription factor regulating gene expression in response to hypoxia (Scherbakov et al., 2009; Kizaka-Kondoh et al., 2009). Patient studies have indicated that HIF-1 activation in tumors is directly correlated with advanced disease stages and resistance

to treatment (Nagle and Zhou, 2009; Kizaka-Kondoh et al., 2009).

Acute hypoxia has, in the MCF-7 cell line, been shown to be associated with a down-regulation of ER-α expression (and thus function) and general loss of hormonal dependency (Kurebayashi et al., 2001; Scherbakov et al., 2009), resulting in a phenotype more resistant to endocrine therapy (Liu et al., 2004; Kurebayashi et al., 2001). In addition, a newly investigated synergetic effect of both hypoxia and estrogen treatment has been shown to degrade ER-α by 95% after 20 hours (Yi et al., 2009). Chronic hypoxia, however, is associated with a partial restoration of ER expression and activity (Scherbakov et al., 2009).

In addition, HIF-1 activation is associated with up-regulation of several other growth factor receptors (Scherbakov et al., 2009). Thus, hypoxia induces estrogen-independent growth in breast cancer (Scherbakov et al., 2009), considered a more malignant phenotype (Kurebayashi et al., 2001). A study of the estrogen-independent cell line MCF-7-5C indicated that estrogen-independent MCF-7-5C tumors contained lower oxygen levels and more hypoxic regions, compared to conventional estrogen-dependent MCF-7 cells (Maity et al., 2001).

Hypoxia and p53

The concentration of p53 is shown to increase in cells exposed to extreme hypoxia (around 0.2% O_2) (Zhao et al., 2009). HIF-1 is known to be able to bind Mdm5 and thus stabilize p53 (Cummins and Taylor, 2005).

However, the function of hypoxia-induced p53 is quite different than stress-mediated p53 in well-oxygenized environments. During hypoxia, *p53 transactivation* (transcription of certain genes) decreases and *p53 transrepression* (repression of certain genes) increases (Zhao et al., 2009). This can be seen as a way used by the cell to adapt to hypoxia, as it consumes less energy (and thus oxygen) to inhibit genes than to transcribe them (Zhao et al., 2009).

MCF-7 cells exposed to long-term hypoxia has been shown to obtain hypoxia tolerance, a property that seems to persist when the cells are transferred to normoxic conditions (Scherbakov et al., 2009).

2.7 Oxygen diffusion and cellular respiration

To study the effect of cellular hypoxia it is important to be able to quantify the cellular respiration.

Cells are dependent on a constant supply of oxygen, and thus of diffusion of oxygen from the gas phase through the medium to the cells.

Fick's first law of diffusion can be expressed as

$$J = -\mathcal{D}\frac{dC'}{dX} \tag{2.33}$$

where J is the oxygen flux toward the cell layer, $\mathcal{D}$ is the diffusion coefficient of the medium and dC'/dX is the slope of the oxygen gradient (Pettersen et al., 2005) where C' is oxygen concentration and X is depth in medium.

2.7.1 Oxygen solubility in the RPMI medium

To perform the calculations, the solubility of oxygen in the medium has to be known, in order to determine the number of water molecules that are present in the vicinity of the cells at any given oxygen concentration. Unisense has published an oxygen profile calculation spreadsheet on their web page (`http:\\www.unisense.com`) where the oxygen molecule concentration in the medium in 21% O_2 was defined as 200 μmol/l (Unisense, 2009), yielding a ratio $K = 9.52$ μM/%.

2.7.2 Oxygen consumption calculation

From equation 2.33 we know that the oxygen profile measured has a slope proportional to the cellular consumption of oxygen, that is, the cellular respiration. Therefore, the slope of the gradient can be used to calculate the respiration.

From Pettersen et al. (2005) we know that the surface tension will influence the results in the first few hundred μmeters. In addition, the sensor is so precise that it matters if it is placed *directly above* an oxygen consuming cell colony in contrast to if placed *between* cell colonies.

Therefore, we must use care when determining which part of the profile we will use to calculate cellular respiration. We found that, given a medium height of 1600 μm, the interval 800-200 μm was sufficient.

The respiration is proportional to the oxygen flux toward the flask bottom, assuming the cells are the only entities present in the medium consuming oxygen and that they are located at the flask floor. Therefore, we can calculate the cellular respiration from Fick's law (equation 2.33), and get

$$R_f \propto \mathcal{D}\frac{dC'}{dX},$$

where R_f are the total cellular respiration in units fmol/h·flask. The diffusion coefficient of the medium is $\mathcal{D} = 3.37 \times 10^{-5}$ cm^2/s (Pettersen et al., 2005).

$$R_f = \left\{ \frac{dC'}{dX} \right\} \frac{\%O_2}{\mu m} \cdot 9.524 \times 10^{-3} \frac{\mu M}{\%O_2} \cdot 3.37 \times 10^{-5} \frac{cm^2}{s}$$
$$= \left\{ \frac{dC'}{dX} \right\} \cdot 2.89 \times 10^{11} \frac{fmol}{flask \cdot h}. \quad (2.34)$$

The (mean) cellular respiration R is simply

$$R = \frac{R_f}{C} \quad (2.35)$$

where C is cells per flask.

The experiment setup is sensitive to such as movement in the medium, since the gradient then will change because we stir and mix oxygen in the medium. From experiments it is plausible to believe that the system needs many hours to stabilize.

The cells have to ”work” to obtain oxygen by pulling it through the medium. If the medium is stirred, the cells have ”free” oxygen whose consumption isn't picked up in this setup.

2.7.3 The stabilizing phase

If the calculated slope of the profile is plotted as a function of time, a stabilizing phase will be seen after each subexperiment initiation (that is, after each recultivation). This is due to (at least) two factors:

- After a recultivation, no oxygen concentration gradient exists in the medium. The gradient only appears, as discussed above, as a result of the cellular respiration. Regardless of cell number, a certain time must be used to accumulate the gradient and thus yield usable data.
- After a recultivation, the cell proliferation will have a lag phase, as presented in section 2.4.2, affecting the duration of the stabilizing phase.

2.8 Some statistical considerations

Throughout this thesis, any measurement with standard error are written on the form $\bar{x} \pm se_x$ where $\bar{x}$ is the arithmetic mean and se_x is the standard error of the data set. Standard errors are always given with two significant figures.

The arithmetic mean is

$$\bar{x} = \frac{\sum_{i=1}^{n} x_i}{n} \quad (2.36)$$

where x_i is the individual data values and n is the total number of entries in the data set. The variance σ^2 is

$$\sigma^2 = \frac{1}{n-1}\sum_{i=1}^{n}(x_i - \bar{x})^2 \tag{2.37}$$

and the root-mean-square deviation (or standard deviation) is (Beneson et al., 2006)

$$\sigma = \sqrt{\sigma^2} = \sqrt{\frac{1}{n-1}\sum_{i=1}^{n}(x_i - \bar{x})^2}. \tag{2.38}$$

Further, the standard error, also called the standard deviation of the mean, is (Boas, 2006)

$$se_{\bar{x}} = \frac{\sigma}{\sqrt{n}} = \sqrt{\frac{\sum_{i=1}^{n}(\bar{x} - x_i)^2}{n(n-1)}}. \tag{2.39}$$

2.8.1 Error propagation

In this thesis, measurements are frequently used as variables in further calculations. Estimating how the measurement uncertainties propagate are therefore crucial in knowing the errors of results.

Having m numbers on the general form $x \pm se_x$, we want to estimate the standard error of any (not necessary linear) combination y of them, where y is

$$y = f(x_1, x_2, x_3, \ldots, x_m).$$

We may linearize y using the Maclaurin series (Boas, 2006)

$$y \approx f^0 + \sum_{i=1}^{m}\frac{\partial y}{\partial x_i}x_i \tag{2.40}$$

where the higher order of derivatives have been discarded, hence the approximation. If the variables are uncorrelated, the variance becomes the sum of the individual variances with the coefficients from 2.40 as weights:

$$\sigma_y^2 \approx \sum_{i=1}^{m}\left[\left(\frac{\partial y}{\partial x_i}\right)\sigma_{x_i}\right]^2$$

and the standard error are thus estimated to be (Beneson et al., 2006)

$$se_y \approx \sqrt{\sum_{j=1}^{m}\left[\left(\frac{\partial y}{\partial x_j}\right)se_{x_j}\right]^2}. \tag{2.41}$$

Chapter 3

Methods

3.1 Cell cultivation and maintenance

The cell lines, needing constant care to survive, were continuously maintained and grown in incubators (National Heinicke Company and Sericult 200 incubator, Forma Science, Houm AS, Oslo) at 37°C.

3.1.1 The MCF-7 human breast cancer cell line

The cell line used in the work with this thesis was the human breast cancer cell line MCF-7 (developed at the Michigan Cancer Foundation, hence the name). The cell line was derived from a pleural effusion taken from a 69-year old patient with metastatic breast cancer (Levenson and Jordan, 1997; Brooks et al., 1973). The patient underwent two mastectomies 3 and 7 years before the primary culture was started (Levenson and Jordan, 1997).

The samples was taken in June of 1970, and a distinct stem line of 88 chromosomes was discovered (Levenson and Jordan, 1997).

The MCF-7 cell line has been shown to contain significant amount of 17β-estradiol receptors (Brooks et al., 1973; Horwitz et al., 1975), and it has been demonstrated that the antiestrogen *tamoxifen* inhibited MCF-7 cell growth, and that estrogen reversed this inhabitation (Levenson and Jordan, 1997). This indicates a strong estrogen-dependency in the MCF-7 cell line.

3.1.2 Laboratory equipment

Bacteria, fungus and viruses have a division rate many times higher than the cells. Thus, to avoid devastating infections, sterility was crucial to maintain. All laboratory tasks involving cell treatment was preformed in a *laminar air flow* (LAF) bench (VB 2040), on a surface sterilized with 70%

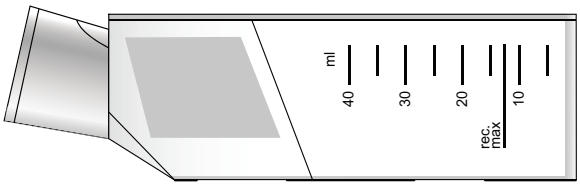

Figure 3.1: *Illustration of the 25 cm^2 cell flask (Nunc, Denmark) used for cell cultivation and experiments in this thesis.*

ethanol (Kemetyl Norge AS, Norway) before and after any cell tasks were performed. Plastic caps and glass bottles openings were always burned with a propane flame (Flameboy eco, Integra Bioscience, Switzerland) immediately before use.

In all tasks, disposable sterile plastic pipettes (Sarstedt, Germany) were used along with electric handles (Pipetus-akku, Hirschmann Laborgeräte). Other laboratory equipment used was washed and sterilized in-house. Glass (Pyrex) bottles and plastic caps were washed with water and soap (Decon 90, Decon Laboratories Limited, Great Britain) for at least 24 hours, before being dry sterilized (Termaks, Bergen, Norway) in 180° C for about two hours.

Rubber and textile equipment was sealed within paper bags and autoclaved (Webco) in 120°C for 20 minutes.

3.1.3 The RPMI medium

The cells were cultivated in cell flasks (Nunc, Denmark), illustrated in figure 3.1, using $NaHCO_3$ buffered *RPMI 1640 medium*, added 10% foetal calf serum, 1% penicillin, 1% streptomyci, 1% L-glutamin and 0.2% insulin[1].

The medium contained all nutrients, vitamins and salts essential for the cells to survive, and calf serum and insulin provided growth factors needed for proliferation. Penicillin and streptomycin are antibiotics preventing bacterial growth in the medium.

The optimal pH for cell growth are 7.2–7.5, and the medium was enriched with the pH indicator phenol red (Merck, Germany) to ease pH monitoring. The color of the medium was used to great extent when determining medium change necessity.

3.1.4 Trypsin

Trypsin is a proteolytic enzyme cleaving the protein bonds between neighboring cells and between cells and the flask floor. It was used to loosen

[1]See appendix H for manufacturers of the chemicals.

the cells from the flasks when a recultivation was to be performed. Free cells, i.e. not attached to any surface or neighboring cells, became spherical (a property used in determining cell size in section 4.2) due to the cell membrane tension.

The trypsin used (PAA Laboratories, Austria) was enriched with EDTA (Fluka, Switzerland), binding Ca^{3+} ions necessary for the intracellular protein bondings.

3.1.5 The cell recultivation process

The cell cultivation process consisted of several steps.

First, the cell medium was removed. Then trypsin (PAA Laboratories, Austria) was administered (1.5 ml to a 25 cm^2 flask 3 ml to a 80 cm^2 flask), and removed after a few seconds. This step was repeated.

The flask was then incubated for 5-10 min while the new flasks were prepared by adding fresh 37° RPMI medium (4.5 ml to a 25 cm^2 flask and 14.5 ml to a 80 cm^2 flask). When the trypsinized flask was ready, medium was added to suspend the cells. The cultivation radio was determined by the amount of added medium to the old flasks in combination with the amount of cell suspension transferred to the new flask. If a ratio of 1:5 was wanted, 2.5 ml PRMI was initially added to the old flask, and 0.5 ml of cell suspension was transferred to the new flask. Then, 4.5 ml new RPMI was added to the new flask to achieve a total of 5 ml medium.

The flask was then flushed with bio-air (5% CO_2) to prevent the cells going in to alkalosis due to too high pH levels.

The cell cultivation was typically done when the cells were near confluency.

When the cells was to be prepared for scintillation counting, the second trypsin addition was never removed, instead an equal amount of medium was added to terminate the effect of the trypsin (see section 3.6.3).

3.1.6 Medium change

When the medium was 2–3 days old, a medium change was needed without recultivating the cells. The fresh medium created a renewed cellular environment by providing new nutrients and correct pH.

If the cells was to be incubated in the lab, a bio-air flush was needed. In the hypoxia cabinet, however, the CO_2 level in the atmosphere was maintained by the gas mixer which provided a controllable and correct environment for the cells, and the flushing became unnecessary.

Within the hypoxia cabinet, evaporation was a problem. It resulted in decreasing medium volume, resulting in increased medium concentration

and thus changed cellular environment.

Up to 10 water dishes was filled with sterile water and placed in the cabinet to reduce the effect of evaporation, and medium height (a clear indicator of medium volume) was monitored and recorded during all experiments.

3.2 Phase-contrast microscopy

A great advantage in working with cells in culture was the possibility to visually watch and study (both qualitative and quantitative) the cells through a microscope.

Throughout in the experimental work with this thesis, a visualization technique called phase-contrast microscopy was used. A Nikon TMS microscope (Nikon, Japan) was used with a 10x lens (Nikon, Japan).

Phase-contrast microscopy exploits the fact that the speed of light traveling through a medium is proportional to $1/n$, where n is the refractive index of the material:

$$n = \frac{c}{c'}$$

where c is the speed of light in vacuum and c' is the speed of light in the material.

Since c' is typically smaller than c[2], n is normally ≥ 1.

Thus, rays of light passing through a cell (whose cytoplasm has a refractive index higher than the surrounding air) will accumulate a phase difference compared to the rays passing outside. Thus, a spatial distribution of refractive indexes becomes a spatial map of phase differences, which in a phase-contrast microscope are used to visualize the information.

3.2.1 Microscope resolution

In order to use the microscopic view in combination with digital imaging to determine cell number (i.e. the area based cell counting method) or cell size, the precise resolution (μm/pixel) of the microscopic field of view had to be known.

The following is a description of the process of determining the resolution and the field of view of the microscope used. The principle was to acquire images of an object of known size, and then determine the actual resolution (μm/pixel) of the set-up.

[2]However, special materials may have $n < 1$, but although c' is larger than c no information can be carried with speed greater than c. c' is merely the phase velocity, not the signal velocity, allowing $c' > c$.

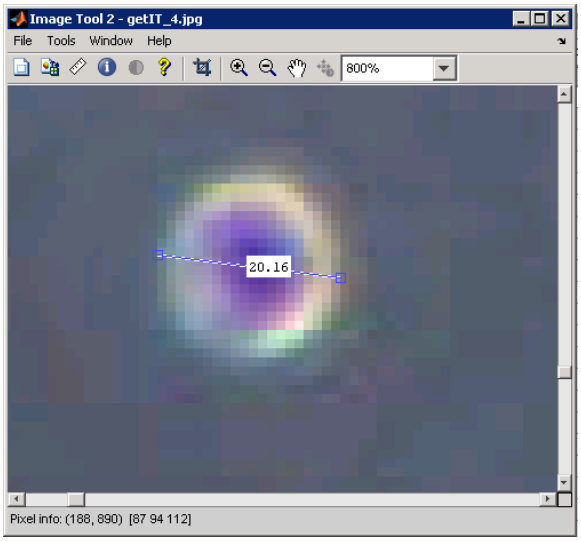

Figure 3.2: *Screen capture of cell measurement using Matlab's Image Tool toolbox. The same program was used to measure nuclei sizes.*

Two different objects was photographed, a Kova plastic chamber (Hycor Biomedical Inc.) and a standard Bürker glass chamber, both designed and used for cell counting. The Kova chamber had marked squares of dimension 1/3 x 1/3 mm and the Bürker chamber of dimension 0.2 x 0.2 mm (see figure 3.3).

Three images was taken of each chamber, capturing different areas of the object. The images was imported to and analyzed in GIMP (Gnu Image Manipulation Program, Kimbal, Mattis and the GIMP Developpment Team) and Matlab (MathWorks Inc., USA), where the measurement of interest was acquired. Then, a total of 36 measurement was taken, six from each image.

The mean was calculated from equation 2.36 and the standard error from equation 2.39.

The process described needed to be repeated for each individual microscope set-up (i.e. the combination of microscope model, lens and camera). Half way through the work with this thesis the microscope and digital camera was changed, and the resolution determination process had to be repeated. However, the same set-up was used for all the hypoxia experiments.

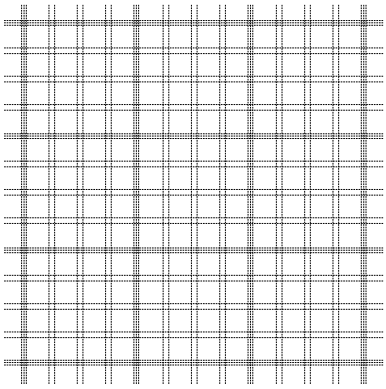

Figure 3.3: *Model of the Bürker chamber used for cell concentration counting and set-up resolution. The area of the smallest squares 0.0025 mm^2, and the area of the larger squares are 0.04 mm^2.*

3.3 Cell and nucleus size determination

The cell size was determined by measuring single cells in pictures taken of recently recultivated cell flask. This way, the cells did not have time to attach to the flask surface and pictures of spherical cells could be acquired. The cell images were analyzed in Matlab's Image Tool toolbox. The process is illustrated in figure 3.2.

The microscopic resolution was measured in section 3.4, and thus the actual cell size was easily determined.

To measure the cell nucleus size, pictures of individual nuclei was acquired (following the procedure described in section 3.6.3) and measured as described above.

3.4 Cell counting

Throughout the experiments it was always the total *flask* respiration that was measured. Because the interesting end point was to know the *cellular* respiration it was fundamentally important to know the number of cells in a flask, preferably at all times.

Two main methods to perform discrete cell counting was used in the current experimental works; one volume based and one area based.

Volume based cell counting The *volume based* cell counting is based on determining the concentration of cells per ml cell suspension, being measured in a chamber of known volume.

The Bürker chamber consisted of two separate grids, each with 3×3

squares. Applying a cover glass yields 10^{-4} ml per square, and by counting number of cells in at least five squares the cell concentration was acquired from

$$\frac{\text{cells}}{\text{ml}} = \frac{\text{cells}}{\text{square}} \cdot \left(10^{-4}\,\frac{\text{ml}}{\text{square}}\right)^{-1}$$

and the cell number from

$$[C] = \frac{\text{cells}}{\text{flask}} = \frac{\text{cells}}{\text{ml}} \cdot \frac{\text{ml}}{\text{flask}}.$$

Thus control of the total number of cells in any suspension was achieved, given that the concentration was constant and that the volume of the suspension was known to the needed precision.

Area based cell counting While the volume based method is precise if executed correctly, the *area based* method has the advantage of not being dependent on a cell suspension, and may be used to determine the dynamic cell count over time without having to resuspend the cells and thus exposing them to the (unnecessary) stress a recultivation cause.

Area based cell counting was executed by studying the cells through the microscope and capturing images of them. By knowing the precise area in the field of view of the microscope, a factor could be found to calculate the number of cells in a flask (i.e. the cell number C) of known flask floor area (assuming that the cells are homogeneously distributed):

$$[C] = \frac{\text{cells}}{\text{flask}} = \frac{\text{cells}}{\text{cm}^2} \cdot \frac{\text{cm}^2}{\text{flask}}$$

or, equivalently,

$$C = P_f \cdot C_p \tag{3.1}$$

where P_f is pictures per flask and C_p is cells per picture.

Each time a cell count was to be performed, three pictures was taken of three different areas of the cell flask floor. Each picture was counted, and the mean and standard error was determined. Then, the resulting number $\bar{C}_p \pm se_{C_p}$ was multiplied by P_f pictures/flask to get an estimate for the cell count per flask, C.

When counting, the cells touching the left or upper picture edge was counted, but the cells touching the right and lower edge was omitted.

The actual cell counts performed in the work with this thesis is listed in appendix D.

3.5 Cell irradiation by ^{3}H-valine incorporation

The radiation dose was delivered to the cells by adding a known fraction radioactive ^{3}*H-valine* (a tritiated version of the essential amino acid valine[3] (Sigma, USA)) to the medium. Being an essential amino acid, valine is incorporated by a cell into its cytoplasm and nucleus (Hall and Giaccia, 2006). The radioactive fraction of valine molecules thus irradiates the cell from within.

The microdosimetric method for calculating the energy deposited in the cells and thus the dose and dose-rate is descried in section 2.3.6.

It is assumed that the dose-rate to the nucleus is a linear function of specific activity of the medium. Thus, if the dosimetric calculations are performed for a known medium specific activity, the dose-rate to the cells can be controlled simply by adjusting the fraction of radioactivity in the medium production.

Søvik (2002) and Bjørhovde (2006) performed the microdosimetric calculations for the T-47D human breast cancer cell using a RPMI medium with specific activity 1.67 μCi/ml, and found the corresponding dose-rates to be 0.010 ± 0.001 Bq/h and 0.015 ± 0.004 Bq/h, respectively. The same medium specific activity was used (initially) in the experimental work with the current thesis.

3.5.1 Production of radioactive medium

Assuming no biological difference between cold (i.e. non-radioactive) valine and ^{3}H-valine, the incorporated amount of radioactivity in the cells was proportional to the ratio of ^{3}H-valine to cold valine in the medium.

Two different media was made. One cold medium medium (labeled KV medium) with a concentration of 1 mM cold valine (i.e. 1 ml valine per 100 ml medium), and one hot medium (labelled ^{3}H medium) with the same concentration of cold valine in addition to a small amount of ^{3}H-valine to provide the radioactivity.

The following describes the method of making radioactive RPMI medium with an activity of 1.67 μCi/ml in addition to a cold valine concentration of 1 mM.

The tritiated valine had a specific activity of 0.852 mCi/ml (see table 3.1), and to achieve 1.67 μCi/ml in the hot medium 0.196 ml ^{3}H-valine was added per 100 ml medium. In addition,

To make a total of 500 ml hot RPMI, the amount of cold valine to be added was 5 ml and of ^{3}H-valine it was 5×0.196 ml = 0.98 ml. Thus,

[3] Valine has the chemical formula $HO_2CCH(NH_2)CH(CH_3)_2$.

Table 3.1: *The specific activity of the ^{3}H-valine used in the irradiation experiments (Fenne pers.comm.).*

Date	Specific activity (mCi/ml)
June 19, 2006	1.000
Jan 1, 2007	0.970
Jan 1, 2008	0.917
Jan 1, 2009	0.867
Apr 22, 2009	0.852

the mixture ratio became 494.02 ml RPMI, 5 ml cold valine and 0.98 ml ^{3}H-valine.

First, 475 ml RPMI and 5 ml cold valine was added to a sterile 500 ml glass bottle, and the solution was stirred. Then, 1 ml ^{3}H-valine was transferred to a small plastic tube, and an auto pipette was used to transfer 980 μl hot valine from the tube to a small glass flask and then mixed with 19.02 ml RPMI. This was then administered through a 0.22 μm filter to the initial medium solution, making 500 ml of radioactive medium with 1 mM cold valine.

In addition to the hot medium a cold medium was made with the same amount (1 mM) of cold valine, without the ^{3}H-valine.

RPMI medium with cold valine (500 ml)

RPMI medium	495 ml
Valine stem solution	5 ml

RPMI medium with specific activity 1.67 μCi/ml (500 ml)

RPMI medium	494.02 ml
Valine stem solution	5 ml
^{3}H-valine	0.98 ml

The actual specific activity of the medium was also experimentally measured and verified, as described in section 4.3.7 on page 89.

3.6 Dosimetry

3.6.1 Measure of cell and nucleus size

The cell and nucleus size was found by visual measurement through the microscope as described in section 3.3. Pictures of whole cells and cell nuclei was acquired and Matlab was used to determine the pixel diameters, and the cell size was found by knowing the microscopic resolution (μm/pixel).

3.6.2 Cell preparation for scintillation counting

The old medium was removed from the cell flasks. Trypsin was added and removed (2 ml in 25 cm^2 flask, 3 ml in 75 cm^2 flask). New trypsin was added and the flask was incubated for 5 min. Then, the cell-trypsin solution was resuspended to a single cell suspension by the use of a canula, and added to a plastic tube along with an equal amount of RPMI. This terminates the effect of the tritium. It was important to avoid air bubbles in the suspension, as this would destroy the cells.

The following steps were conducted with the samples either on ice or in 4°C centrifuge (Labofuge 400R, Heraeus Instruments, Germany).

The cell-medium-trypsin solution was centrifugated with 1200 RPM for 4 minutes, and the medium-trypsin-solution was removed using a water aspirator. Caution was used to avoided sucking up the cell pellet.

The cells were washed by adding 3 ml PBS, vortexing the tube (IKA MS 3 digital vortexer, IKA Works Inc., USA) at 3000 Hz to suspend the cells, and centrifugating the tube (1200 RPM/4 min/5°C). PBS was removed and 3 ml 10% PCA (Percloric acid; Merck, Germany) was added to fixate the cells. The tube was vortexed and rested in ice for 15 min. The tube was then centrifugated (1200 RPM/4 min/5°C) and the PCA was removed.

Then, 3 ml 2% PCA was added, the tube vortexed and centrifugated and the PCA was removed. This step was repeated another two times, and before the last centrifugation 0.5 ml PCA-cell-suspension was removed to be counted in Bürker chamber.

After the fourth PCA step, the cell pellet was vortexed with 2 ml 0.4% NaDOC[4] (Sigma, USA), and the tube was incubated for 30 min in 37°C.

Then 1 ml of the cell suspension was added to two scintillation flasks along with 7 ml scintillation fluid. This was run though the scintillation counter to measure the total activity (the scintillation counting is described in section 3.6.4).

[4]NaDOC has chemical formula $C_{24}H_{39}O_4Na$.

By counting the cells in Bürker chamber, the total cell number in the scintillation flasks was estimated and the specific cellular activity was found.

3.6.3 Nucleus preparation for scintillation counting

To prepare the nuclei for scintillation counting, the same procedure as in the former section was followed. In addition, Buffer A with a protease inhibitor cocktail tablet (Roche Diagnostics, Germany) was added to lyse[5] the cells and thus isolate the nucleus. A single protease inhibitor cocktail tablet was added to 20 ml of Buffer A. Buffer A was administered as a separate step after the first PBS wash, before the 10% PCA step. Before continuing the above procedure, the Buffer A was removed by centrifugation and water suction.

An important task was to determine the exposure time of the cells to Buffer A. Earlier it had been established that the NHIK-3025 cells needed 15 minutes, and that the T-47D cell line needed 30 minutes (Bjørhovde, 2006).

Initially, a nucleus preparation procedure with a Buffer A exposure time of 20 minutes was used. This resulted, however, in destroyed nuclear membranes and caused the DNA to leak from the nucleus, which made counting impossible. It was assumed that this happened due to a too long Buffer A exposure time.

Thus, three different exposure times was therefore tested in separate experiments—10, 12 and 15 minutes. All of these three experiments yielded good results (see section 4.3.1).

3.6.4 Liquid scintillation counting

As the energy released from the tritium decay is low (18.6 keV, see section 2.1.2), it is nearly impossible to detect and quantify the β-particle directly. In this work, a process called *liquid scintillation counting* was used to quantify the activity.

The activity sample was mixed with a scintillation fluid (Emulsifier-Safe), containing solvent and fluorescent molecules (PPO and bis-MSB) and placed in a transparent plastic tube. The scintillation counting was performed by placing the sample tubes in a metal holder that was run through the scintillation counter (Tri-Carb 2100TR, Packard Instruments, Laborel, Oslo). A user set-up programmed by Søvik (2002) for tritium activity measurement was applied.

[5]Cell lysis refers to cell death by breaking of the cellular membrane

When an electron was released as a result of a tritium decay, it interacted with and transferred energy to the solvent molecules in the scintillation fluid. Then, the ionized or exited solvent molecule released photons transferring their energy to the fluorescent molecules, which in turn released photons in the ultraviolet energy range. This way, a single decay resulted in multiple photons, traveling through the fluid, ultimately reaching the detectors.

In the detectors, the signal was greatly amplified through a photomultiplier tube (PMT), resulting in a far more energetic signal whose intensity was proportional with the initial photon energy. The signals from the two detector were added and the mean signal intensity was calculated, compensating for different photon attenuation (being a function of photon traveling length, since the distance from a decaying tritium atom to the two detectors typically would not be the same).

Having two detectors is a efficient way of noise reduction, since a signal had to occur in *both* detectors within a certain window of time to be registered. This eliminated spontaneous and random processes leading to signals, as the probability of this occurring in both detectors within the given time frame was very small.

The signals from the detectors that satisfies the demand of simultaneity were digitalized in a *analog-to-digital converter* (ADC) and stored in a computer.

The user input consisted of parameters such as counting time, number of repetitions (to increase signal-to-noise ratio) and nuclide measured. The latter was used by the scintillation counter to calculate DPM (decays per minute) from CPM (counts per minute), as this will depend on the nuclide of interest. In addition, having information of nuclide being measured, the scintillation counter could minimize the impact of artifacts such as insufficient energy to produce a scintillation, or artifacts due to limited detector efficiency.

3.7 Quantifying cellular response to hypoxia

To study hypoxic cells, the lower threshold concentration of O_2 (that is, what % O_2^{gp}) at which the cells do survive was important to determine. In addition, the respirational behavior of the cells experiencing different gas phase oxygen concentrations (% O_2^{gp}), as well as low dose-rate irradiation, was interesting to study.

In practice, this was done by measuring the vertical oxygen concentration gradient throughout the medium (as is illustrated in figure 3.4) in addition to monitoring the cellular proliferation, and calculate e.g. the

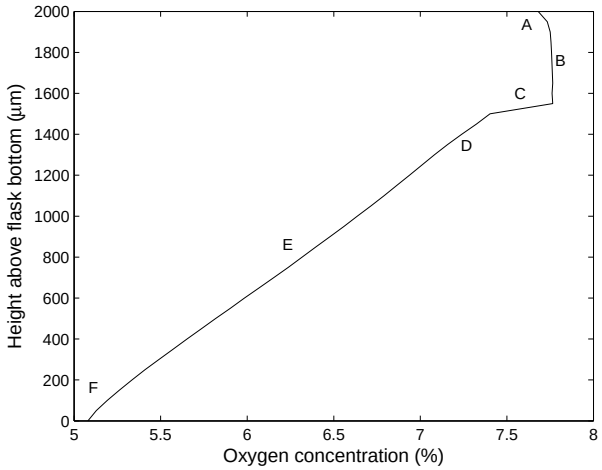

Figure 3.4: *An example of an oxygen profile. The interval 800–200 µm was used to estimate the slope of the profile. The following properties are described.*
A) This artifact is probably due to the fact that the sensor rests at 500 µm, and that the oxygen concentration at that depth produces a lag in the measurement.
B) This vertical asymptote represents the measured oxygen concentration in the gas phase inside the flask (however, as is to be discussed in section 5.6.2, the oxygen probe signal was 4% higher in the gas phase). This does not *necessary equal the gas phase concentration outside the flask, due to limited gas exchange through the flask neck.*
C) The medium level, characterized by the medium edge.
D) Artifact due to surface tension.
E) This is the range at which the slope is measured, trying to avoid the artifacts from both area d) and f).
F) The local environment of the probe at flask bottom.

respiration using the theory presented in section 2.7.

Specifically, the pericellular oxygen concentration (hereby abbreviated POC) was the oxygen concentration experienced by the cells, i.e. the O_2 level at flask bottom. The POC was dependent on several factors such as % O_2^{gp} (gas phase oxygen concentration), medium depth, cellular respiration and cell number. In addition, the measured POC was a result of the local environment of the probe, and thus not necessary representative for the whole flask. See figure 3.5 for an illustration of different local environments that would yield different POC values for the same flask and cellular respiration.

3.7.1 O_2 concentration profile acquirement

The equipment used for measuring local oxygen concentration was produced by Unisense A/S, Aarhus, Denmark. The set-up consisted of an

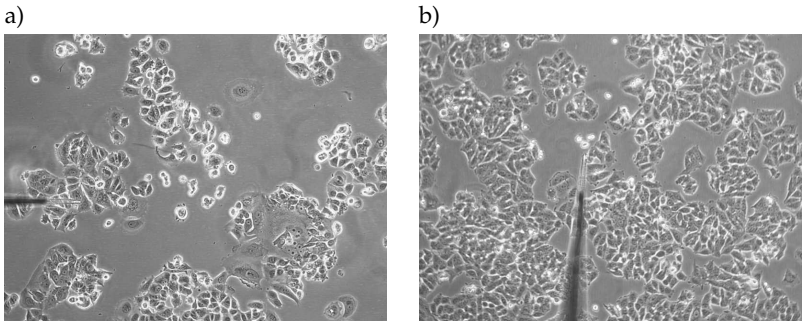

Figure 3.5: *Difference in local environment of the probe tip. The local environment of the probe at 0 µm is not necessary corresponding to the mean environment of the flask bottom. This gives rise to the effect described in figure 3.4 at point F).*
Figure a) is from experiment 081013 and b) is from experiment 081212.

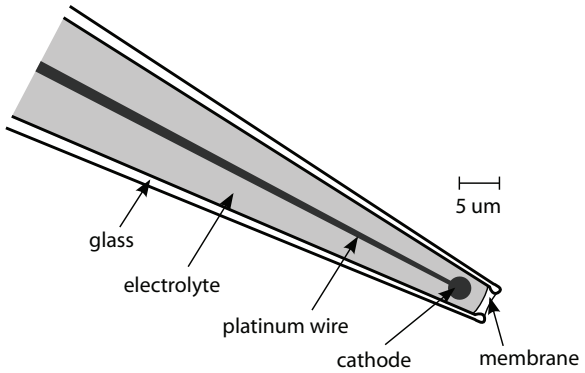

Figure 3.6: *Illustration of the sensor tip of the 5 µm oxygen probe used to acquire oxygen concentration profiles (Illustration from Pettersen et al. (2005), modified).*

Figure 3.7: *The PicoAmmeter and the motor controller (both: Unisense, Denmark) used in the hypoxia experiments. Both pictures from* `www.unisense.com`.

oxygen microsensor (see figure 3.6) mounted on a computer-controlled micromanipulator (controlled via the Unisense Motor Controller I USB interface (Unisense A/S, Denmark) as shown in figure 3.7). The weak electric current (10^{-12} - 10^{-10} A) from the sensor was registered by the Unisense PA2000 picoammeter (Unisense A/S, Denmark), also shown in figure 3.7, whose signal was processed by the Unisense ADC 216 USB interface (Unisense A/S, Denmark)) communicating with dedicated computer software SensorTrace Profiler 1.1 (Unisense A/S, Denmark) (Pettersen et al., 2005). The current measured through the oxygen probe was assumed to be proportional to the oxygen concentration at the probe tip.

The amperemeter's reading was coded as electric potential and sent to the AD-converter through an coaxial cable, and from there sent to a computer through the serial port. The final signal, in units mV, was recorded in the dedicated computer software.

Inside the hypoxia cabinet (InVivo), the oxygen microsensor was controlled by the micromanipulator. The software recording the oxygen readings also controlled the position of the microsensor, operating with a resolution of 1 μm.

The oxygen probe was placed in the micromanipulator so that the probe tip was directly above the microscope lens (i.e. within the microscopic field of view). The set-up is pictured in figure 3.8.

Assuming that the microsensor signal was proportional to the actual oxygen concentration at the sensor tip, it was found sufficient to calibrate the software at two concentrations. This was done by first reading the signal in the cabinet's gas phase and using the oxygen concentration reading on the gas mixer as reference, and second to read the signal in an anoxic solution made from 0.2 g sodium sulfite (Sigma, USA) in 10 ml Milli-Q water (Millipore, France) and defining that to be 0% O_2. An accurate weight (AG245 Mettler Toledo, Switzerland) was used to measure the sodium sulfite. The process of aquiring the calibration points was done in the dedicated calibration section of the Unisense software.

As the experimental set-up was subject to electrical drift (see section

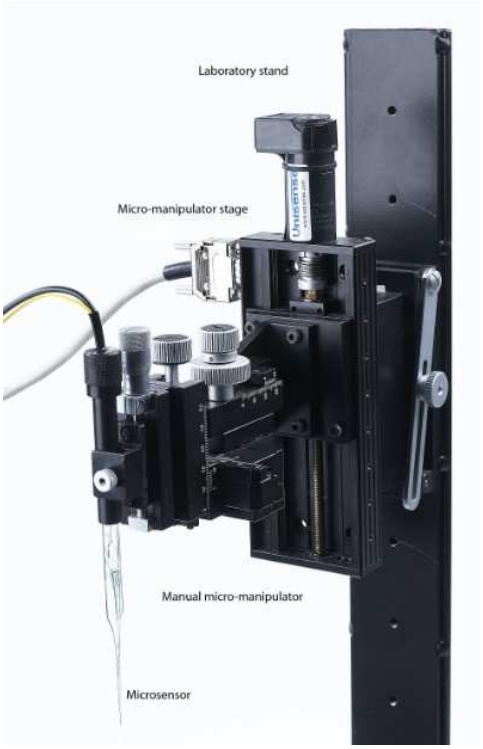

Figure 3.8: *The oxygen probe mounted on the micromanipulator (Unisense, Denmark). Picture from* `www.unisense.com`.

Figure 3.9: *The InVivo2 hypoxia cabinet (Ruskinn, Great Britain) used in all the hypoxia experiments (from Ruskinn, 2009).*

3.8.1) the calibration was performed twice in each experiment.

When oxygen profiles was to be acquired, the sensor was cleaned in Milli-Q water (Millipore, USA), calibrated in the anoxic solution, again cleaned in the water and then sterilized in 70% ethanol. The probe was then mounted on the micromanipulator and finally calibrated in the gas phase concentration.

3.7.2 Experimental set-up in the cabinet

The cells were cultivated in an InVivo2 hypoxia cabinet (Ruskinn, Great Britain) in a gas mixture controlled by dedicated gas mixer (Ruskinn, Great Britain), both shown in figure 3.9. All recultivations and medium changes was performed within the cabinet with equipment that had experienced the current oxygen concentration (or anoxia) for at least 24 hours, to archive greatest possible control of the cellular oxygen aviliability.

The cell flask was then placed on the microscope with the microsensor through the flask neck (this set-up is illustrated in figure 3.10). Then, the microscope was focused on the cells attached at the flask bottom, and this made it possible, by using the focal plane as guide, to move the microsensor very close to the cells without touching the flask floor and thereby destroying the probe. The flask floor was defined as the zero-level of the profile.

As the software measured the position of the sensor in depth, the height above the flask bottom (with depth=0 mm) was regarded as negative depth.

The software was then programmed to record profiles from depth -2000μm to 0 μm in 50 μm steps, with 3 s pause between recordings of 3 s duration. Furthermore, the software was programmed to wait 1000 s (this was the maximum value) between profile acquirements. Assuming a motor movement time of about 1 s, there was about 1287 seconds or

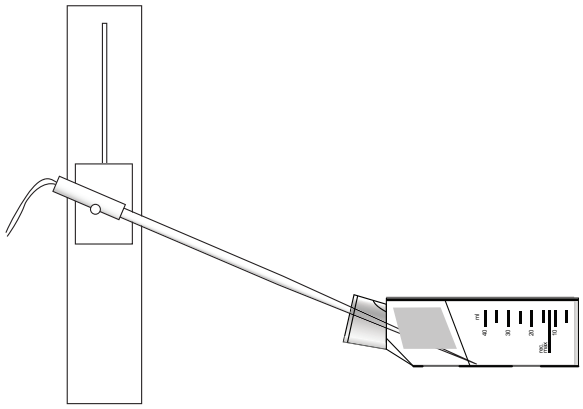

Figure 3.10: *The set-up of the micromanipulator, the oxygen microsensor and the cell flask.*

close to 21.5 min between two consecutive profile acquirements.

3.8 Analyzing the respirational data

The computer software wrote the output data to an `.xls`-file (Microsoft Excel, Microsoft Corporation) in the following format:

```
Sensor 1
Time (h)            Depth (um) Concentration (%) Signal (mV)
18.11.2008 15:53:42 -2000      10,53918171       499,8892212
                    -1950      10,36980534       491,9443665
                    -1900      10,2682457        487,1806335
                    -1850      10,1900301        483,5118103
                    -1800      10,11281109       479,88974
                    -1750      10,03975487       476,4629517
                    -1700      9,967673302       473,0818787
                    -1650      9,895000458       469,6730347
                    -1600      9,821796417       466,2393188
                    -1550      10,34157658       490,6203003
                    -1500      10,50525475       498,2978516
                    -1450      10,68349934       506,6586304
                    -1400      10,87244797       515,5214844
                    -1350      11,03206444       523,0085449
                    .....      .....             .....
```

The original software (Unisense) could also be used to plot and examine the data, but to calculate respiration (i.e. gradient slope) and other quantities on a dynamic scale was not possible in this program.

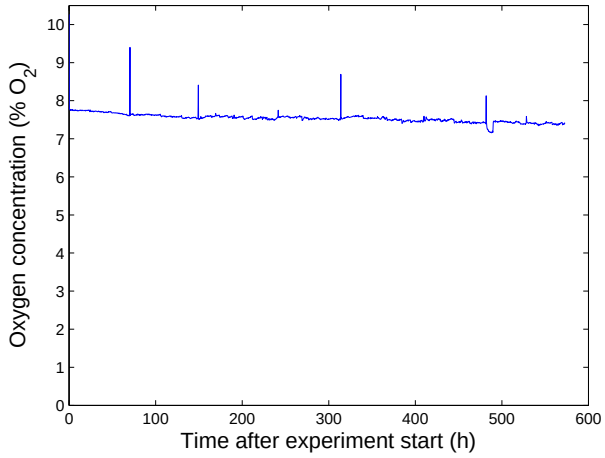

Figure 3.11: *The gas phase measurements during experiment 081118, motivating the drift compensation to be a linear function of time. The cabinet oxygen concentration was constantly maintained by the gas mixer. The spikes are due to medium change.*

Therefore, a central part of the work on this thesis was to develop a dedicated software able to read, plot and analyze the data from the original `.xls`-file. The software was written in Matlab. The source code of the program in its whole can be found in appendix A. The following is a short summary of the program's main features.

3.8.1 Sensor calibration

The program read the time, position and the mV-signal from the `.xls`-file, and the calibration data was fed to the software by the user.

The oxygen sensor and its interface was subject to electronic drift. The behavior was different between different sensors, so it was assumed to be individual (see figure 3.11).

Experience made it plausible to assume that the drift was linear with time and signal, leading to an assumption that, given a time t and a signal S, the oxygen concentration could be calculated from

$$C(S,t) = X_1 \cdot S + X_2 \cdot t + X_3 \cdot St + X_4. \tag{3.2}$$

Being an equation with four unknown coefficients, four different calibration points were needed.

In the experiments in this thesis, calibration was performed twice (at the beginning and end) in each experiment, and the resulting data points was used to determine the unknown coefficients for that experiment.

At time $t = 0$, two measurements was made, one in the gas phase and one in an anoxic 2% sodium sulfite solution (Sigma, USA). The same was done at the end of the experiment $t = t_{\text{end}}$.

The resulting data was inserted into the three vectors

$$\vec{S} = \begin{bmatrix} S_1 \\ S_2 \\ S_3 \\ S_4 \end{bmatrix}, \vec{C} = \begin{bmatrix} C_1 \\ C_2 \\ C_3 \\ C_4 \end{bmatrix}, \vec{t} = \begin{bmatrix} t_1 \\ t_2 \\ t_3 \\ t_4 \end{bmatrix}.$$

Equation 3.2 can be written on a matrix form

$$\vec{C} = \mathbf{V} \cdot \vec{X}, \tag{3.3}$$

where $\vec{X}$ are the desired coefficients and $\mathbf{V}$ (the Vandermonde matrix) is a matrix constructed from $\vec{S}$ and $\vec{t}$

$$\mathbf{V} = \begin{bmatrix} S_1 & t_1 & S_1 t_1 & 1 \\ S_2 & t_2 & S_2 t_2 & 1 \\ S_3 & t_3 & S_3 t_3 & 1 \\ S_4 & t_4 & S_4 t_4 & 1 \end{bmatrix},$$

and the vector $\vec{X}$ yielding the coefficients in equation 3.2 can be found using linear algebra:

$$\begin{aligned} \vec{C} &= \mathbf{V} \cdot \vec{X} \\ \mathbf{V}^{-1} \cdot \vec{C} &= \mathbf{V}^{-1}\mathbf{V} \cdot \vec{X} \\ \vec{X} &= \mathbf{V}^{-1} \cdot \vec{C}. \end{aligned}$$

The resulting coefficients (i.e. the components of $\vec{X}$), calculated in Matlab, was used in equation 3.2 to determine the calibrated oxygen concentration corresponding to any given signal S at any time t.

3.8.2 Data input

The Matlab function `xlsread{}` was used to read the profile data from the Unisense file. The output of `xlsread{'file_name','Profiles','B:D'}` was a $n \times 3$ matrix with depth, O_2 concentration and measured signal as columns. As described in section 3.8.1, only the depth and the signal intensity were used, as the calibrated oxygen concentration was calculated from equation 3.2.

3.8.3 Timing

The Matlab program was unable to read the profile timing directly from the Excel file. To determine the time point of each single profile, the number of acquirements was counted and the total experiment time were set by the user. Then the *average* time between consecutive profiles was found.

3.8.4 Cell count

Following the description in section 3.4, the cell number was determined at discrete times (typically during cell maintenance) by counting the cells in three different pictures representing different areas at flask bottom. The mean cell number in a picture was calculated from

$$\bar{C_p} = \frac{\sum_{i=1}^{n} (C_p)_i}{n} \tag{3.4}$$

where $(C_p)_i$ are the individual values and n is the total number of measurements. The standard error is

$$se_{C_p} = \frac{s}{\sqrt{n}} = \sqrt{\frac{\sum_{i=1}^{n} (\bar{C_p} - (C_p)_i)^2}{n(n-1)}}. \tag{3.5}$$

A single function was needed to get the cell number at any time during the experiment, following an exponential interpolation between individual counts performed.

This was done by performing a linear interpolation of time `t_C` and the natural logarithm of the cell counts `log(C)`, with the command line

```
fit_exp = fit(t_C,log(C),'linearinterp') .
```

Then, by calling the function `fit_exp`, the cell number at any given time `t` was given from

```
exp(fit_exp(t)) .
```

The mean doubling time in each interval was called by

```
log(2)./fit_exp.p.coefs(:,1).
```

In addition, $\bar{T_2}$ can be calculated from

$$\bar{T_2} = \ln 2 \cdot \frac{t_2 - t_1}{\ln(C_2/C_1)}. \tag{3.6}$$

3.8.5 Truncating the data

According to the user-set values of `t_start` and `t_stop`, the data matrix `profile_data` was truncated to fit the set interval.

3.8.6 Medium level detection

By searching through each individual profile, the medium level was found by comparing the signal difference between two consecutive concentration measurements (acquired every 50 μmeters), and detecting the medium edge in the profile (seen as point C in figure 3.4 on page 63).

The medium level was then stored in a dedicated array as a function of profile number.

3.8.7 Profile plotting (2D and 3D)

A 2D plot of the individual profiles was made using a `for`-loop, running through every single profile in the `profile_data` matrix, and plotting them with the `plot` tool with oxygen concentration as abscissa and depth as ordinate.

To produce the 3D plots (seen in the *Results and analysis* chapter) with time as the third axis the `plot3` function was used. These plots provides an unique view on the dynamic development of the profiles, with respect to factors as cellular respiration, pericellular oxygen concentrations, medium levels and cell maintenance artifact.

3.8.8 Gas phase and flask bottom oxygen concentration

The gas phase and flask bottom oxygen concentration (i.e. the pericellular oxygen concentration) was plotted by looking up the wanted depths in the `profile_data` matrix and finding the corresponding oxygen concentration values.

3.8.9 Slope calculation

To avoid the oxygen gradient artifacts shown in figure 3.4 on page 63, but still obtain results with high signal-to-noise ratio, great care was used when choosing the profile interval used as source.

Using a trial-and-error method left the interval 200–800 μm as the best option for the regression analysis (Beneson et al., 2006) fitting a linear curve to the data.

The slope of the desired interval of profile was determined by the `fit` function in Matlab. Using a linear (i.e. a first degree polynomial) fit, named `poly1`, the two coefficients of the polynomial $ax + b$ was found:

```
fitted = fit(data_vector,'poly1')
```

and the coefficients a and b was found from

```
a = fitted.p1;
b = fitted.p2;
```

The concentration slope $|dC'/dX|$ from equation 2.33 on page 48 was thus

$$\left|\frac{dC'}{dX}\right| = b^{-1}$$

since the original profile was acquired and read with depth as a function of concentration.

3.8.10 Plotting of experiment data

In figure 3.12 on page 74, example plots associated with a specific experiment fraction are shown.

As seen, figure a) (cellular respiration) is based on cell counting (in addition to the interpolation described in section 3.8.4 on page 71) while figure b), c) and e) are purely based on acquired data. Plot d) shows the cell counts and the associated interpolation.

The respirational data from the stabilizing phase has been omitted from the plots.

Plot a): Cellular respiration

The cellular respiration R was calculated from equation 2.35 where $|dC'/dX|$ was found as described in section 3.8.9 and the cell number C was determined from the individual cell counting and interpolation plotted in figure d).

Strictly speaking, plot a) is nothing but the data in plot b) divided by the data in plot d).

It is important to point out that respirational data from the stabilizing periods have been deleted from the plots.

Plot b): Flask respiration

The total respiration R_f as calculated from equation 2.34 was plotted on semilogarithmic axis as a function of time.

A straight line represents a pure exponential increase in flask respiration, indicating a exponential cell growth (assuming constant cellular respiration).

Again, data from the stabilizing phases has been deleted from the plots.

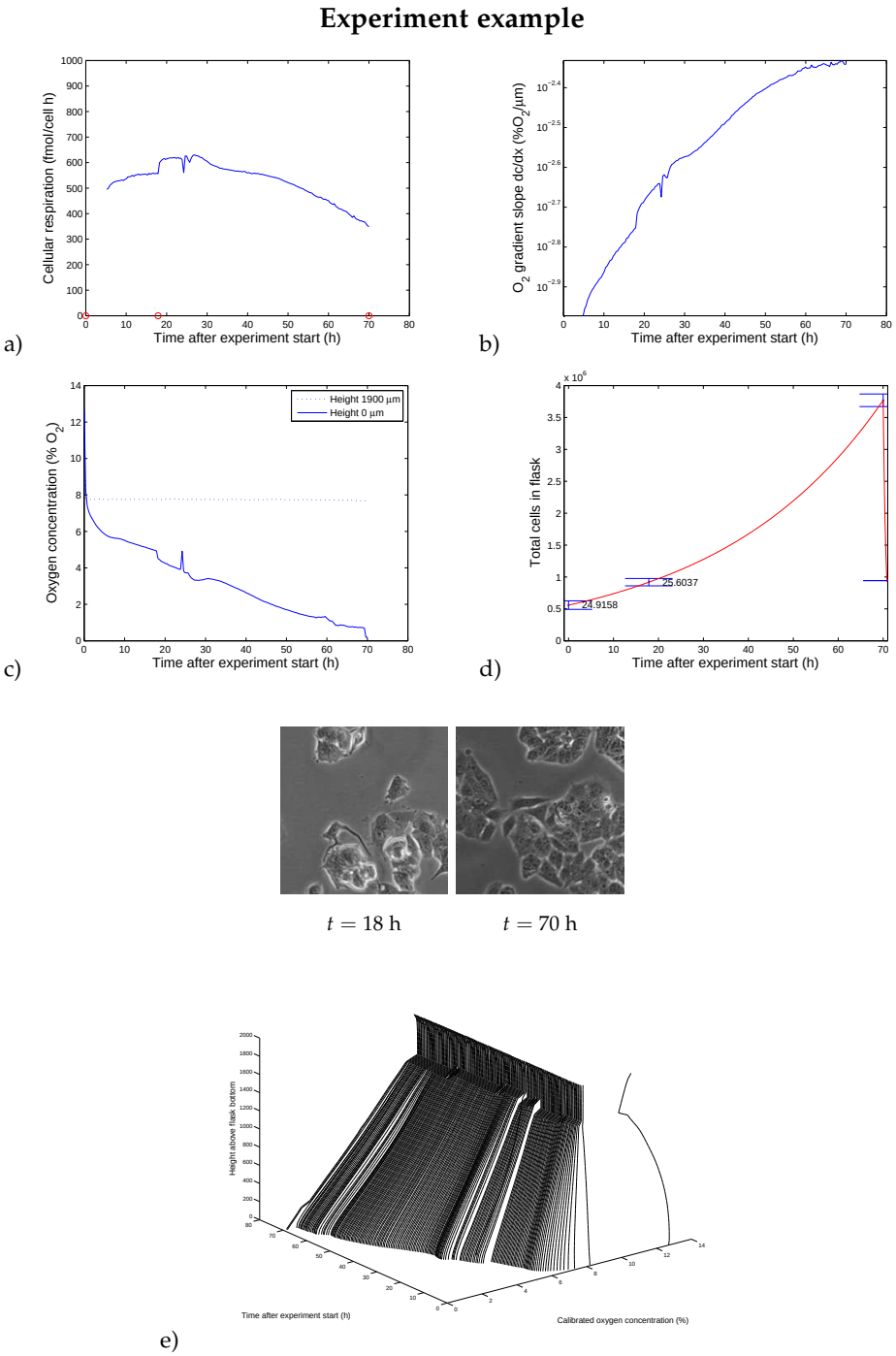

Figure 3.12: *An experiment example illustrating a selection of the plots produced by the Matlab software. The actual data is taken from experiment 081118, fraction 1.*

Plot c): Oxygen levels

This plot simply shows the measured oxygen concentration in the gas phase and the flask bottom (i.e. the POC). This data was collected directly from the calibrated data.

Plot d): Cell number

The cell number, acquired as described in section 3.8.4, is plotted. The discrete cell counting are marked with their standard errors, and the intermediate exponential interpolations are plotted as solid lines.

The estimated mean cellular doubling time between consecutive counts, $\bar{T}_2$, is also shown in the plots.

Plot e): 3D profile plot

This plot is intended to be used on a qualitative scale, as it shows the raw data acquired during the experiment. Its data, in addition to cell counting, lays the basis for all other analysis.

Flask respiration against cell count (app B)

In the plots in appendix B, plots of total respiration against interpolated cell number are shown. Given a constant cellular respiration and a cell number that is correct at all times, the plot would be a straight line (as total respiration would then be a simple linear function of cell number, the slope being the cellular respiration). If a nonlinear trend is observed, one or both of the above conditions were violated[6]. This plot does therefore, in general, provide an indication of the general health state of the cells in a *relative and dynamic* perspective. If the cellular respiration is to be considered on an *absolute* basis, the number of cells needs to be known (as it is at the time of cell counting).

It is important to remember that the cellular respiration plots are based on the information in the d) plots, the cell number. It can therefore be difficult to separate the two possible effects described in the last paragraph.

In addition, a strong correlation between mean cellular respiration and the mean doubling time of the culture probably exists, and the two factors would therefore collaborate to the slope of this plots.

[6]If possible additional (external) artifacts are negligible

3.9 Cellular survival experiments

Two cell cultures with ^{3}H medium and KV medium, respectively, was cultivated for four weeks. Each week, 200 cells were seeded to ten cell flasks (five with 200 ^{3}H cells and five with 200 KV cells), and the flasks were incubated. The cells were allowed to proliferate for several days until the colonies were easily visible without microscope.

The medium was then removed and the cells were washed with PBS (Euroclone, Great Britain). The colonies was fixated by exposing them to 96% ethanol for 2 minutes, and dyed with methylene blue (Merck, Germany) for approximately 2 minutes before washed with tepid water.

The cell colonies consisting of more than 50 cells was counted through a magnifying glass (Gerber Instruments, Germany). Colonies with a cell number close to 50 was inspected through the microscope.

3.9.1 Calculating plating efficiency and cellular surviving fraction

The *plating efficiency* (i.e. the fraction of cells administered to the flask that ends up as colonies with > 50 cells) were calculated based on the KV cells. It was assumed that the mean plating efficiency of the KV cells was identical to the mean plating efficiency of the ^{3}H cells.

The plating efficiency PE is given as

$$PE = \frac{C}{C_0} \tag{3.7}$$

where C_0 is the initially cell number added (in this case 200) to the KV flasks and C is the mean number of colonies with more than 50 cells in each KV flask.

The survival fraction SF of the ^{3}H cells was then calculated from

$$SF = \frac{N}{N_0 \cdot PE}$$

where N_0 is the number of cells seeded (200) and N is the number of colonies with more than 50 cells, and PE is the plating efficiency from equation 3.7.

The complete formula for the surviving fraction of the ^{3}H cells then becomes

$$SF = \frac{N}{N_0} \cdot \left(\frac{C}{C_0}\right)^{-1} = \frac{N}{C} \tag{3.8}$$

since $C_0 = N_0$.

The standard error of the plating efficiency is

$$se_{PE} = \frac{se_C}{C_0} \tag{3.9}$$

and the standard error of the surviving fraction is

$$\begin{aligned} se_{SF} &= \sqrt{\left(\frac{\partial SF}{\partial C}\, se_C\right)^2 + \left(\frac{\partial SF}{\partial N}\, se_N\right)^2} \\ &= \sqrt{\left(\frac{-C_0 \cdot N}{N_0 \cdot C^2}\, se_C\right)^2 + \left(\frac{C_0}{N_0 \cdot C}\, se_N\right)^2} \end{aligned} \tag{3.10}$$

Chapter 4

Results and analysis

4.1 Microscope resolution

The first set-up consisted of a Nikon TS100 microscope (Nikon, Japan) fitted with a 10x lens (Nikon, Japan) and a Paxcam 3 (PaxCam, USA) digital camera communicating to a Dell laptop running the dedicated Pax-It acquiring software. The second set-up consisted of a Nikon TMS-F (Nikon, Japan) microscope with a 10x Nikon lens and a Olympus SC20 (Olympus, Japan) digital camera, communicating with a Dell stationary PC running dedicated image acquisition software.

For each set-up, six pictures was taken of both the Bürker and the Kova chamber, and a total of 36 measurements was made. The measurements performed are listed in table 4.1 and 4.2 for set-up 1 and 2, respectively.

The data are used to calculate the mean and the standard error for each chamber, and the results for both set-ups are given in table 4.3.

The difference in results between Kova and Bürker chamber may be due to difference in distance from the cross board on the microscope to the object in focus, in production of the chambers as well as experimental error.

Throughout this thesis the mean of the measurements is used.

With the microscope resolution determined, P_f (pictures per flask) can be calculated from equation 3.1 on page 57.

4.1.1 Determining pictures per flask (set-up 1)

In this set-up, each picture had a digital resolution of 1024×768 pixels^2, and the microscopic resolution was found (from table 4.3) to be 1.2325 ± 0.0011 μm/px.

Table 4.1: *Measurements of known distances in the chamber images, three pictures of each chamber with six measurements performed per picture (set-up 1). K = Kova chamber picture, B = Bürker chamber picture. The measured distances were 1/3 mm and 0.2 mm, respectively.*

Picture	Meas. 1 (px)	Meas. 2 (px)	Meas. 3 (px)	Meas. 4 (px)	Meas. 5 (px)	Meas. 6 (px)
K#1	272	270	269	271	269	270
K#2	270	266	271	269	273	269
K#3	272	273	269	269	271	269
B#1	162	162	162	163	161	162
B#2	163	162	163	163	162	163
B#3	162	162	163	163	163	163

Table 4.2: *Measurements of known distances in the chamber images, three pictures of each chamber with six measurements performed per picture (set-up 2). K = Kova chamber picture, B = Bürker chamber picture. The measured distances were 1/3 mm and 0.2 mm, respectively.*

Picture	Meas. 1 (px)	Meas. 2 (px)	Meas. 3 (px)	Meas. 4 (px)	Meas. 5 (px)	Meas. 6 (px)
K#1	370	366	373	369	372	367
K#2	372	369	370	369	370	369
K#3	372	371	371	368	370	368
B#1	226	225	225	224	225	226
B#2	226	226	226	225	225	224
B#3	227	226	224	225	225	224

Table 4.3: *The average microscope resolution with standard errors.*

Set-up	Chamber	Mean measurement (px)	Resolution (μm/px)
1	Kova	270.1 ± 0.40	1.234 ± 0.0018
	Bürker	162.4 ± 0.15	1.231 ± 0.0011
	Mean		1.2325 ± 0.0011
2	Kova	369.78 ± 0.44	0.9014 ± 0.0011
	Bürker	225.08 ± 0.19	0.8886 ± 0.00073
	Mean		0.8950 ± 0.00064

The numbers of pictures per flask, P_f, is

$$P_f = 25\,\frac{\text{cm}^2}{\text{flask}} \cdot \left((1.2325 \pm 0.0011) \times 10^{-4}\,\frac{\text{cm}}{\text{pixels}} \right)^{-2} \cdot \left(1024 \times 768\,\frac{\text{pixels}^2}{\text{picture}} \right)^{-1}$$

and the cell number formula thus becomes

$$\begin{aligned} C &= 25\,\frac{\text{cm}^2}{\text{flask}} \cdot \left((1.2325 \pm 0.0011) \times 10^{-4}\,\frac{\text{cm}}{\text{pixels}} \right)^{-2} \\ &\quad \cdot \left(1024 \times 768\,\frac{\text{pixels}^2}{\text{picture}} \right)^{-1} \cdot \{C_p\}\,\frac{\text{cells}}{\text{picture}} \\ &\approx (2093 \pm 1.8) \cdot \{C_p\}\,\frac{\text{cells}}{\text{flask}}. \end{aligned}$$

Set-up 1 gave us 2093 pictures per flask.

4.1.2 Determining pictures per flask (set-up 2)

In this set-up, each picture had a digital resolution of 1596×1196 pixels^2, and the final microscopic resolution was (from table 4.3) 0.8950 ± 0.00064 μm/px.

The new P_f is found from

$$P_f = 25\,\frac{\text{cm}^2}{\text{flask}} \cdot \left((0.8950 \pm 0.00064) \times 10^{-4}\,\frac{\text{cm}}{\text{pixels}} \right)^{-2} \cdot \left(1596 \times 1196\,\frac{\text{pixels}^2}{\text{picture}} \right)^{-1}$$

and thus the formula for determining the cell number becomes

$$\begin{aligned} C &= 25\,\frac{\text{cm}^2}{\text{flask}} \cdot \left((0.8950 \pm 0.00064) \times 10^{-4}\,\frac{\text{cm}}{\text{pixels}} \right)^{-2} \\ &\quad \cdot \left(1596 \times 1196\,\frac{\text{pixels}^2}{\text{picture}} \right)^{-1} \cdot \{C_p\}\,\frac{\text{cells}}{\text{picture}} \\ &\approx (1635 \pm 1.2) \cdot \{C_p\}\,\frac{\text{cells}}{\text{flask}}. \end{aligned}$$

Set-up 2 thus yielded 1635 pictures per flask. Compared to the former 2093 pictures/flask, the second set-up had a lower resolution (i.e. higher μm/pixel and thus fewer pictures per flask and increased microscopic field of view) compared to the first.

When the Pax-it camera were used with set-up 2 instead of the Olympus camera, the mean resolution was found to be 1.3654 μm/pixel. It is seen from this that the camera indeed had a significant effect to the resolution.

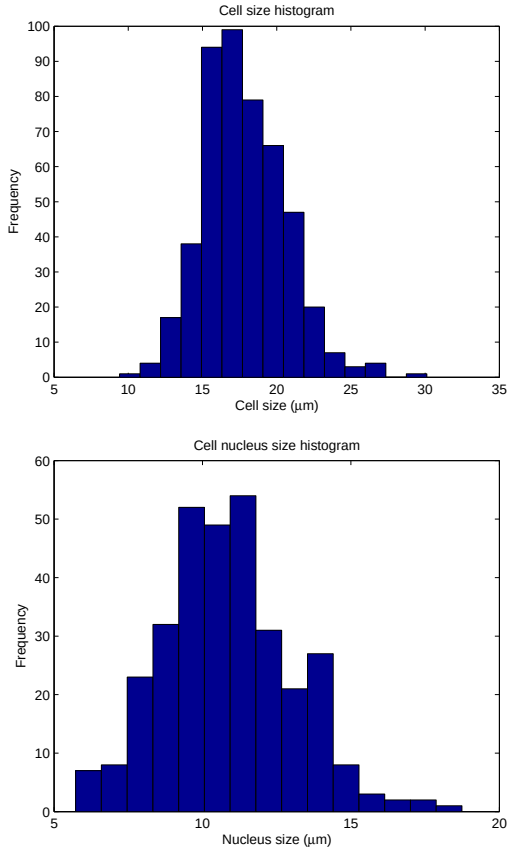

Figure 4.1: *Histogram of the 480 cell sizes and 320 nucleus sizes measured.*

4.2 Cell and nucleus size measurement

A total of 480 cells and 320 nuclei were measured using Matlab as described in section 3.3. A histogram of the resulting data is shown in figure 4.1.

The calculated mean diameters and standard errors are found in table 4.4.

Assuming that the cell and the nucleus were perfect spheres, their volumes can be estimated from their respective measured sizes:

$$V = \frac{4}{3}\pi\left(\frac{D}{2}\right)^3$$

and the standard error (see equation 2.41) becomes

$$se_V = 4\pi r^2 \cdot se_r.$$

These estimates can also be found in table 4.4.

Table 4.4: *The measured MCF-7 cell and nucleus sizes. An unpaired t-test yields a significant difference ($p < 0.0001$).*

Object	Diameter (μm)	Volume estimation (μm^3)	(ml)
Cell	17.82 ± 0.13	$(29.65 \pm 0.63) \times 10^2$	$(29.65 \pm 0.63) \times 10^{-10}$
Nucleus	10.84 ± 0.12	$(6.662 \pm 0.23) \times 10^2$	$(6.662 \pm 0.23) \times 10^{-10}$

4.3 Dosimetry

4.3.1 Cellular and nuclear activity

As described by Søvik (2002), an initial non-steady state phase existed before the cellular activity reached a stable value. The T-47D cells had such an initial phase lasting for about 100 hours (Søvik, 2002; Bjørhovde, 2006).

Søvik (2002) and Bjørhovde (2006) argues that the cellular activity slope in this interval can be approximated by the function

$$A(t) = \frac{at}{b+t} \tag{4.1}$$

as this function has the properties

$$A(0) = 0 \qquad \text{and} \qquad A(t \to \infty) \to a$$

i.e. the activity at time $t = 0$ is zero and it approaches a stable value when equilibrium is reached at time $t \to \infty$.

Cellular activity

The cellular activity was measured at three times, 72, 168 and 336 hours (that is, 3, 7 and 14 days) after the first exposure to the cells by radioactive medium. The resulting data is seen in figure 4.2, along with a fitted curve on the form of equation 4.1. The resulting activities are listed in table 4.5.

As the activity after 150 hours was assumed to be constant, the mean of the two measurements of $t > 150$ h is used to estimate the cellular activity.

Nuclear activity

To determine the fraction of the total activity contained in the nucleus, that is, the f_N value in equation 2.20 on page 17, the nuclear activity A_N was measured in addition to the cellular activity A_C.

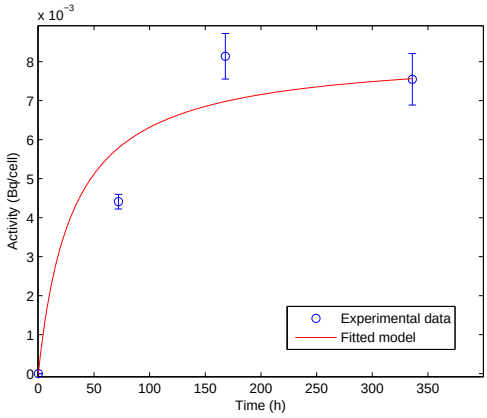

Figure 4.2: *The cellular activity as a function of time after first recultivation using 1.67 µCi/ml medium. The fitted curve has coefficients* $a = 0.008255$ *Bq and* $b = 30.72$ *h if t has unit hours (as in the plot), and* $a = 0.008255$ *Bq and* $b = 1.1059 \times 10^5$ *s if t has unit seconds (as in the calculations to come). The data indicates that steady state is reached before about 150 hours.*

Table 4.5: *The measured cellular activities* A_C *for both hot 1.67 µCi/ml RPMI and cold RPMI medium experiments. In addition, the mean of the two latter hot experiments, when equilibrium is assumed to be reached, is calculated.*

Time after initiation (h)	A_C (1.67 μCi/ml RPMI) (Bq/cell)	A_C (KV RPMI) (Bq/cell)
72 h	$(4.410 \pm 0.15) \times 10^{-3}$	$(1.567 \pm 0.052) \times 10^{-5}$
168 h	$(8.138 \pm 0.47) \times 10^{-3}$	-
336 h	$(7.546 \pm 0.37) \times 10^{-3}$	-
Mean	$(7.842 \pm 0.30) \times 10^{-3}$	$(1.567 \pm 0.052) \times 10^{-5}$

Table 4.6: *The measured nuclear activities in the three experiments performed as described in section 3.6.3.*

Buffer A exposure (min)	A_N (1.67 μCi/ml RPMI) (Bq/nucleus)
10	$(4.444 \pm 0.53) \times 10^{-3}$
12	$(4.865 \pm 0.53) \times 10^{-3}$
15	$(5.952 \pm 1.4) \times 10^{-3}$
Mean	$(5.087 \pm 0.54) \times 10^{-3}$

Three parallel experiments were performed with different exposure times to Buffer A (see section 3.6.3); 10, 12 and 15 minutes respectively. The measured activities are listed in table 4.6.

4.3.2 Determining the f values

To calculate the dose-rate to the nucleus (equation 2.20 on page 17) f_N and f_{Cy}, i.e. the distribution of the activity within the cell, needed to be determined. Their definitions are

$$f_N = \frac{A_N}{A_C} \tag{4.2}$$

and

$$f_{Cy} = \frac{A_{Cy}}{A_C} = \frac{A_C - A_N}{A_C} = 1 - f_N. \tag{4.3}$$

By means of scintillation counting the mean cellular activity and the mean nuclear activity were measured, and the results are found in table 4.5 and table 4.6.

In addition, the background activity A_B was measured in a KV sample. Assuming that this noise was evenly distributed and thus has a intracellular distribution proportional to the volume distribution, the actual f_N can be estimated from

$$f_N = \frac{A'_N - f_N^V \cdot A_B}{A'_C - A_B} \tag{4.4}$$

where A'_N and A'_C are the measured nuclear and cellular activities, and f_N^V is the nuclear volume fraction:

$$f_N^V = \frac{V_N}{V_C} = \frac{(4/3)\pi r_N^3}{(4/3)\pi r_C^3} = \frac{r_N^3}{r_C^3}.$$

The cell and nucleus diameters were measured in section 4.2 and found to be 17.824 ± 0.13 μm and 10.836 ± 0.12 μm, respectively. The nuclear

Table 4.7: *The measured activity distributions expressed as f values. f_N is the fraction of the total cellular activity contained in the nucleus, and f_{Cy} is the fraction in the cytoplasm. f_N^V is the volume fraction of the nucleus.*

f_N	f_{Cy}	f_N^V
0.650 ± 0.073	0.350 ∓ 0.073	0.2247 ± 0.0090

volume is calculated and found in table 4.7. The standard error of f_N^V is calculated from

$$se_{f_N^V} = \sqrt{\left(\frac{3r_N^2}{r_C^3} \cdot se_{r_N}\right)^2 + \left(\frac{-3r_N^3}{r_C^4} \cdot se_{r_C}\right)^2}.$$

The fraction of activity contained in the nucleus is thus calculated from equation 4.4. The resulting fractions f_N and f_{Cy} are found in table 4.7.

The standard errors are calculated from

$$se_{f_N} = \sqrt{\left(\frac{\partial f_N}{\partial A'_N} \cdot se_{A'_N}\right)^2 + \left(\frac{\partial f_N}{\partial A'_C} \cdot se_{A'_C}\right)^2 + \left(\frac{\partial f_N}{\partial f_N^V} \cdot se_{f_N^V}\right)^2 + \left(\frac{\partial f_N}{\partial A_B} \cdot se_{A_B}\right)^2}$$

and

$$se_{f_{Cy}} = \sqrt{\left(\frac{\partial f_{Cy}}{\partial f_N} \cdot se_{f_N}\right)^2} = -se_{f_N}$$

4.3.3 Determining the cellular S values

To determine the cellular S values, the cell and nucleus size needed to be known. The cell radius has been measured to be $8.912 \approx 9$ μm, and the nucleus radius $5.418 \approx 5$ μm.

A cellular S values list are found in appendix F. However, in this table the S values are a function of integer cellular and nuclear radii. In an attempt to increase the accuracy of the dose-rate calculation, interpolation was used to estimate the S values for the MCF-7 radii measured in this thesis. This was done in Matlab, but it was seen that using simple interpolation and trying to estimate the cellular S values for the radii measured, the final dose-rate was changed less than 1%, and therefore the integer S values was deemed appropriate.

This yields the S values from appendix F found in table 4.8.

Table 4.8: *The S values from appendix F for cell and nucleus radii 9 and 5 µm, respectively.*

$S(R_N \leftarrow R_N)$ (Gy/Bq·s)	$S(R_N \leftarrow R_{Cy})$ (Gy/Bq·s)
1.43×10^{-3}	7.86×10^{-5}

Table 4.9: *The calculated dose-rate to the MCF-7 nucleus after equilibrium was reached with two different medium specific activities.*

Medium specific activity A^S_{RPMI} (μCi/ml)	Dose-rate $\dot{D}$ (Gy/h)
1.67	0.0270 ± 0.0030
0.735	0.0119 ± 0.0013

4.3.4 Dose-rate to the nucleus

The dose-rate to the nucleus can be calculated using the theory presented in section 2.3.6.

Equation 2.20 reads

$$\dot{D}_N = A_C \left[f_N S(R_N \leftarrow R_N) + f_{Cy} S(R_N \leftarrow R_{Cy}) \right]$$

and the standard error becomes (equation 2.21)

$$se_{\dot{D}} = \sqrt{\left(\frac{\partial \dot{D}}{\partial A_C} \cdot se_{A_C} \right)^2 + \left(\frac{\partial \dot{D}}{\partial f_N} \cdot se_{f_N} \right)^2 + \left(\frac{\partial \dot{D}}{\partial f_{Cy}} \cdot se_{f_{Cy}} \right)^2}$$

The dose-rate and standard error are found in table 4.9.

4.3.5 Dose-rate as a function of medium specific activity

Assuming that the intracellular activity A_C was proportional to the extracellular specific activity A^S_{RPMI}, and that the intracellular activity distribution f_N and $f_C y$ were independent of extracellular specific activity, the dose and dose-rate are simply linear functions of medium activity:

$$\dot{D}(A^S_{\text{RPMI}}) = a + b \cdot A^S_{\text{RPMI}}. \tag{4.5}$$

This can be used to determine the medium specific activity necessary to achieve any wanted dose-rate. Assuming that $\dot{D}(0) = 0$, it follows that $a = 0$. b thus has a numerical value of

$$\{b\} = \left\{ \frac{\dot{D}(A_1)}{A_1} \right\} = (1.6235 \pm 0.18) \times 10^{-2}$$

and have units $[b] = (\text{Gy}\cdot\text{ml})/(\mu\text{Ci}\cdot\text{h})$. The standard error is calculated using equation 2.41.

This yields the following linear relation between the specific activity of the RPMI medium and the dose-rate to the nucleus in the MCF-7 cell:

$$\dot{D}(A) = (1.6235 \pm 0.18) \times 10^{-2} \cdot A. \tag{4.6}$$

When a dose-rate of 0.012 Gy/h was needed in experiments, a ^{3}H RPMI specific activity of 0.7391 μCi/ml was required. This is roughly 0.44 of the original 1.67 μCi/ml RPMI, and was easily produced by adding KV RPMI with a ratio 1.261:1 to the original ^{3}H RPMI.

4.3.6 Accumulated activity and dose to the nucleus

In addition to the dose-rate it is important to consider the total dose D delivered to the nucleus. The dose delivered in a specified time interval (t_0, t_1) can be written as a function of $\dot{D}$:

$$D = \int_{t_0}^{t_1} \dot{D}(t)\, dt \tag{4.7}$$

If $\dot{D}$ is constant in time, D is simply

$$D = \dot{D} \cdot (t_1 - t_0). \tag{4.8}$$

During the initial phase before reaching steady state (hereby called *pre-steady state phase*), the dose-rate to the nucleus was indeed not constant, but rather a function of time.

Using the micro dosimetry theory presented in section 2.3.6, the accumulated dose can be calculated from the activities using the S values. Equation 4.1 estimates the total activity as a function of time in the pre-steady state phase, and by integrating it the accumulated activity can be found. This can be used in equation 2.22 to estimate the total dose delivered in this interval. Equation 4.1 yields an increase in dose-rate even after steady state is reached, and therefore it will overestimate the dose delivered to the nucleus after stability is acquired. Thus, this equation is

Table 4.10: *The calculated integrated cellular activity $\tilde{A}_C$ using a medium of specific activity 1.67 µCi/ml. As the pre-steady state dose has no standard error due to the fitted function, the standard errors of the integrated activities are a result solely of calculations with $t \geq 150$ h.*

Time interval (h)	$\tilde{A}_C$ (Bq s)
0–150 (pre-steady state)	2.8399×10^3
0–168 (1 week)	$(3.3481 \pm 0.0000054) \times 10^3$
0–336 (2 weeks)	$(8.091 \pm 0.00005) \times 10^3$
0–504 (3 weeks)	$(12.834 \pm 0.00011) \times 10^3$

only used to estimate the dose delivered during the initial pre-steady state phase, and after steady state is reached the dose is calculated using the values in table 4.9.

Integrating equation 4.1 yields

$$A_{t=(t_0,t_1)} = \int_{t_0}^{t_1} \frac{at}{b+t}\, dt = at - ab\ln(b+t)\big|_{t_0}^{t_1}. \tag{4.9}$$

As indicated in figure 4.2, the initial phase lasts for about 150 hours. The calculated integrated activity for the pre-steady state phase is found in table 4.10.

The mean absorbed dose in the nucleus is given in equation 2.22:

$$D_N = \tilde{A}_C \left[f_N S(R_N \leftarrow R_N) + f_{Cy} S(R_N \leftarrow R_{Cy}) \right]$$

and the standard error are given in equation 2.23:

$$se_D = \sqrt{\left(\frac{\partial D}{\partial \tilde{A}_C} \cdot se_{S_C}\right)^2 + \left(\frac{\partial D}{\partial f_N} \cdot se_{f_N}\right)^2 + \left(\frac{\partial D}{\partial f_{Cy}} \cdot se_{f_{Cy}}\right)^2}.$$

Solving the equations above for the intervals in table 4.10 results in the accumulated doses. The results are found in table 4.11.

4.3.7 Radioactive medium activity measurement

The specific activity of the radioactive medium used was checked in the scintillation counter. Two samples of 0.5 ml ^{3}H RPMI were vortexed with 8 ml scintillation fluid each. The results of the scintillation counting are found in table 4.12.

Table 4.11: *Estimate of the total accumulated dose delivered to the nucleus. As in table 4.10, the standard errors of the integrated activities used in the calculation from $t \geq 150$ h. In addition, in calculating the delivered dose, standard errors in the f values contribute (using equation 2.41). The values for 0.735 μCi/ml RPMI are calculated assuming the linear relationship presented in section 4.3.5.*

A^S_{RPMI} (μCi/ml)	Time interval	Dose D (Gy)
1.67	0–150 (pre-steady state)	2.716 ± 0.28
	0–168 (1 week)	3.2019 ± 0.33
	0–336 (2 weeks)	7.738 ± 0.80
	0–504 (3 weeks)	12.274 ± 1.3
0.735	0–150 (pre-steady state)	1.195 ± 0.12
	0–168 (1 week)	1.409 ± 0.15
	0–336 (2 weeks)	3.406 ± 0.35
	0–504 (3 weeks)	5.402 ± 0.56

Table 4.12: *The measured specific activity of the 1.67 μCi/ml medium used.*

Sample	A^S_{RPMI} (Bq/ml)	(μCi/ml)
# 1	6.025×10^4	1.6267
# 2	6.294×10^4	1.6993
Mean	$(6.159 \pm 0.14) \times 10^4$	1.6630 ± 0.036

Table 4.13: *The extracellular, intracellular and intranuclear specific activities, as well as the ratio of the intracellular and -nuclear specific activities to the extracellular (medium) specific activity. The latter illustrates the accumulation of radioactivity inside the cell and nucleus. The theoretical specific activity of the medium was 1.67 μCi/ml.*

	Specific activity (Bq/ml)	Ratio $X : A^S_{\text{RPMI}}$
Extracellular (A^S_{RPMI})	$(6.159 \pm 0.14) \times 10^4$	1:1
Intracellular (A^S_C)	$(2.645 \pm 0.012) \times 10^6$	43:1
Intranuclear (A^S_N)	$(7.636 \pm 0.084) \times 10^6$	124:1

4.3.8 The extracellular and intracellular specific activities

The extracellular specific activity is just the medium specific activity, given in table 4.12.

The intracellular specific activity, however, must be calculated. The activity data from table 4.5 and 4.6 are given as Bq/cell and Bq/nucleus. The specific cell and nucleus activities are given from equation 2.2 on page 5:

$$A^S_C = \frac{A_C}{V_C}$$

and

$$A^S_N = \frac{A_N}{V_N}.$$

V_C and V_N are estimated in table 4.4. The resulting specific activities are listen in table 4.13.

From the data it is seen that the intracellular activity was over 40 times higher than the extracellular specific activity. This indicates, as was assumed, that the cell accumulated a radioactivity concentration. The intranuclear specific activity was more than 120 times the extracellular activity, suggesting a very high accumulation of radioactivity in the nucleus.

4.3.9 Control of the T-47D dose-rate

The T-47D cell line dosimetry har been studied and described by Bjørhovde (2006) and Søvik (2002). With a specific medium activity of 1.67 μCi/ml, the dose-rates found in their work are listed in table 4.14.

As a side experiment, the nucleus activity for T-47D with the same ^{3}H RPMI medium as used with the MCF-7 cells has been measured utilizing the method described in section 3.6.3. The cells had been cultivated in

Table 4.14: *The measured cellular activity A_C, nuclear activity fraction f_N and the calculated dose-rate $\dot{D}$ to the T-47D nucleus after equilibrium was reached. In all cases the specific medium activity was 1.67 μCi/ml.*
†: f and S values from Søvik (2002) are used in calculations.
**: f and S values from Bjørhovde (2006) are used in calculations.*

Source	A_N (Bq)	f_N	$\dot{D}$ (Gy/h)
Søvik (2002)	$(3.84 \pm 0.35) \times 10^{-3}$	0.24 ± 0.02	0.010 ± 0.001
Bjørhovde (2006)	$(4.20 \pm 1.2) \times 10^{-3}$	0.6 ± 0.05	0.015 ± 0.004
Storhaug (2008)	$(4.74 \pm 1.4) \times 10^{-3}$	0.6 ± 0.05*	0.016 ± 0.004*
Current thesis	$(3.47 \pm 0.12) \times 10^{-3}$	$0.24 \pm 0.02^{\dagger}$ 0.6 ± 0.05*	$0.0897 \pm 0.00092^{\dagger}$ 0.0124 ± 0.0013*

the radioactive medium for one week before the nucleus preparation and scintillation counting was performed, and it was thus assumed that steady state was reached (As also assumed by both Søvik (2002) and Bjørhovde (2006)).

Assuming the f values and cell and nucleus sizes (and thus the respective S values) to be identical to the work of Bjørhovde (2006) or Søvik (2002), the respective dose-rates to the T-47D nucleus can be calculated and are found in table 4.14.

4.4 Overview: Hypoxia experiments

A total of six hypoxia experiments were performed, listed below.

Exp. title	No. of fractions	O_2 concentration	Medium activity
081020	1	10% O_2	cold RPMI
081103	4	12% O_2	cold RPMI
081118	7	8% O_2	cold RPMI
081212	2	6% O_2	cold RPMI
090608	3	8% O_2	1.67 μCi/ml
090622	2	8% O_2	0.735 μCi/ml

First, the respirational effect of confluence in 10% O_2^{gp} was investigated in experiment 081020.

Then, the respirational effect of hypoxia in three different gas phase oxygen concentrations were performed; 081103 (in 12% O_2^{gp}), 081118 (in 8% O_2^{gp}) and 081212 (in 6% O_2^{gp}).

Finally, the 8% O_2^{gp} experiment was repeated with a radioactive medium. However, as presented earlier, the dose-rate to the nucleus was considerably higher than expected and therefore two experiments was performed; 090608 (8% O_2^{gp} with 1.67 μCi/ml RPMI) and 090622 (8% O_2^{gp} with 0.735 μCi/ml RPMI).

The hypoxia experiments resulted in large amounts of data, and are in this chapter presented in the following way. In sections 4.5 and 4.6, the data plots from all the hypoxia experiments are presented, in chronological order, along with some comments to the plots. In section 4.7 the data from the confluence hypoxia experiment is presented.

In addition, in sections 4.8, 4.9 and 4.10, the most important results are presented in a more clear way to easily allow comparison.

Throughout the presentation, analyzation and discussion of the data, the experiment are identified by experiment title and/or gas phase concentration. If radioactive medium was used, it is always explicitly stated.

4.5 Data from the hypoxia experiments without irradiation

The main goal of experiments 081103, 081118 and 081212 was to determine the lower threshold value of oxygen concentration (in the gas phase) at which the cells did survive the oxygen deprivation.

Three oxygen concentration was tested, 12% O_2^{gp}, 8% O_2^{gp} and 6% O_2^{gp}. The experiment initiation date was used to identify each experiment, and was labeled 081103, 081118 and 081212, respectively.

In this chapter some of the raw data obtained from the hypoxia experiments without irradiation are presented in the form of plots, along with some processed plots from Matlab used for analyzation. In addition some general observations are addressed, along with some interesting features of the plots.

As a single experiment contained several cell recultivations, the experiments was divided into experiment fractions, representing the FORLØP between two recultivations. The experiment fractions was distinguished by a suffix.

The main discussion is saved for chapter 5.

4.5.1 Data from experiment 081103 (12% O_2^{gp})

The main goal of experiment 081103 was to determine the cellular behavior and respiration in 12% O_2^{gp}, and potentially observe any effects of possible hypoxia. This experiment lasted for 358 hours and consisted of four experiment fractions.

The calculated discrete respirations are listed in table 4.16, and the experiment progress and individual events are listed in table 4.15.

Table 4.15: *The events of experiment 081103 (12% O_2^{gp})*

Time (h)	Event
0	Experiment start
21.00	Cell count
42.00	Medium change, cell count
67.00	Cell count
93.66	Cell count, recultivation 1:2
166.00	Medium change, cell count
192.50	Cell count, recultivation 1:3
214.60	Cell count
238.90	Cell count, recultivation 1:5
239.30	Cell count
359.00	Cell count, experiment end

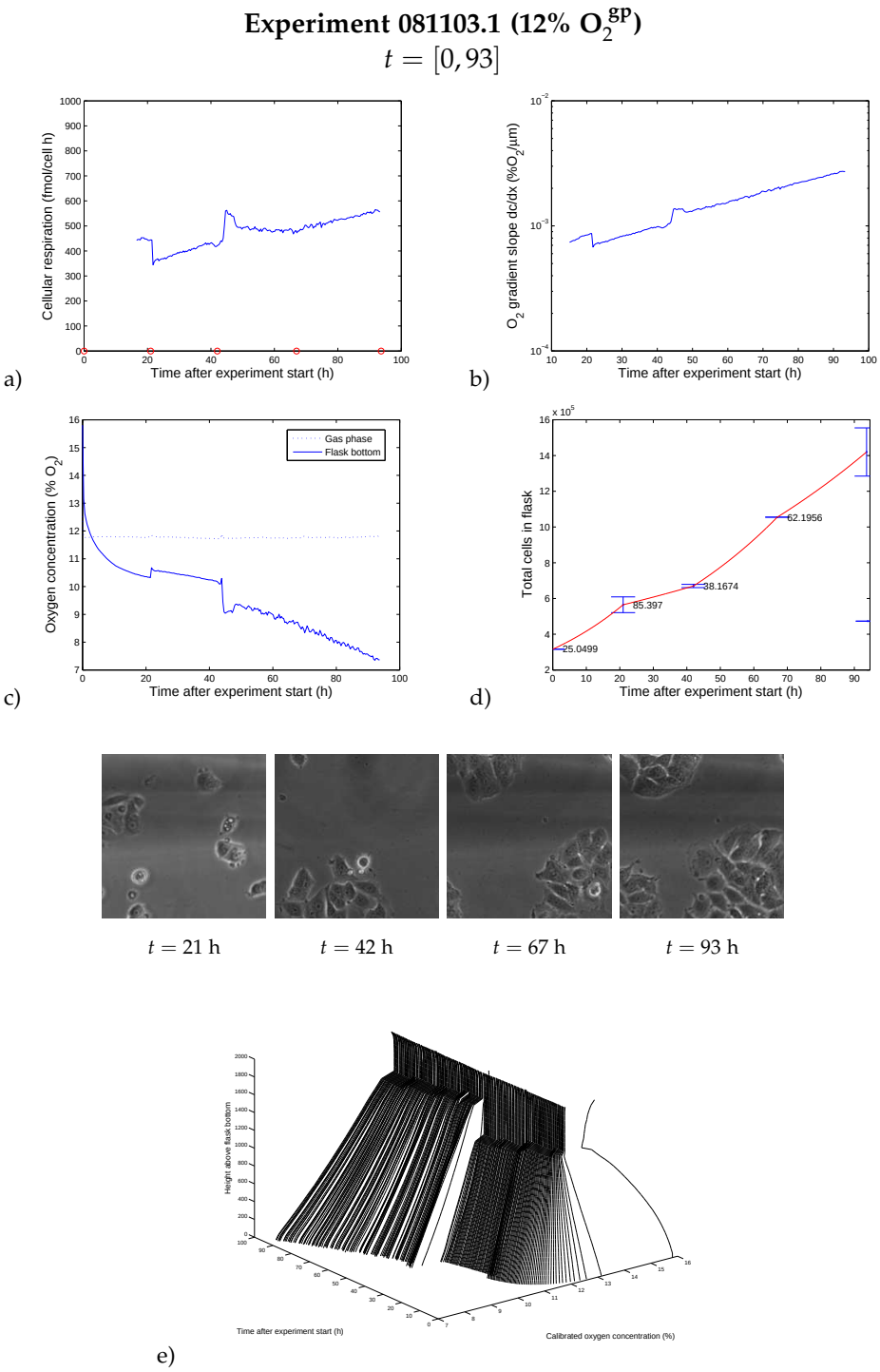

Figure 4.3: *Plots showing the data acquired during experiment 081103 (12% O_2^{gp}) in the time interval 0-93 h.*

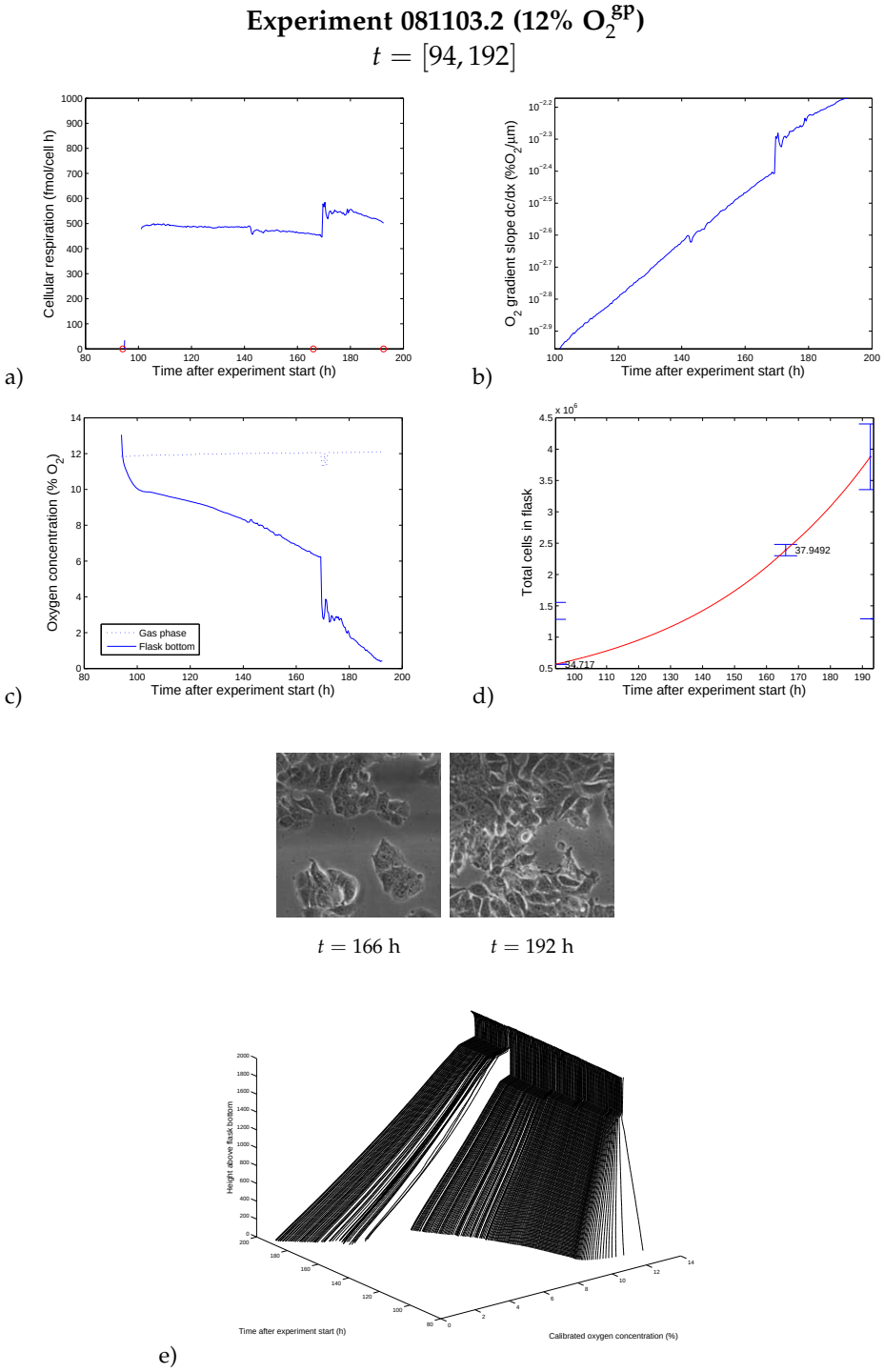

Figure 4.4: *Plots showing the data acquired during experiment 081103 (12% O_2^{gp}) in the time interval 94-192 h.*

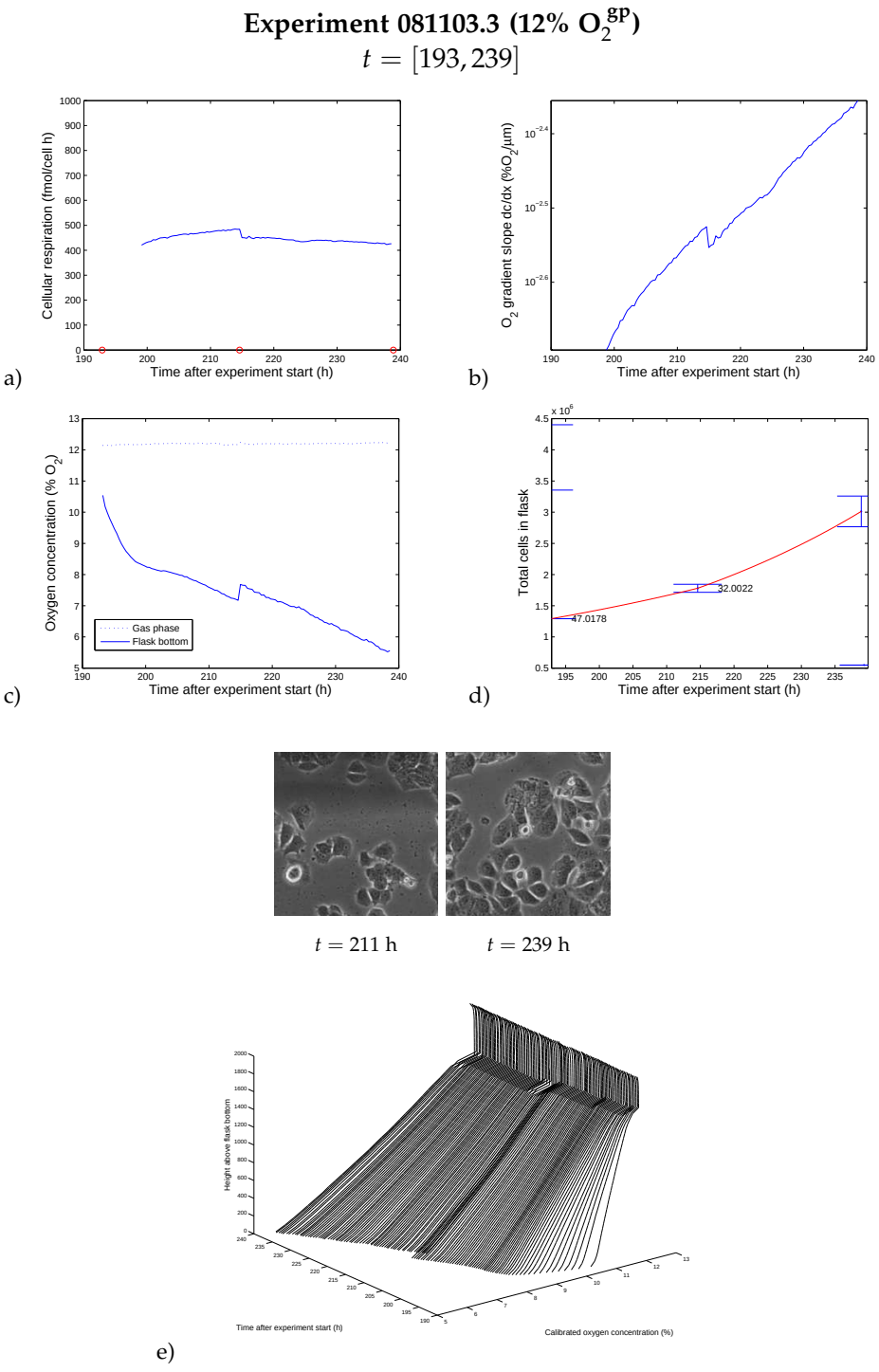

Figure 4.5: *Plots showing the data acquired during experiment 081103 (12% O_2^{gp}) in the time interval 193-239 h.*

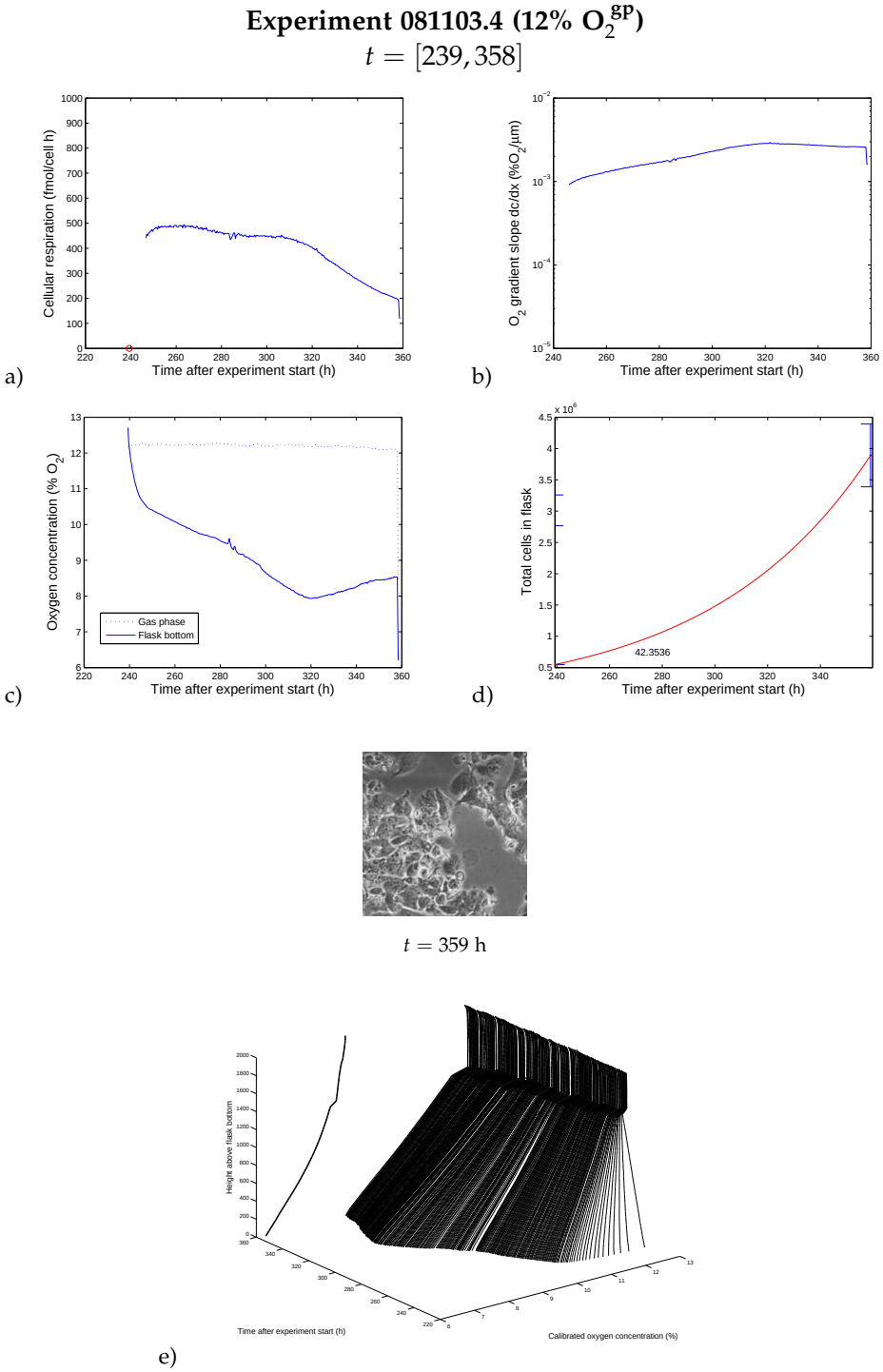

Figure 4.6: *Plots showing the data acquired during experiment 081103 (12% O_2^{gp}) in the time interval 239-358 h.*

Table 4.16: *Cellular respiration calculated when cell counting was performed in experiment 081103 (12% O_2^{gp}). The mean, excluding the last measurement, is 467.24 fmol/h·cell.*

Time (h)	Cell resp (fmol/h·cell)
21.00	445.0 ± 35
42.00	427.2 ± 5.8
67.00	479.6
93.66	553.4 ± 53
166.00	455.9 ± 18
192.50	501.6 ± 68
211.00	452.0 ± 16
239.30	423.2 ± 35
359.00	187.2 ± 24

Table 4.17: *The mean doubling times, $\bar{T}_2$, of experiment 081103 (12% O_2^{gp}). The doubling times are calculated based on the first and last cell count in every interval.*

Fraction	Mean doubling time (h)
081103.1	43.20
081103.2	35.53
081103.3	37.68
081103.4	42.35
Mean	39.69 ± 1.8

Fraction 081103.1, 0-93 h

This experiment fraction shows us the behavior of the cells experiencing a considerable oxygen difference, coming from 21% O_2^{gp} in the lab to a 12% O_2^{gp} in the cabinet. The measurements started within 30 mins after the transfer.

From the plots in figure 4.3, a stabilizing phase is seen before the system reached equilibrium. As seen from the data, the system used about 20 hours to stabilize. This was probably due to the excess oxygen from the lab that needed to either be consumed by the cells, or to travel via diffusion to the gas phase above the medium. The cell number was low, and from the plots it seems that the diffusion of oxygen from the medium

to the gas phase was low.

In addition, the effect of cell counting (and thus medium stirring) and medium change is seen as data artifacts at times 21 h and 42 h. The cell counting at 21 h, performed before equilibrium of the system was reached, seems to disturb the stabilizing process.

On the other hand, once equilibrium was reached, the profile was quickly reformed after the the medium change at 42 h, despite this being a much more extensive event.

Fraction 081103.2, 94-192 h

At this experiment fraction start, the cells had been in 12% O_2^{gp} for 4 days. The cells was recultivated within the cabinet and therefore never exposed to atmospheric oxygen concentrations during handling.

The stabilizing phase was considerably shorter in this fraction relative to 081103.1.

There was no counting performed after the recultivation at 94 h, so the cellular respiration progression between 94 h and 166 h should not be taken into account. The cell count at 94 h was estimated from an assumed plating efficiency and the recultivation fraction.

Fraction 081103.3, 193-239 h

At this experiment fraction start, the cells had been in 12% O_2^{gp} for 8 days. The recultivation was performed within the cabinet.

The system was stable after 198.8 hours, yielding a stabilizing period lasting for 6 hours.

Fraction 081103.4, 239-358 h

At 239 h the cells had been in 12% O_2^{gp} for 10 days. The recultivation at time 239 was performed in the cabinet.

This experiment fraction was special with respect to the absence of any cell maintenance, i.e. medium change and recultivation.

The system reached equilibrium after 247.4 h, 8 hours after fraction initiation.

4.5.2 Experiment 081103 (12% O_2^{gp}) summary

Experiment 081103 investigated the (respirational) effect of prolonged exposure to 12% O_2^{gp} on the MCF-7 human cancer cell line. Some of the most interesting quantitative data are listed in table 4.18 on page 103.

After the cell flask was brought from the lab into the cabinet, the system initially used close to 20 hours to reach equilibrium. This is, as previously discussed, highly probably due to excess oxygen that was present in the medium (this is supported by oxygen readings), and the fact that this oxygen either had to diffuse to the gas phase or be consumed by the cells. At this time, the cell number was low. In the later fractions, this phase lasted between 6 and 10 hours. The overall mean stabilizing phase duration was 10.70 ± 2.7 h.

Before equilibrium was reached, a medium disturbance seems to result in a major set-back in the stabilizing process. In contrast, after the system had reached equilibrium, the unwanted effects of cell maintenance seems to be less expressed and thus less of a problem.

Pericellular oxygen concentration

During this experiment, the POC was below 4% O_2 for a limited time only (less than 22 hours). This occured when the medium level was higher than normal during fraction 081103.2. In this fraction, the oxygen concentration at flask bottom never fell below 0.39% O_2 (minimum occuring at time 191.80 h).

With normal medium level, the POC never reached below 5.5% O_2.

No clear effect of the lower oxygen aviliability can be seen in the plot (the characteristic POC slope change seen in later experiments is absent), with a possible subtle exception when the POC fell below 0.6% O_2.

The effects seen after 300 hours were probably due to the absence of cell maintenance, where an increase in POC is seen.

In fraction 1, as the medium contained 21% O_2 from the atmosphere, a lengthy stabilizing phase is seen in the plots as the excess oxygen either had to diffuse to the gas phase or be consumed by the cells. This probably also contributed to the effect seen when cell counting was performed, as the delicate oxygen gradient in the medium was disturbed.

The stabilizing phase in fraction 2 was shorter than in fraction 1, probably partly due to the fact that cell number was considerably higher when fraction 2 was initiated in addition to the effect of lab oxygen residues in the first fraction.

As medium levels always increased as a result of medium changes (due to water evaporation in the old medium), a maintained absolute cellular

Table 4.18: *Selected quantitative data from experiment 081103 (12% O_2^{gp} without irradiation), including stabilizing phase duration and maximum respiration level as well as POC values at respiration maximum and at POC slope change. In addition, if a (transient) equilibrium at a low POC value is seen (i.e. a horizontal POC plot), the floor POC level are listed.*

Fraction	Stab. phase duration (h)	Max. resp (fmol/h·cell)	(% O_2)	POC slope change (% O_2)	Floor POC level (% O_2)
081103.1	18.44	565.5	7.382	never	none
081103.2	10.37	584.9	2.746	0.4655	none
081103.3	5.9	484.8	7.233	never	none
081103.4	8.1	494.8	9.957	7.932	none
Mean	10.70 ± 2.7	532.5 ± 25	6.830 ± 1.5	4.20 ± 3.7	-

respiration (that is, the same oxygen gradient slope) would yield lower POC values than before the medium change, due to an increased diffusion distance (see equation 2.33 on page 48). This may result in an effect in the respiration as the oxygen availability was abruptly reduced, further affecting the slope of the POC.

In fraction 3, a local probe environment difference (see figure 3.5 on page 64) may explain the effect of different POC with the same cellular respiration.

Experiment fraction 4 seemed to progress similar to the former fractions. But after 320 h (3 days and 9 hours), both the flask respiration and the estimated cellular respiration decreased, and the POC therefore increased. The minimum occured at 320.1 hours, when the POC was 7.93% O_2. This is highly probable due to the absence of cell maintenance tasks.

In all earlier experiment fractions, lower pericellular oxygen concentrations than 7.98% O_2 were reached without any noticeable cellular response. This suggests that the indicated cellular discomfort after 230 hours did not occur (at least solely) due to lower oxygen concentrations.

Flask and cellular respiration

In fraction 1, 2 and 3, after the initial stabilizing phase, the total flask respiration seems to be increasing exponentially with time. The cell count and medium change are clearly visible in the plots.

Excluding the initial stabilizing phases and the decrease trends at the end, the cellular respiration were always between 420 and 580 fmol/h·cell. The mean cellular respiration was 467.24 fmol/h·cell (table 4.16), and the mean maximum respiration was 532.5 $\pm$ 25 fmol/h·cell(table 4.18).

In general, an increase in cellular respiration is seen when a medium change is performed, probably due to improved cellular access to nutrients and more favorable pH level. In addition, other effects are possible, discussed in section 5.7.3. After each medium change, the system used about 10 hours to regain usable profiles and thus provided the cells with up to 10 hours of higher oxygen levels.

When a proper cell count (i.e. a task involving flask movement and thus medium stirring) was performed (only once in this experiment, at time 214.60 h) the respiration decreased some.

As a result of the absent cell maintenance in the last fraction, the cellular respiration decreased after about 300 h. This was mirrored in the increased POC, as the oxygen gradients became less steep. When the experiment was terminated the cellular respiration was below 190 fmol/h·cell.

In fraction 2, the measured oxygen concentration in the local environment of the cells reached about 0.39% O_2 before recultivation, considerably

lower than any other experiment fraction of experiment 081103.

The cell count artifact at 214 hours in fraction 3 is visible, and it seems from the plot that the event caused a setback in the flask respiration as the slope seems to be parallel displaced.

As seen in figure 4.5 a), the cellular respiration in fraction 3 was relatively stable, however, after the cell count the cellular respiration had a somewhat linear decrease from 450 to 420 fmol/h·cell.

In fraction 4 the flask respiration seemed to have an exponential slope. However, as cell maintenance was eventually ceased, after around 320 hours a maximum value was reached and a somewhat linear decrease is observed in the flask respiration plot until experiment termination. At 230 h the cell number was (from the exponential fit) approximately 2.05×10^6 cells (plot d)), but this is probably an underestimate since the mean doubling time probably decreased as the experiment fraction progressed. At 359 hours, the cellular respiration was 187.2 ± 24 fmol/h·cell, a value very low compared to the other experiment fractions, and a clear indication of cellular non-prosperity.

Cellular proliferation

The mean cellular doubling time varied from 32 h to 85 h, depending on interval of measurement. Results indicates that $\bar{T}_2$ was lowest in the middle of a fraction, and higher at the start and at the end. This is consistent with the existence of a lag time after a recultivation (at fraction start), and possible an effect of confluence or near-confluence, in addition to possible effects due to lower oxygen aviliability (at fraction end).

In fraction 1, the mean doubling time was high (85.4 hours) in the interval from 25 h to 85 h during the first part of the fraction. This may have been a reaction to the lower oxygen concentration, as the POC decreaed from 21 % to just over 10 % in 20 h (see figure 4.3 c)). The decrease in cell doubling rate may also have been a consequence of lower medium level due to evaporation and therefore increased medium concentration. At the current cell number ($\sim$600.000 cells), the cells were certanly not confluent.

After the medium change at 43 h, the mean doubling time the next hours decreased to 38 h, before increasing to 62 h. This time, the medium volume was larger, and the effect of evaporation (the surface area being the same) and thus medium concentration were therefore probably less significant.

The doubling time in fractions 2 and 3 are not statistically different, 36.7 h vs 37.9 h. No sign in decreased proliferation can (yet) be seen as a consequence of a lengthy exposure to 12% O_2^{gp}.

In fraction 4, the mean doubling time was 42.4 hours, but from the

other plots it is reasonable to assume that the cellular proliferation rate decreased after 320 hours. In other words, $\bar{T}_2$ was probably less than 42.4 at $t < 320$ h and greater at 42.4 h at $t > 320$ h.

4.5.3 Data from experiment 081118 (8% O_2^{gp})

The main goal of experiment 081118 was to determine the cellular respiration in 8% O_2^{gp}. It lasted for 573 hours (i.e. almost 24 days) and consisted of 7 experiment fractions. The experiment progress and individual events is listed in table 4.19. The reason for the lengthy duration was to increase the possibility to observe effects due to hypoxia before experiment end.

This experiment was *not* an extension of experiment 081103, meaning that the cells used in this experiment did not have a history of experiencing 12% O_2^{gp}. No inter-experimental adaptation effect is therefore considered in this thesis. This is for the sake of reproducibility.

The calculated discrete respirations are listed in table 4.20.

Table 4.19: *The events of experiment 081118 (8% O_2^{gp})*

Time (h)	Event
0	Experiment start, cell count
17.87	Medium change, cell count
70.01	Cell count, recultivation 1:4
149.00	Cell count, recultivation 1:4
149.30	Cell count
169.10	Cell count
190.30	Medium change, cell count
241.30	Cell count, recultivation 1:5
241.70	Cell count
313.60	Cell count, recultivation 1:7
313.90	Cell count
358.20	Medium change, cell count
385.80	Cell count
409.60	Cell count, recultivation 1:6
410.00	Cell count
453.75	Cell count
481.50	Cell count, recultivation 1:3
481.90	Cell count
501.20	Cell count
528.00	Medium change, cell count
549.25	Cell count
573.75	Cell count, experiment end

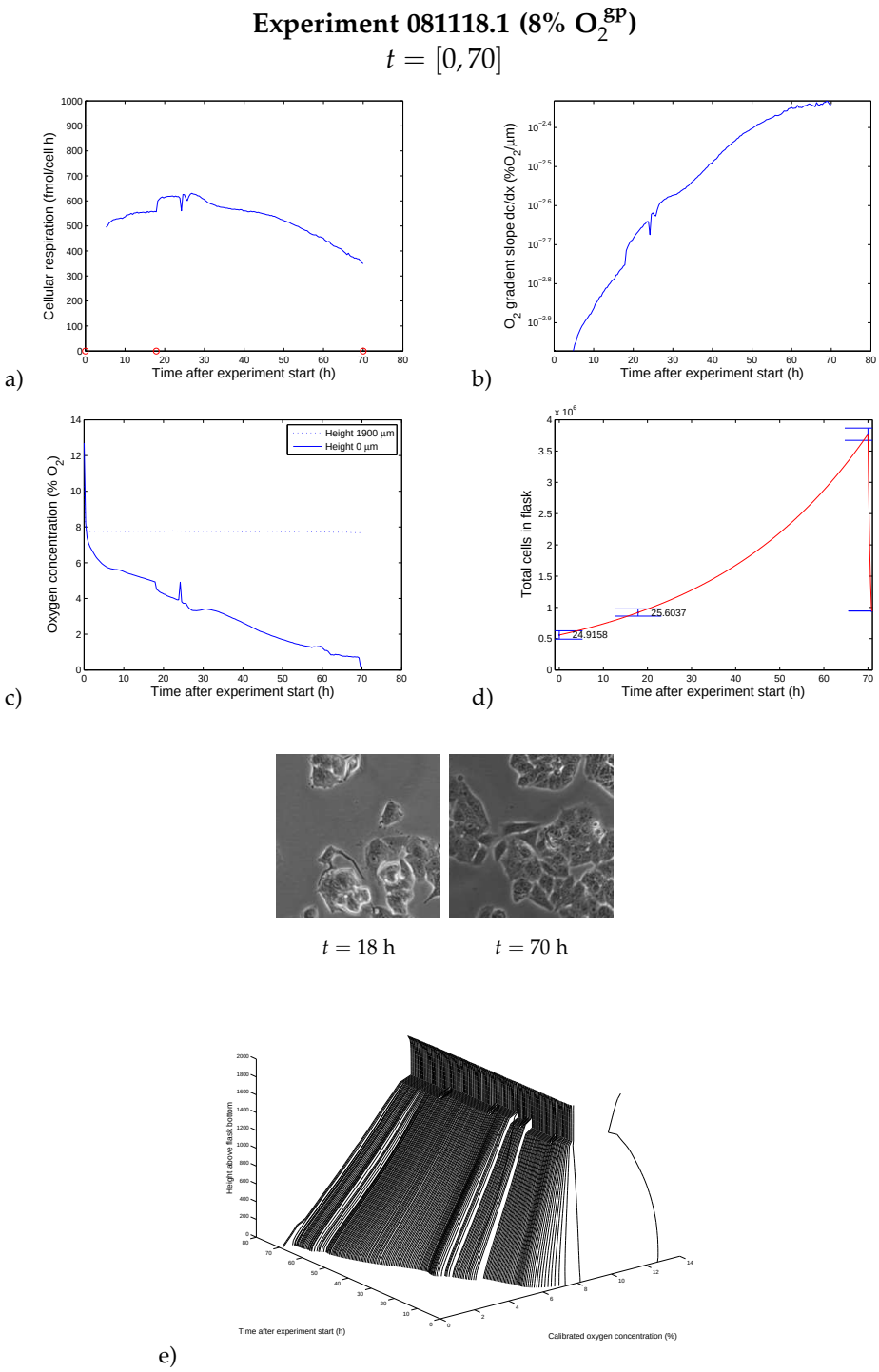

Figure 4.7: *Plots showing the data acquired during experiment 081118 (8% O_2^{gp}) in the time interval 0-70 h.*

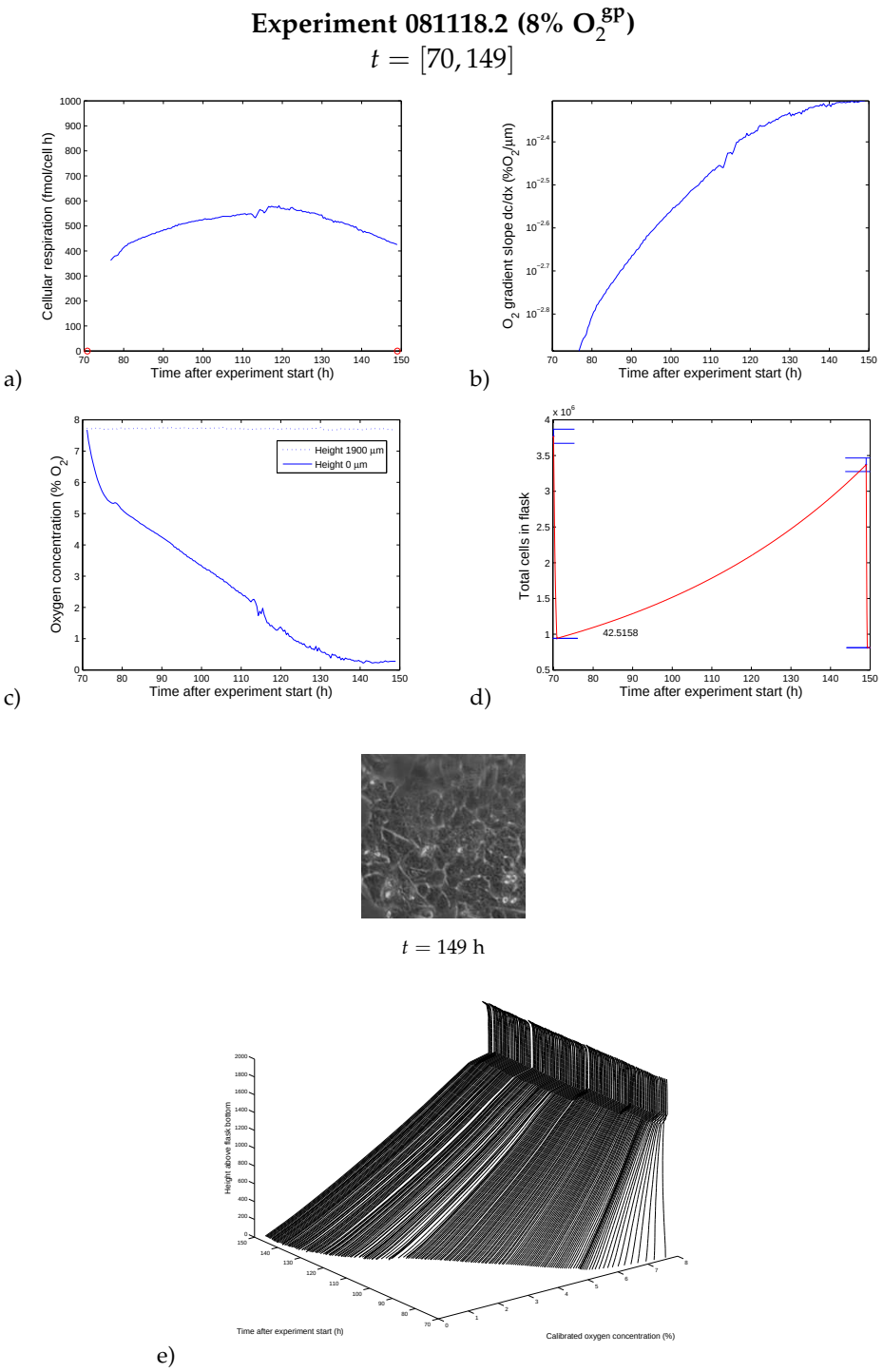

Figure 4.8: *Plots showing the data acquired during experiment 081118 (8% O_2^{gp}) in the time interval 70-149 h.*

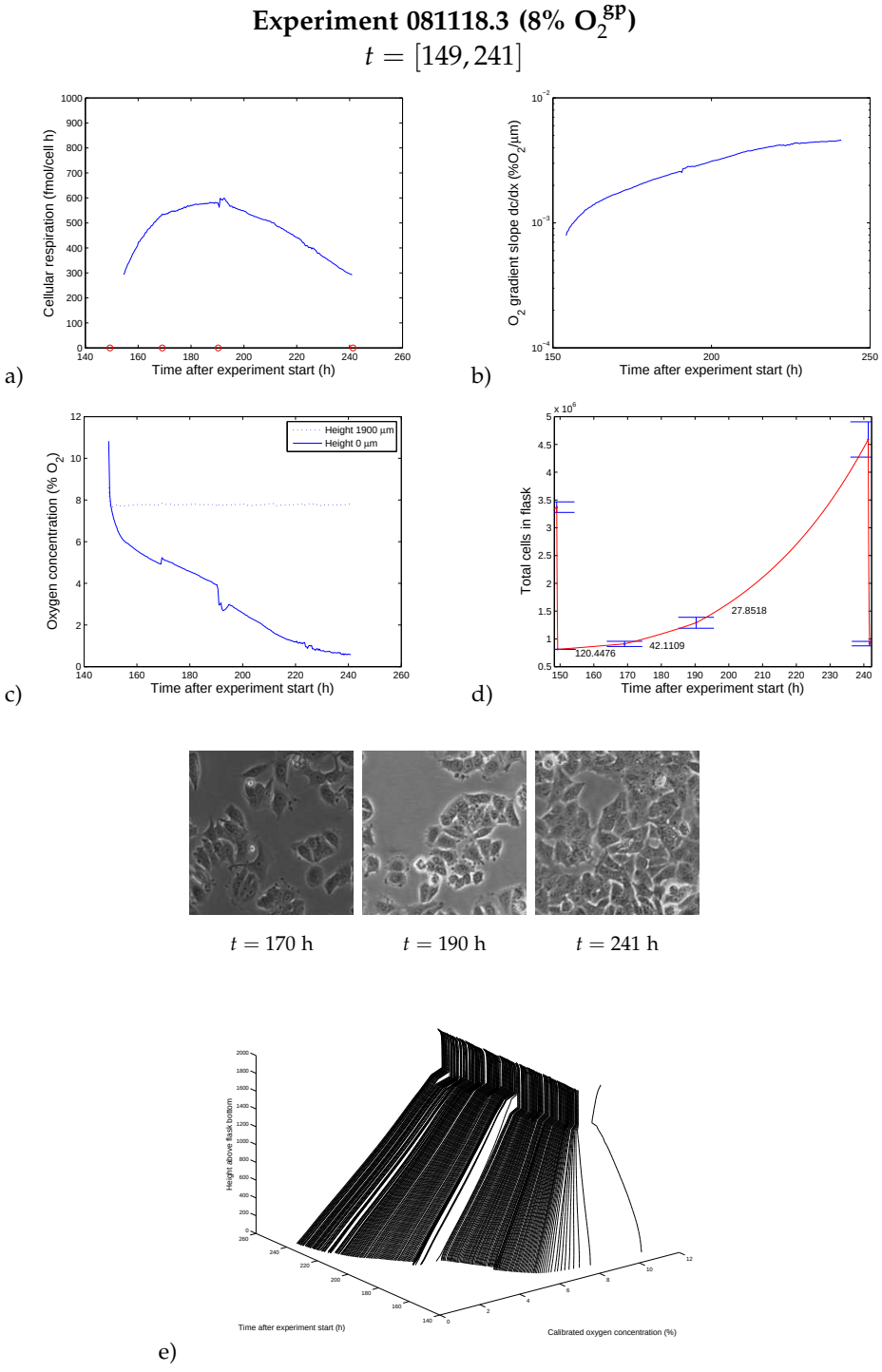

Figure 4.9: *Plots showing the data acquired during experiment 081118 (8% O_2^{gp}) in the time interval 149-241 h.*

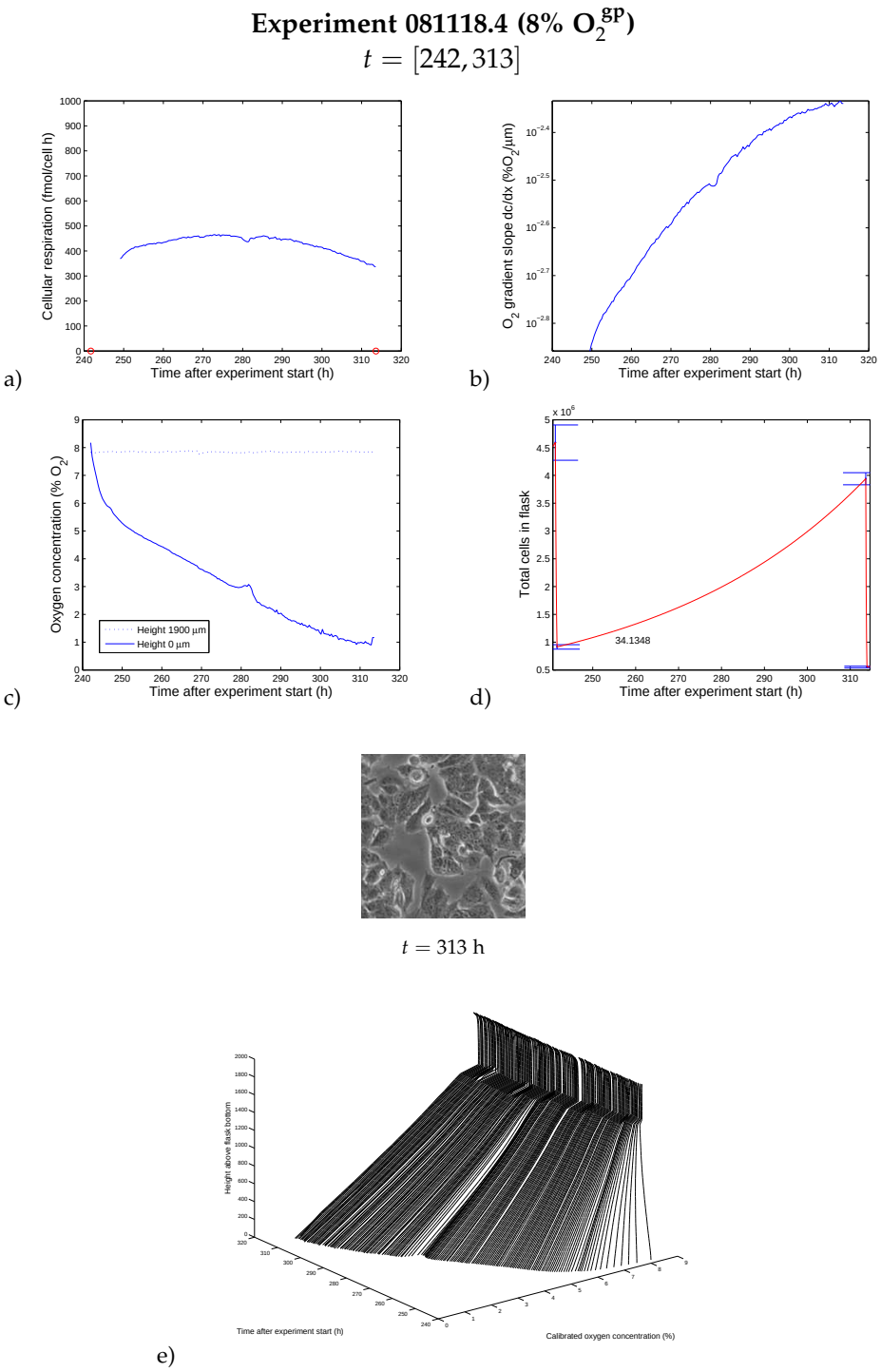

Figure 4.10: *Plots showing the data acquired during experiment 081118 (8% O_2^{gp}) in the time interval 242-313 h.*

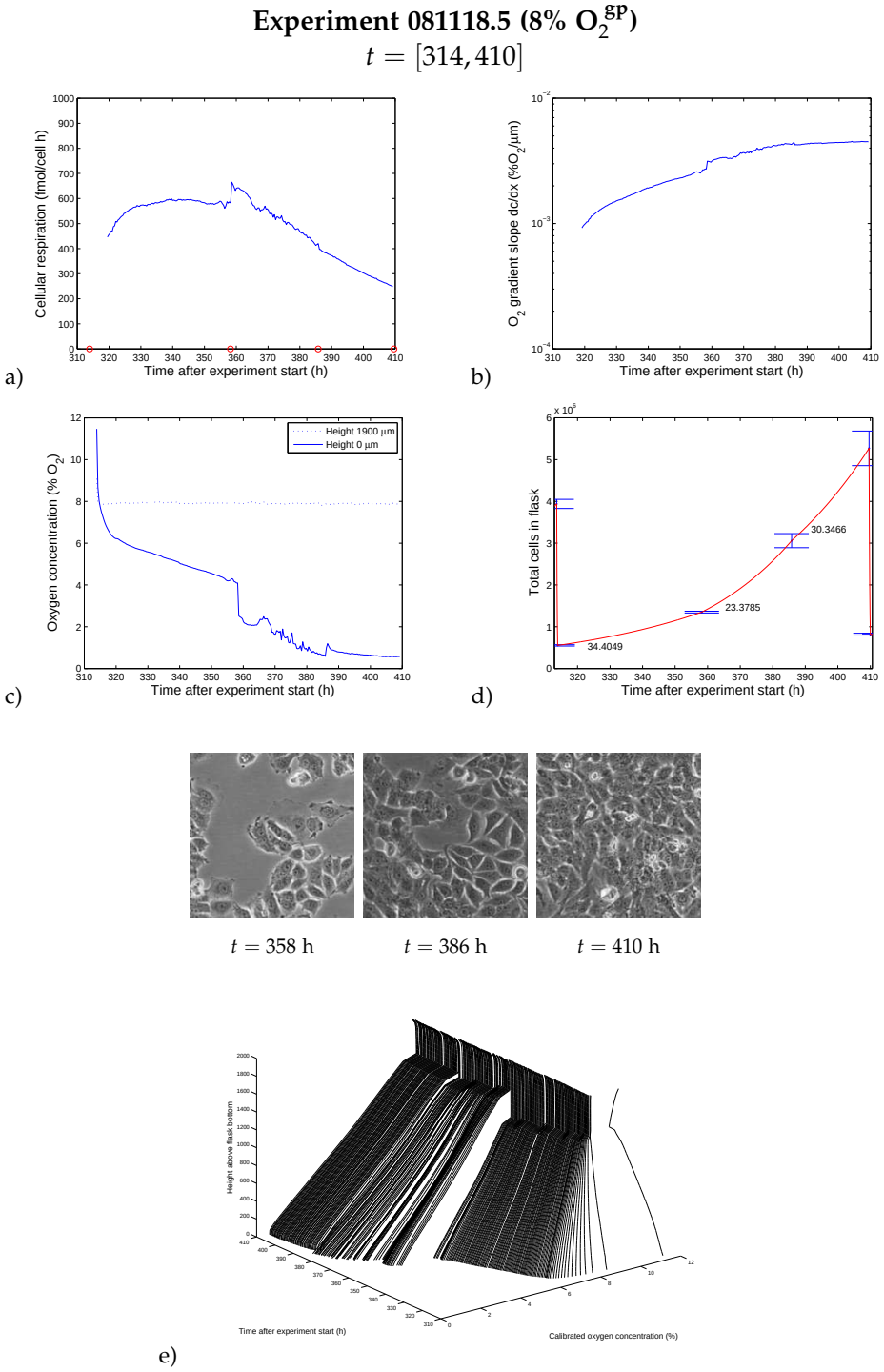

Figure 4.11: *Plots showing the data acquired during experiment 081118 (8% O_2^{gp}) in the time interval 314-410 h.*

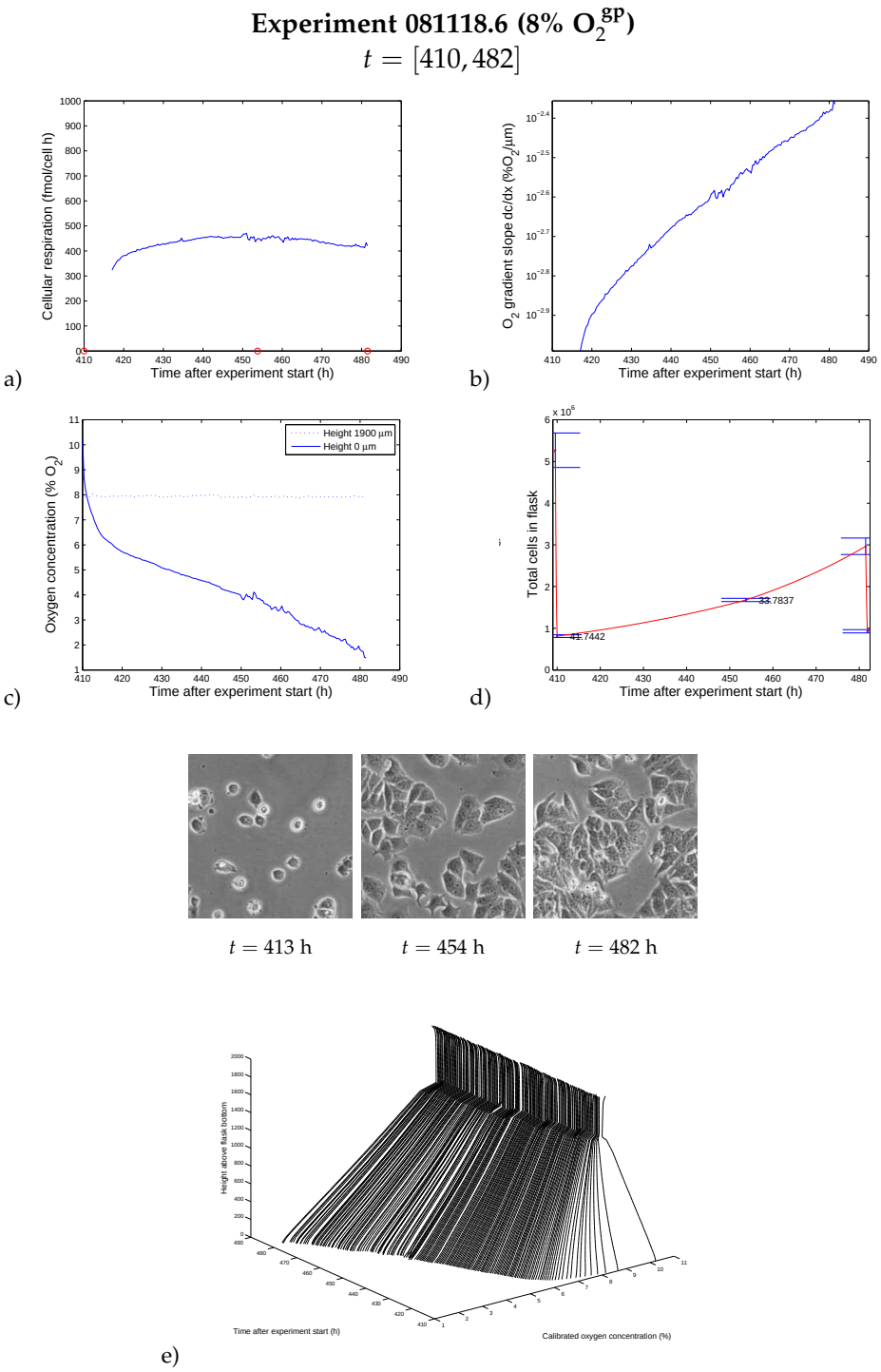

Figure 4.12: *Plots showing the data acquired during experiment 081118 (8% O_2^{gp}) in the time interval 410-482 h.*

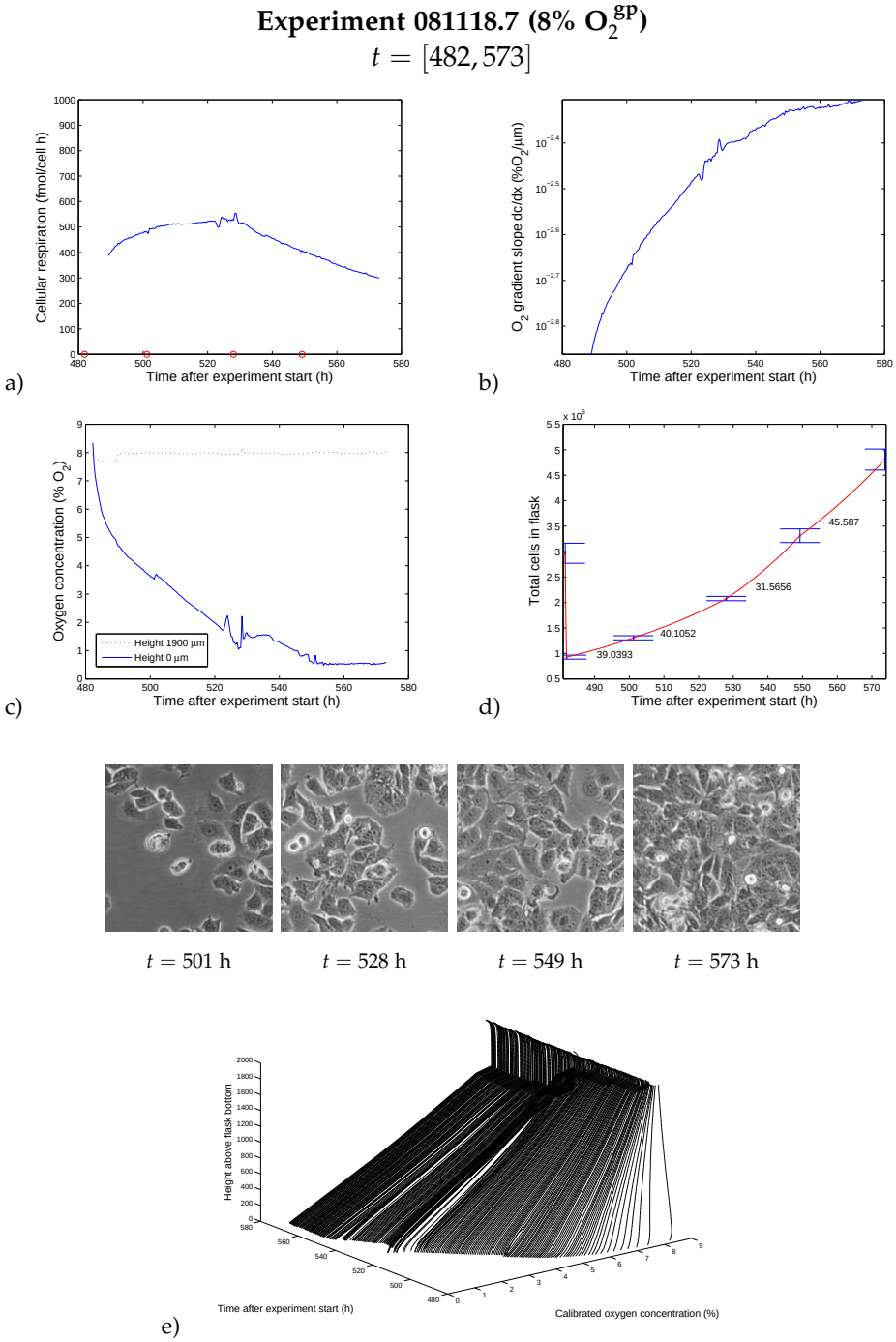

Figure 4.13: *Plots showing the data acquired during experiment 081118 (8% O_2^{gp}) in the time interval 482-573 h.*

Table 4.20: *Cellular respiration calculated when cell counting was performed in experiment 081118 (8% O_2^{gp}). The mean respiration is 423.9 fmol/h·cell.*

Time (h)	Cell resp (fmol/h·cell)
17.87	445.0 ± 35
70.01	348.9 ± 9.1
149.00	425.0 ± 12
169.10	534.5 ± 28
190.30	576.4 ± 44
241.30	289.5 ± 20
313.60	336.3 ± 9.3
358.20	581.9 ± 8.8
385.80	419.4 ± 23
409.60	246.5 ± 19
453.75	445.1 ± 11
481.50	420.7 ± 28
501.20	481.7 ± 15
528.00	526.9 ± 11
549.25	407.8 ± 17
573.75	296.3 ± 13

Fraction 081118.1, 0-70 h

This experiment fraction showed us, just as experiment 081103.1, the behavior of the cells experiencing the oxygen difference between the lab (21% O_2^{gp}) and the cabinet (8% O_2^{gp}). The measurements (i.e. $t = 0$) started within 30 minutes of the transfer.

A similar transient stabilizing phase as in experiment 081103 is seen in the plots in figure 4.7, and the time used by the system to achieve equilibrium is under 10 hours. Compared to 081103.1, this stabilizing period was considerably shorter. A contributing cause of this was probably the higher cell number in this experiment, and thus more cells that used oxygen and therefore achievieved equilibrium.

The effect of medium change is seen in the plot.

Fraction 081118.2, 70-149 h

At this experiment fraction start, the cells had been in 8% O_2^{gp} for close to 3 days. A transient stabilizing phase is observed in the plots, and with respect to oxygen concentration the time required for the system to achieve

Table 4.21: *The mean doubling times, $\bar{T}_2$, of experiment 081118 (8% O_2^{gp}). The doubling times are calculated based on the first and last cell count in every interval.*

Fraction	Mean doubling time (h)
081118.1	25.42
081118.2	42.52
081118.3	36.82
081118.4	34.13
081118.5	29.42
081118.6	38.25
081118.7	38.70
Mean	33.61 ± 2.3

equilibrium was about the same as before, about 8 hours.

Fraction 081118.3, 149-241 h

At 149 h, the cells had been in 8% O_2^{gp} for 6 days. Again, a stabilizing period is observed in the plots (figure 4.9), seemingly with a different time span with respect to respiration versus POC.

The effect of cell counting (i.e. flask movement) is seen at 169.10 hours. This seemed to have a greater influence on the POC than cellular respiration, the latter being nearly undisturbed (in contrast to what happened in fraction 081103.3). This indicates that, at this oxygen level (around 5% O_2 pericellular), the cellular respiration was not (yet) affected by pericellular oxygen.

However, the effect of medium change at 190.30 h had a significantly greater effect on both POC *and* cellular respiration.

It is worth noting that it seemed that the POC in early measurements in this fraction yielded a result $>$ 8% O_2. This indicates that atmospheric oxygen levels was present in the medium or trypsin used during recultivation at 149.00 h.

Fraction 081118.4, 242-313 h

At the start of this fraction, the cells had been in 8% O_2^{gp} for over 10 days. No cell maintenance tasks was performed during this fraction.

The POC stabilizing phase seen in figure 4.10 c) is somewhat concurrent with the former fractions, lasting less than 10 hours.

The artifact at 281 hours remains unexplained.

Fraction 081118.5, 314-410 h

At the start of fraction 081118.5 (figure 4.11) the cells had been in 8% O_2^{gp} for 13 days. By visual examination, the cells did not show any observable sign of hypoxia at this time.

The POC reached equilibrium within about 8 hours, and the cellular respiration seemed to reach a somewhat stable value of about 600 fmol/h·cellafter 15-20 hours.

The plots shows the effect of the medium change, and in the POC plot the cell count artifact at 385.80 h is seen.

Fraction 081118.6, 410-482 h

When this experiment fraction was initiated, the cells had been living in 8% O_2^{gp} for 17 days. The cell count at 453.75 did not seem to cause any major artifacts in the data.

This fraction stands out as it shows a nearly constant cellular respiration after the initial stabilizing phase. This is indicated in both respiration plots a) and b) in figure 4.12.

Equilibrium in POC was reached within 8 hours, and the cellular respiration seemed to reach a somewhat stable value after 15-20 hours.

Fraction 081118.7, 482-573 h

In this last fraction of experiment 081118, beginning 20 days after experiment initiation, a POC stabilizing phase lasting approx. 10 hours was seen.

The artifact due to cell count (501.20 h) is visible in the POC plot c) and in the respiration figure 4.13 a). At 528.00 h, medium change was performed, and this is clearly seen in all relevant plots.

The cell count at 549.35 h did, seemingly, have very little effect on the data.

4.5.4 Experiment 081118 (8% O_2^{gp}) summary

Experiment 081118 investigated the (respirational) effect of prolonged exposure to 8% O_2^{gp} on the MCF-7 human cancer cell line. In table 4.22 on page 120 some of the most interesting quantitative datas are listed.

Pericellular oxygen concentration

The POC did in this experiment (in nearly every fraction) reach oxygen levels resulting in clear effects with respect to POC slope change. From table 4.22 the mean POC level when this effect occured was 1.085 ± 0.10 % O_2.

In fraction 1 in this experiment, the respiration began decreasing when the POC reached 3.38% O_2.

In the interval between 80 and 112 hours in fraction 2, the POC showed a steady decrease. As the POC reached 2.1% O_2 at 112 hours, some scruffy trends are observed. The bottom reading then decreased faster than before, as the cellular respiration increased. A floor POC value of about 0.2 was reached.

The stabilizing phase in fraction 3 was shorter than in both fraction 1 and 2, and increased medium depth after medium change resulted in lower POC. At around 1.1% O_2 POC, the slope changed, possibly as a consequence of an effect of the low pericellular oxygen availability.

In fraction 5, again, the POC seemed to suffer from excess atmospheric oxygen in the initiation of this experiment fraction. This was probably due to medium or trypsin used in recultivation between fraction 4 and 5.

The POC showed the effect of the medium change performed in fraction 5, and due to a deeper medium and thus longer oxygen diffusion distance the POC decreased nearly instantly. Between the medium change and the cell counting in the same fraction the POC was unstable and scruffy, but after the cell count (and thus flask movement) a significantly more stable POC was measured. The slope changed around 1.25% O_2, and the POC never reached values below 0.47% O_2, but seems to stabilize.

The trend seen in all earlier fractions of experiment 081118, that the slope of the POC decreases as the oxygen concentration decreases, is *not* observed in fraction 6. Interestingly, a somewhat opposite effect is instead indicated, as the POC slope seemed to increase as the oxygen aviliability at flask bottom was below 4% O_2. This is consistent with an exponential increase in cell number, as it would yield a negative exponential POC curve.

Table 4.22: *Selected quantitative data from experiment 081118 (8% O_2^{gp} without irradiation), including stabilizing phase duration and maximum respiration level as well as POC values at respiration maximum and at POC slope change. In addition, if a (transient) equilibrium at a low POC value is seen (i.e. a horizontal POC plot), the floor POC level are listed.*

Fraction	Stab. phase duration (h)	Max. resp (fmol/h·cell)	(% O_2)	POC slope change (% O_2)	Floor POC level (% O_2)
081118.1	8.565	630.5	3.38	0.8584	
081118.2	9.31	580.9	1.234	0.9867	none
081118.3	7.1	599.2	2.591	1.306	0.2338 ± 0.0044
081118.4	11.2	465.6	3.251	1.509	none
081118.5	8.2	642.7	2.015	1.058	none
081118.6	8.6	470.8	3.634	never	none
081118.7	10	554.5	1.251	0.7898	0.4100 ± 0.0029
Mean	8.996 ± 0.50	563.5 ± 27	2.479 ± 0.38	1.085 ± 0.10	0.3219 ± 0.0026

Flask and cellular respiration

Every fraction in this experiment showed a respiration maximum and a following clear decrease. The mean respiration maximum was 563.5 $\pm$ 27 fmol/h·cell, occurring at a mean POC value of 2.479 $\pm$ 0.38% O_2 (table 4.22).

As in experiment 081103, the effects of cell maintenance is evident in the plots, and fresh medium seemed to boost cellular respiration. The medium changes was performed close to or after the respiration maximum, and compared to 081103 the related medium change effects were, in general, more subtle.

The most striking difference between the cellular respiration plots in this experiment and experiment 081103 is arguably the clear decreasing trend. This was never observed to any significance in experiment 081103 (except the last fraction 081103.4, when cell maintenance was absent).

The medium change in fraction 1 seemed to result in an increase in the cellular respiration. This happened probably as a consequence of a better proliferation environment for the cells due to fresh medium.

The fact that the respiration was somewhat constant after 18 hours (with a higher value than before the medium change, as seen in the plots from fraction 1, figure 4.7 on page 109), while the POC continued to decrease (with a greater slope due to higher respiration), may indicate that the medium freshness effect was the dominant factor[1].

The cellular respiration typically never reached a stable value before reaching its maximum value and then decreasing.

In fraction 3, the cellular respiration did not seem to be affected much by the cell counting at 169.10 hours, except for a noticeable (but small) decrease in curve slope. The medium change, however, induced a small temporarily increase in the cellular respiration.

In fraction 4, the cellular respiration was more stable compared to former fractions. However, a small deflection from the exponential increase in O_2 gradient slope (i.e. total flask respiration) is seen in plot b) as before, especially after 290 h when the cellular respiration began its decrease. This result may, however, have been affected by the over-simplification due to the exponential fit of the cell proliferation (plot d)). If the actual doubling time was shorter early in the fraction (and thus cell number higher in the early phase), the initial slope in plot a) is overestimated.

In fraction 5, the total flask respiration seems to approach a stable value, indicating a constant flask respiration. Since total respiration is a

[1] If a lower pericellular oxygen concentration would be the cause of the observed respiration increase, the cellular respiration would probably increase as the pericelluar oxygen concentration decreases.

simple linear function of cell number and cellular respiration, and plot d) indicates that $T_2 \neq 0$ (i.e. the cell number is *not* constant), the cellular respiration must decrease as the cell number increase. This is also suggested in plots a) and in figure B.8 on page 221 (a plot the flask respiration versus cell number of function 5), as the total oxygen consumption has a very slow increase when the cell number is estimated between 3.5 and 5 million cells.

Fraction 6 has seemingly a more stable cellular respiration compared to the former experiment fractions. In addition, figure B.9 on page 222 (a plot the flask respiration versus cell number of function 6) shows a close to linear relationship between total respiration and cell number, also indicating a constant trend in the cellular respiration.

The plots of fraction 7 indicates an initial exponential increase before the total flask respiration seems to approach a more stable value after 530 hours, indicating a decrease in cellular respiration in addition to the seen increase in cellular doubling time.

As seen in figure 4.13 a), the cellular respiration decreases after the medium change performed at 528.00 h. This is supported by the total flaks respiration plot b).

Cellular proliferation

In 081118, compared to 081103, the cellular proliferation seems more stable. Again is the estimated doubling time lowest in the middle of a fraction, consistent with the suggestion of a lag phase after recultivation and a plateau phase, in addition to a reduced proliferation as POC and cellular respiration decreases.

The mean overall doubling time is 33.89 ± 1.9 h.

The mean doubling time in fraction 2 is calculated to be 42.5 hours, significantly higher than in fraction 1. However, as seen in table 4.19, there was no cell counting performed at 70 h after the recultivation. Thus, the cell number at 70 h was calculated from the ratio used in the seeding. This indicates that the estimated cell number after the recultivation is overestimated, and thus that the plating efficiency is, not surprisingly, lower than 100 %.

The consequence of this error source is that the *absolute* values of cellular respiration early in fraction 2 should be disregarded, but the *relative* measurements and thus the slope of the respiration as the experiment progresses is both valid (to a certain degree) and interesting.

Between the counting at 149.30 h and 169.10 h in fraction 3, the doubling time is calculated to 120.4 h, much higher than any other calculation so far. It is however important to note that the cell number estimated at

149.30 h is based on only one picture (while the others typically are based on three), and it may seem that this is an overestimate of the actual cell number in the flask.

In fraction 4, cell counts was performed only at the start and the end of the fraction. This yields a single estimate for the mean doubling time of this fraction, 34.1 hours.

It may seem from figure 4.10 a) and b) that after about 290 hours the cellular activity is reduced, and thus probably that the actual T_2 is reduced. This means also that T_2 early in the fraction is overestimated.

In fraction 5, the cellular respiration decreases after 370 hours (figure 4.11 a)), and seems to be reflected in the doubling time, as its estimate increases from 23.4 h to 30.3 hours.

As indicated in the plots, a decreasing POC (as a result of increased cell number at a given medium depth) leads to decreasing cellular respiration and thus a longer doubling time. It is possible to interpret this as a cellular reaction to the low oxygen aviliability. In this fraction, the effect is seen at POC $\leq$ 2% O_2.

In fraction 6, it seems that the oxygen aviliability never reaches values to trigger any of the previously seen effects. No increase in mean doubling time is measured (rather the opposite), and no major decrease in cellular respiration supports this.

Table 4.23: *The events of experiment 081212 (6% O_2^{gp})*

Time (h)	Event
0	Experiment start, cell count
73.06	Cell count
98.26	Cell count, recultivation 1:4
98.63	Cell count
118.70	Cell count
170.20	Medium change, cell count
239.30	Cell count, experiment end

4.5.5 Data from experiment 081212 (6% O_2^{gp})

The main goal of experiment 081212 was to determine the cellular respiration in 6% O_2^{gp}.

It lasted for 240 hours (10 days) and consisted of two experiment fractions. The experiment progress and individual events is listed in table 4.23.

Here comes the experimental data and some observations.

The calculated discrete respirations are listed in table 4.24.

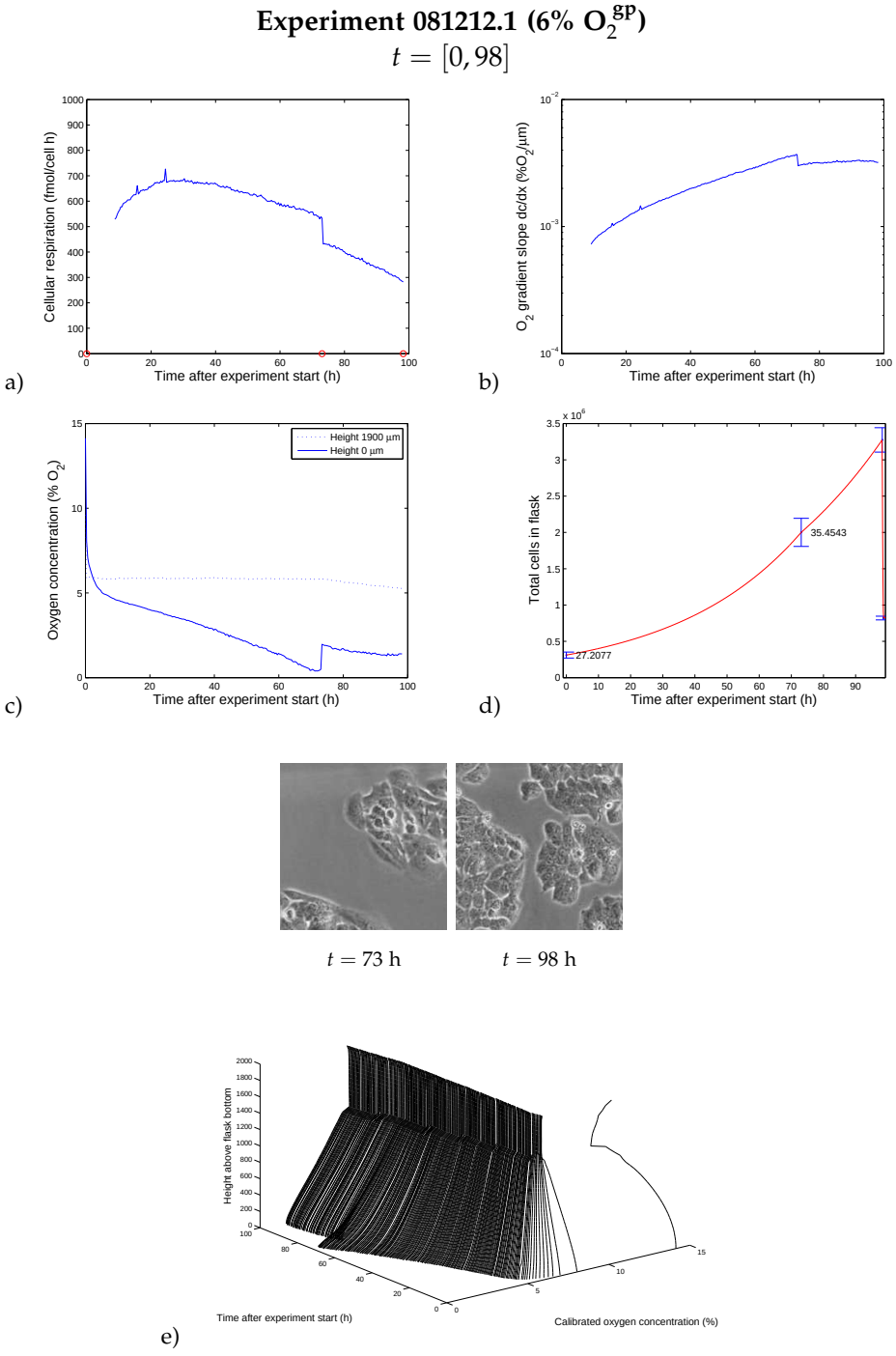

Figure 4.14: *Plots showing the data acquired during experiment 081212 (6% O_2^{gp}) in the time interval 0-98 h.*

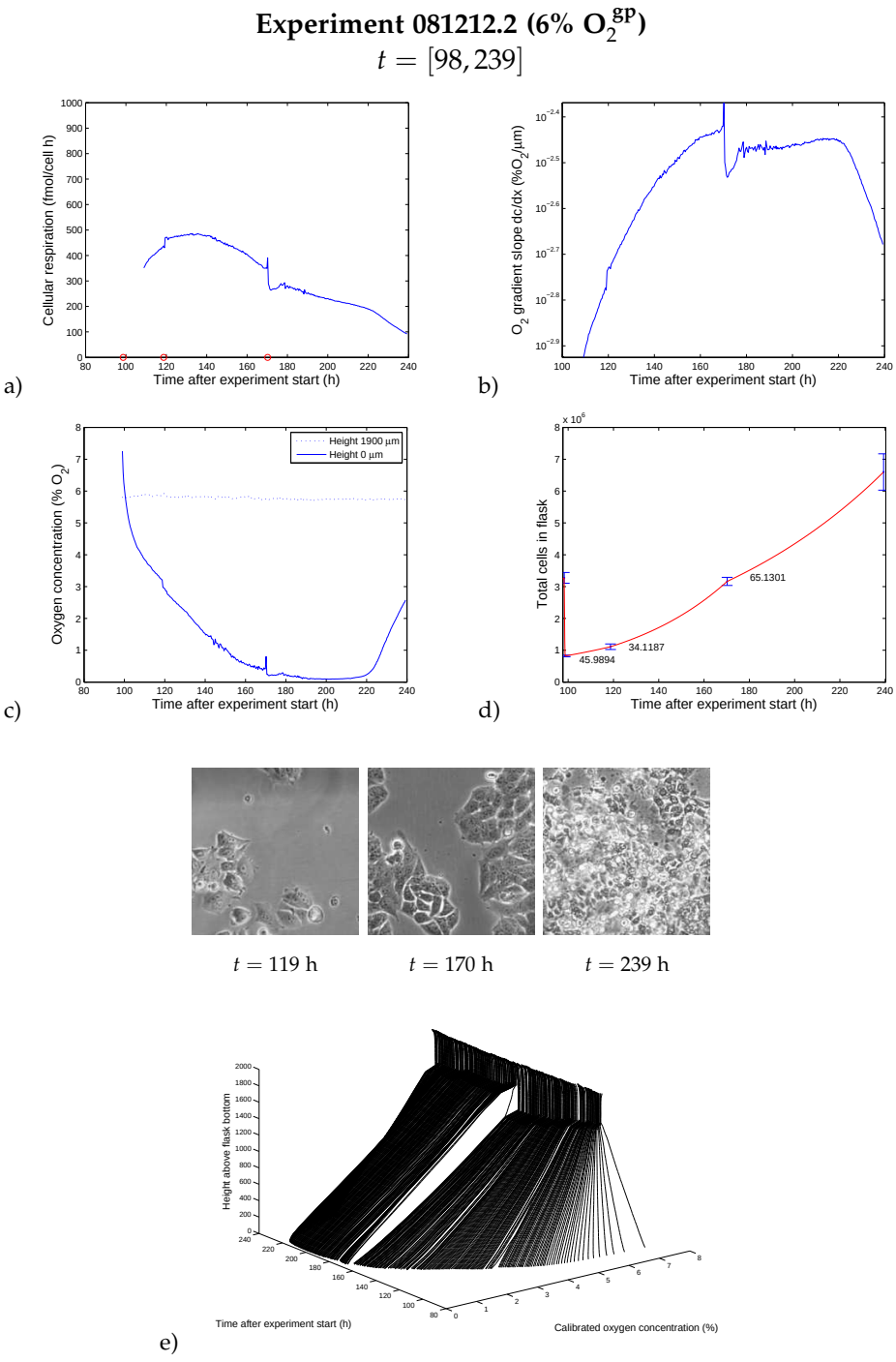

Figure 4.15: *Plots showing the data acquired during experiment 081212 (6% O_2^{gp}) in the time interval 98-239 h.*

Table 4.24: *Cellular respiration calculated when cell counting was performed in experiment 081212 (6% O_2^{gp}).*

Time (h)	Cell resp (fmol/h·cell)
73.06	532.9 ± 52
98.26	282.6 ± 15
118.70	433.6 ± 34
170.20	347.0 ± 14
239.30	91.83 ± 8.0

Table 4.25: *The mean doubling times, $\bar{T}_2$, of experiment 081212 (6% O_2^{gp}). The doubling times are calculated based on the first and last cell count in every interval.*

Fraction	Mean doubling time (h)
081212.1	28.93
081212.2	46.78
Mean	37.86 ± 8.9

Fraction 081212.1, 0-98 h

At initiation of experiment 081212, cells were brought from atmospheric conditions to 6% O_2^{gp}.

The initial stabilizing phase (lasting 8 hours) is clearly seen in figure 4.14 c). The duration of this phase is consistent with observations from the former experiment with higher gas phase oxygen levels.

Artifacts from the cell count (73 hours) is clearly seen in the plots. The spike at 24 h (726.6 fmol/h·cell) is possibly an artifact (see also plot b)) and is therefore ignored.

Fraction 081212.2, 98-239 h

At the start of 081212.2, the cells had been in 6% O_2^{gp} for 4 days.

As before, a stabilizing period is observed, lasting for 11 hours. The cell count performed at 118.7 hours visible in the plots, as well as the medium change at 170.2 hours.

4.5.6 Experiment 081212 (6% O_2^{gp}) summary

Experiment 081212 investigates the effect of prolonged exposure to 6% O_2^{gp} on the MCF-7 human cancer cell line. A selection of interesting quantitative data from this experiment are listed in table 4.26 on page 129.

After the cell flask was brought into the cabinet from atmospheric conditions, the system initially uses about 8 hours to reach equilibrium. This is comparable to experiment 081118.

The mean stabilizing phase duration for both fractions in experiment 081212 is 9.503 $\pm$ 1.5 h.

Pericellular oxygen concentration

During this experiment the POC is under 5% O_2 most of the time (except immediately after recultivation).

After the initial stabilizing phase, a clean decrease is seen in both fractions. However, again there is a clear effect of low oxygen availability to the POC slope, with a mean threshold value of 1.5175 $\pm$ 0.15% O_2 (table 4.26).

The cell count at 73 hours in fraction 1 stirs the medium and the POC increases dramatically (to 1.97% O_2, a relative increase of over 400%). After the disturbance the POC decrease is less pronounced. It seems that the pericellular oxygen concentration approaches a constant value of 1.4% O_2 before experiment fraction end.

In fraction 2, the medium change at 170.2 h (when POC is 0.4% O_2) does not seem to affect the behavior of the POC, reaching its minimum at 201 h (0.092% O_2).

Near experiment termination, an increase is seen in the POC, indicating pronounced decreased flask respiration.

Flask and cellular respiration

In this experiment, no respiration boost is observed when a medium change is performed. On the contrary a decrease in cellular respiration is seen when fresh medium is administered.

When the medium is stirred as a consequence of a proper cell count the respiration increases some.

In fraction 1, the maximum cellular respiration value is reached at 30 h (688.7 fmol/h·cell), when the POC is 3.5% O_2. The respiration is clearly lower in fraction 2, and the maximum is reached at 133 h (485.8 fmol/h·cell) when the POC is 2.021 % O_2.

The medium change in fraction 2 results in a pronounced drop in the total flask respiration plot. Together with the cellular respiration plot (ex-

Table 4.26: *Selected quantitative data from experiment 081212 (6% O_2^{gp} without irradiation), including stabilizing phase duration and maximum respiration level as well as POC values at respiration maximum and at POC slope change. In addition, if a (transient) equilibrium at a low POC value is seen (i.e. a horizontal POC plot), the floor POC level are listed.*

Fraction	Stab. phase duration (h)	Max. resp (fmol/h·cell)	(% O_2)	POC slope change (% O_2)	Floor POC level (% O_2)
081212.1	8.036	688.7	3.459	1.67	none
081212.2	10.97	485.8	2.021	1.365	0.1055 ± 0.0012
Mean	9.503 ± 1.5	587.25 ± 101	2.74 ± 0.72	1.5175 ± 0.15	0.1055 ± 0.0012

cluding the possibility of this being just an artifact) this indicates an abrupt drop in total (and thus cellular) respiration.

Near experiment end, flask and cellular respiration decreases dramatically, consistent with the significant increase in the POC. The cellular respiration reaches 91.87 fmol/h·cellbefore experiment termination.

Cellular proliferation

The mean cellular respiration varies between 27 to 65 h, depending on interval. The doubling time is at its largest at the end of each fraction. The latter fraction indicates, consistent with earlier observations, that it is the middle section of a fraction that has the most rapidly divided cells (i.e. the lowest mean doubling time).

In addition, the doubling time clearly increases as the last experiment fraction progresses. This mirrors the trend seen in the other plots—the respiration decreases clearly as the experiment progresses beyond the respiration maximum.

4.6 Data from the hypoxia experiments with irradiation

The main goal of experiments 090608 and 090622 was to study the respiration of the cells experiencing hypoxia (8% O_2^{gp}) *and* irradiation (by 1.67 μCi/ml and 0.735 μCi/ml RPMI, respectively).

Unfortunately, due to time constraints, these experiments yields very little information about cell survival. However, when it comes to respiration and POC levels, interesting features are to be seen.

Only oxygen concentration was used, 8% O_2^{gp}, determined from experiment 081118 as an oxygen aviliability yielding hypoxia but still viable cells. The experiment initiation date was as before used to identify each experiment, and was labeled 090608 and 090622, respectively.

In this chapter some of the raw data obtained from the hypoxia experiments without irradiation is presented in the form of plots, along with some processed plots from Matlab used for analyzation. In addition some general observations are addressed, along with some interesting features of the plots.

As with the experiments without irradiation, a single experiment contained several cell recultivations, the experiments was divided into experiment fractions, representing the time between two recultivations. The experiment fractions was distinguished by a suffix.

The main discussion is still saved for chapter 5.

Table 4.27: *The events of experiment 090608 (8% O_2^{gp} with 1.67 μCi/ml RPMI)*

Time (h)	Event
0	Experiment start, cell count
22.5	Cell count
45.17	Cell count, recultivation 1:7
45.52	Cell count
71	Cell count
92.09	Medium change, cell count
114	Cell count
164	Medium change, cell count
213.6	Cell count, recultivation 1:4
214	Cell count
239.75	Cell count
251.4	Medium change, cell count
331.5	Cell count, experiment end

4.6.1 Data from experiment 090608 (8% O_2^{gp} with 1.67 μCi/ml RPMI)

The main goal of experiment 090608 was to determine the cellular behavior and respiration in 8% O_2^{gp} with 1.67 μCi/ml RPMI, and potentially observe any combination effects of hypoxia and irradiation. This experiment lasted for 332 hours and consisted of three experiment fractions.

It is interesting to remember the connection to experiment 081118, being conducted using the same gas phase oxygen concentration, however without radioactive medium. Thus, comparing the two experiments may yield information of changed cellular behavior due to the low dose-rate irradiation.

The calculated discrete respirations are listed in table 4.28, and the experiment progress and individual events is listed in table 4.27.

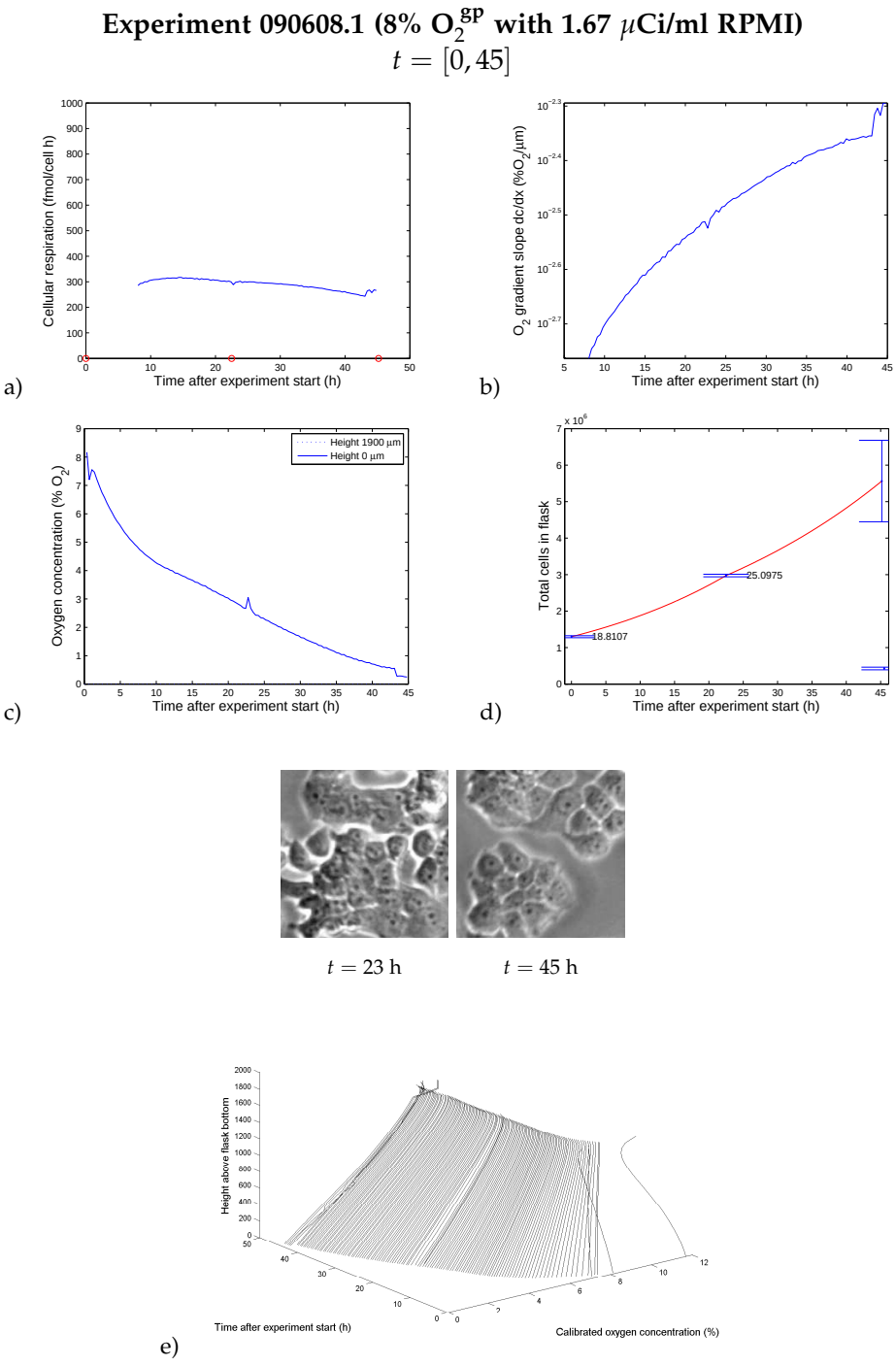

Figure 4.16: *Plots showing the data acquired during experiment 090608 (8% O_2^{gp} with 1.67 µCi/ml RPMI) in the time interval 0-45 h.*

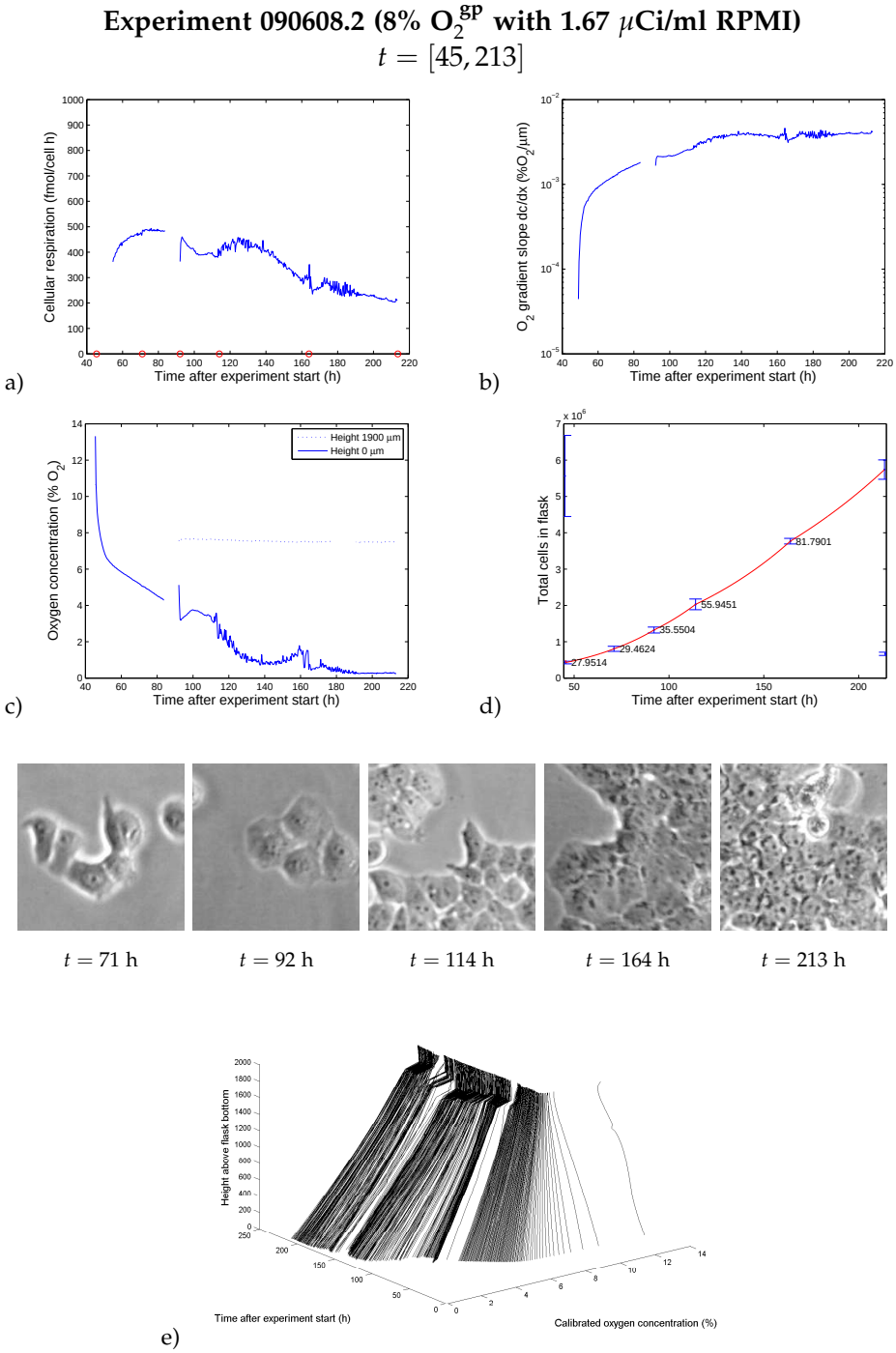

Figure 4.17: *Plots showing the data acquired during experiment 090608 (8% O_2^{gp} with 1.67 µCi/ml RPMI) in the time interval 45-213 h.*

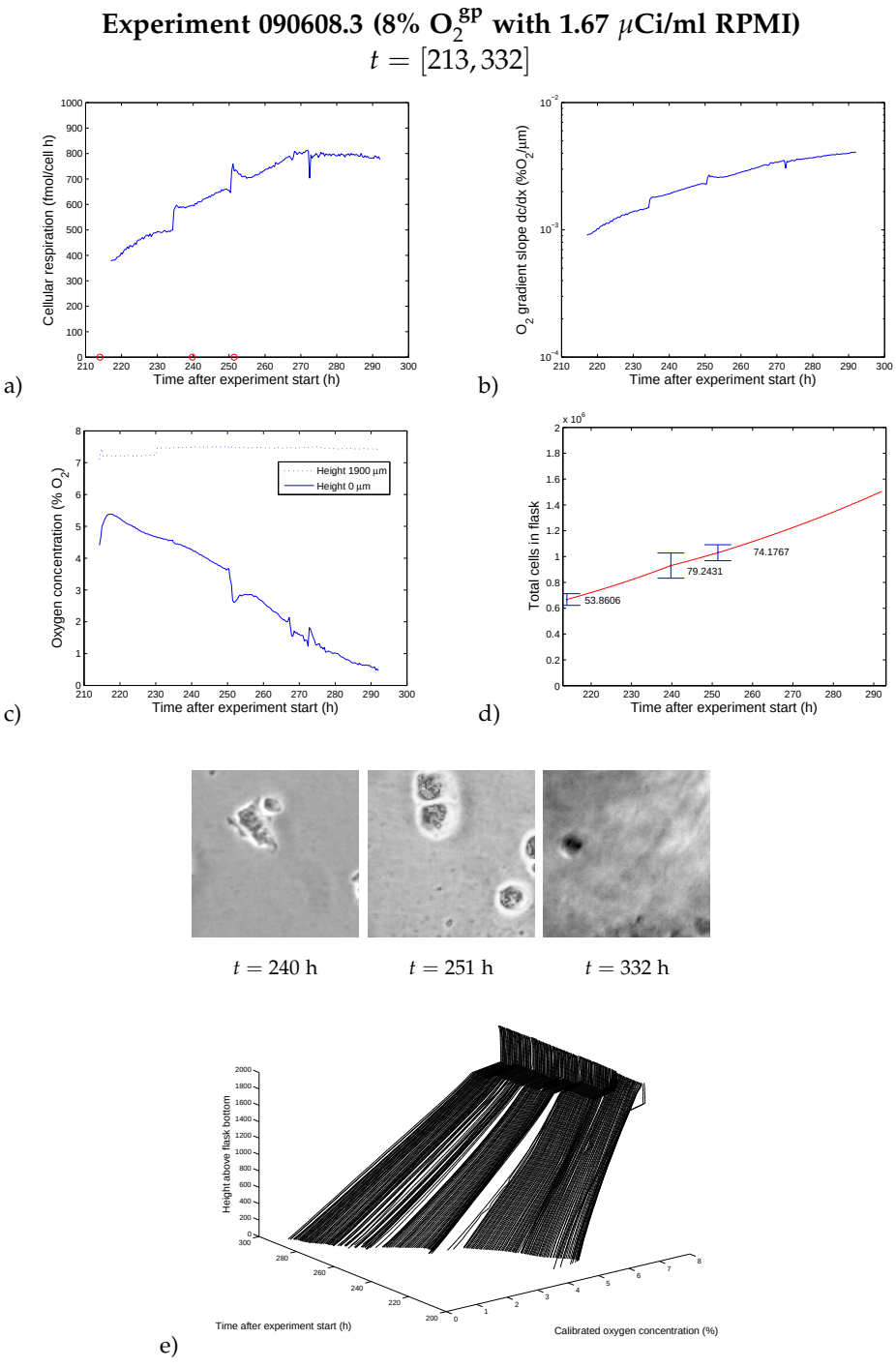

Figure 4.18: *Plots showing the data acquired during experiment 090608 (8% O_2^{gp} with 1.67 µCi/ml RPMI) in the time interval 213-332 h.*

Table 4.28: *Cellular respiration calculated when cell counting was performed in experiment 090608 (8% O_2^{gp} with 1.67 µCi/ml RPMI). The doubling times are calculated based on the first and last cell count in every interval.*

Time (h)	Cell resp (fmol/h·cell)
22.5	298.73 ± 3.6
45.17	263.81 ± 53
71	485.97 ± 42
92.09	469.70 ± 29
114	385.46 ± 28
164	297.01 ± 6.1
213.6	208.08 ± 9.7
239.75	593.86 ± 62
251.4	731.7 ± 44

Table 4.29: *The mean doubling times, $\bar{T}_2$, of experiment 090608 (8% O_2^{gp} with 1.67 µCi/ml RPMI).*

Fraction	Mean doubling time (h)
090608.1	21.52
090608.2	44.89
090608.3	68.92
Mean	45.11 ± 13

Fraction 090608.1, 0-45 h

The measurements started within 30 mins after the transfer and exposure to hot RPMI.

From the plots in figure 4.16, a stabilizing phase of about 9 h is seen before the system reaches equilibrium. At time 22 h, the artifact due to cell counting (and thus flask movement) is seen.

Fraction 090608.2, 45-213 h

When fraction 090608.2 was initiated, the cells had been experiencing a medium activity of 1.67 μCi/ml in 8% O_2^{gp} for about two days. In section 4.3.1 it is argued that the system needs about 100 hours to accumulate a steady dose-rate to the nucleus, and thus this has not yet occurred at 45 h.

Again, a stabilizing phase of about 9 hours is seen. In general, the data are noticeably more scruffy in this fraction than earlier experiment fractions.

A chunk of data before the medium change at 92 hours was unfortunately lost due to a computer error[2], but the effect of medium change is clearly seen at both 92 h and 164 h.

Fraction 090608.3, 213-332 h

Before this fraction, the cells had been in 8% O_2^{gp} with 1.67 μCi/ml RPMI for nearly 9 days.

A stabilizing phase of about 11 hours is seen. In addition, the artifact from the cell count and the medium change are clearly visible.

[2]Windows Update rebooted the computer in the middle of the night...

4.6.2 Experiment 090608 (8% O_2^{gp} with 1.67 μCi/ml RPMI) summary

Experiment 090608 investigates the (respirational) effect of exposure to 8% O_2^{gp} in 1.67 μCi/ml RPMI on the MCF-7 human cancer cell line. The most interesting quantitive features are listed in table 4.30 on page 138.

Pericellular oxygen concentration

The mean stabilizing phase in this experiment is 9.57 ± 0.82 h.

In fractions 1 and 2, a POC plateau phase is seen, with a mean oxygen concentration of 0.27% O_2. In the third (and last) fraction, no plateau phase is seen.

In fraction 2 the POC is very scruffy after reaching below about 4% O_2. Two mimima occurs in this fraction, separated by a medium change. A seemingly stable POC plateau phase occurs at 0.27% O_2.

Flask and cellular respiration

In none of the fractions does the total flask respiration become purely exponential (i.e. a straight line in the semilogarithmic plot). This is probably a combination effect of a non-exponential cell growth in addition to decreasing trends in the cellular respiration plots.

The cellular respiration in fraction 1 is, in contrast to the two other fractions, somewhat stable around 250–300 fmol/h·cell. However, a decreasing trend is visible in the plot as the fraction progresses.

In fraction 2, however, a significant maximum and a following decrease is seen in the plots. Also, consistent with the scruffy POC measurements, the total flask respiration plot in fraction 2 becomes, apperantly, very noisy.

In fraction 3, the cellular respiration reaches values far greater than ever before seen in the experiments. When the POC is 1.43% O_2, the mean cellular respiration is 812.1 fmol/h·cell, more than twice the value measured in the first fraction.

In this fraction, a somewhat steady increase (when the artifacts are left out) in cellular respiration is seen until about 275 h. Unfortunately, the cell flask used for respiration measurements got a severe infection (as can be seen as the "blur" in the last cell picture at $t = 332$ h). This cannot be ruled out of having a contributing effect to the decrease in cellular respiration slope seen after 275 h.

Cellular proliferation

The mean overall doubling time in this experiment is 48.19 ± 7.6 h.

Table 4.30: *Selected quantitative data from experiment 090608 (8% O_2^{gp} with 1.67 µCi/ml RPMI), including stabilizing phase duration and maximum respiration level as well as POC values at respiration maximum and at POC slope change. In addition, if a (transient) equilibrium at a low POC value is seen (i.e. a horizontal POC plot), the floor POC level are listed.*

Fraction	Stab. phase duration (h)	Max. resp (fmol/h·cell)	(% O_2)	POC slope change (% O_2)	Floor POC level (% O_2)
090608.1	8.75	317.1	3.69	0.884	0.2682 ± 0.0069
090608.2	8.76	493.8	4.81	1.16 (bf. m.c.) 0.4655 (af. m.c.)	0.2706 ± 0.002
090608.3	11.2	812.1	1.43	0.7183	none
Mean	9.57 ± 0.82	541 ± 145	3.31 ± 0.99	0.812 ± 0.14	0.2694 ± 0.0036

Due to the limited number of cell counts performed, no information of lag phases is seen in this plots, but in all fractions, the mean doubling time increase as the fractions progress. This may correspond to an approach toward plateau phases.

In fraction 2 and 3, doubling times over 70 hours are seen, considerably higher than any measurement in the corresponding non-radioactive experiment (081118, having 8% O_2^{gp} without irradiation).

Table 4.31: *The events of experiment 090622 (8% O_2^{gp} with 0.735 μCi/ml RPMI)*

Time (h)	Event
0	Experiment start, cell count
23.67	Cell count
44.47	Cell count, recultivation 1:4
44.82	Cell count
68.67	Cell count
91.74	Medium change, cell count
161.17	Cell count, experiment end

4.6.3 Data from experiment 090622 (8% O_2^{gp} with 0.735 μCi/ml RPMI)

As the calculated dose-rate to the nucleus are considerably higher than expected, a second experiment was performed with lower medium activity.

The main goal of experiment 090622 was to determine the cellular respiration during the initial phases of 8% O_2^{gp} with 0.735 μCi/ml RPMI. It lasted for 162 hours (almost 7 days) and consisted of two experiment fractions. The experiment progress and individual events is listed in table 4.31.

This experiment is *not* an extension of experiment 090608, meaning that the cells used in this experiment did not have a history of experiencing 8% O_2^{gp} and/or irradiation.

The calculated discrete respirations are listed in table 4.32.

Experiment 090622.1 (8% O_2^{gp} with 0.735 μCi/ml RPMI)

$t = [0, 44]$

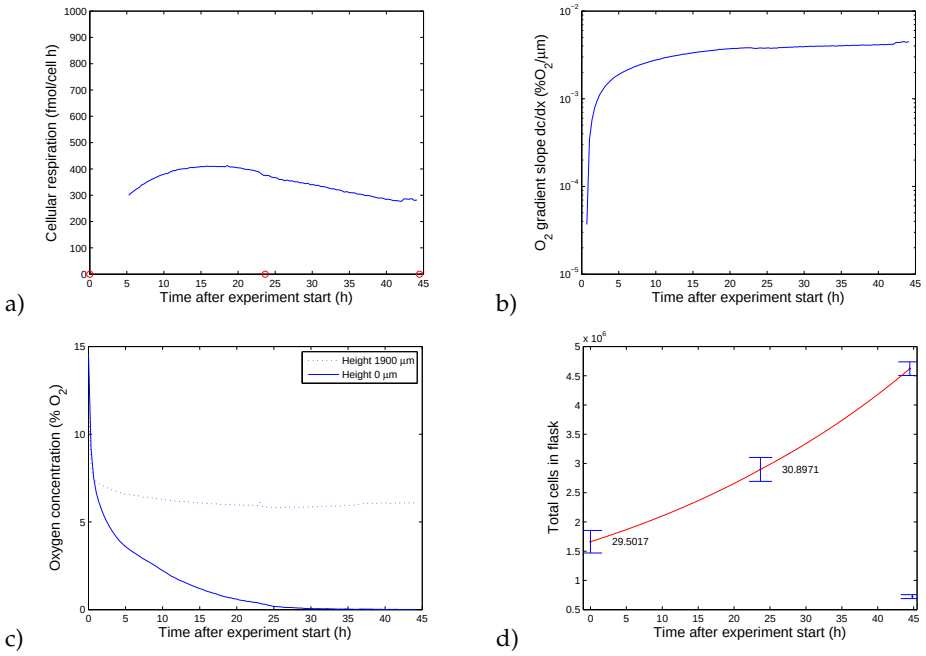

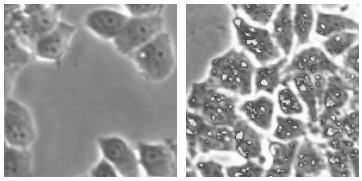

$t = 23$ h $\qquad$ $t = 44$ h

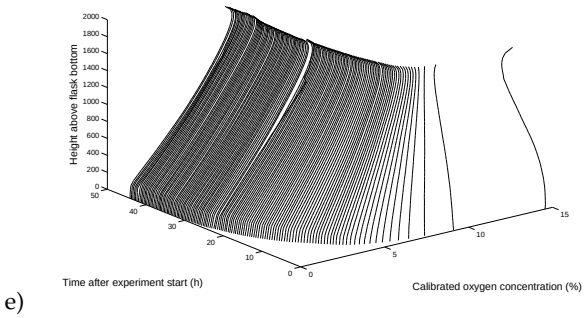

Figure 4.19: *Plots showing the data acquired during experiment 090622 (8% O_2^{gp} with 0.735 µCi/ml RPMI) in the time interval 0-44 h.*

Experiment 090622.2 (8% O_2^{gp} with 0.735 μCi/ml RPMI)
$t = [44, 161]$

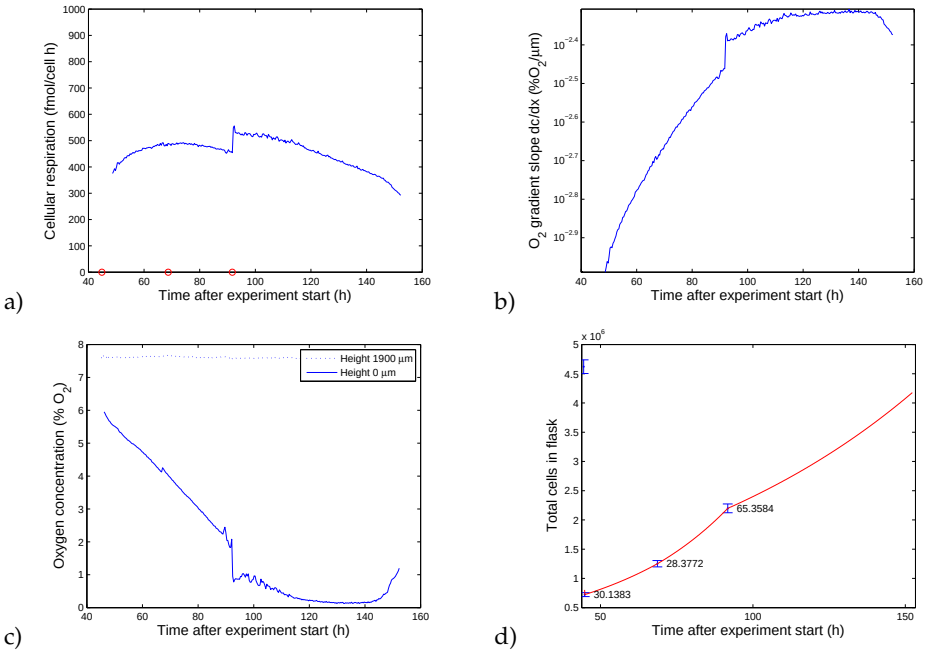

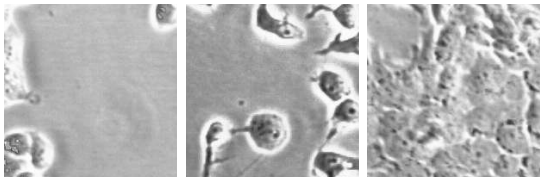

$t = 69$ h $t = 92$ h $t = 161$ h

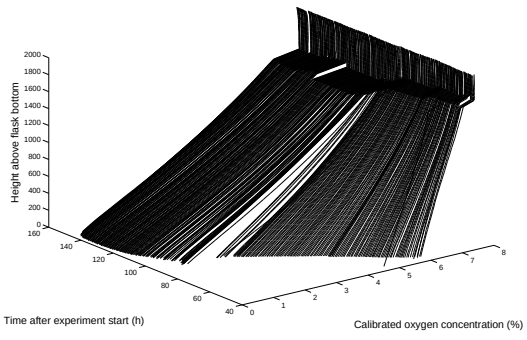

Figure 4.20: *Plots showing the data acquired during experiment 090622 (8% O_2^{gp} with 0.735 µCi/ml RPMI) in the time interval 44-161 h.*

Table 4.32: *Cellular respiration calculated when cell counting was performed in experiment 090622 (8% O_2^{gp} with 0.735 µCi/ml RPMI).*

Time (h)	Cell resp (fmol/h·cell)
23.67	376.84 ± 27
44.47	279.85 ± 7.1
68.67	468.3 ± 20
91.74	454.2 ± 16

Table 4.33: *The mean doubling times, $\bar{T}_2$, of experiment 090622 (8% O_2^{gp} with 0.735 µCi/ml RPMI). The doubling times are calculated based on the first and last cell count in every interval.*

Fraction	Mean doubling time (h)
090622.1	30.14
090622.2	43.63
Mean	36.89 ± 6.8

Fraction 090622.1, 0-44 h

This experiment fraction (figure 4.19) shows us the behavior of irradiated cells experiencing a decrease in oxygen aviliability, coming from 21% O_2^{gp} in the lab to a 8% O_2^{gp} in the cabinet. The cells are recultivated with a radioactive medium (with specific activity 0.735 μCi/ml).

The measurements started within 30 mins after the transfer and exposure to hot RPMI.

From the plots in figure 4.19, a stabilizing phase of about 4 h is seen before the system reaches equilibrium.

A cell count was performed at 24 h, but are not clearly visible in the plots.

Fraction 090622.2, 44-161 h

Fraction 090622.2 was initiated when the cells had been experiencing a medium activity of 0.735 μCi/ml in 8% O_2^{gp} for about two days. As with experiment 090608.2, a stable dose-rate to the nucleus has not yet been reached.

A stabilizing phase of about 5 hours is seen.

4.6.4 Experiment 090622 (8% O_2^{gp} with 0.735 μCi/ml RPMI) summary

Experiment 090622 investigates the (respirational) effect of exposure to 8% O_2^{gp} in 0.735 μCi/ml RPMI on the MCF-7 human cancer cell line. The most interesting quantitive features are listed in table 4.34 on page 146.

Pericellular oxygen concentration

The stabilizing phases in both experiment fractions are considerably lower than in experiment 090608.

After a medium change at 92 h, the POC decreases rapidly from about 2% O_2 to about 1% O_2, corresponding to the increased respiration.

Fraction 1 has a POC that reaches a plateau phase lower than in any other experiment (0.027 $\pm$ 0.0030% O_2), while fraction 2 has a POC floor level of 0.16% O_2.

Flask and cellular respiration

Again, the total flask respiration in either fraction never becomes purely exponential. This is probably due to a non-exponential cell growth, as wel as the decreasing trends seen in the cellular respiration plots.

The cellular respiration plots both have a respirational maximum and a decrease toward fraction end. The respiration in fraction 2 is higher than in fraction 1.

In addition, in fraction 2, the respiration increases rapidly after the medium change at 92 h.

Cellular proliferation

In fraction 1, the mean doubling time is somewhat similar in both the early and the late fraction half. This does probably, however, mask a more complex proliferation curve, not seen in these plots due to limited cell counting.

In fraction 2, the doubling time increases toward the latter half of the fraction.

The mean overall doubling time is 48.19 $\pm$ 7.6 h.

4.7 Confluence experiment

In a small additional experiment, the respirational effect of confluence is studied.

Table 4.34: *Selected quantitative data from experiment 090622 (8% O_2^{gp} with 0.735 µCi/ml RPMI), including stabilizing phase duration and maximum respiration level as well as POC values at respiration maximum and at POC slope change. In addition, if a (transient) equilibrium at a low POC value is seen (i.e. a horizontal POC plot), the floor POC level are listed.*

Fraction	Stab. phase duration (h)	Max. resp (fmol/h·cell)	(% O_2)	POC slope change (% O_2)	Floor POC level (% O_2)
090622.1	3.4	412.4	0.7209	0.1916	0.0265 ± 0.0030
090622.2	5.25	530.3	0.7796	0.576	0.1529 ± 0.0024
Mean	4.33 ± 0.93	471.4 ± 58.95	0.75 ± 0.029	0.3838 ± 0.19	0.0897 ± 0.0019

4.7.1 Data from experiment 081020 (10% O_2^{gp})

In this experiment, cells were cultivated in 10% O_2^{gp} for 91 hours. During the experiment, no cell maintenance tasks were performed.

The reason for this was to observe the respirational effect of confluence, and maybe to achieve a greater understanding of the features of more complex plots in the other experiments.

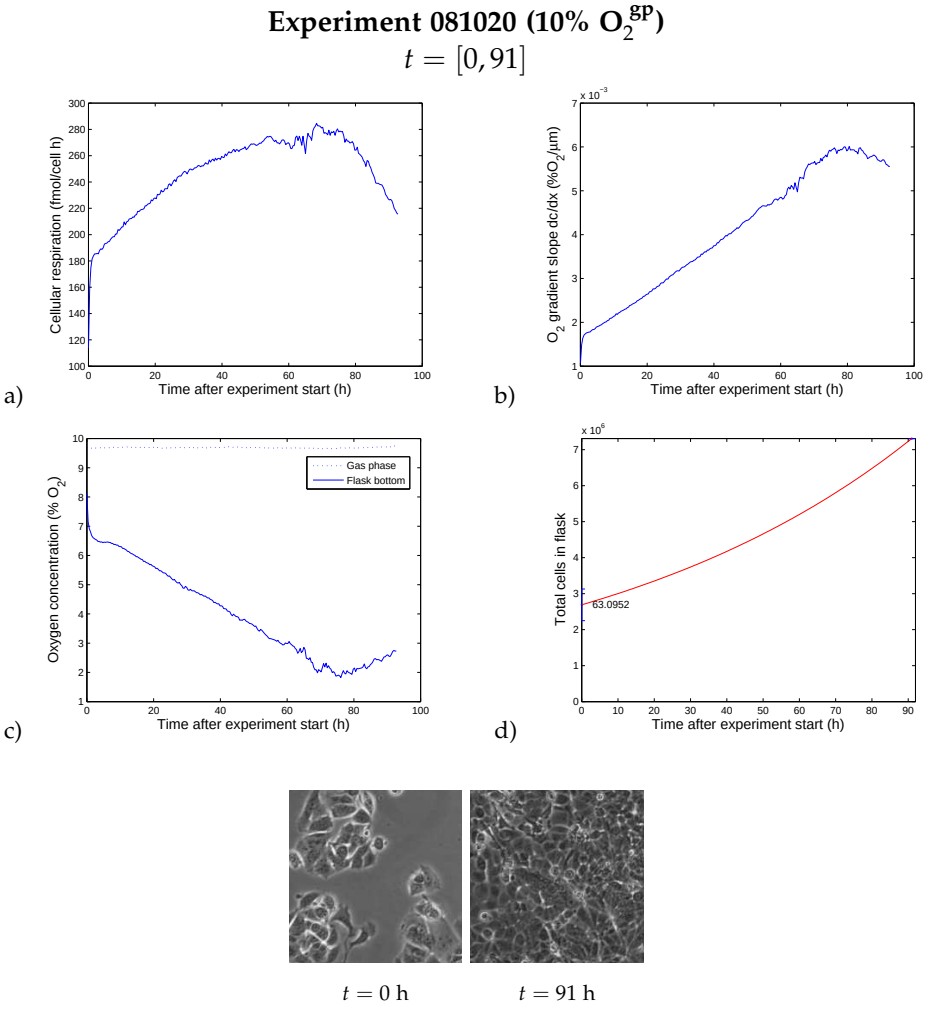

Figure 4.21: *Plots showing the data acquired during experiment 081020 (10% O_2^{gp}) in the time interval 0-91 h.*

4.7.2 Experiment 081020 (10% O_2^{gp}) summary

When the cells reaches confluence, it is interesting to observe the respirational consequence of this. This experiment was started when the cells were just below 3×10^6 cells, at a time where, normally, a recultivation is necessary.

However, in this experiment, the cells were allowed to continue their proliferation, to see at what limit (with respect to cell number) a decrease in respiration would be seen, at this gas phase oxygen concentration.

Pericellular oxygen concentration

A rather short stabilizing phase is seen, with a following steady decrease in POC.

After about 60 h, when the estimated cell number is about 5×10^6 cells, a scruffy tendency is seen in the POC slope. This may be due to cells loosening from the flask bottom and disturbing the O_2 gradient by consuming oxygen at a different depth than flask floor.

After 75 hours, the cell number is just above 6×10^6 cells, the POC reaches its minimum at 1.8% O_2 and starts to increase.

Flask and cellular respiration

We see a evident decrease in the respiration of individual cells as the space between cells decreases. It seems that a cell number of $6 - 7 \times 10^6$ make the cell flask confluent, assuming that the cell doubling time was approximately constant during the experiment.

In addition, a decrease in medium level due to evaporation probably has an effect on the cells, and cannot be ruled out to be a contributing factor.

Cellular proliferation

Since only two cell countings were performed, and a significant change in respiration is seen during the experiment, it is reasonable to assume that the cellular doubling time was not constant in the interval.

It is probable that $\bar{T}_2$ in reality decreases as the cells become confluent, meaning that the mean cellular doubling time early in the experiment is an over-estimate (i.e. the cells divide more rapidly than the fitted function assumes), and an under-estimate in the latter part of the experiment. The calculated $\bar{T}_2$, 63.1 h, is however the mean doubling time over the whole interval.

4.8 Comparison: Cellular proliferation and doubling time

In this section, the cell number plots are plotted for all five main experiments in figure 4.22, for the sake of comparison.

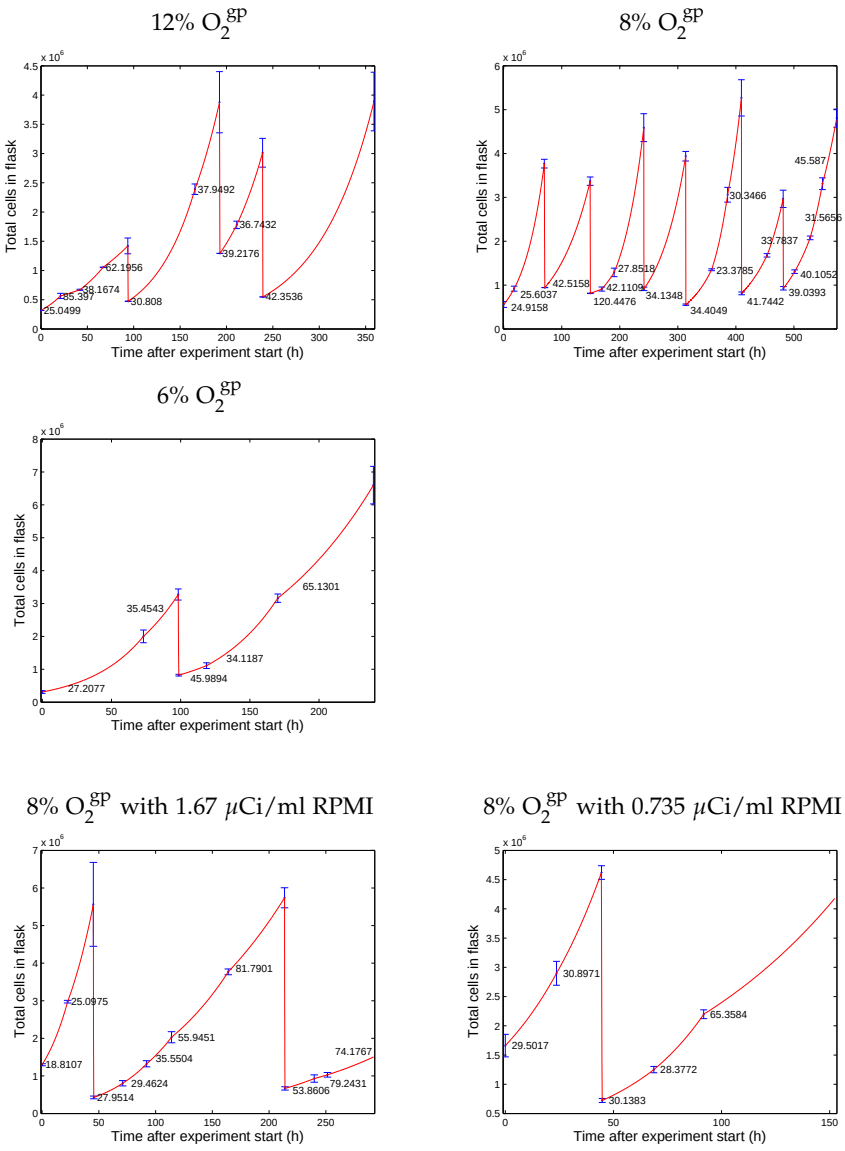

Figure 4.22: *Plots showing the cell counts as well as the exponential interpolations during the 12% O_2^{gp}, 8% O_2^{gp} and 6% O_2^{gp} experiments without irradiation and 8% O_2^{gp} experiments with irradiation.*

Table 4.35: *Mean doubling time for the whole cell population within experiments, calculated from the first and last cell count in each single fraction. Data from tables 4.17, 4.21, 4.25, 4.29 and 4.33.*

Experiment	O_2 level (gp) (% O_2^{gp})	RPMI activity (μCi/ml)	Mean doubling time (h)
081103	12	cold RPMI	39.69 ± 1.8
081118	8	cold RPMI	33.61 ± 2.3
081212	6	cold RPMI	37.86 ± 8.9
090608	12	1.67 μCi/ml	45.11 ± 14
090622	12	0.735 μCi/ml	36.89 ± 6.8

4.9 Comparison: Pericellular oxygen concentration (POC)

In figure 4.23, all POC slopes are plotted, for the sake of comparison.

Interesting features are stabilizing times, POC slope change levels and floor levels. It is important to bear in mind that the POC is dependent on medium height. The selected POC data is found in table 4.36.

12% O_2^{gp}

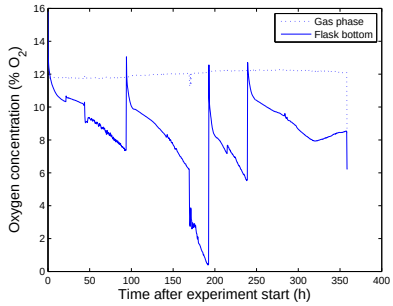

8% O_2^{gp}

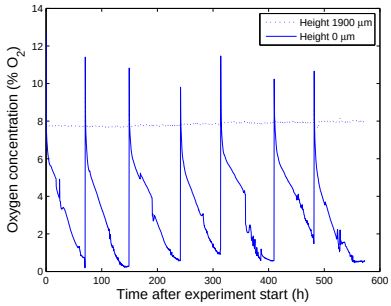

6% O_2^{gp}

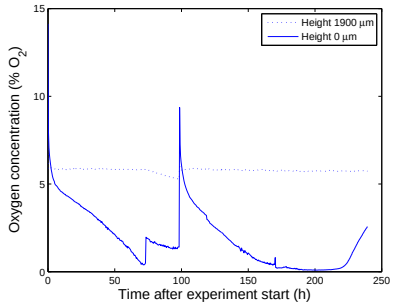

8% O_2^{gp} with 1.67 μCi/ml RPMI

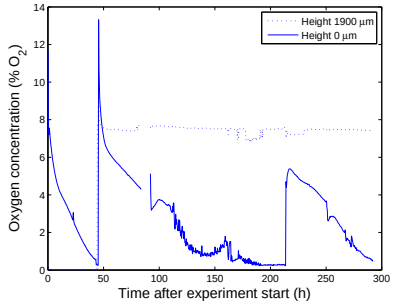

8% O_2^{gp} with 0.735 μCi/ml RPMI

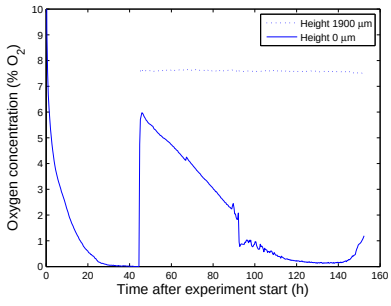

Figure 4.23: *Plots showing the pericellular oxygen concentration during the 12% O_2^{gp}, 8% O_2^{gp} and 6% O_2^{gp} experiments without irradiation and 8% O_2^{gp} experiments with irradiation.*

Table 4.36: *POC data from all experiments. Stab.phase, at which a slope change is seen, floor POC level. Data is taken from tables 4.18, 4.22, 4.26, 4.30 and 4.34.*

Experiment	O_2 level (gp) (% O_2^{gp})	RPMI activity (μCi/ml)	Stab. phase duration (h)	POC slope change (% O_2)	Floor POC level (% O_2)
081103	12	cold RPMI	10.70 ± 2.7	4.20 ± 3.7	none
081118	8	cold RPMI	8.996 ± 0.50	1.085 ± 0.10	0.3219 ± 0.0026
081112	6	cold RPMI	9.503 ± 1.5	1.5175 ± 0.15	0.1055 ± 0.0012
090608	8	1.67	9.57 ± 0.82	0.812 ± 0.14	0.2694 ± 0.0036
090622	8	0.735	4.33 ± 0.93	0.3838 ± 0.19	0.0897 ± 0.0019

4.10 Comparison: Cellular respiration

In this section, the cellular respiration plots are shown in figure 4.24 to ease comparison between experiments.

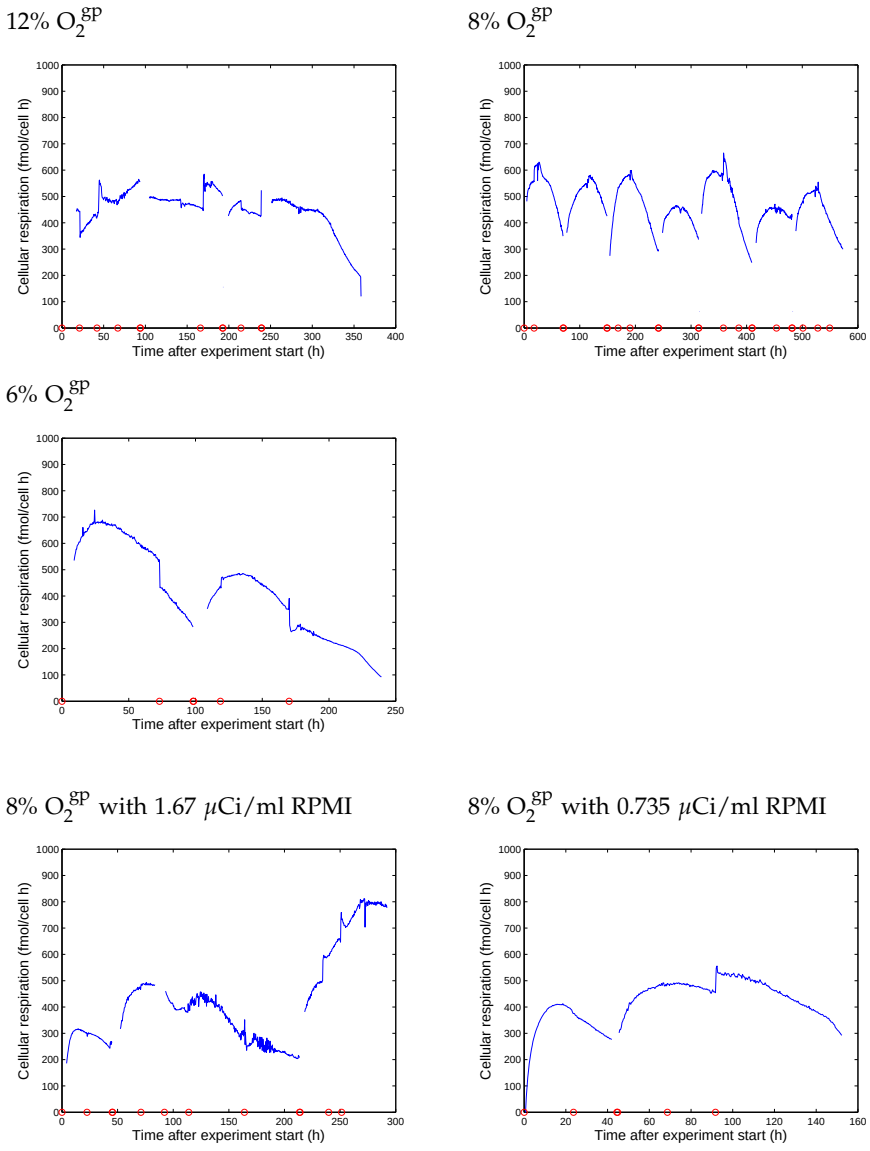

Figure 4.24: *Plots showing the cellular respiration from the 12% O_2^{gp} , 8% O_2^{gp} and 6% O_2^{gp} experiments without irradiation, as well as the 8% O_2^{gp} experiments with irradiation.*

Table 4.37: *Mean maximum respiration measured in the experiments and what POC they appeared at. Data from tables (4.18, 4.22, 4.26, 4.30 and 4.34).*

Experiment	O_2 level (gp) (% O_2^{gp})	RPMI activity (μCi/ml)	Max. resp. (fmol/h·cell)	(% O_2)
081103	12	cold RPMI	532.5 $\pm$ 25	6.830 $\pm$ 1.5
081118	8	cold RPMI	563.5 $\pm$ 27	2.479 $\pm$ 0.38
081112	6	cold RPMI	587.3 $\pm$ 102	2.74 $\pm$ 0.72
090608	8	1.67	541 $\pm$ 145	3.31 $\pm$ 0.99
090622	8	0.735	471 $\pm$ 59	0.7503 $\pm$ 0.029

4.11 Cellular survival experiments

The cellular survival was determined over four weeks for cells with 1.67 μCi/ml RPMI and KV RPMI in 21% O_2 and one week for cells with 1.67 μCi/ml RPMI and KV RPMI in 8% O_2.

The resulting surviving fraction SF of the irradiated cells is aquired by calculating the ratio from equation 3.8 on page 76, where the surviving fraction of the KV cells was used as an estimate of the plating efficency.

The results are seen in figure 4.25.

4.12 The degrading of scintillation samples

As a side project it was interesting to measure the measured activity in the scintillation samples as a function of time after preparation. The so-called ^{3}H samples were whole cells and the ^{3}Hn samples were nuclei. Furthermore, the ^{3}H-RPMI samples were pure radioactive medium and the KV samples were the cold valine cells.

The data are plotted in figure 4.26.

4.12.1 ^{3}H and ^{3}Hn samples

The ^{3}H samples (figure 4.26 a)) all have activities that decreases as a function of time. The decrease rate seems to be dependent on the initial activity, as high initial activity ($\sim$20.000 Bq) seems to result in a more rapid decrease compared to the samples with low initial activity ($\sim$5000 Bq). As the two ^{3}H-2704 samples indicates, there is no reason to suspect that there is a single equilibrium activity common to all samples.

The ^{3}Hn-samples (figure 4.26 b)) seem to express the same behavior, as a high relative initial activity ($\sim$3500 Bq) has a more rapid decrease

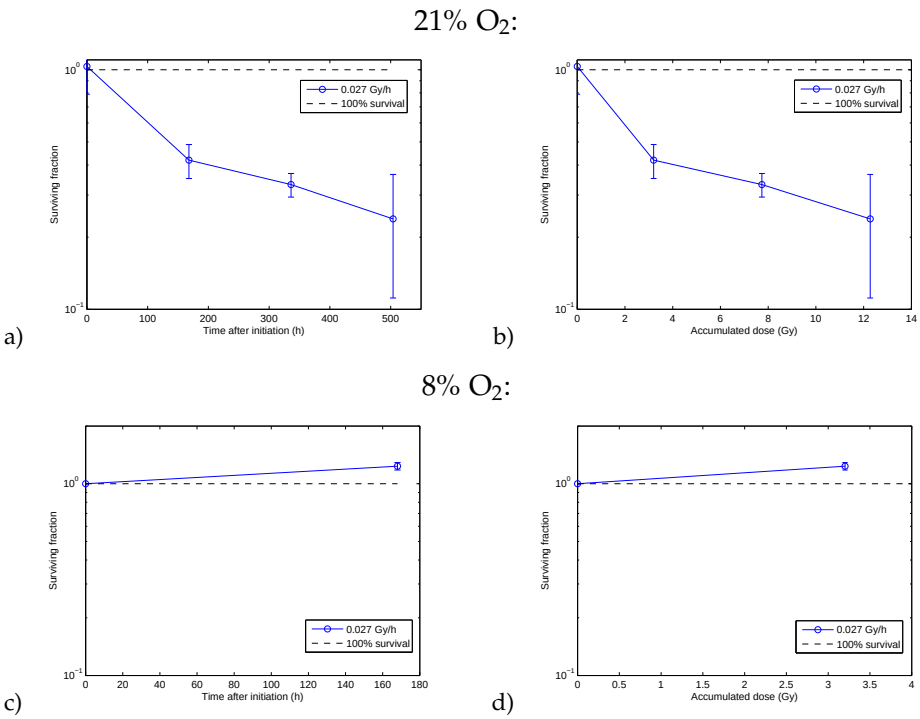

Figure 4.25: *The surviving fraction of MCF-7 cells in 1.67 µCi/ml RPMI medium in 21% O_2 and 8% O_2, relative to the KV cells. These cells are exposed to a dose-rate of* 0.027 ± 0.0030 *Gy/h SF is plotted as a function of time after first recultivation using radioactive medium (plot a) and c)) and as a function of estimated accumulated dose (plot b) and d)).*
Since accumulated dose was not a linear function of time, separate plots were necessary.

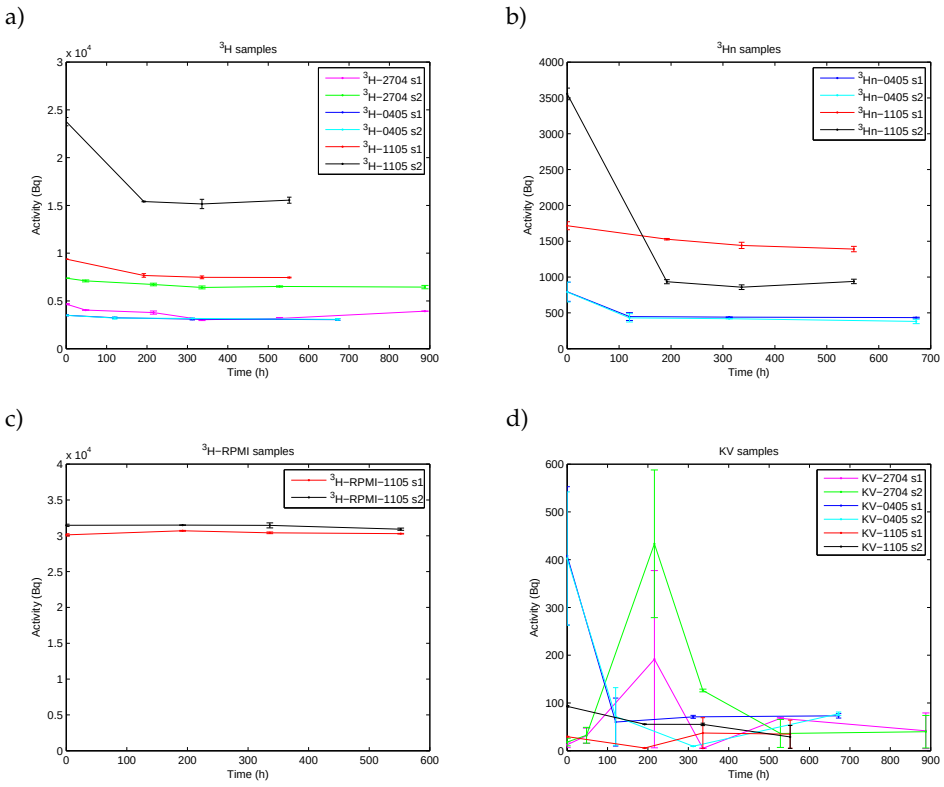

Figure 4.26: *The measured activities in the scintillation samples used in this thesis as a function of time after cell preparation.*

in activity compared to the lower initial activity samples (∼750 Bq). The ^{3}Hn-0405-samples seem to approach a equilibrium after 100 hours.

4.12.2 ^{3}H-RPMI samples

Compared to the cell samples, the medium sample (figure 4.26 c)) has a different behavior. Although having a relatively high activity, no decrease is observed. On the other hand, a small *increase* in activity is seen.

4.12.3 KV samples

The KV (cold valine) samples (figure 4.26 d)) has an initial low activity, as no radioactive component is present. A background measurement is seen, however.

The seemingly chaotic behavior also demonstrates the unstable characteristic of the samples. It is seen, however, that the 0405 and 1105 samples experience a decrease and the 2704 sample a net increase.

Chapter 5

Discussion

5.1 Cell cultivation and maintenance

The success of all cell experiments in this thesis depended on accurately and meticulously performed cell maintenance tasks, such as cell recultivation and medium change.

By following the routines punctiliously, issues such as low plating efficiency, cell culture infections or contaminations and cross-contamination (i.e. mixing two different cell lines) could be reduced to a minimum.

In the current experiments, the only cell line treated was MCF-7[1]. However, in the hypoxia/irradiation experiments, two different RPMI mediums were used (one with tritiated valine, and one with cold valine), and it was of great importance to avoid any contamination to cells with the wrong medium.

In addition, the labs were used by scientists studying other cell lines, so cleaning and sterilizing tasks before and after use of common equipment (such as the LAF bench) was meticulously performed.

During the experimental work, no cross-contamination was suspected. However, experiment 090608 (the 8% O_2^{gp} experiment with 1.67 μCi/ml medium) had to be aborted due to an infection inside the hypoxia cabinet. This is clearly seen in the last cell picture in figure 4.18 on page 134.

5.2 Microscopic resolution

The microscopic resolution factor μm/px and its derived P_f (pictures per flask) was fundamental quantities in calculating cell numbers during the

[1]With one exception—the T-47D cell line were used in a small supplementing experiment, but it was not performed parallel with any MCF-7 experiments.

hypoxia experiments. In addition, microscopic images was used to determine the cell and nucleus size used in dosimetric calculations. Thus, any errors in microscopic resolution calculating would have extensive effects on nearly all experimental results.

The calculation of the microscopic resolution are found in section 4.1 on page 79, and was found to be 1.2325 ± 0.011 μm/px in the first set-up and 0.8950 ± 0.00064 μm/px in the second set-up. The relative standard errors are less than 1% and 0.1%, respectively, and may be due to small deviations in the Bürker and Kova chamber and/or different distance from the lens, in addition to experimental error. However, the errors are very small and the microscopic resolution can therefore be said to have been determined with a satisfying precision.

However, using two different set-ups was not an optimal solution when performing experiments whose results are to be compared. But, as it turned out, only set-up 1 was used in the hypoxia and hypoxia/irradiation experiments. Set-up 2 was used solely to photograph cells for cell and nucleus size measurement.

5.2.1 Cell counting

The cell counts in the experiments consisted of the acquisition of three images of the flask floor, and multiplying the mean cell number per picture, C_p, with the factor P_f, pictures per flask. The quality and associated error of the resulting cell number were thus dependent on both the three images, the counting process itself as well as the precision of the P_f factor.

The mean cell number in the three images acquired needed to represent the mean density of cells on the surface. Pettersen et al. (2007) describes found that cells grown in the neck region of the cell flask had higher survival, attributing this to a lower medium height and thus shorter oxygen diffusion length (leading to higher POC at a given respiration, relative to other areas on the flask floor). Thus, the pictures used for cell counting was taken from areas of equal distance to the flask neck, assuming a comparable medium height and growth environment.

Further, the accuracy of the actual counting process was important. This was done manually, using a pen tool to mark the cells counted in Microsoft Paint (Microsoft, USA). A freeware program called OdoPlus (Fridgesoft, Germany) counted the mouse clicks and thus cell number, reducing the risk of counting errors.

The, P_f was calculated as described in section 4.1.

The relative standard errors in the resulting cell numbers were in the order of 1–20%. In figure 5.1 the relative standard errors in cell number in experiment 090608 and 090622 are plotted against the actual cell number.

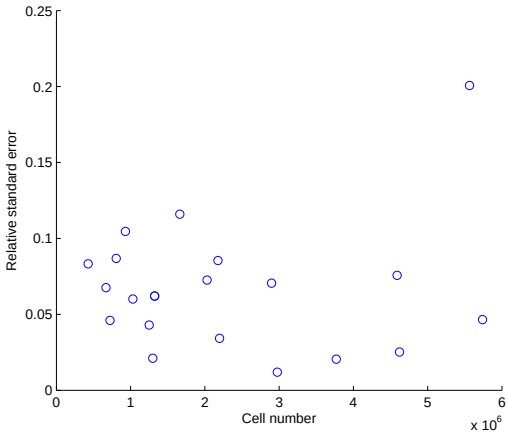

Figure 5.1: *Scatter plot of relative standard error of cell number plotted against absolute cell number. The data are taken from experiment 090608 and 090622. The linear correlation coefficient ρ is 0.119.*

No clear-cut correlation can be seen in the plot (ρ=0.119), as would be expected if the error is random and that the cell counting procedure is adequate.

As the cellular respiration calculation depended on the cell number, large uncertainties in the counting process would cause further significant uncertainties in the cellular respiration. If the cell number were overestimated, the calculated cellular respiration would have been an underestimate, and vice versa.

Volume based cell counting (section 3.4) was used to little extent in the present experiments. However, in the scintillation and survival experiments, the cells were counted using the volume based process, and it was important to assemble the Bürker chamber correctly to achieve a correct sample volume and thus cell number.

5.2.2 Cell and nucleus size determination

In the process of determining the cell and nucleus size, several hundred cells and nuclei was photographed (using microscope set-up 2). Using the Image Toolbox in Matlab, the diameter of 480 cells and over 320 nuclei were measured manually. The resulting mean diameters was calculated in section 4.2. The results were, as was to be expected, significantly different.

Studying the histograms in figure 4.1 on page 82, the data is skewed to the right (i.e. positive skewness), indicating fewer large cells than small cells. Immediately before the cell division, the volume of a cell is twice the volume of its daughter cells (the diameter is thus about 26% larger).

The skewness in the cell size histogram thus indicates that a given cell spends more time in the early phases of the cell cycle than in the later phases, possibly due to a long G_1 phase. This is consistent with the cell cycle theory presented in section 2.4.1 on page 18.

Despite this, the estimated cell diameter has a relative standard error of less than 1%.

The cell size calculation were based on measuring living cells in suspension, assuming that they are spherical and that the trypsination process did not change the cell size. If, however, the cells in fact were ellipsoids, the phase contrast images would reveal a two dimensional projection whose apparent size would depend on the orientation of the cell. Then, by measuring only spherical cells (that would be cells with their long axis perpendicular to the focal plane), the result would be an underestimate of the cell size. However, in the cell suspension images nearly all the cells were circular (by visual examination), indicating that the cells, under these circumstances, indeed can be treated as spherical objects.

Only single cells were measured, to avoid artifacts due to interaction with neighboring cells.

The nucleus size measurement procedure are more difficult, as the nuclei had been subject to a extensive preparation process. The outcome of the nucleus size measurement did therefore depend on a correctly performed preparation process (described in section 3.6.3). A superior method would be to use fluorescence to visualize the nuclei (as Søvik (2002)), but this was not done due to time constraints. Still, the standard error of the mean nucleus diameter is low, indicating a good result. In addition, an unpaired t-test yields an extremely significant difference between the cell diameter and nucleus diameter ($p < 0.0001$).

As the dosimetric model used yielded a dose-rate and accumulated dose that are, as mentioned in section 2.3.6 on page 15, average values for a population of cells, the mean cell and nucleus size were used in calculations. It is assumed that the resulting quantities are representable for the MCF-7 cell line.

The measurements of the whole cells were performed on unirradiated cells, while the nucleus size measurements were performed in connection to the nuclear activity experiment, and thus performed on cells having experienced 1.67 μCi/ml RPMI for a week. However, no morphological differenced between unirradiated cells (exp 081118) and irradiated cells (exp 090608 and 090622) can be seen in the cell pictures, indicating that the difference in morphology between unirradiated and irradiated cells, after one week, was (if present) small, justifying the measuring procedure.

5.3 Cell irradiation

Throughout this thesis the doses were delivered by the means of β-radiation following the decay of tritium.

5.3.1 Radioactive medium activity

As described in section 3.5.1 on page 58 , the radioactive medium was made to have a specific activity of 1.67 μCi/ml. The reason for this choice is that a medium of activity 1.67 μCi/ml had been used in earlier studies to irradiate the T-47D cell, and a resulting dose-rate of about 0.10–0.15 Gy/h had been found (Søvik, 2002; Bjørhovde, 2006; Pettersen et al., 2007; Storhaug, 2008). At this dose-rate, well-oxygenized T-47D cells were found to survive more than 150 days of continuous irradiation, as illustrated in figure 5.3 on page 170 (Pettersen et al., 2007). It was therefore guessed that the same medium activity would yield a dose-rate to the MCF-7 of comparable magnitude.

The specific activity of the medium was experimentally measured as described in section 4.3.7 on page 89, and found to be 1.66 ± 0.036 μCi/ml, not significantly different from the theoretical value.

Tritium has a half-life of over 12 years, and all irradiation experiments were performed within two months after the initial ^{3}H activity calculation. During this time, the radioactive decay theoretically decreased the activity of the tritium by 0.91%, which in this context is regarded as negligible.

5.3.2 Electron versus gamma irradiation

In the current experiment, the radiation quality used to deliver the dose to the cells was electron radiation. One might ask the transfer value of the results found with regard to gamma radiation.

As presented in section 2.2, photons and electrons have very different way of depositing energy. However, it is the biological effect that matters in the present context, motivating a comparison of the relative biological effect.

In figure 5.2 the LET for both electron and gamma radiation as a function of energy are plotted, and the electron and gamma slopes are treated as equal (Schwartz et al., 1966). Further, in figure 2.18 on page 43 the relative biological effect is shown as a function of LET. Thus, as electron and gamma radiation (in this energy range) has equal LET, they have equal RBE.

However, charged particles still does have a different energy deposition pattern than photons, and from the mass collision stopping power equa-

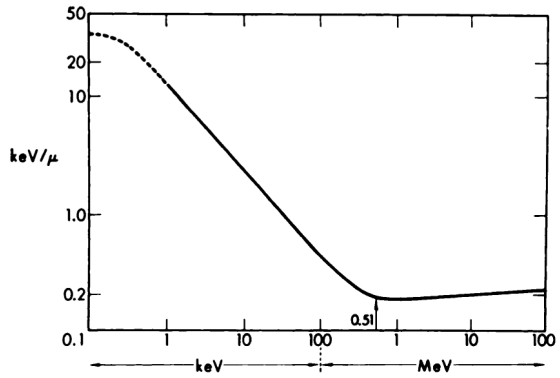

Figure 5.2: LET as a function of radiation energy for both β- and γ-radiation (from Schwartz et al., 1966).

tion 2.11 on page 12 it is known that the energy transferred by the particle is inversely proportional to the square of its velocity. A large amount of energy will therefore be deposited in the final moments of the particles travel through the cell.

Indeed, Monte Carlo simulations has indicated that tritium β-particles may create more complex DNA breaks than gamma irradiation (Moiseenko et al., 1998), indicating that the radiation quality used in this work yields more severe DNA damage than photons. But as the dose-rate was low, the cellular repair mechanism had more time to perform repair processes, and this might help justifying the above assumption.

5.4 Dosimetry

5.4.1 Problems with the cellular tritium microdosimetric model

Several issues about the microdosimetric model should be addressed.

First, the model does not include the effect δ-electrons, that is, secondary electrons that receives a large fraction of the initial energy and transport and deposit it (far) away from the primary track (see figure 2.4 on page 16). The perturbation of δ-electron has been studied by Goddu et al. (1994) in Monte Carlo simulations, and has been found to be negligible for low energy electrons.

In addition, energy traveling from potential extracellular sources (a reverse E_6 in figure 2.4) may increase the dose to the cell. But for tritium, being a low energy β-emitter, this has been shown to be negligible (Goddu et al., 1994).

Geometric issues

The geometric assumption illustrated in figure 2.3 on page 15, that the cell consists of two concentric spheres, is a simplification. In suspension (i.e. before the cells reaches the flask floor) they were in fact rather spherical, but as they reached the surface and flattens, their geometry radically changes. In addition, since cells grow in colonies, neighboring cells would affect the cell shape.

However, as the contribution to the dose to the nucleus from the cytoplasm was only about 5.5% of the contribution from the nucleus itself (since $S(R_N \leftarrow R_N)$ is more than 18 times higher than $S(R_N \leftarrow R_{Cy})$, from table 4.8[2]) and that the change in nucleus geomtry is less affected by the above factors, the error induced by the simplified geometric assumptions is not expected to be a significant source of error.

Another simplification is shown in figure 2.4, an assumption that the electron tracks are straight lines. This will, to a certain extent, induce errors in the dosimetry. However, due to the fact that the system (i.e. the cell) is large (18 μm) compared to the range of the electrons (average range in water 0.56 μm (Chen, 2006)), this effect can be assumed to be negligible. In addition, if sophisticated methods such as Monte Carlo simulation are to be applied to account for complex electron tracks, a higher degree of precision in cell and nucleus size and geometry is required to produce more precise results.

Averaging

The microdosimetry model only results in a mean dose-rate and accumulated dose over a cell population. Individual cells will, on the contrary, experience different dose-rates, since the S values in equation 2.20 are functions of the cellular geometry[3]. Measurements performed in the work with this thesis (section section 4.2) indicated a significant dispersion in cell and nucleus sizes.

However, the mean dose-rate and accumulated dose to a cell population are useful when it comes to the study of the radiobiological response to a population. Being low LET radiation (see section 2.3.3), the tritium β decay needs a large number of energy depositions to impart a significant dose, justifying the assumption that the variance in the spatial energy deposition pattern is low.

[2]This is due to the fact that the tritium β-particle range is low compared to the size of the nucleus

[3]In addition will effects of varying activity density, cell geometry and the stochastical nature of energy depositions contribute.

5.4.2 Scintillation counting and specific activity

Scintillation counting is a method with very high precision, and assuming a correct preparation process and sufficient high cell number (making the relative errors in activity measurement small), the experimental standard deviations are in order of 1/1000. The activity measured by the scintillation counter can thus be assumed to be somewhat correct.

However, to calculate the cellular and nuclear activities, a precise cell number had to be found. Significant errors in the cell and nucleus number would thus yield errornous activities and thus wrong dose-rate.

The cell and nucleus preparation process

The cell and nucleus preparation process, described in section 3.6.2 on page 60, consisted of several centrifugation steps. Between each step, it could be difficult to resuspend the cells to avoid lumps of cells. These cell groups potentially made counting in Bürker chamber more challenging and could thus induce errors in the counting.

Using the Bürker chamber in cell counting was also a potential source of error. The cover glass must be correct placed to create a correct volume. A volume too large would yield an overestimate in cell/nucleus density. In addition, cells/nuclei may attach[4] to the tip of the pipette used to transfer the suspension to the counting chamber, resulting in an underestimate in cell/nucleus number in the studied suspension.

In addition, before the last step in the scintillation preparation procedure, a separate sample of the cell (and nucleus) suspension was taken and counted. As this happens before the last centrifugation, any cell loss as a result of this last step would lead to a underestimate in specific activity.

It was also important to transfer the correct amount of test suspension to the scintillation flasks, as the calculated cell number is based on the counted cell/nucleus density and the volume of the suspension.

Any potential residues of extracellular radioactivity that may have been present in the cell or nucleus suspension after the preparation process would lead to an overestimate of specific activity. It was thus important to perform the cell and nucleus preparation process for scintillation counting meticulously.

The time effect on scintillation samples

In section 4.12, the stability of the scintillation samples were investigated. In figure 4.26 it is clearly shown that the sample activities are not stable in

[4] I.e. more cells or nuclei than water.

time. To achieve correct scintillation results, the measurements had to be performed within a few hours after the preparation process.

5.4.3 Dose-rate and accumulated dose

The dosimetric calculations yielded dose-rates and accumulated doses that were, as mentioned in section 2.3.6, average values for a population of cells. In addition, the cell and nucleus size were only measured a single time, assuming constant mean cell and nucleus size[5] throughout the experiment. The dosimetric model itself did not consider any change in cell and nucleus sizes, helping to justify the use of the mean measured sizes.

The calculated accumulated dose were based on the dose-rate buildup function fitted in section 4.3.6 on page 88. This does probably, as indicated in figure 4.2 on page 84, not correspond to the actual incorporation curve slope, affecting the accumulated dose calculations. In additon, no uncertainties are available for the initial slope, leaving the total standard error for accumulated dose unrealisticly low.

To provide a better estimate of the initial dose-rate, a model focusing on protein synthesis and degradation would potentially yield a better incorporation curve.

The S values

The S values, i.e. dose-rate per activity, are listed in appendix F and taken from Goddu et al. (1997). The values are a function of cell and nucleus size.

Since the cell and nucleus radii in section 4.2 on page 82 were measured with a high degree of precision, and the S values are only given for integer radii, an effort was made to interpolate the S values from Goddu et al. (1997) to better fit the measured cell and nucleus sizes.

This was, as described in section 4.3.3, done in Matlab by a linear regression with two covariates (i.e. cell and nucleus size). However, it was seen that the regression-based cellular S values estimate changed the final dose-rate with less than 1% compared to the calculation using the integer S values. The latter was therefore concidered appropriate.

5.4.4 Comparison to earlier studies of the T-47D cell line

In table 5.1, activity and dosimetric data from previous T-47D studies are compared to the current MCF-7 study. Comparing the dose-rate calculated

[5]The *individual* cell and nucleus sizes varies as they progress through the cell cycle, but the mean population size is assumed to be constant.

Table 5.1: *A comparison of the cell and nuclei sizes (V_C and V_N), the measured cellular activities A_C and nuclear activities A_N, the nuclear activity fractions f_N, the specific intracellular and intranuclear activities A_C^S and A_N^S, and the calculated dose-rate $\dot{D}$ to the nucleus for the T-47D cell and the MCF-7 cell. In all cases the specific medium activity was 1.66 μCi/ml.*

Cell line	MCF-7 (current thesis)	T-47D (Pettersen et al., 2007)
V_C ($\times 10^3$ μm^3)	3.00 ± 0.063	1.4 ± 0.3
V_N ($\times 10^3$ μm^3)	0.666 ± 0.023	0.7 ± 0.2
A_C ($\times 10^3$ Bq)	7.84 ± 0.30	7 ± 2
A_N ($\times 10^3$ Bq)	5.09 ± 0.54	2.8 ± 0.8
f_N	0.65 ± 0.073	0.40 ± 0.16
A_C^S ($\times 10^6$ Bq/ml)	2.65 ± 0.012	4.9 ± 1.7
A_N^S ($\times 10^6$ Bq/ml)	7.64 ± 0.084	4.0 ± 1.6
$\dot{D}$ (Gy/h)	0.0270 ± 0.0030	0.015 ± 0.004

for the MCF-7 cell with previous studies of the T-47D cell using the same microdosimetric method (Søvik, 2002; Bjørhovde, 2006; Pettersen et al., 2007), a puzzling difference is seen. By exposing the cells to the same specific medium activity, 1.67 μCi/ml, very different dose-rates accumulated.

The MCF-7 cellular activity was in the current experiments found to be $(7.84 \pm 0.30) \times 10^{-3}$ Bq/cell, and the intracellular specific activity was found to be $(2.645 \pm 0.012) \times 10^6$ Bq/ml. In comparison, the T-47D cellular activity was found, by Pettersen et al. (2007), to be $(7 \pm 2) \times 10^{-3}$ Bq/cell, i.e. not significantly different from the MCF-7 cellular activity, but the intracellular T-47D specific activity was in the same work found to be $(4.9 \pm 1.7) \times 10^6$ Bq/ml, almost twice the specific activity found for the MCF-7 cell.

Thus, the comparison indicates a similar total cellular activity, but lower intracellular specific activity for the MCF-7 cell. This means that the *total* activity within a single cell is about the same, but the *concentration* of activity, i.e. decays per volume unit, are lower in the MCF-7 cell. This suggests that the MCF-7 cell is larger, and this is supported by the data in table 5.1, indicating that the MCF-7 cell has more than twice the volume of the T-47D cell.

It is possibly even more interesting to look at the nucleus data. The nucleus sizes listed in table 5.1 suggests a similar size of the MCF-7 nucleus and the T-47D nucleus, even though the MCF-7 cell is overall larger.

Table 5.2: *A comparison of the S values used in the dosimetric calculations for the T-47D cell and the MCF-7 cell. In addition, the contribution ratio (i.e. the ratio of the contribution to the final dose-rate from the nucleus to the contribution from the cytoplasm) is listed. In all cases the specific medium activity was 1.66 µCi/ml. The MCF-7 data are from the current thesis, and the T-47D data are from Pettersen et al. (2007).*

Cell line	$S(R_N \leftarrow R_N)$ (Gy/Bq·s)	$S(R_N \leftarrow R_{Cy})$ (Gy/Bq·s)	Contrib. ratio
MCF-7	1.43×10^{-3}	7.86×10^{-5}	18.2:1
T-47D	0.861×10^{-3}	19.9×10^{-5}	4.3:1

Furthermore, the total activity within the nucleus was almost twice as high in the MCF-7 cell, suggesting a more concentrated radioactivity in the MCF-7 nucleus than in the T-47D nucleus. This is also supported by the A_N^S (specific nuclear activity) values.

Thus, the intracellular specific activity are significantly lower but the intranuclear specific activity are significantly higher in the MCF-7 cell relative the T-47D cell. While the T-47D data has little or no significant difference between intracellular and -nuclear specific activity, this is certainly not the case regarding the MCF-7 cell.

A possible interpretation of this comparison can be done using the plausible connection between activity distribution and protein distribution, since most of the activity probably is due to the radioactive incorporated amino acid. Thus, comparing the data from the current work with the work of Pettersen et al. (2007), it seems like, in the MCF-7 cell, a higher fraction of the radioactivity accumulates in the nucleus than in the cytoplasm (reflected by the difference in f_N values). And since the total cellular activity is not significantly different, the radioactivity has a higher density within the MCF-7 nucleus than in the T-47D nucleus.

As the mean range of the tritium β-particle in water is short compared to the MCF-7 nucleus size, only about 5% compared to the nucleus diameter, an increased intranuclear activity density means that the average distance from the tritium atom to the DNA is smaller. This can possibly help explaining the high dose-rate calculated.

All in all, the increased dose-rate is a direct consequence of the higher S values for the MCF-7 cell, listed for comparison in table 5.2. It is seen, for the MCF-7 cell, that the contribution to the total dose from the nucleus into itself is more than 18 times greater than the contribution from the cytoplasm. This is a far higher ratio than for the T-47D cell, where the

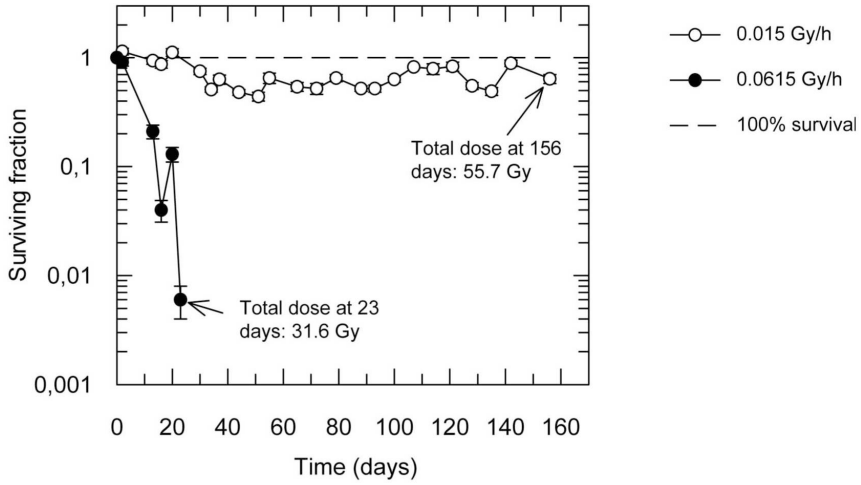

Figure 5.3: *The survival of the T-47D cell exposed to two different dose-rates under atmospheric conditions (Pettersen et al., 2007). A dose-rate of 0.015 Gy/h resulted in a stable surviving fraction of 60–70%, when a dose-rate of 0.062 Gy/h resulted in extensive cell death and a surviving fraction below 1% after 20 days. The figure is taken from Pettersen et al. (2007).*

dose contribution from the nucleus into itself is only just above 4 times higher than the cytoplasm contribution (Pettersen et al., 2007).

5.5 Cell survival experiments

In the survival experiment performed in this work, the survival of irradiated cells (with 0.027 Gy/h) were measured once a week for three weeks (for cells experiencing 21% O_2^{gp}) and for one week (for cells experiencing 8% O_2^{gp}).

The well-oxygenized cells has a significant decrease in survival during the experiment. After the third week just over 20% of the cells are able to forming countable colonies.

A similar experiment (see figure 5.3) was performed on well-oxygenized T-47D cells exposed to 0.015 Gy/h and 0.0615 Gy/h (Pettersen et al., 2007). Then, the cells experiencing 0.015 Gy/h seemed to stabilize at 70–80% survival. The cells exposed to 0.0615 Gy/h, however, had a survival below 1% after 20 days.

It may seem like the MCF-7 survival curve is in between these two T-47D cases, but the experiment was unfortunately not run long enough to conclude any long-term behavior.

In addition, a one-week experiment was performed on 8% O_2^{gp} cells exposed to 0.027 Gy/h, yielding a survival after one week of over 100%.

Again, the experiment was not run long enough to yield any long-term information.

It is important to keep in mind that the data plotted are the relative surviving fraction, where the surviving fraction of the KV cells were used as the plating efficiency of the irradiated cells. Thus, the plots show the survival of the irradiated cells relative to the survival of the unirradiated cells.

5.6 Hypoxia experiments: The experimental set-up and data analysis

5.6.1 Control of the oxygen concentration

The oxygen concentration within the hypoxia cabinet was monitored and controlled by the dedicated gas mixer. However, several precautions had to be taken to avoid contaminating the experiments with excess oxygen.

From the POC plots in the experiment sections 4.5–4.7, the gas phase reading are plotted with a dotted line. This was primarily used as a control on the gas phase oxygen concentration, in addition to mapping out oxygen probe drift. This reading was performed in depth -1900 μm.

However, if the medium depth was more than 1.9 mm, the gas phase level reading became in reality a reading of oxygen concentration in the medium. This happened e.g. in experiment fraction 090608.1 and .2, as can be seen in figures 4.16 and 4.17 on pages 132 and 133.

Another observation made during the experiments was that the gas phase reading within the flask was lower than outside—an effect that can be explained due to limited gas exchange through the flask neck. Thus, nearly all gas phase oxygen readings in the POC plots are below the actual gas phase oxygen concentration within the cabinet.

Oxygen supplied by equipment brought into cabinet

As mentioned, it was vital to the experiments to maintain greatest possible control over the availability of oxygen to the cells. Thus, when medium, trypsin or equipment was to be used, it needed to be exposed to hypoxic or anoxic conditions at least 24 hours before brought in contact with the cells.

The hypoxia cabinet used (picture in figure 3.9 on page 67) had a middle section where equipment could be kept in anoxic conditions (i.e. 0% O_2^{gp}). E.g. cell flasks and pipettes to be used were kept here.

Chemicals to be used on the cells, such as trypsin and medium, needed to be at 37°C when used, and was therefore kept inside the section of the

cabinet used for measurements. However, to avoid accelerated degradation of the chemicals due to the high temperature, it was brought in only one or two days before being used.

5.6.2 Oxygen measurement

According to Pettersen et al. (2005), the oxygen probe used would yield a 4% higher signal in gas than in a liquid, due to higher oxygen diffusivity in air. As two of the four calibration points used to calibrate the oxygen probe are performed in the gas phase, this will result in an error of maximum 4% in the measurements of oxygen concentration, as long as the signal used for calibration in the anoxic solution are ≥ 0 and the oxygen concentration of interest is in the interval spanned by the calibration points. These conditions were always met.

This is also a probable contributor to the artifact seen (point c) in figure 3.4 on page 63) when the probe arrives at the medium surface, as a significant decrease in oxygen reading occurs.

Oxygen solubility

To calculate the oxygen consumption, the density of molecular oxygen needed to be calculated from the measured oxygen concentration. The determination of this relationship proved to be a challenge. The quest was to determine the factor K (used in in equation 2.34 on page 49) whose unit is

$$[K] = \frac{\mu\text{M O}_2}{\%\text{O}_2} = \frac{\mu\text{M}}{\%}.$$

The value of K depend on several factor, such as salinity, temperature, and surrounding pressure. Several papers with different assumptions were found, all with different values for K.

Early in the work with this thesis, a factor $K = 9.52\ \frac{\mu\text{M}}{\%}$ was found in a spreadsheet published by Unisense (Unisense, 2009), the manufacturer of the oxygen measurement system. This was used in the software developed during the current work, and all analysis in this thesis are based on this value of K.

Later, several different K values were found, and are presented below.

- In Renner and Gnaiger (2003), 19.63% O_2 is said to equal 207.3 μM in pure 37°C water. This yields a K of 10.6 $\frac{\mu\text{M}}{\%}$. Furthermore, a RPMI oxygen solubility factor (i.e. oxygen solubility relative to pure water) are given to be 0.89, yielding $K = 9.40\ \frac{\mu\text{M}}{\%}$.
- A figure published in Probst et al. (1988) has K just shy of 100 μM/ppm, or just under 10 $\frac{\mu\text{M}}{\%}$.

- Froese (1961) uses 0.187 mmHg (i.e. 0.025% O_2) as an equal to 0.264 μM O_2, resulting in a factor of $K = 10.5\ \frac{\mu M}{\%}$.
- Pettersen et al. (2007) uses 0.13 % O_2 to equal 1.7 μM O_2, resulting in $K = 13.08\ \frac{\mu M}{\%}$.

Slope calculation

The measurement of the slope used to calculate the respiration was done in the Matlab software.

As presented in section 2.7.2, the choice of interval of the profile used to measure the slope was important. Effects on the slope of factors such as medium surface tension and varying local environment (as illustrated in figure 3.5 on page 64) at the flask floor should be kept to a minimum.

It was found by trial-and-error that the interval 800–200 μm resulted in the highest signal-to-noise ratio and was less subject to artifacts. In addition, this was an interval less troubled by the evaporation effect, i.e. the decrease of medium height over time due to water evaporation.

There is an intrinsic delay between flask respiration and the oxygen gradient slope. If the flask respiration were to change more rapid than the time used by the system to change the gradient, a mean value would be measured. If the slope is non-linear due to changing respiration, the use of linear fitting to estimate the slope is more likely to capture the appropriate mean respiration than if only two points are used to calculate the slope.

Gradient stabilizing phase and its effect on measured respiration and POC

In all experiment, a transient phase occurred before equilibrium was reached (the mean phase duration for each experiment is listed in table 4.36 on page 153). The existence of such a phase can be associated with (at least) to two factors:

1. The oxygen concentration gradient used in calculating flask and cellular respiration uses some time to form. Fresh medium does not have an oxygen concentration gradient, as it can only form due to oxygen consuming cells in the flask in combination with oxygen supply from the gas phase (in, of course, a medium of non-infinity diffusivity). See section 5.6.2 for more discussion about this.

2. The cell growth rate immediately after a recultivation is low, due to the previously described lag phase in cell population growth (described in section 2.4.2 on page 21). During this lag phase, the mean

cell doubling time is high and will result in little or no decrease in POC value.

The first factor would result in an underestimated respiration (i.e. too steep gradient), and the second factor represent a mechanism due to a cell phase with actual low respiration[6]. Both these factors will thus result in a low initial respiration.

On the other hand, with regard to POC value, the first factor will result in an initially rapidly decreasing POC (as the gradient stabilizes), and the second factor will result in a near horizontal POC (due to low oxygen consumption).

Thus, since the so-called stabilizing phase are measured based on the POC data, and whose length is determined from the POC plots, it seems plausible that it is the first factor alone who dominates to the initial, transient phase. The second factor, whose direct effect probably is masked in the plots, does contribute to the stabilizing phase duration by the limited initial oxygen consumption. This is supported by the fact that medium changes, completely destroying the oxygen gradient, does have a much shorter stabilizing phase. At the time of medium changes, the cell growth rate are typically much higher, forming the gradient in a much shorter time.

In addition, the second factor may help explain the increase in respiration seen in the respiration plots, having a duration many times longer. Respirational effects are further discussed in section 5.7.5.

In 12% O_2^{gp} (experiment 081103), a medium disturbance early in the experiment (thus possibly when the cells still are in a lag phase) seems to result in a major setback in the stabilizing process. In contrast, later in the experiment, the unwanted effects of cell maintenance seems to be less expressed. This supports the above consideration of the effect of the second factor (that is, the initial growth lag phase) on the stabilizing phase.

In 6% O_2^{gp} (081212.1) the system initially uses about 8 hours to reach equilibrium after experiment initiation. This is comparable to the 8% O_2^{gp} experiment (081118.1). The initial cell number in 6% O_2^{gp} was 3.1×10^5, about the same as in 12% O_2^{gp} (081103), but the latter used nearly 20 hours to stabilize, indicating that there are effects in addition to varying cell number contributing to stabilizing phase duration. In this case, it is seen from the cellular respiration plots that the respiration in 6% O_2^{gp} is about 650 fmol/h·cell after 20 hours, while in 12% O_2^{gp} the respiration is 450 fmol/h·cell after about 20 hours. This may explain the lengthy stabilizing phase duration in 12% O_2^{gp}.

[6] Assuming that the respiration is low during the lag phase

Possible artifacts from medium stirring

It is interesting to look at the possible effect of motion in the medium, i.e. as a consequence of cell counting, to help explain effects seen in the plots. The following is a back-of-the-envelope calculation giving a possibility to quantify the possible influence of medium stirring. The most general case is assuming that, after the stirring, the medium oxygen gradient is completely destroyed and the oxygen molecules are homogeneously distributed.

Given a gas phase oxygen concentration of 8.0% O_2^{gp} and a cell number of 2.000.000, a typical percellular oxygen concentration is 2% O_2. Knowing from Fick's law (equation 2.33) that the oxygen gradient is linear[7], the mean oxygen concentration in the medium is 5% O_2, or about 47 μmol/l.

The cell flask has an bottom area of 25 cm^2 and the medium has a depth of typically 1.7 mm, giving an medium volume of 4.25×10^{-3} l. Thus, there is a total of 1.998×10^{-7} mol O_2 in the medium.

Assuming further that the cellular respiration is in order of 300 fmol/h·cell, the total oxygen consumption in the flask is 6.0×10^{-7} mol/h.

By dividing the total amount of oxygen present in the medium with the total respiration, the total time needed to consume *all* the oxygen in the medium is calculated. Clearly, this will not happen in the lab, because the medium has a constant oxygen supply from the surrounding gas. But the calculated time will provide an idea of the maximum time needed to stabilize the system (that is, form the oxygen gradient) after an external disturbance.

In this example the time needed to consume all medium-dissolved oxygen is just under 20 minutes, a timespan shorter than the inter-profile waiting time. This concludes that if a effect of considerable longer time scale is observed after a system disturbance, it can not be explained from oxygen homogenizing.

After a medium change, the system is typically stable after one profile acquirement, supporting this assumption. However, after a recultivation (i.e. at the start of an experiment fraction), the cellular growth rate is low (due to the expected initial lag phase), the cell number is low and the respiration is not 300 fmol/h·cell. Thus, a longer stabilizing phase is to be expected at experiment fraction initiations, as is observed. The stabilizing phase is discussed to greater detail in section 5.6.2.

[7] Assuming that the oxygen consumption (that is, the cells) is located at the flask bottom only and that the total respiration is not changing rapidly.

Possible local effect due to microsensor movement

The movement of the microsensor in the medium will inevitable be a source of medium stirring. It may be interesting to see if there is any local difference in cell proliferation in the close vicinity of the microsensor placement, compared to other areas of the flask bottom.

Every proper cell count is performed by counting three different areas of the flask bottom. The first counting is performed without moving the flask, thus at the site of the oxygen microsensor during the freshly terminated experiment fraction. It may therefore be interesting to see if there is any correlation between picture number (i.e. picture area distance from microsensor) and relative cell number. It is assumed that the two last pictures of each time is taken one or two constant arbitrary distances from the first picture.

To do this, a $n \times 3$ matrix labeled `data` is constructed where each row represent each time (a total of n discrete counting times). The three columns contain the actual cell number in the three pictures (i.e. C_p).

Then, a small Matlab program was written containing a loop and the arguments for plotting and linear correlation calculation:

```
j=1;
for i=1:length(data(:,1))

    %The distances from first picture
    diffs(j,1)   = 0;
    diffs(j+1,1) = 1;
    diffs(j+2,1) = 2;

    %The relative cell number at time i
    diffs(j,2)   = (data(i,1)-data(i,1))/data(i,1)+1;
    diffs(j+1,2) = (data(i,2)-data(i,1))/data(i,1)+1;
    diffs(j+2,2) = (data(i,3)-data(i,1))/data(i,1)+1;
    j=j+3;

end
```

Now, the `diffs` matrix contains the cell numbers scaled relative to the first counting at each time. Then, the correlation is calculated by the command

```
corr(diffs(:,1),diffs(:,2))
```

The linear correlation coefficients from the experiments are listed in table 5.3. A negative correlation coefficient means a tendency toward increased cellular survival close to the microsensor.

Table 5.3: *Linear correlation coefficients ρ between cell localization relative to oxygen microsensor and relative cell count differences.*

Experiment	ρ
081103	0.0019
081118	-0.0836
081212	0.1970

5.6.3 Issues with the analysis software

Cellular growth fit

Between consecutive cell counts the software performs an exponential fit (as seen in all the d)-plots in the hypoxia experiment result section).

The quality and accuracy of the fitted curve depends on the interval between cell counts, meaning that proliferation information is lost in fractions where few cell numbers are acquired (e.g. as in fraction 081118.4, figure 4.10 on page 112), compared to fractions with several cell counts few hours apart (e.g. as in fraction 081118.7, figure 4.13 on page 115).

If too few counts are performed, the information of proliferation phases (presented in section 2.4.2 on page 21) during a fraction is not acquired.

A simple exponential fit would, in such a case, most likely result in an overestimate in cell number early in the fraction (due to the lag phase), and an underestimate late in the fraction (due to the plateau phase). Further, this errors would propagate to the calculation of cellular respiration, yielding an underestimate in respiration early in the fraction and vice versa.

Timing

As described in section 3.8, the analysis software was unable to read the time code used in the Unisense data sheets. The timing of each profile was thus calculated from an approximation using a mean inter-profile time.

The errors from this approximation, due to interruption of the experimental cycle such as medium shifts or cell cultivation, may result in both increase or decrease of the inter-profile time interval (since, after restarting the software, the first profile is recorded immediately). Any error in timing will therefore accumulate throughout the experiment.

However, during a week, typically three maintenance tasks were performed. Each maintenance task would mean a timing disturbance of maximum the waiting interval between two profiles, or about 21.5 minutes. During a week this results in an error of maximum 64.5 minutes, or 0.64%

of the week. This is thus assumed to be a negligible source of error.

5.7 Cellular effects of hypoxia and low dose-rate irradiation

In this section, some interesting results from the hypoxia (081103, 081118 and 081212) and hypoxia/irradiation (090608 and 090622) experiments are discussed. Experiment are referred to by experiment title and/or gas phase oxygen concentration, and if radioactive medium is used this is always explicitly stated.

Figure 4.3–4.20 on page 96–142 shows the individual experimental data. In addition, figure 4.22 (p. 150), 4.23 (p. 152) and 4.24 (p. 154) shows the most interesting plots in a more systematic way, making comparison easier.

5.7.1 Determining the appropriate gas phase oxygen concentration

The three large initial experiments investigated the respirational (and, to some degree, proliferational) response of the cells to varying degrees of hypoxia.

It was found that 8% O_2^{gp} was the appropriate gas phase oxygen concentration, due to the fact that 8% O_2^{gp} resulted in sufficient low transient POC values to yield probable hypoxic effects (as compared to a gas phase oxygen concentration of 12%), and that the culture exposed to 6% O_2^{gp} seemed to experience significant cell loss after just over a week.

For comparison, Pettersen et al. (2007) and Storhaug (2008), studying the T-47D cell line, used a gas phase oxygen concentration of 4% O_2 to achieve the above goals, indicating that the MCF-7 cell line is in general more sensitive to hypoxia than the T-47D cell line.

5.7.2 Effects of medium evaporation

As the gas blend in the box was restlessly monitored and controlled by the gas mixer, considerable gas exchange did occur. This caused loss of water vapor in the box, and induced evaporation of any available water within the box, including the medium used to cultivate the cells.

In an attempt to limit the scale of medium evaporation, up to 10 water dishes with sterile water were kept inside the cabinet, and refilled when required. However, some medium did inevitably evaporate resulting in a steadily decreasing medium volume and thus height.

The decrease in medium height is clearly visible in the 3D profile plots in figures 4.3–4.20 (pages 96–142).

As a reduced medium volume due to water evaporation in turn leads to increased medium concentration, the quality of the growth environment for the cells decreased, from now on called the *evaporation effect*. This made the medium change procedure particularly important in the cabinet.

A higher medium volume would yield a lower evaporation effects, due to a constant surface area and therefore constant evaporation rate, and thus smaller relative evaporation.

5.7.3 Effects of medium change and cell counting

If the total flask respiration was maintained after a medium change, it would (after the short stabilizing phase) yield lower POC values than before due to increased diffusion length. This is due to an unchanged gradient slope (after it has stabilized). This is supported by the plots, where every medium change seemingly lead to lower POC values.

It seems evident from the plots that the cellular respiration increased as a result of medium change (as is clearly visible in a.o. 081103.2, 081118.1, 081118.3 and 081118.5, see figure 4.24 on page 154).

Due to evaporation, the old medium most likely had a reduced growth environment quality. Thus, the most obvious reason for the increased respiration is probably the fact that the new medium has no evaporation effect in addition to a.o. fresh nutrients and a more favorable pH level, resulting in a better growth environment for the cells and thus increased respiration.

But in the 6% O_2^{gp} experiment, a cell count in the first fraction destroyed the oxygen gradient resulting in a higher POC (figure 4.23 on page 152) and at the same time a significant *decrease* in respiration (figure 4.24 on page 154), indicating a relationship between absolute POC level and cellular respiration.

This suggests another effect that cannot be ruled out: an abrupt change in medium height and thus diffusion distance (due to a medium change) may be associated with changed respiration due to different POC values—i.e. that increased oxygen availability may lead to decreased respiration and, as well, possibly the other way around.

Furthermore, decreased respiration will decrease the POC slope, and increased oxygen consumption will lead to even lower oxygen availability.

In the 12% O_2^{gp}, third fraction, a cell count disturbed the oxygen gradient resulting in a POC level increase (see figure 4.23 on page 152). At the same time, the flask and cellular respiration decreased (figure 4.24 on page 154). This is probably not a technical artifact (due to gradient stabilizing

and thus loss of respiration data), since the lowered respiration never increases afterwords and the POC slope is stable, indicating a stabilizing period duration shorter than the inter-profile interval (about 20 min).

It is clear from the data that the respiration increases after a medium change, but an understanding of the precise mechanism explaining the respirational behavior after a medium change is difficult to obtain, as it may be due to one or both of the above processes.

5.7.4 Cellular proliferation

In table 4.35 on page 151 the mean doubling time within each experiment are listed, calculated from the first and last cell count in each fraction.

The mean population doubling times in the experiments without irradiation were 39.69 ± 1.8 h in the 12% O_2^{gp}experiment, 33.61 ± 2.3 h in the 8% O_2^{gp} experiment and 37.86 ± 8.9 in the 6% O_2^{gp} experiment. The data indicates a slightly lower doubling time (i.e. higher proliferation) in 8% O_2^{gp} relative 12% O_2^{gp} and 6% O_2^{gp}. However, the 6% O_2^{gp} experiment had a high standard error, mirroring the low (mean) proliferation in the second fraction in the experiment (with $\bar{T}_2 = 46.8$ h), so the difference is probably not significant. The lowered proliferation in the second fraction of the 6% O_2^{gp} experiment may possibly be indicating a hypo-proliferative response to hypoxia.

In the 0.027 Gy/h 8% O_2^{gp} experiment, the mean doubling time was higher than in the corresponding non-radioactive experiment, as was the standard error (45.11 ± 14 h). From table 4.29 it is seen that the mean interfraction doubling time increased as the accumulated dose increased, resulting in the high standard error. With regard to the second fractions in the irradiation experiments only, where the dose-rate to the nucleus approaches its stable value, there is a relative increase of 34% and 30% relative to the unirradiated cells. This is comparable to the findings of Pettersen et al. (2007), where the irradiated T-47D cell has a increase of 20–30% in doubling time compared to the unirradiated control cells.

In the 0.012 Gy/h 8% O_2^{gp} experiment, the cellular proliferation was not significantly different from the estimated proliferation of the unirradiated cells.

Earlier studies has found that unirradiated MCF-7 cells had a mean doubling time of 24.6 h in atmospheric conditions and 72.6 h in severe chronic hypoxia (1% O_2 for 4 days). A subculture of hypoxia-tolerant MCF-7/H cells had an estimated $\bar{T}_2$ of 48.0 h (Scherbakov et al., 2009).

The present experiments did not expose the cells to chronic hypoxia at those levels, and no proliferation rate as low as $\bar{T}_2 = 72.6$ h has been observed. The highest $\bar{T}_2$ measured in the non-radioactive experiments

was 46.8 h, in the latter half of the 6% O_2^{gp} experiment.

In the lab, the MCF-7 cell line are typically recultivated with a ratio of 1:5 every fourth or fifth day, indicating a mean population doubling time of roughly 36.2 ± 3.7 h. This is comparable to the proliferation measured in the non-irradiation experiments mentioned above.

The present data suggests that the MCF-7 cell does not shorten its cell cycle (and thus dose per cycle) as a response to the continuous irradiation, a property that has been observed in some other cell lines (Pettersen et al., 2007).

5.7.5 Oxygen consumption slope and associated POC values

Probably the most interesting single quantity from these experiments are the cellular respiration. Some general and special observations will here be made.

In the 12% O_2^{gp} experiments, the respiration was somewhat constant within each experiment fraction. Due to the relatively high oxygen availability, no POC value was reached where clear respirational effects (i.e. a significant decrease in respiration) could be observed.

In the 8% O_2^{gp} and 6% O_2^{gp} experiments, however, the respiration had, in every fraction, a somewhat slow initial increase to a pronounced maximum, after which a subsequent decrease was observed. The mean respirational maxima[8] was 563.5 ± 27 (in the 8% O_2^{gp} experiment) and 587.25 ± 101 fmol/h·cell (in the 6% O_2^{gp} experiment), and the mean POC value at which the maximum occurred was 2.48 ± 0.38 % O_2 and 2.74 ± 0.72 % O_2, respectively.

Compared to the 12% O_2^{gp} experiment, this seems to suggest a respirational effect of low oxygen availability, with respect to both the slow initial respirational increase and the subsequent decrease. The cells seemed to be in trouble establishing a constant respiration, in contrast to the 12% O_2^{gp} experiment.

With respect to the stabilizing phase addressed in section 5.6.2, the cellular respiration in the 12% O_2^{gp} experiment reached stability more rapidly than the oxygen gradient formation (i.e. the cellular respiration is somewhat stable, at the latest, when usable oxygen profiles have formed), in contrast to the experiment with lower gas phase oxygen concentration, where the cellular respiration was still increasing after gradient formation.

In the 8% O_2^{gp} experiment with irradiation, the mean POC values at which respiration maxima occurred found was 3.31 ± 0.99 % O_2 (in the 0.027 Gy/h 8% O_2^{gp} experiment) and 0.7503 ± 0.030 % O_2 (in the 0.012

[8] Taken from tables 4.22 and 4.26.

Gy/h 8% O_2^{gp} experiment). The respirational maxia was 541 ± 145 and 471.4 ± 59 fmol/h·cell, respectively.

Lower threshold for maximum respiration

It can be useful to look at the POC value at which maximum respiration occurs, as it can be interpreted as a lower threshold for maintained full cellular respiration (Froese, 1961). The present results indicates that the lower POC limit for full respiration of the unirradiated MCF-7 cells was $2.55 \pm 0.28\%$ O_2, being the mean POC value at which the respiration maxima was measured[9].

As presented in the previous section, the irradiated MCF-7 cells had a full respiration POC threshold measured as 3.31 ± 0.99 % O_2 (0.027 Gy/h) and 0.750 ± 0.029 % O_2 (0.012 Gy/h). In other words, the 0.012 Gy/h cells but not the 0.027 Gy/h cells had a significantly lower POC at which respiration maximum occurs. There was no such significant difference observed between the 0.027 Gy/h experiment and the experiment without irradiation.

Figure 5.4 shows a plot of the cellular respiration in the 8% O_2^{gp} without irradiation experiment as a function of POC, illustrating the coincidence of the threshold for full respiration.

For comparison, the lower (POC) limit for full respiration for the T-47D cell line are reported to be 0.1% O_2 (Pettersen et al., 2005). For the bacterium *Microsossus candidans* the lower threshold of full respiration has been determined to be 0.00526% O_2, and for ascites tumor cells the threshold is at about 0.13% O_2 (Froese, 1961).

Furthermore, Froese (1961) defines the *respiratory constant* K_m, defined as the oxygen concentration at which the respiration is reduced to half of its maximum. The estimated respiratory constant for the unirradiated MCF-7 cell line was[10] $K_m = 0.623 \pm 0.22\%$ O_2.

The respiratory constant for the ascites tumor cells in 37°C was estimated to be 0.0246% O_2 (Froese, 1961).

POC floor value and POC slope change values

When the POC value approached 0% O_2, it seemed to stabilize at a minimum value (labeled *POC floor value*), being 0.3219 ± 0.0026 % O_2 in the

[9] Calculated from experiments 081103, 081118 and 081112. In 081103 the POC did reach below 6% O_2 in one fraction only, and the data from the other fractions in 081103 are thus omitted in the calculations.

[10] From experiment 081118 (fractions 3, 5 and 7) and experiment 081212 (fractions 1 and 2). These were the only fractions were the respiration did decrease to half of its maximum value before recultivation was performed.

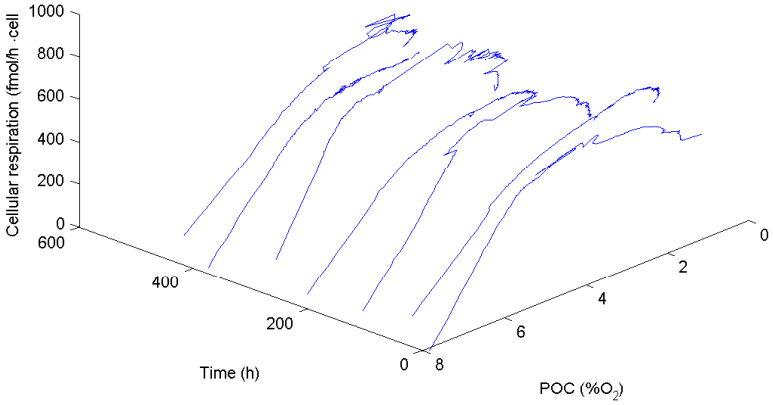

Figure 5.4: *Cellular respiration in experiment 081118 (8% O_2^{gp} without irradiation) plotted against pericellular oxygen concentration and time after experiment initiation, showing when respiration has its maximums. The mean POC value at which respiration maxima was seen for all experiments (without irradiation) was* $2.55 \pm 0.28\%$ *O_2.*

8% O_2^{gp} experiment and 0.1055 ± 0.0012 % O_2 in the 6% O_2^{gp} experiment. In the 12% O_2^{gp} experiment the POC did not reach values low enough to reach any potential POC floor effect.

Irradiated cells in 8% O_2^{gp} seemed to yield POC values even lower, as the POC floor values was 0.2694 ± 0.0036 in the 0.027 Gy/h experiment and 0.0897 ± 0.0019 % O_2 in the 0.012 Gy/h experiment. Both these floor values were significantly lower than the floor value experienced by the unirradiated cells.

In addition, the quantity labeled *POC slope change value*, i.e. the pericellular oxygen concentration at which a POC slope change is seen, did possibly indicate changed respiration and/or proliferation due to limited oxygen availability. Despite being a qualitative property of the POC plot, it can serve as a somewhat crude indicator of a threshold value at which possible effects of hypoxia is seen.

Regarding the experiments without irradiation, the POC slope change was 4.20 ± 3.7 % O_2 in the 12% O_2^{gp} experiment, and 1.085 ± 0.10 % O_2 and 1.52 ± 0.15 % O_2 in the 8% O_2^{gp} and 6% O_2^{gp} experiments, respectively.

In the experiment with irradiation, however, a significantly lower POC slope change value was measured, at 0.812 ± 0.14 % O_2 and 0.384 ± 0.19 % O_2 (in the 0.027 Gy/h and the 0.012 Gy/h experiments, respectively).

Consistent with the findings of Pettersen et al. (2007), but in disagreement with the conclusion of Storhaug (2008), these results suggests that the irradiated cells accumulated a lower POC value than unirradiated cells. Furthermore, it is indicated that this is (at least partly) due to increased respiration of irradiated cells.

A possible interpretation of the seemingly reduced response to lowered oxygen concentrations of the irradiated cells is that the increased respiration is associated with a decrease in environment monitoring, allowing the irradiated cells to consume more oxygen than the unirradiated would.

5.7.6 Comparative respirational trends

When comparing the 8% O_2^{gp} experiment with the radioactive equivalents, it is indicated that prolonged (i.e. $>$ 200 h) exposure to the radioactive medium (1.67 μCi/ml) resulted in an increased cellular respiration. Respiration values up to 812.1 fmol/h·cell was reached, considerably higher than in any other experiment.

The 0.012 Gy/h 8% O_2^{gp} experiment was, unfortunately, not run long enough (due to time constraints) to potentially confirm this effect. However, other studies (Pettersen et al., 2007; Storhaug, 2008) have shown that hypoxia cancer cells (T-47D) experiencing 0.015 Gy/h (close to the estimated dose-rate to the MCF-7 cells at 0.735 μCi/ml) indeed have increased respiration under irradiation compared to unirradiated cells.

A factor that may contribute to the apparently increasing respiration is radiolytic oxygen depletion, i.e. the dissociation of water molecules by radiation. It would decrease the POC and thus make the oxygen concentration gradient less steep, and being interpreted as increased cellular oxygen consumption. However, at these dose-rates, the radiolytic effect is assumed to be negligible (Pettersen et al., 2007).

5.7.7 Possible effects due to non-constant dose-rate

As the system needed around 150 hours to reach a stable dose-rate (see figure 4.2 on page 84), one could argue that no major differences between the 8% O_2^{gp}, 8% O_2^{gp} (0.027 Gy/h) and 8% O_2^{gp} (0.012 Gy/h) experiments would be expected to be seen during the initial phases of the experiments, when the dose-rate is low.

However, by studying the cellular respiration plots, it seems like the oxygen consumption per cell in the initial phases of the experiments was *lower* for the irradiated cells than the unirradiated. The maximum respiration measured on the unirradiated cells was 630.5 fmol/h·cell in the first fraction of the 8% O_2^{gp} experiment. On the contrary, the respiration of

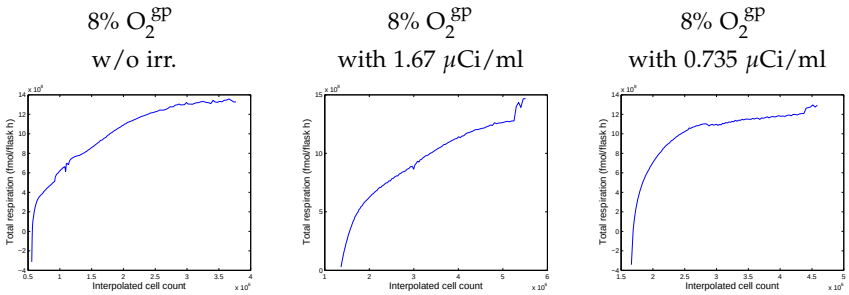

Figure 5.5: *Cellular respiration plotted against cell number, from experiment 081118.1, experiment 090608.1 and experiment 090622.1. Taken from appendix B. Note the more expressed shoulder in the two experiments with irradiation, possibly indicating a longer respirational lag phase.*

the irradiated cells was pronouncedly lower—317.1 fmol/h·cell and 412.4 fmol/h·cell for the 0.027 and 0.012 Gy/h experiments, respectively.

This may indicate a early respirational response by the cells on the irradiation. Still, the proliferation during the first fractions cannot be said to reflect this response (as previously discussed).

In figure 5.5, plots of total (flask) respiration versus cell number from the initial fractions from the three 8% O_2^{gp} experiments is seen. These plots may help explain the effect discussed, as it illustrates the respiration as a function of cell number rather than as a function of time. When the plotting technique was presented in section 3.8.10, it was noted that a constant cellular respiration would yield a straight line in these plots. In appendix B, these plots for all experiment fractions are shown.

However, there is a pronounced difference in slope, as the unirradiated cells seems to yield a somewhat shoulderless curve (at least initially), as compared to the irradiated cells where a broader shoulder is pronounced. This indicates a lower initial respiration per cell when it is irradiated, also supported by the cellular respiration plots discussed above. It also indicates a longer respirational (*not* proliferative) lag phase. This cannot be excluded as a cellular response to the low dose-rate irradiation.

From these data, it is not possible to predict the respirational response to a system with constant dose-rate (i.e. lacking the initial stabilizing phase). In addition, no conclusion can be made from these data distinguishing the effect of constant dose-rate exposure and accumulated total dose. However, as discussed below, former studies support the possibility of a dose-rate dependent response.

5.7.8 The relationship between respiration and proliferation

A short quantitative comparison from experiment 081118 (8% O_2^{gp}) may illustrate the relationship between cellular respiration and proliferation.

The mean cellular respiration $\bar{R}$ in the second interval is 533.3 fmol/h·cell, while $\bar{T}_2$ is 23.4 h. In the third interval $\bar{R} = 403.8$ fmol/h·cell while $\bar{T}_2$ is 30.3 h. $\bar{R}$ thus show a relative decrease of 24.3 %, and $\bar{T}_2$ a relative increase of 24.7 %, indicating a remarkably close (but not surprising) relationship between cellular respiration and mean doubling time. In other words, this indicates a close and possibly linear relationship between the division rate of the cells and their respiration.

5.7.9 Comparison to earlier studies

Pettersen et al. (2005) found the mean respiration of the T-47D cell line experiencing 4% O_2^{gp} to be 177 ± 23 fmol/h·cell.

In another study by Pettersen et al. (2007), the T-47D cell line was simultaneously exposed to 4% O_2^{gp} and 0.015 Gy/h electron irradiation. The cellular respiration exceeded 900 fmol/h·cell during the measurement. Prior to the measurement, the cells had been exposed to 4% O_2^{gp} and 1.6 μCi/ml medium (yielding a dose-rate of 0.015 ± 0.004 Gy/h) for 3 weeks.

The T-47D cells increased respiration 2–4 times due to the low dose-rate irradiation, increased the oxygen depletion and thus lowered the POC, explaining the cell death observed.

Studying the survival of these cells, Pettersen et al. (2007) found that cell proliferation stopped after about 3 weeks. This was attributed to a combination effect of 0.015 Gy/h irradiation and a low oxygen availability (due to the fact that cells grown in a shallower layer of medium, and thus experiencing a higher POC, did *not* die).

T-47D cells grown in atmospheric conditions exposed to 0.015 Gy/h were grown for more than 150 days, seemingly stabilizing at 60–70% survival, whereas cells irradiated with 0.062 Gy/h in athmospheric conditions had a surviving fraction below 1% after 20 days (Pettersen et al., 2007).

Finally, the radiosensitivity of hypoxic cells to acute irradiation was not found to differ from well-oxygenized cells. This supported the above theory that the increased respiration due to low dose-rate irradiation increased oxygen depletion and thus killed the cells by asphyxiation.

However, in another study on melanoma and squamous carcinoma cells, chronic hypoxia was shown to increase radiosensitivity to acute (1 Gy/min) irradiation compared to acute hypoxic cells (Zölzer and Streffer, 2002), suggesting the existence of additional mechanisms controlling the

radiosensitivity to hypoxic cells. A study of the NHIK 3025 human cervix cancer cell under extreme hypoxia ($< 0.004\%$ O_2^{gp}) for 20 hours, found that the cells in a reoxygenized state were rendered more radiosensitive to acute irradiation than cells not previously exposed to hypoxia (Pettersen and Wang, 1996; Koritzinsky et al., 2001). This property sustained for at least 50 hours after reoxygenation (Koritzinsky et al., 2001).

5.8 Cellular effects of hypoxia and confluency

In experiment 081020 the combined effects of hypoxia, confluency and absent medium change were seen.

What was observed was a scruffy tendency after 60 hours, in both POC and respiration plots. This may indicate a state of confluency and/or possible hypoxia effects. In other hypoxia experiments, a change in POC slope was observed at about 1% O_2, a level never reached in this experiment.

The minimum in POC value occurs when the cell number in the flask is about 6×10^6 cells, a cell number hardly ever occurring in the other experiments.

However, it is not possible to rule out the possible contributing effect of absent medium change, as the last fraction in the 12% O_2^{gp} experiment, also lacking cell maintenance, had a POC slope behaving the same way, with cell numbers far lower. However, the scruffiness of the plots is *not* seen in the 12% O_2^{gp} experiment, suggesting that this property is concurrent with high cell number.

The scruffiness itself can be understood as an artifact from loose cells, consuming oxygen at depths other than the flask floor. This would affect the slope of the oxygen gradient and thus have a possibility to create the observed effect.

5.9 Suggestions for further investigations

Based on the results and limitations of the present experiments, several suggestions for further investigations can be made.

- The long-term survival of the MCF-7 cell experiencing hypoxia (without irradiation) should be examined. In this work, one experiment may indicate that the MCF-7 cell survive without significant cell loss at least 3 weeks in 8% O_2^{gp}, but no satisfying survival experiments were performed and the survival could thus not be quantified.

- In addition, the long-term survival of the MCF-7 cell experiencing both chronic hypoxia and low dose-rate irradiation should be stud-

ied. In this work, the cells did only experience this combination for merely 1.5 week. No conclusion can therefore be made of long-term cell survival under these circumstances. In addition, it would be interesting to study any possible low dose hyper-radiosensitivity.

- Furthermore, the long-term respirational behavior of the MCF-7 cell experiencing the above duality could be examined.
- A study of the response to acute irradiation after or during chronic hypoxia could also be interesting.
- In addition, the difficulties presented in section 5.6.2 regarding determination of the K value (i.e. dissolved molecular oxygen concentration per percent O_2) should be studied and further conclusions should be made regarding which value to use.
- In the current work, no conclusion could be made regarding mechanism associated with several results and indications. This may potentially be interesting to investigate further. This concerns the possible mechanisms behind current indications such as
  - The high specific activity within the MCF-7 nucleus
  - The behavior of the accumulating dose-rate during the initial phase, with respect to radioactivity incorporation
  - The increased respiration in hypoxia/irradiation experiments
  - The reduced POC in hypoxia/irradiation experiments
  - The seemingly different maximum respiration POC values at different dose-rates.

Chapter 6

Conclusion

The main objectives of this thesis could be divided into three main categories; to develop a custom made software to analyze the respirational data, to apply a microdosimetric method to calculate the dose-rate to the nucleus of the MCF-7 cell due to electron irradiation from incorporated tritiated valine, and finally to investigate the respirational effects of the MCF-7 cell line both under exposure to chronic hypoxia alone, and under simultaneous exposure to chronic hypoxia and low dose-rate irradiation .

1. A analysis and plotting software was written in Matlab and the source code are found in appendix A. This program was used to produce all original plots in this thesis.

2. Grown in a medium of specific activity of 1.67 μCi/ml, the final dose-rate to the MCF-7 nucleus was found to be 0.0270 ± 0.0030 Gy/h. As this was higher than expected, further calculations estimated the final dose-rate to the same system exposed to a medium of specific activity of 0.735 μCi/ml to be 0.0119 ± 0.0013 Gy/h. This dose-rate was more similar to earlier similar studies.

   Comparing the MCF-7 cell with the much studied T-47D cell, the same medium activity resulted in a higher dose-rate to the MCF-7 nucleus. This is probably connected to the fact that the although the total cellular activity was not significantly different between the cell lines, the intracellular activity *distribution* was different. The specific activity (i.e. the activity concentration) within the nucleus was considerably higher in the MCF-7 nucleus than in the T-47D nucleus, and the average distance from a tritium atom to the DNA was therefore less in the MCF-7 cell, possibly resulting in a higher dose-rate. In addition, this may indicate a higher protein density in the MCF-7 nucleus.

3. Investigating the response of the MCF-7 cell to chronic hypoxia, results indicated that a gas phase oxygen concentration of 8% O_2 resulted in interesting hypoxia effects without observed significant cell death due to low oxygen availability. In this experiment, the mean cellular respiration was found to be 563.5 ± 27 fmol/h·cell, and the maximum respiration measured was 642.7 fmol/h·cell.

   When the cells later were exposed to 0.027 Gy/h electron irradiation in 8% O_2^{gp}, the respiration did eventually increase to 812.1 fmol/h·cell. This occurred after about 11 days of irradiation and an accumulated total dose of 5.96 ± 0.61 Gy. The experiment exposing the cells to a dose-rate of 0.012 Gy/h, however, was not run long enough to make any respirational conclusions.

   The lower pericellular oxygen (POC) threshold for maximum respiration for unirradiated MCF-7 cells was estimated to be 2.55 ± 0.28 % O_2. Furthermore, the lower POC threshold for maximum respiration for irradiated MCF-7 cells in 8% O_2^{gp} was measured to be 3.31 ± 0.99 % O_2 (0.027 Gy/h) and 0.750 ± 0.029 % O_2 (0.012 Gy/h). Thus, these results indicate that a dose-rate of 0.012 Gy/h yields a significantly decreased lower POC threshold for maximum respiration. The same was not seen for a dose-rate of 0.027 Gy/h, indicating that the lower dose-rate of 0.012 Gy/h results in a greater cellular response. In addition did cells exposed to a dose-rate of 0.012 Gy/h yield significant lower POC values than both 0.027 Gy/h cells and unirradiated cells.

   The results suggests that cells irradiated with 0.012 Gy/h accumulate lower POC value than unirradiated cells, possibly due to increased respiration. The mechanism behind this observation was not studied in this thesis, but a possible interpretation of the results is a downgrade of the cellular environment monitoring, allowing the irradiated cells to consume more oxygen and thus accumulating more severe hypoxia.

In conclusion, the experiments in this work seems to confirm for MCF-7 what was found by Pettersen et al. (2007) regarding T-47D—that low dose-rate irradiation under chronic hypoxia is associated with an increase in cellular respiration, making the hypoxia more severe, thus suggesting a mechanism for increased cellular radiosensitivity to low dose-rate irradiation under chronic hypoxia.

In addition, it was also indicated that the MCF-7 cell does experience a higher dose-rate than the T-47D cell when exposed to the same medium activity due to higher intranuclear specific activity. The experiments did also provide indications that the MCF-7 cell is more sensitive to hypoxia

than the T-47D cell.

List of Tables

2.1 Typical LET values for a selection of radiation qualities . . . 13

3.1 Specific activity of ^{3}H-valine 59

4.1 Chamber measurements (set-up 1) 80
4.2 Chamber measurements (set-up 2) 80
4.3 The average microscope resolution with standard errors. . . 80
4.4 Measured cell sizes 83
4.5 Cellular activity 84
4.6 Nuclear activities 85
4.7 Cellular f values 86
4.8 Cellular S values 87
4.9 Dose-rate 87
4.10 Integrated activity in pre-steady state phase 89
4.11 Total accumulated dose estimate 90
4.12 Hot medium scintillation counting 90
4.13 Intra- and extracellular specific activities 91
4.14 T-47D nucleus activity and dose-rate 92
4.15 Experiment 081103 (12% O_2^{gp}) events 95
4.16 Cellular respiration in experiment 081103 (12% O_2^{gp}) 100
4.17 Experiment 081103 (12% O_2^{gp}) mean doubling times 100
4.18 Selected data from experiment 081103 (12% O_2^{gp}) 103
4.19 Experiment 081118 (8% O_2^{gp}) events 108
4.20 Cellular respiration in experiment 081118 (8% O_2^{gp}) 116
4.21 Experiment 081118 (8% O_2^{gp}) mean doubling times 117
4.22 Selected data from experiment 081118 (8% O_2^{gp}) 120
4.23 Experiment 081212 (6% O_2^{gp}) events 124
4.24 Cellular respiration in experiment 081212 (6% O_2^{gp}) 127
4.25 Experiment 081212 (6% O_2^{gp}) mean doubling times 127
4.26 Selected data from experiment 081212 (6% O_2^{gp}) 129
4.27 Experiment 090608 (8% O_2^{gp} with 1.67 μCi/ml RPMI) events 131

4.28 Cellular respiration in experiment 090608 (8% O_2^{gp} with 1.67 μCi/ml RPMI) . . . 135
4.29 Experiment 090608 (8% O_2^{gp} with 1.67 μCi/ml RPMI) mean doubling times . . . 135
4.30 Selected data from experiment 090608 (8% O_2^{gp} with 1.67 μCi/ml RPMI) . . . 138
4.31 Experiment 090622 (8% O_2^{gp} with 0.735 μCi/ml RPMI) events 140
4.32 Cellular respiration in experiment 090622 (8% O_2^{gp} with 0.735 μCi/ml RPMI) . . . 143
4.33 Experiment 090622 (8% O_2^{gp} with 0.735 μCi/ml RPMI) mean doubling times . . . 143
4.34 Selected data from experiment 090622 (8% O_2^{gp} with 0.735 μCi/ml RPMI) . . . 146
4.36 POC data from all experiments. Stab.phase, at which a slope change is seen, floor POC level. Data is taken from tables 4.18, 4.22, 4.26, 4.30 and 4.34. . . . 153

5.1 Comparison of activities and dose-rate . . . 168
5.2 Comparison of the S values . . . 169
5.3 Correlation between cell placement and cell count . . . 177

D.1 Experiment 081103: Cell countings . . . 239
D.2 Experiment 081118: Cell countings . . . 240
D.3 Experiment 081212: Cell countings . . . 240
D.4 Experiment 090608: Cell countings . . . 241
D.5 Experiment 090622: Cell countings . . . 241

F.1 S values . . . 246

H.1 Chemical list . . . 250

List of Figures

1.1 Clonal evolution 2

2.1 Impact parameters a and b 9
2.2 Electron stopping power 11
2.3 Simplified cell model 15
2.4 Energy transport scenarios within cell 16
2.5 Cell cycle 18
2.6 The DNA double helix 23
2.7 Perre Curie 24
2.8 Cellular repair processes 27
2.9 Cell survival curve 31
2.10 LET survival plots 32
2.11 Indirect and direct effect 33
2.12 Sensitivity in the cell cycle 35
2.13 The oxygen effect 38
2.14 OER 38
2.15 Dose-rate effect 39
2.16 Dose-rate effects 41
2.17 Fractionated irradiation 41
2.18 RBE 43
2.19 Cellular hypoxia 44
2.20 Hypoxia induced changes in cellular processes 46

3.1 Cell flask 52
3.2 Cell measurement 55
3.3 Bürker chamber 56
3.4 Oxygen profile 63
3.5 Difference in local environment of the probe tip 64
3.6 Sensor tip of the oxygen probe 64
3.7 The motor controller 65
3.8 The oxygen probe and micromanipulator 66
3.9 The hypoxia cabinet 67

3.10 The set-up of the micromanipulator, probe and cell flask . . 68
3.11 Drift in time 69
3.12 Experiment example 74

4.1 Cell size histogram 82
4.2 Cellular activity 84
4.3 Experiment 081103 (12% O_2^{gp}), time 0-93 96
4.4 Experiment 081103 (12% O_2^{gp}), time 94-192 97
4.5 Experiment 081103 (12% O_2^{gp}), time 193-239 98
4.6 Experiment 081103 (12% O_2^{gp}), time 239-358 99
4.7 Experiment 081118 (8% O_2^{gp}), time 0-70 109
4.8 Experiment 081118 (8% O_2^{gp}), time 70-149 110
4.9 Experiment 081118 (8% O_2^{gp}), time 149-241 111
4.10 Experiment 081118 (8% O_2^{gp}), time 242-313 112
4.11 Experiment 081118 (8% O_2^{gp}), time 314-410 113
4.12 Experiment 081118 (8% O_2^{gp}), time 410-482 114
4.13 Experiment 081118 (8% O_2^{gp}), time 482-573 115
4.14 Experiment 081212 (6% O_2^{gp}), time 0-98 125
4.15 Experiment 081212 (6% O_2^{gp}), time 98-239 126
4.16 090608 (8% O_2^{gp} with ^3H), time 0-45 132
4.17 090608 (8% O_2^{gp} with ^3H), time 45-213 133
4.18 090608 (8% O_2^{gp} with ^3H), time 213-332 134
4.19 090622 (8% O_2^{gp} with ^3H), time 0-44 141
4.20 090622 (8% O_2^{gp} with ^3H), time 44-161 142
4.21 081020 (8 10% O_2^{gp}), time 0-91 148
4.25 Cellular surviving fraction 156
4.26 Scintillation sample time effect 157

5.1 Cell count error plot 161
5.2 LET as function of rad. energy 164
5.3 The survival curve for T-47D 170
5.4 Cellular respiration versus POCs. 183
5.5 Respiration vs cell number 185

B.1 Respiration vs cell number (exp. 081103.1) 219
B.2 Respiration vs cell number (exp. 081103.2) 219
B.3 Respiration vs cell number (exp. 081103.3) 220
B.4 Respiration vs cell number (exp. 081118.1) 220
B.5 Respiration vs cell number (exp. 081118.2) 220
B.6 Respiration vs cell number (exp. 081118.3) 221
B.7 Respiration vs cell number (exp. 081118.4) 221
B.8 Respiration vs cell number (exp. 081118.5) 221

B.9 Respiration vs cell number (exp. 081118.6) 222
B.10 Respiration vs cell number (exp. 081118.7) 222
B.11 Respiration vs cell number (exp. 081212.1) 222
B.12 Respiration vs cell number (exp. 081212.2) 223
B.13 Respiration vs cell number (exp. 090608.1) 223
B.14 Respiration vs cell number (exp. 090608.2) 223
B.15 Respiration vs cell number (exp. 090608.3) 224
B.16 Respiration vs cell number (exp. 090622.1) 224
B.17 Respiration vs cell number (exp. 090622.2) 224

Bibliography

G. Acs, M. Chen, X. W. Xu, P. Acs, A. Verma, and C. J. Koch. Autocrine erythropoietin signaling inhibits hypoxia-induced apoptosis in human breast carcinoma cells. *Cancer Letters*, 214:243–251, 2004.

B. Alberts, A. Johnson, J. Lewis, M. Raff, K. Roberts, and P. Walter. *Molecular biology of the cell*. Garland Scence, Taylor & Francis Group, 5. edition, 2008.

M. Ashcroft, Y. Taya, and K. H. Vousden. Stress signals utilize multiple pathways to stabilize p53. *Molecular and Cellular Biology*, 20:3224–3233, 2000.

F. H. Attix. *Introducion to Radiological Physics and Radiation Dosimetry*. Wiley-VCH Verlag GmbH & Co, 2004.

H. Bando, M. Toi, K. Kitada, and M. Koike. Genes commonly upregulated by hypoxia in human breast cancer cells mcf-7 and mda-mb-231. *Biomedicine & Pharmacotherapy*, 57:333–340, 2003.

W. Beneson, J. W. Harris, H. Stocker, and H. Lutz, editors. *Handbook of Pysics*. Springer Science+Business Media, 2006.

R. S. Bindra, P. J. Schaffer, A. Meng, J. Woo, K. Maseide, M. E. Roth, P. Lizardi, D. W. Hedley, R. G. Bristow, and P. M. Glazer. Down-regulation of rad51 and decreased homologous recombination in hypoxic cancer cells. *Molecular and Cellular Biology*, 24:8504–8518, 2004.

I. Bjørhovde. Undersøkingar av celler sin respons på intern bestråling med lågenergetiske elektron ved ultralåge doseratar. Master's thesis, Universitetet i Oslo, 2006.

M. L. Boas. *Mathematical Methods in the Physical Science*. John Wiley & Sons Inc., 2006.

S. C. Brooks, E. R. Locke, and H. D. Soule. Estrogen receptor in a human cell line (mcf-7) from breast carcinoma. *The Journal of Biological Chemistry*, 248:6251–6253, 1973.

K. H. Chadwick and H. P. Leenhouts. A molecular theory of cell survuval. *Physics in Medicine and Biology*, 18(1):78–87, 1973.

N. S. Chandel, M. G. VanderHeiden, C. B. Thompson, and P. T. Schumacker. Redox regulation of p53 during hypoxia. *Oncogene*, 19:3840–3848, 2000.

J. D. Chapman. Single-hit mechanicm of tumor cell killing by radiation. *International Journal for Radiation Biology*, 79(2):71–81, 2003.

J. Chen. Radiation quality of tritium. *Radiation Protection Dosimetry*, 122: 546–548, 2006.

E. P. Cummins and C. T. Taylor. Hypoxia-responsive transcription factors. *Pflügers Archiv European Journal of Physiology*, 450:363–371, 2005.

J. M. Davis, editor. *Basic Cell Culture*. Oxford University Press Inc., 2. edition, 1996.

H. Dertinger and H. Jung. *Molecular Radiation Biology: The Action of Ionizing Radiation on Elementary Biological Objects*. English Unicersities Press, London, 1970.

T. L. DeWeese, J. C. Walsh, L. E. Dillehay, T. D. Kessis, L. Hedrick, K. R. Cho, and W. G. Nelson. Human papillomavirus e6 and e7 oncoproteins alter cell cycle progession but not radiosensitivity of carcinoma cells treated wth low-dose-rate radiation. *International Journal for Radiation Oncology • Biology • Physics*, 37:145–154, 1997.

M. W. Dewhirst, H. Kimura, S. W. E. Rehmus, R. D. Braun, D. Papahadjopoulos, K. Hong, and T. W. Secomb. Microvascular studies on the origins of perfusion-limited hypoxia. *British Journal of Cancer*, 74:247–251, 1996.

H. Dworschak. *Safety in Tritium Handling Technology*. Kluwer Academic Publishers, 1993.

F. Essmann, I. H. Engels, G. Totzke, K. Schulze-Osthoff, and R. U. Jänicke. Apoptosis resistance of mcf-7 breast carcinoma cells to ionizing radiation is independent of p53 and cell cycle control but caused by the lack of caspase-3 and a caffeine-inhibitable event. *Cancer Research*, 64:7065–7072, 2004.

S. J. Fan, M. L. Smith, D. J. Rivet, D. Duba, Q. M. Zhan, K. W. Kohn, A. J. Fornance, and P. M. O'Connor. Disruption of p53 function sensitizes breast-cancer mcf-7 cells to cisplatin and pentoxifylline. *Cancer Research*, 55:1649–1654, 1995.

L. E. Feinenegen. *Tritium-Labeled Molecules in Biology and Medicine*. Academic Press Inc., New York, 1967.

L. Formigli, S. Z. Orlandini, S. Capaccioli, M. F. Pupon, and D. Bani. Energy-dependent types of cell death in mcf-7 breast cancer cell tumors implanted into nude mice. *Cells Tissues Organs*, 170:99–110, 2002.

G. Froese. The respiration of ascites tumor cells at low oxygen concentrations. *Biochimica Et Biophysica Acta*, 57:509–519, 1961.

S. M. Goddu, R. W. Howell, and D. V. Rao. Cellular dosimetry: Absorbed fractions for monoenergetic electron and alpha paricle sources and s-values for radionuclides uniformly distributed in different cell compartments. *The Journal of Nuclear Medicine*, 35(2):303–316, 1994.

S. M. Goddu, R. W. Howell, L. G. Bouchet, W. E. Bolch, and D. V. Rao. *MIRD cellular S-values: Self-absorbed dose per unit accumulated activity for selected radionuclides and monoenergetic electron and alpha particle emitters incorporated into different cell compartments*. Society of Nuclear Medicine, Reston, 1997.

D. Guirado, M. Aranda, M. Vilche, M. Villalobos, and A. M. Lallena. Dose dependence of the growth rate of multicellular tumor spheroids after irradiation. *The British Journal of Radiology*, 76:19–116, 2003.

M. Guppy, S. Brunner, and M. Buchanan. Metabolic depression: a response of cancer cells to hypoxia? *Comperative Biochemistry and Physiology B-Biochemistry & Molecular Biology*, 140:233–239, 2005.

J. Hain, E. M. Weller, T. Jung, and W. Burkart. Effects of ionizing - and uv-b-radiation on proteins controlling cell cycle progression in human cells: Comparison of the mcf-7 adenocarcinoma and the scl-2 squamos cel carcinoma cell line. *International Journal for Radiation Biology*, 70(3): 261–271, 1996.

E. J. Hall and A. J. Giaccia. *Radiobiology for the Radiologist*. Lippincott Williams & Wilkins, sixth edition edition, 2006.

M. Hockel and P. Vaupel. Tumor hypoxia: Definitions and current clinical, biologic, and molecular aspects. *Journal of the National Cancer Institute*, 93:266–276, 2001.

K. B. Horwitz, M. E. Costlow, and W. L. McGuire. Mcf-7: a human breast cancer cell line with estrogen, androgen, progesterone and glucocorticoid receptors. *Steroids*, 26:785–795, 1975.

S. Kizaka-Kondoh, S. Tanaka, and H. Harada nd M. Hiraoka. The hif-1 active microenvironment: An environmental target for cancer therapy. *Advanced Drug Delivery Reviews*, 61:623–632, 2009.

M. Koritzinsky, B. G. Wouters, O. Amellem, and E. O. Pettersen. Cell cycle progression and radiation survival following prolonged hypoxia and re-oxygenation. *International Journal of Radiation Biology*, 77:319–328, 2001.

Kreftforeningen. Hva er kreft, accessed on 09/2009, 2009. URL `http://www.kreftforeningen.no/`.

B. Kumar, J. Joshi, A. Kumar, B. N. Pandey, B. Hazra, and K. P. Mishra. Radiosensitization by dispyrin diethylether in mcf-7 breast canrcinoma cell line. *Molecular cell biochemistry*, 304:287–296, 2007.

J. Kurebayashi, T. Otsuki, T. Moriya, and H. Sonoo. Hypoxia reduces hormone responsiveness of human breast cancer cells. *Japanese Journal of Cancer Research*, 92:1093–1101, 2001.

M. Lacroix, R. Toillon, and G. Leclercq. p53 and breast cancer, an update. *Endocrine-Related Cancer*, 13:293–325, 2006.

A. S. Levenson and V. C. Jordan. Mcf-7: The first hormone-responsive breast cancer cell line. *Cancer Research*, 57:3071–3078, 1997.

D.-L. Lin and C. Chang. p53 is a mediator for radiation-repressed human tr2 orphan receptor expression in mcf-7 cells, a new pathway from tumor suppessor to member of the steroid receptor superfamily. *The Journal of Biological Chemistry*, 271:14649–14652, 1996.

G. Liu, K. Shen, Z. Shao, and Z. Shen. Hypoxia induces down-regulation of estrogen receptor alpha in human breast cancer. *Zhonghua Zhongliu Zazhi*, 26:664–668, 2004.

A. Maity, W. Sall, C. J. Koch, and P. R. Oprysko andS. M. Evans. Low po(2) and beta-estradiol induce vegf in mcf-7 and mcf-7-5c cells: Relationship to in vivo hypoxia. *Breast Cancer Research and Treatment*, 67:51–60, 2001.

P. Mayles, A. Nahum, and J.C. Rosenwald, editors. *Handbook of Radiotherapy Physics*. Taylor & Francis, 2007.

O. Åmellem, T. Stokke, J. A. Sandvik, L. Smedshammer, and E. O. Pettersen. Hypoxia-induced apoptosis in human cells with normal p53 status and function, without any alteration in the nuclear protein level. *Experimental Cell Research*, 232:361–370, 1997.

V. V. Moiseenko, R. N.Hamm, A. J. Waker, and W. V. Prestwich. Modelling dna damage induced by different energy photons and tritium beta-particles. *International Journal for Radiation Biology*, 74:533–550, 1998.

V. V. Moiseenko, A. J. Waker, R. N. Hamm, and W. V. Prestwich. Calculation of radiation-induced dna damage from photons and tritium beta-particles. *Radiation Enviromental Biophysics*, 40:33–38, 2001.

D. G. Nagle and Y. D. Zhou. Marine natural products as inhibitors of hypoxic signaling in tumors. *Phytochemistry reviews*, 8:415–429, 2009.

E. O. Pettersen. *Cellulær Radiobiologi*. Universitetet i Oslo, 2007. Compendium in FYS4720, Personal communication.

E. O. Pettersen and H. Wang. Radiation-modifying effect of oxygen in synchronized cells pre-treated with acute or prolonged hypoxia. *International Journal of Radiation Biology*, 70:319–326, 1996.

E. O. Pettersen, L. H. Larsen, N. B. Ramsing, and P. Ebbesen. Pericellular oxygen depletion during ordinary tissue culturing, measured with oxygen micrometers. *Cell Proliferation*, 38:257–267, 2005.

E. O. Pettersen, I. Bjørhovde, Å. Søvik, N. F. J. Edin, V. Zachar, E. O. Hole, J. A. Sandvik, and P. Ebbesen. Response of chronic hypoxic cells to low dose-rate irridation. *International Journal for Radiation Biology*, 83(5): 331–345, May 2007.

E. B. Podgorsak, editor. *Radiation Oncology Physics: A Handbook for Teachers and Students*. International Atomic Energy Agency, 2005.

H. Probst, H. Schiffer, V. Gekeler, H. Kienzle-Pfeilsticker, U. Stropp, K. Stöter, and I. Frenzel-Stöter. Oxygen dependent regulation of dna synthesis and growth of ehrlich ascits tumor cells *in Vitro* and *in Vivo*. *Cancer Research*, 48:2053–2060, 1988.

K. Renner and E. Gnaiger. Course on high-resolution respirometry: High-resolution respirometry with leukemia cells: Routine respiration, respiratory control and coupling. *Oroboros Instrumental: Mithocontrial Physiology Network*, 2003. URL `www.oroboros.at`.

R. E. Rowberg. *The Department of Energy's Tritium Production Program*. Congressional Research Service, 2001.

Ruskinn. accessed on 09/2009, 2009. URL `http://www.ruskinn.com/`.

A. M. Scherbakov, Y. S Lebanova, V. A. Shatskaya, and M A. Krasil'nikov. The breast cancer cells response to chronic hypoxia involves the opposite regulation of nf-kb and estrogen receptor signaling. *Steroids*, 74:535–542, 2009.

G. Schwartz, R. Berg, and C. Botstein. Changes in the relatice biological effectiveness of a 35 mev electron beam as a function of tissue depth. *American Journal of Roentgenology*, 97:1049–1052, 1966.

J. Seim, P. Graff, Ø. Åmellem, K. S. Landsverk, T. Stokke, and E. O. Pettersen. Hypoxia-induced irreversible s-phase arrest involves down-regulation of cyclin a. *Cell Proliferation*, 36:321–332, 2003.

G. Storhaug. Undersøkelse av kronisk hypoksiske cellers respons på lavdoseratebestråling. Master's thesis, Universitetet i Oslo, 2008.

T. Straume and A. Carsten. Tritium radiobiology and relative biological effectiveness. *Health Physics*, 65:657–672, 1993.

Å. Søvik. Lavdoseratebestråling av humane celler i kultur, dosimetri og effektmålinger. Master's thesis, Universitetet i Oslo, 2002.

Unisense. Freeware macros and spreadsheet for data-analysis, accessed on 06/2009, 2009. URL `http://www.unisense.com/`.

J. R. Williams, Y. Zhang, H. Zhou, D. S. Gridley, C. J. Koch, J. M. Slater, and J. B. Little. Overview of radiosensitivity of human tumor cells to low-dose-rate irradiation. *International Journal for Radiation Oncology • Biology • Physics*, 72(3):909–917, 2008.

S. M. Wuerzberger, J. J. Pink, S. M. Planchon, K. L. Byers, W. G. Bornmann, and D. A. Boothman. Induction of apoptosis in mcf-7:ws8 breast cancer cells by β-lapachone. *Cancer Research*, 58:1876–1885, 1998.

J. M. Yi, H. Y. Kwon, J. Y. Cho, and Y. J. Lee. Estrogen and hypoxia regulate estrogen receptor alpha in a synergetic manner. *Biochemical and Biophysical Research Communications*, 378:842–846, 2009.

Y. H. Young, E. J. Lim, M. Y. Lee, J. H. Parka, S. K. Ye, E. U. Park, S. Y. Kim, Z. Zhang, K. J. Lee, D K. Park, T. Park, W. K. Moon, and M. Y. Young. Hypoxia activates the cyclin d1 promotor wia the jak1/stat5b pathway

in breast cancer cells. *Experimental and Molecular Medicine*, 37:353–364, 2005.

Y. Zhao, X. Chen, and J. Du. Cellular adaptation to hypoxia and p53 transcription regulation. *Journal of Zhejiang University*, 10:404–410, 2009.

F. Zölzer and C. Streffer. Increased radiosensitivity with chronic hypoxia in four human tumor cell lines. *International Journal for Radiation Oncology • Biology • Physics*, 54(3):910–920, 2002.

Appendix A

The program used to read, analyze and plot the data

The following program is written in Matlab R2007b 7.5.0.342 (MathWorks Inc.), and was executed on a Windows computer.

```
%%%%%%%%%%%%%%%%%%%%%%%%%%%%%%%%%%
% Oxygen profile analysis software %
%%%%%%%%%%%%%%%%%%%%%%%%%%%%%%%%%%

clear;

data = xlsread('081118','Profiles','B:D');
%B:D is sensor 1, F:H is sensor 2

eksperiment = char('081118');
o2pst =char('8');
font_size = 14;          %Font size in plots
r = 41;                  %Measuring points in each profile
delay = 1340.6;          %Inter profile time
N = 1;                   %Plot each N'th profile
interv=1;                %Which interval to be plotted
                          (1 = full experiment)

%Intervals
I = [0 10000             %Full experiment
    0 70.01              %Interval 2
    70.83 149            %Interval 3
    149.3 241.3          %Interval 4
    241.7 313.6          %Interval 5
```

```
    313.9 409.6         %Interval 6
    410   481.5         %Interval 7
    481.9 10000         %Interval 8
    ];

t_start = I(interv,1);  %start reading here
t_stop = I(interv,2);   %stop reading here (latest)

%Heigth plotting:
top_value = 1900;       %Gass phase
middle_value = 200;     %Middle measurement
bottom_value = 0;       %Cell level/flask floor

%Plot few single profiles:
profile_number = 1;
t_plot=[15];            %At times (h)

%Plot and determine slope:
med_lvl = 800;          %Upper limit
cell_lvl = 400;         %Lower limit

%Margins in Unisense file:
t_top = 0;              %Empty on top
t_middle = 1;           %Empty between profiles
t_last = 0;             %Empty at end

%Medium level detection:
threshold = 10          %Threshold level, signal (mV)

%Calibration:
x = [380.7856 5.535 380.7856 5.535]'; %Input signal (mV)
t = [0 0 555 555]';     %Input time (h)
y = [8 0 8 0 ]';        %Output concentration (%O2)
V = [x.*t x t ones(size(x))]; %Vandermonde matrix
c = V^-1 * y;           %Constants

%Profile calculation:
M=size(data,1);         %Total lines in the data vector
P = (M+1-t_top-t_last)/(r+t_middle); %Number of profiles
%Creating the work vector profile_data
for i=1:P
```

```
  for j=1:r
    i_d = i-1;
    j_d = j;
    profile_data(i_d*(r) + j_d,1) =
      -data(i_d*(r+t_middle)+j_d+t_top,1);
    profile_data(i_d*(r) + j_d,2) =
      data(i_d*(r+t_middle)+j_d+t_top,3);
    profile_data(i_d*(r) + j_d,3) =
      delay*(i-1)/(60*60);
  end
end

%Shortens t_stop if necessary:
if t_stop > max(profile_data(:,3))
    t_stop = max(profile_data(:,3));
end

%Cell counting (time:cell count:standard error):
Cells = [0      5.59e5      0.669e5
        17.87    9.19e5      0.574e5
        70.01   3.77e6      9.89e4
        70.83   3.77e6/4    0
        149     3.371e6     9.488e4
        149.3   8.120e5     0
        169.1   9.10e5      0.47e5
        190.3   1.29e6      0.98e5
        241.3   4.59e6      3.18e5
        241.7   9.15e5      4.0e4
        313.6   3.94e6      1.09e5
        313.9   5.53e5      1.55e4
        358.2   1.35e6      20551
        385.8   3.06e6      168772
        409.6   5.27e6      413672
        410     8.12e5      32034
        412.75  8.35e5      0
        453.75  1.679e6     3.945e4
        481.5   2.967e6     1.971e5
        481.9   9.278e5     3.942e4
        501.2   1.307e6     4.075e4
        528     2.077e6     4.222e4
        549.25  3.312e6     1.341e5
```

```
        573.75  4.807e6     2.069e5
        ];

t_C = Cells(:,1);
C   = Cells(:,2);
C_se= Cells(:,3);

%Fitting an linear interpolation between log-values:
C_log = log(C);
fit_exp = fit(t_C,C_log,'linearinterp')
%(The real exponential fits are then e^(fit_exp))

%Calculating doubling times:
t2s = log(2)./fit_exp.p.coefs(:,1);

%Plotting cell countings with errorbar plot:
t = [0:0.1:max(profile_data(:,3))];
errorbar(t_C,C,C_se,'.')
hold on

%Plotting interpolation:
plot(t,exp(fit_exp(t)),'r')
for n=1:length(t_C)-1
    if t2s(n)>0
        text(t_C(n)+3,C(n),num2str(t2s(n)))
    end
end
axis([t_start-1 t_stop+1 0 max(C)])
axis auto(y)
xlabel('Time after experiment start (h)','fontsize',font_size)
ylabel('Total cells in flask','fontsize',font_size)
figure

%Truncating profile_data according to t_start og t_stop:
m=1;
for i=1:(P*r)
    if profile_data(i,3) >= t_start
        if profile_data(i,3) <= t_stop
                profile_data_trunc(m,1) = profile_data(i,1);
                profile_data_trunc(m,2) = profile_data(i,2);
                profile_data_trunc(m,3) = profile_data(i,3);
```

```
                m=m+1;
        end
    end
end

m=1
for i=1:length(t_C)
    if t_C(i) >= t_start
        if t_C(i) <= t_stop
                t_C_trunc(m)=t_C(i);
                m=m+1
        end
    end
end

%Resetting profile_data to the truncated vector:
profile_data = profile_data_trunc;
t_C = t_C_trunc
P = length(profile_data)/r;

%O2 consentration calculation:
profile_data(:,4) = c(1) .* profile_data(:,2) .*
                      profile_data(:,3)
                    + c(2).* profile_data(:,2)
                    + c(3).* profile_data(:,3)
                    + c(4);

%Profile_data now contains four columns:
%1: Depth (um)
%2: Signal (mV)
%3: Time (h)
%4: Oxygen concentration (%O2)

time = (0:delay:delay*(P-1));    %time axis (s)
time_h = time/(60*60);           %time axis (h)

%Medium level detection:
n=1;
last_time = 0;
for k=1:(length(profile_data)-1)
  if abs(profile_data(k,2)-profile_data(k+1,2)) >= threshold
```

```
    if profile_data(k,1) > 0
      if last_time ~= profile_data(k,3)
        last_time = profile_data(k,3);
        med_niv(n,1) = profile_data(k,1);
        med_niv(n,2) = profile_data(k,3);
        n=n+1;
      end
    end
  end
end

%Medium level plotting:
plot(med_niv(:,2),med_niv(:,1))
xlabel('Time (h)','fontsize',font_size)
ylabel('Medium height above flask bottom ({\mu}m)',
       'fontsize',font_size)
axis([min(med_niv(:,2)) max(med_niv(:,2)) 0 2000])
figure

%Signal profile plotting:
n=1;
for k=1:P
if n==N
plot(profile_data(r*(k-1)+1:r*(k),2),
         profile_data(r*(k-1)+1:r*(k),1),'-r')
hold on
    n=1;
  else
    n=n+1;
  end
end
xlabel('Signal (mV)','fontsize',font_size)
ylabel('Depth above flask bottom (um)','fontsize',font_size)
hold off
figure

%2D-plot:
n=1;
for k=1:P
    if n==N
        plot(profile_data(r*(k-1)+1:r*(k),4),
```

```
          profile_data(r*(k-1)+1:r*(k),1),'-k')
        hold on
        n=1;
    else
        n=n+1;
    end
end
xlabel('Compensated oxygen concentration (%)',
       'fontsize',font_size)
ylabel('Height above flask bottom','fontsize',font_size)
hold off
figure

%3D-plot:
n=1;
for k=1:P
if n==N
plot3(profile_data(r*(k-1)+1:r*(k),4),
profile_data(r*(k-1)+1:r*(k),3),
profile_data(r*(k-1)+1:r*(k),1),'-k')
    hold on
    n=1;
  else
    n=n+1;
  end
end
xlabel('Calibrated oxygen concentration (%)',
       'fontsize',font_size)
ylabel('Time after experiment start (h)','fontsize',font_size)
zlabel('Height above flask bottom','fontsize',font_size)
hold off
figure

%Gas phase and POC plot:
x=1;
for k=1:(P*r)
    if profile_data(k,1) == top_value
        top_vektor(x,1) = profile_data(k,3);
        top_vektor(x,2) = profile_data(k,2);
        top_vektor(x,3) = profile_data(k,4);
        x=x+1;
```

```
    end
end
x=1;
for k=1:P*r
    if profile_data(k,1) == middle_value
        middle_vektor(x,1) = profile_data(k,3);
        middle_vektor(x,2) = profile_data(k,2);
        middle_vektor(x,3) = profile_data(k,4);
        x=x+1;
    end
end
x=1;
for k=1:P*r
    if profile_data(k,1) == bottom_value
        bottom_vektor(x,1) = profile_data(k,3);
        bottom_vektor(x,2) = profile_data(k,2);
        bottom_vektor(x,3) = profile_data(k,4);
        x=x+1;
    end
end

%Top value and POC plotting:
plot(top_vektor(:,1),top_vektor(:,3),':')
hold on
plot(bottom_vektor(:,1),bottom_vektor(:,3),'-')
xlabel('Time after experiment start (h)','fontsize',font_size)
ylabel('Oxygen concentration (% O_2)','fontsize',font_size)
legend(['Height ', num2str(top_value),' {\mu}m'],
       ['Height ', num2str(bottom_value),' {\mu}m'])
figure

%Plot of oxygen difference:
plot(top_vektor(:,1),top_vektor(:,3)-bottom_vektor(:,3),'.-k')
xlabel('Time after experiment start (h)',
       'fontsize',font_size)
ylabel('Difference in oxygen concentration (% O_2)',
       'fontsize',font_size)
figure


%plot of correction factors:
```

```
x=(0:1:1000);
t=t_start;
O = c(1).*x*t + c(2).* x + c(3)*t + c(4);
t=t_stop;
O_mrk = c(1).*x*t + c(2).* x + c(3)*t + c(4);
plot(x,O,'r')
hold on
plot(x,O_mrk,'k')
xlabel('Input value (mV)','fontsize',font_size)
ylabel('Output value (% O_2)','fontsize',font_size)
legend(['Experiment start (t=', num2str(t_start), ')'],...
['Re-calibration (t=', num2str(t_stop), ')'])
hold off
figure

%Few single profiles plot:
for f=1:profile_number
    plotplot = 0;
    for k=1:P
        if profile_data(r*(k-1)+1,3) >= t_plot(f)
            if plotplot == 0
                plot(profile_data(r*(k-1)+1:r*(k),4),
                     profile_data(r*(k-1)+1:r*(k),1),
                     '-k')
                plotplot = 1;
                hold on
            end
        end
    end
end
xlabel('Oxygen concentration (%)','fontsize',font_size)
ylabel('Height above flask bottom ({\mu}m)',
       'fontsize',font_size)
figure

%The fitting and plotting of the oxygen gradient:
r0 = (med_lvl-cell_lvl)/(profile_data(1,1)
      -profile_data(2,1)) + 1;

%Vector shaving:
j=1;
```

```
for i=1:length(profile_data)
    if profile_data(i,1) <= med_lvl
        if profile_data(i,1) >= cell_lvl
            profile_data_shaved(j,:) = profile_data(i,:);
            j=j+1;
        end
    end
end


%Special profile plot:
n=1;
g=1;
subplot(1,2,1)
for k=1:P
    if n==N
        plot(profile_data(r*(k-1)+1:r*(k),4),
        profile_data(r*(k-1)+1:r*(k),1),'-k')
        hold on
        n=1;
    else
        n=n+1;
    end
end
hold off
xlabel('Compensated oxygen concentration (%)',
       'fontsize',font_size)
ylabel('Height above flask bottom','fontsize',font_size)
subplot(1,2,2)

%Slope calculation:
for k=1:P
    if n==N
        plot(profile_data_shaved(r0*(k-1)+1:r0*(k),4),
             profile_data_shaved(r0*(k-1)+1:r0*(k),1),
             '-k')
        fitted = fit(profile_data_shaved(r0*(k-1)+1:r0*(k),4),
            profile_data_shaved(r0*(k-1)+1:r0*(k),1),'poly1');
        stign_tall(g,1)=1 / fitted.p1;
        stign_tall(g,2)=profile_data_shaved(r0*(k-1)+1,3);
        g=g+1;
```

```
        hold on
        n=1;
    else
        n=n+1;
    end
end

title(['dc/cx mean = ', num2str(mean(stign_tall(:,1))),
       ' \pm ', num2str(std(stign_tall(:,1))/
       sqrt(length(stign_tall(:,1))))]);
xlabel('Compensated oxygen concentration (%)',
       'fontsize',font_size)
ylabel('Height above flask bottom','fontsize',font_size)
hold off
figure
semilogy(stign_tall(:,2),stign_tall(:,1))
xlabel('Time after experiment start (h)','fontsize',font_size)
ylabel('O_2 gradient slope dc/dx ({%}O{_2}/{\mu}m)',
       'fontsize',font_size)

figure
resp = (stign_tall(:,1)*2.89e11) ./
       exp(fit_exp(stign_tall(:,2)));
flaskresp = stign_tall(:,1)*2.89e11;
plot(stign_tall(:,2),resp)
hold on
plot(t_C,0,'or')
axis([min(stign_tall(:,2)) max(stign_tall(:,2)) 0 1000])
axis auto(x)
xlabel('Time after experiment start (h)',
       'fontsize',font_size)
ylabel('Cellular respiration (fmol/cell h)',
       'fontsize',font_size)

%Flask respiration versus cell number plot:
figure
plot(exp(fit_exp(stign_tall(:,2))),flaskresp);
xlabel('Interpolated cell count','fontsize',font_size)
ylabel('Total respiration (fmol/flask h)',
       'fontsize',font_size)
```

Appendix B

Respiration versus cell number plots

In this appendix, the respiration of the cells are plotted against cell numner.

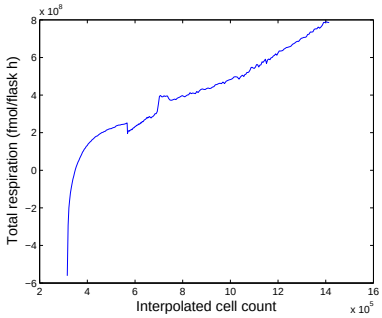

Figure B.1: *Cellular respiration plotted against cell number, from experiment 081103.1 (time interval 0-93 h).*

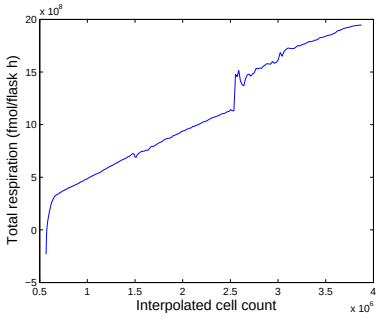

Figure B.2: *Cellular respiration plotted against cell number, from experiment 081103.2 (time interval 94-192 h).*

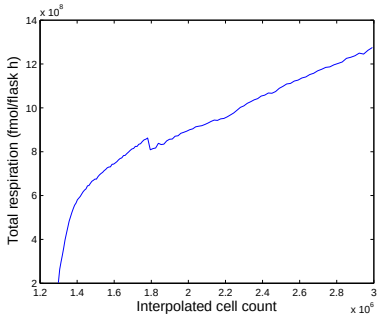

Figure B.3: *Cellular respiration plotted against cell number, from experiment 081103.3 (time interval 193-239 h).*

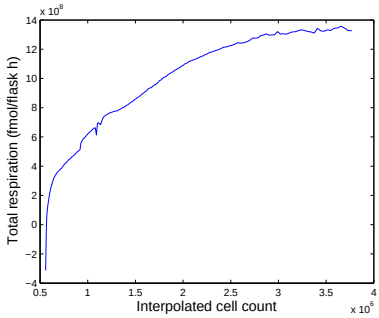

Figure B.4: *Cellular respiration plotted against cell number, from experiment 081118.1 (time interval 0-70 h).*

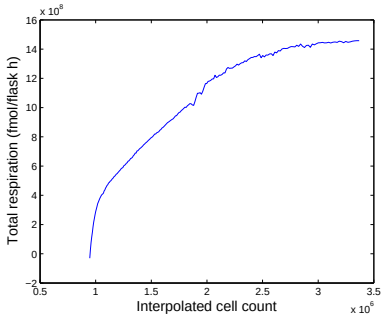

Figure B.5: *Cellular respiration plotted against cell number, from experiment 081118.2 (time interval 70-149 h).*

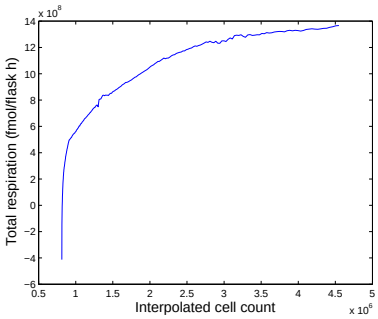

Figure B.6: *Cellular respiration plotted against cell number, from experiment 081118.3 (time interval 149-241 h).*

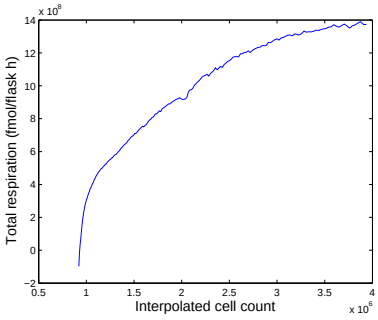

Figure B.7: *Cellular respiration plotted against cell number, from experiment 081118.4 (time interval 242-313 h).*

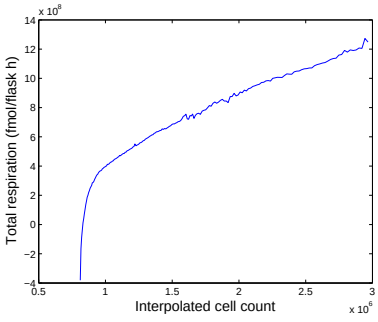

Figure B.8: *Cellular respiration plotted against cell number, from experiment 081118.5 (time interval 314-410 h).*

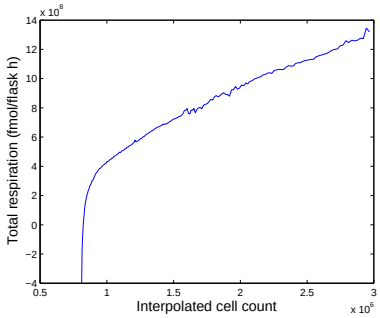

Figure B.9: *Cellular respiration plotted against cell number, from experiment 081118.6 (time interval 410-482 h).*

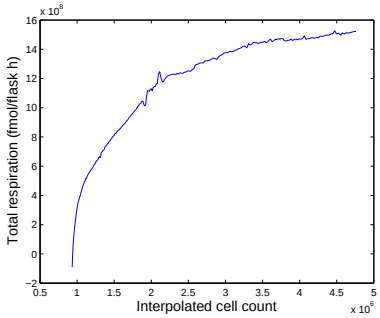

Figure B.10: *Cellular respiration plotted against cell number, from experiment 081118.7 (time interval 482-573 h).*

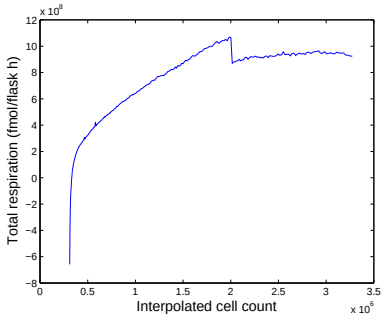

Figure B.11: *Cellular respiration plotted against cell number, from experiment 081212.1 (time interval 0-98 h).*

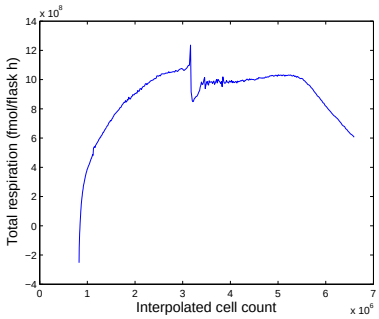

Figure B.12: *Cellular respiration plotted against cell number, from experiment 081212.2 (time interval 98-239 h).*

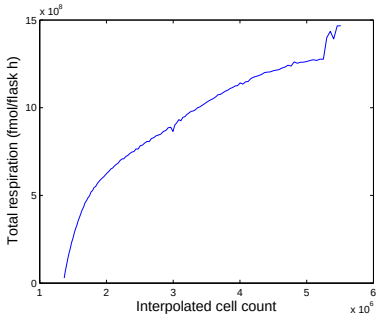

Figure B.13: *Cellular respiration plotted against cell number, from experiment 090608.1 (time interval 0-45 h).*

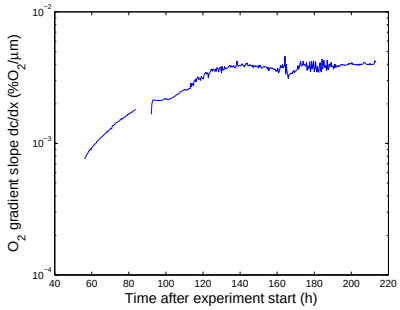

Figure B.14: *Cellular respiration plotted against cell number, from experiment 090608.2 (time interval 45-213 h).*

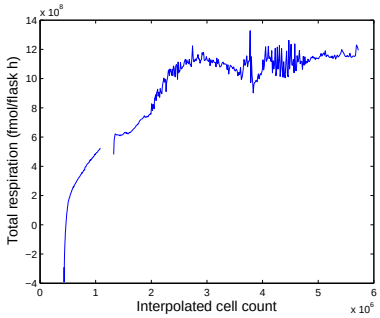

Figure B.15: *Cellular respiration plotted against cell number, from experiment 090608.3 (time interval 213-332 h).*

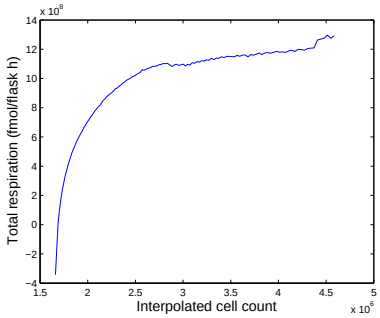

Figure B.16: *Cellular respiration plotted against cell number, from experiment 090622.1 (time interval 0-44 h).*

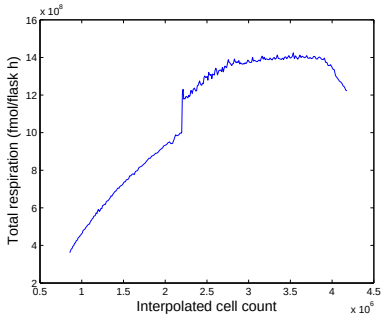

Figure B.17: *Cellular respiration plotted against cell number, from experiment 090622.2 (time interval 44-161 h).*

Appendix C

Cell pictures

In this appendix, pictures of the different stages of each main experiment is shown. At each time, three pictures was typically taken. Here is one of each.

Experiment 081103

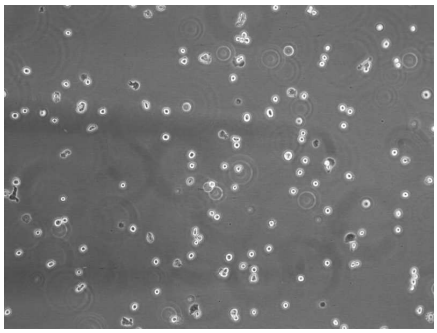

Experiment 081103 at time 0 h

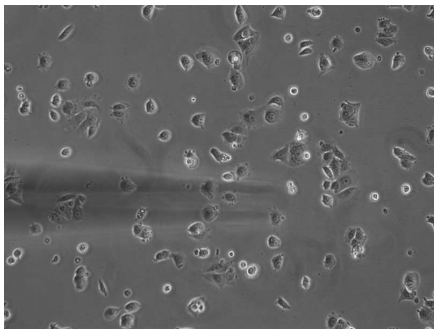

Experiment 081103 at time 21 h

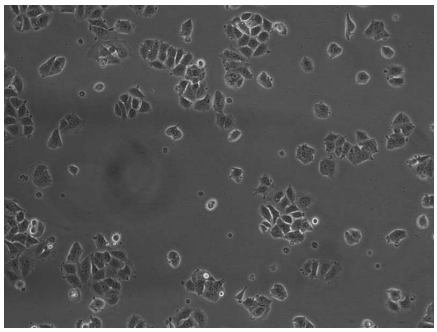

Experiment 081103 at time 42 h

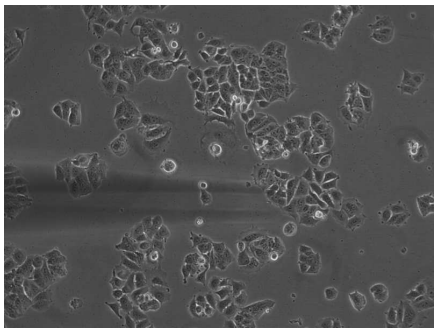

Experiment 081103 at time 67 h

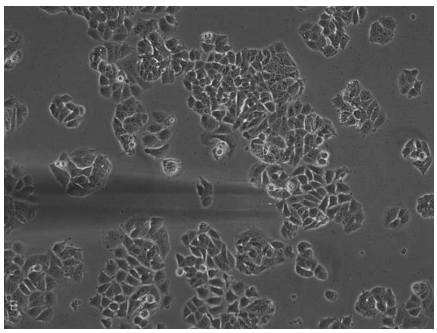

Experiment 081103 at time 93.66 h

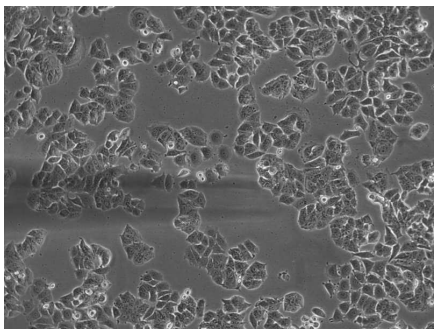

Experiment 081103 at time 166 h

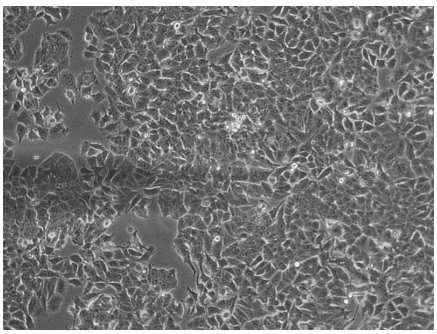

Experiment 081103 at time 192.5 h

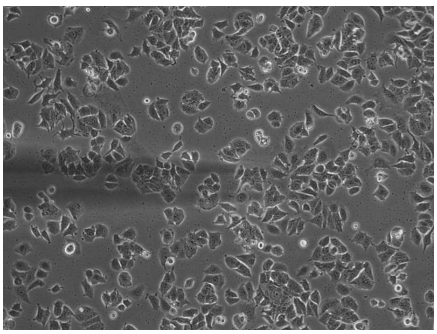

Experiment 081103 at time 211 h

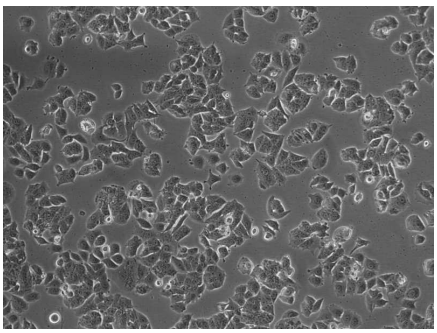

Experiment 081103 at time 238.9 h

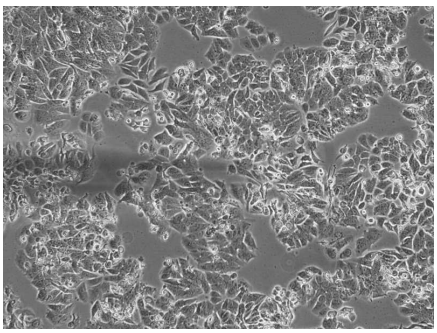

Experiment 081103 at time 359 h

Experiment 081118

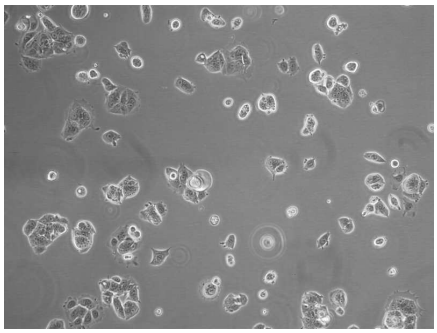

Experiment 081118 at time 0 h

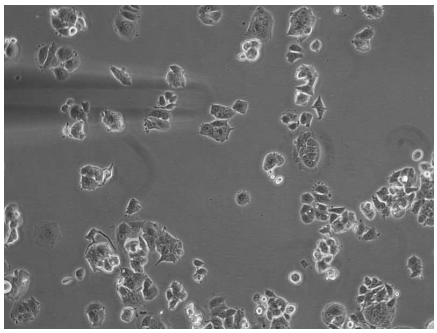

Experiment 081118 at time 17.87 h

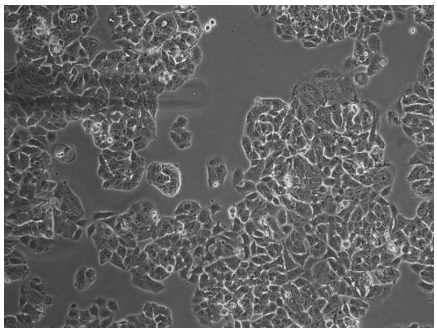

Experiment 081118 at time 70 h

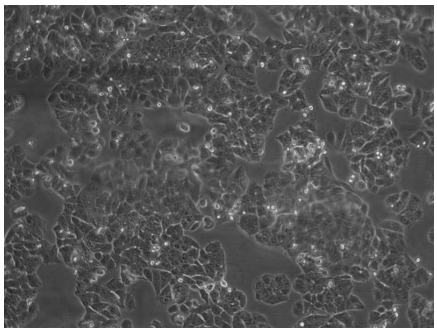

Experiment 081118 at time 149 h

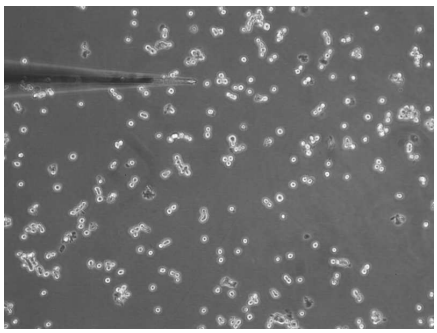

Experiment 081118 at time 149.3 h

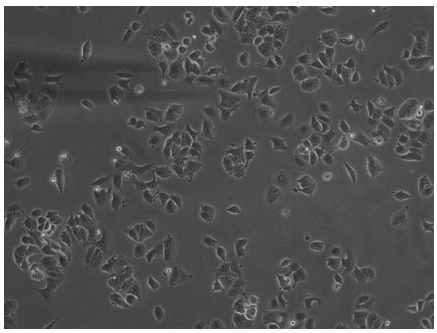

Experiment 081118 at time 169.1 h

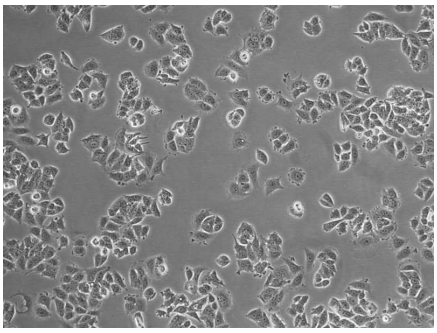

Experiment 081118 at time 190.3 h

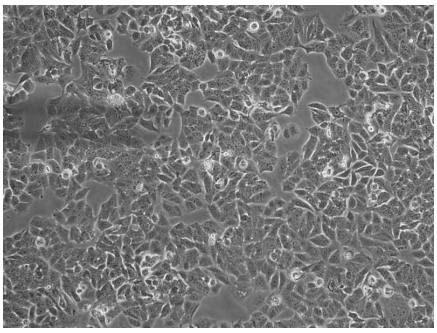

Experiment 081118 at time 241.3 h

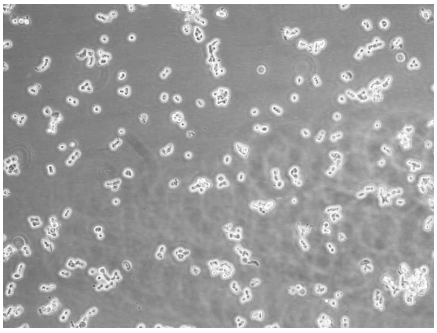

Experiment 081118 at time 241.7 h

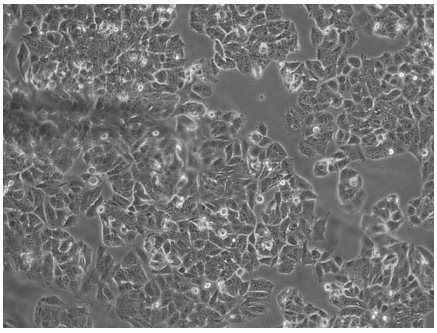

Experiment 081118 at time 313.6 h

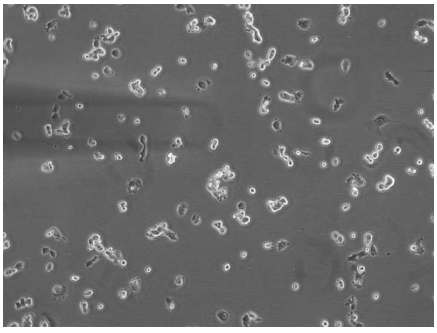

Experiment 081118 at time 313.9 h

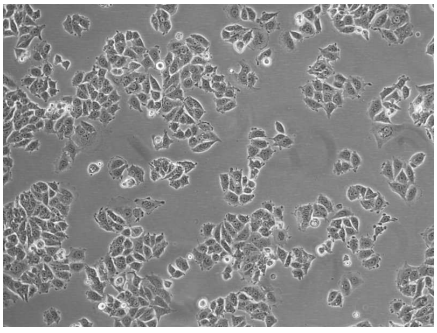

Experiment 081118 at time 358.2 h

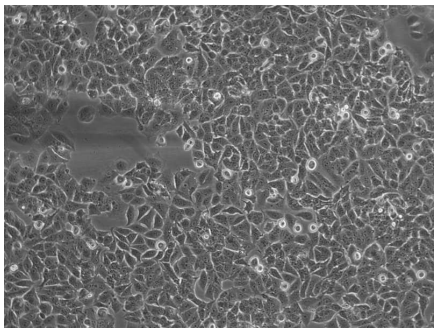

Experiment 081118 at time 385.8 h

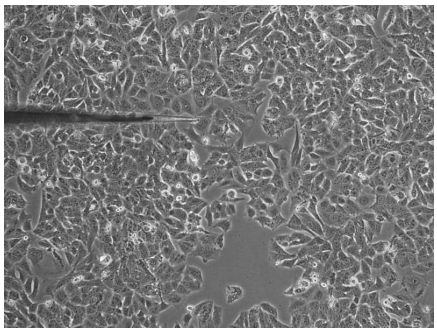

Experiment 081118 at time 409.6 h

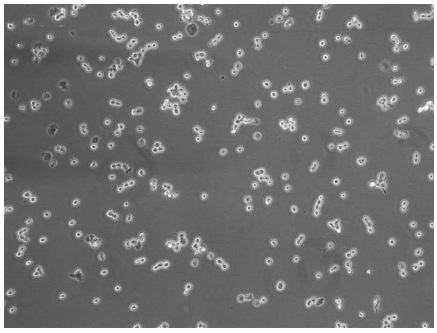

Experiment 081118 at time 410 h

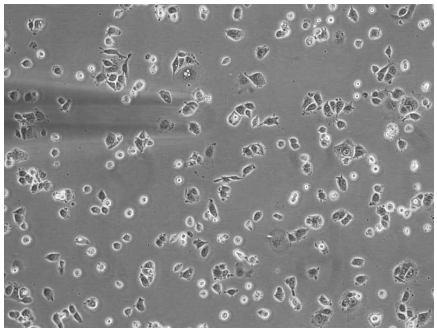

Experiment 081118 at time 412.75 h

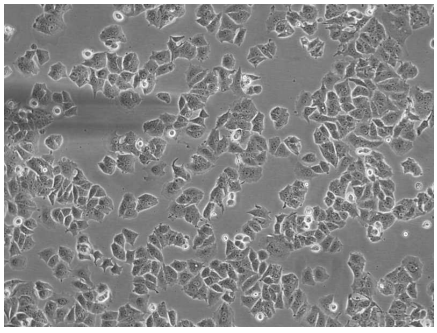

Experiment 081118 at time 453.75 h

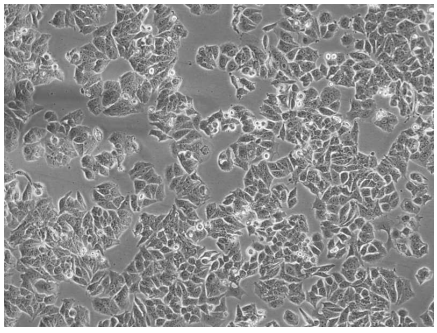

Experiment 081118 at time 481.5 h

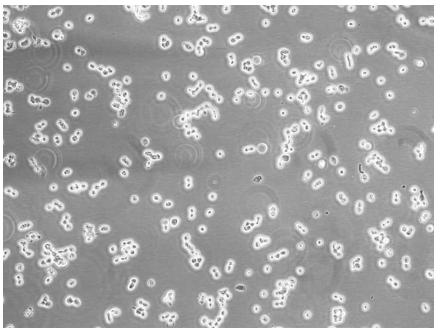

Experiment 081118 at time 481.9 h

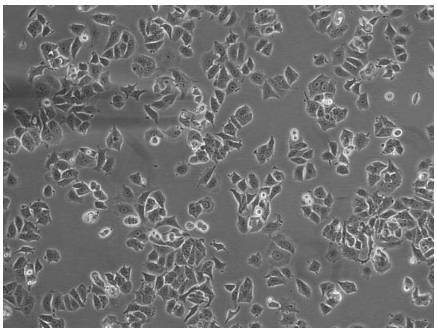

Experiment 081118 at time 501.2 h

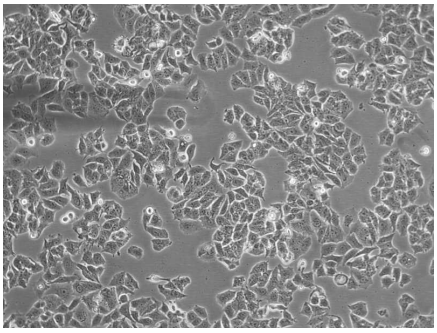

Experiment 081118 at time 528 h

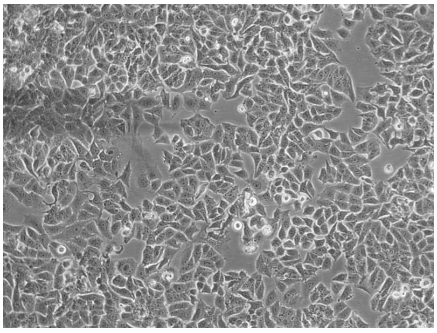

Experiment 081118 at time 549.25 h

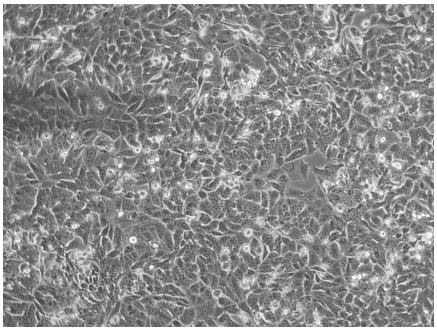

Experiment 081118 at time 573.75 h

Experiment 081212

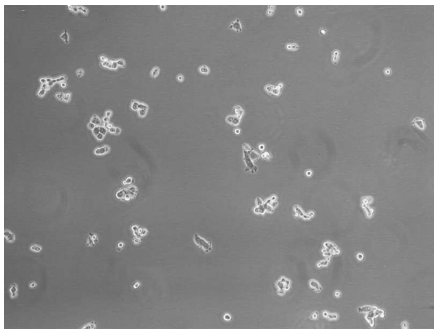

Experiment 081212 at time 0 h

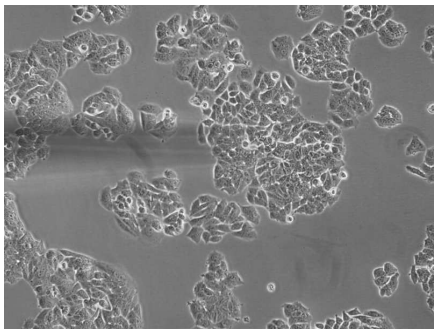

Experiment 081212 at time 73.06 h

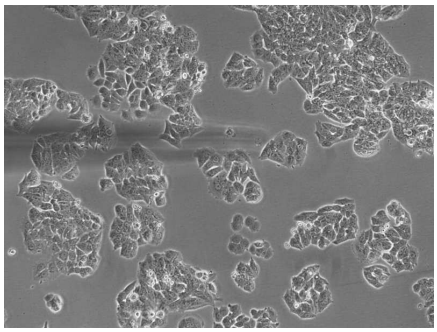

Experiment 081212 at time 98.26 h

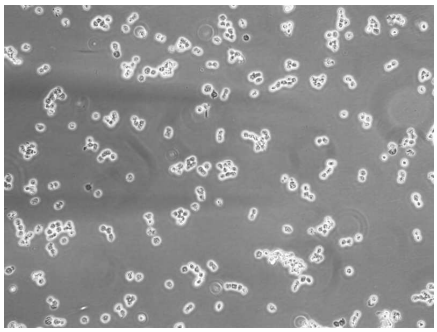

Experiment 081212 at time 98.63 h

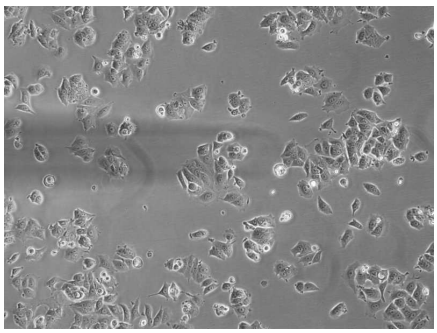

Experiment 081212 at time 118.7 h

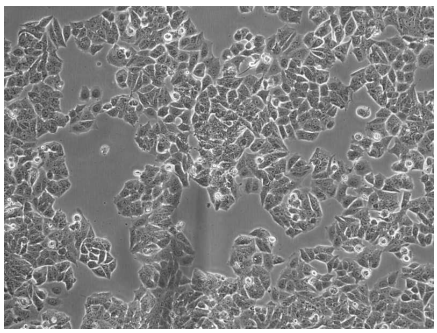

Experiment 081212 at time 170.2 h

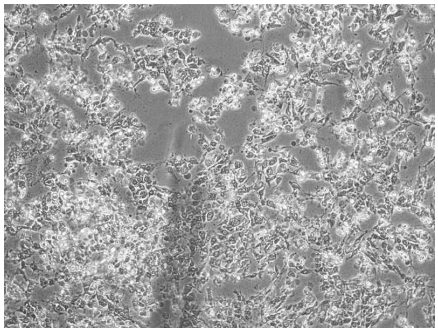

Experiment 081212 at time 239.3 h

Experiment 090608

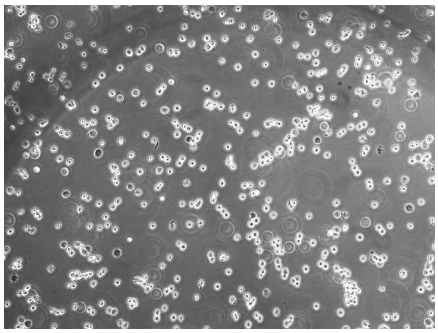

Experiment 090608 at time 0 h

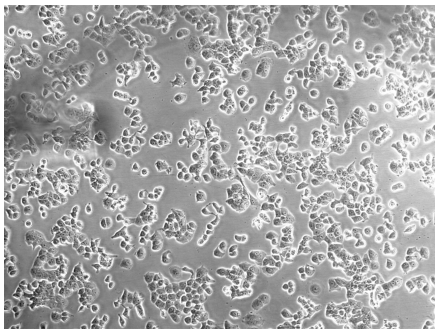

Experiment 090608 at time 22.5 h

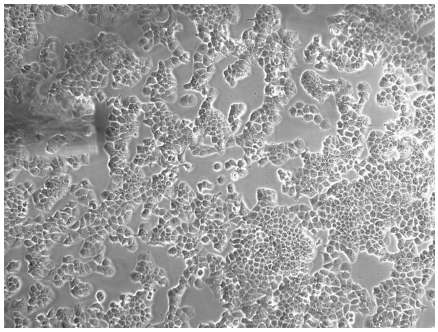

Experiment 090608 at time 45.2 h

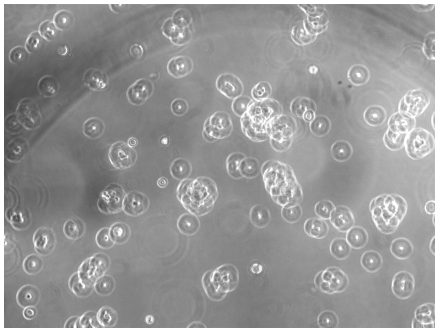

Experiment 090608 at time 45.5 h

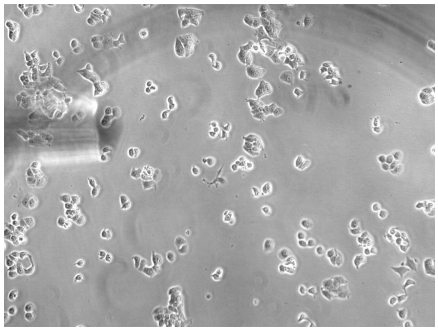

Experiment 090608 at time 71 h

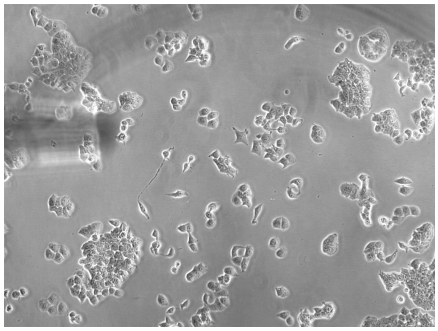

Experiment 090608 at time 92 h

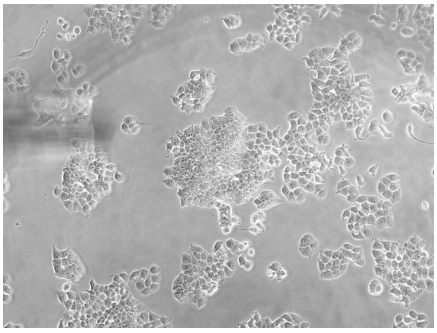

Experiment 090608 at time 114 h

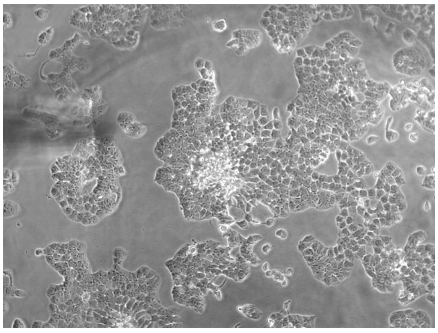

Experiment 090608 at time 164 h

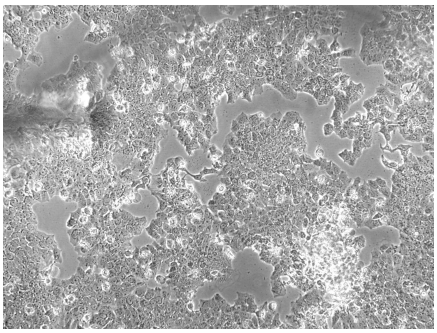

Experiment 090608 at time 213.6 h

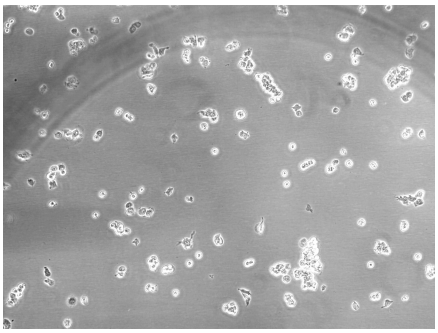

Experiment 090608 at time 214 h

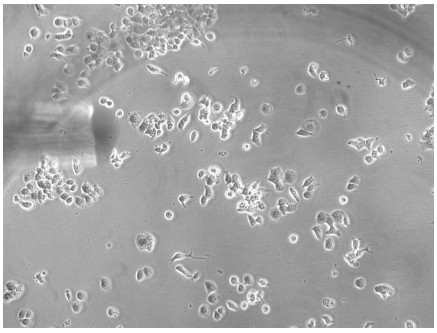

Experiment 090608 at time 239.8 h

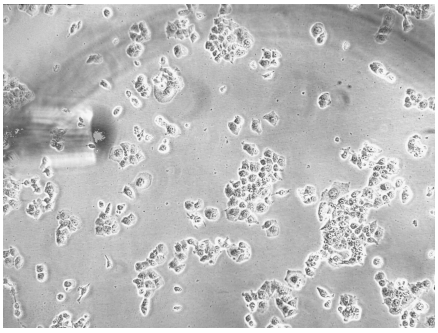

Experiment 090608 at time 251.4 h

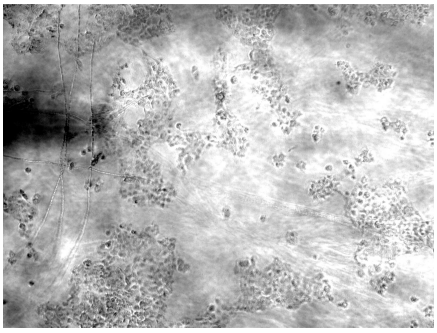

Experiment 090608 at time 331.5 h

Experiment 090622

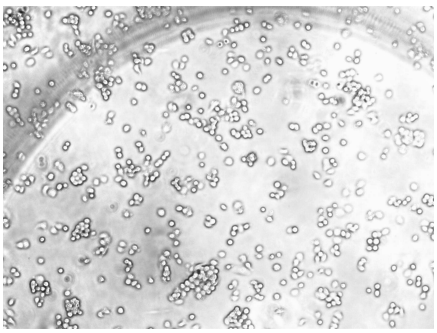

Experiment 090622 at time 0 h

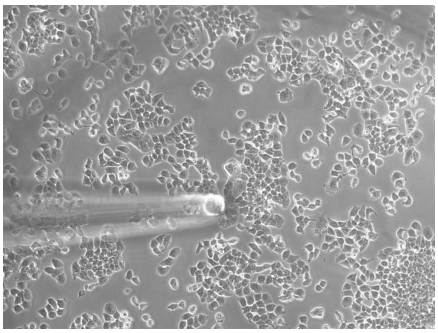

Experiment 090622 at time 23.7 h

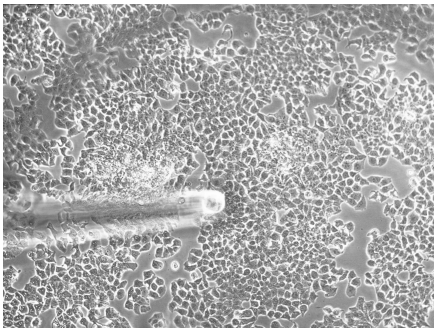

Experiment 090622 at time 44.5 h

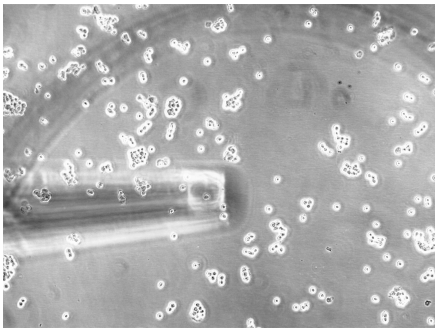

Experiment 090622 at time 44.8 h

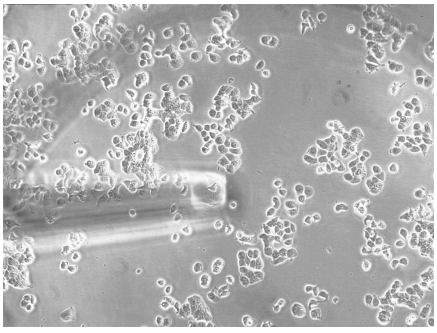

Experiment 090622 at time 68.7 h

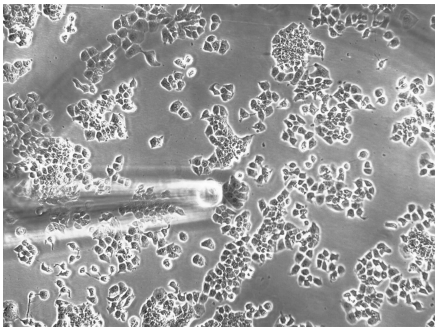

Experiment 090622 at time 91.7 h

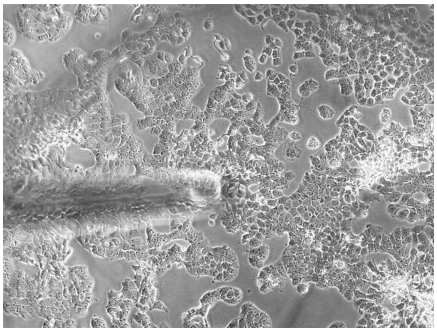

Experiment 090622 at time 161.2 h

Appendix D

Cell counts

In this appendix all the cell counts used is listed, with picture cell countings and the flask cell counts[1].

Table D.1: *Cell countings from experiment 081103 (12% O_2^{gp} without irradiation)*

Time	Pic 1	Pic 2	Pic 3	Mean cell number ($\times 10^6$)
0 h	151	–	–	0.316
21.00 h	282	299	229	0.565 ± 0.044
42.00 h	319	328	313	0.670 ± 0.00091
67.00 h	504	–	–	1.055
90.50 h	741	550	746	1.21 ± 0.14
165.50 h	1097	1099	1231	2.391 ± 0.030
188.50 h	1510	2340	1709	3.878 ± 0.52
211.00 h	828	912	815	1.782 ± 0.064
235.50 h	1206	1534	1580	3.013 ± 0.25
235.50 h	262	–	–	0.548
359.00 h	2363	1791	1556	3.983 ± 0.50

[1]Calculated as descriped in section 3.4

Table D.2: *Cell countings from experiment 081118 (8% O_2^{gp} without irradiation)*

Time	Pic 1	Pic 2	Pic 3	Mean cell number ($\times 10^6$)
0 h	329	251	222	0.559 ± 0.0070
17.87 h	387	450	480	0.919 ± 0.0057
70.01 h	1773	1896	1741	3.774 ± 0.0099
70.83 h	–	–	–	–
149.00 h	1657	1520	1655	3.371 ± 0.0095
149.30 h	388	–	–	0.812
169.10 h	454	461	390	0.910 ± 0.0047
190.30 h	642	684	527	1.293 ± 0.0098
241.30 h	1923	2449	2205	4.588 ± 0.032
241.70 h	471	435	405	0.915 ± 0.0040
313.60 h	1805	1857	1980	3.936 ± 0.011
313.90 h	255	259	279	0.553 ± 0.0016
358.20 h	627	653	659	1.353 ± 0.0021
385.80 h	1608	1456	1329	3.064 ± 0.017
409.60 h	2316	2912	2322	5.267 ± 0.041
410.00 h	361	414	389	0.812 ± 0.0032
412.75 h	399	–	–	0.835
453.75 h	840	782	785	1.679 ± 0.0040
481.50 h	1606	1326	1321	2.967 ± 0.020
481.90 h	481	424	425	0.928 ± 0.0039
501.20 h	601	663	609	1.307 ± 0.0041
528.00 h	1031	963	983	2.077 ± 0.0042
549.25 h	1479	1647	1622	3.312 ± 0.013
573.75 h	2262	2146	2483	4.807 ± 0.021

Table D.3: *Cell countings from experiment 081212 (6% O_2^{gp} without irradiation)*

Time	Pic 1	Pic 2	Pic 3	Mean cell number ($\times 10^6$)
0 h	168	109	169	0.3111 ± 0.042
73.06 h	1138	–	–	2.001
98.26 h	1405	1657	1633	3.275 ± 0.17
98.63 h	380	380	417	0.8210 ± 0.026
118.70 h	572	447	573	1.111 ± 0.088
170.20 h	1632	1444	1458	3.163 ± 0.13
239.30 h	3008	2770	3682	6.559 ± 0.57

Table D.4: *Cell countings from experiment 090608 (8% O_2^{gp} with 1.67 µCi/ml RPMI)*

Time	Pic 1	Pic 2	Pic 3	Mean cell number ($\times 10^6$)
0 h	612	603	646	1.298 ± 0.027
22.5 h	1407	1402	1455	2.975 ± 0.035
45.2 h	2264	1997	3714	5.564 ± 1.1
45.5 h	175	234	205	0.428 ± 0.036
71 h	366	450	339	0.8058 ± 0.070
92 h	667	676	554	1.323 ± 0.082
114 h	1106	872	930	2.029 ± 0.15
164 h	1746	1786	1871	3.769 ± 0.077
213.6 h	2989	2674	2563	5.739 ± 0.27
214 h	338	343	276	0.668 ± 0.0045
239.8 h	481	500	352	0.930 ± 0.097
251.4 h	531	434	511	1.030 ± 0.062
331.5 h	908	1209	1003	2.177 ± 0.19

Table D.5: *Cell countings from experiment 090622 (8% O_2^{gp} with 0.735 µCi/ml RPMI)*

Time	Pic 1	Pic 2	Pic 3	Mean cell number ($\times 10^6$)
0 h	679	727	976	1.662 ± 0.19
23.7 h	1580	1285	1289	2.898 ± 0.20
44.5 h	2311	2193	2120	4.621 ± 0.12
44.8 h	345	318	373	0.723 ± 0.033
68.7 h	638	550	605	1.251 ± 0.054
91.7 h	1095	1076	979	2.198 ± 0.075
161.2 h	2508	1945	2125	4.589 ± 0.35

Appendix E

The geometric reduction factors and electron ranges

E.1 Geometric reduction factors

The geometric reduction factors from Goddu et al. (1994). r_n and r_c is the radii of the nucleus and the cell, respectively.

$$\Psi_{R_n \leftarrow R_c}(x) = \begin{cases} Qx^2\left(r_n^2 - \frac{1}{12}x^2\right) & \text{if } r_c \leq 3r_n \text{ and } 0 \leq r_c - r_n \\ & \text{or if } r_c \geq 3r_n \text{ and } 0 \leq x \leq 2r_n, \\ Q\left[\frac{1}{2}\left(r_c^2 - r_n^2\right)\left(r_n^2 - x^2\right) + \right. & \\ \left. \frac{2x}{3}\left(r_c^3 - r_n^3\right) - \frac{1}{4}\left(r_c^4 - r_n^4\right)\right] & \text{if } r_c \leq 3r_n \text{ and } r_c - r_n \leq x \leq 2r_n, \\ \frac{r_n^3}{r_c^3 - r_n^3} & \text{if } r_c \geq 3r_n, \\ \frac{Q}{12}\left[x^4 - 3\left(r_c^4 + r_n^4\right) + \right. & \\ \left. 6\left(r_c^2 r_n^2 - x^2 r_n^2 - x^2 r_c^2\right) + \left(r_c^3 + r_n^3\right)\right] & \text{if } r_c \leq 3r_n \text{ and } 2r_n \leq x \leq r_c + r_n \\ & \text{or if } r_c \geq 3r_n \text{ and } r_c - r_n \leq x \leq r_c + r_n, \\ 0 & \text{else} \end{cases}$$

where

$$Q = \frac{3}{4x\left(r_c^3 - r_n^3\right)}$$

$$\Psi_{r_n \leftarrow r_n}(x) = \begin{cases} 1 - \frac{3}{4}\left(\frac{x}{r_n}\right) + \frac{1}{16}\left(\frac{x}{r_n}\right)^3 & \text{if } 0 \leq x \leq 2r_n \\ 0 & \text{if } x > 2r_n \end{cases}$$

E.2 Electron stopping power as function of energy

The approximate relation between the electon energy E (in keV) and the electron range $\mathcal{R}_e$ (in μm) in media of densiy 1.0 g/cm^3. Taken from Goddu et al. (1994).

0.4 keV - 20 keV

$$E(\mathcal{R}_e) = 5.9(\mathcal{R}_e + 0.007)^{0.565} + 0.00413\mathcal{R}_e^{1.33} - 0.367$$
$$\frac{dE}{d\mathcal{R}_e} = 3.333(\mathcal{R}_e + 0.007)^{-0.435} + 0.0055\mathcal{R}_e^{0.33}$$

0.06 keV - 0.4 keV

$$\mathcal{R}_e(E) = 1.524 \times 10^{-3} + 3.815 \times 10^{-2}E - 7.018 \times 10^{-4}E^2 + 3.628 \times 10^{-2}E^3$$
$$\frac{dE}{d\mathcal{R}_e} = 29.5 - 666.7\mathcal{R}_e$$

0 keV - 0.06 keV

$$\mathcal{R}_e(E) = 0.0123E + 2.25E^2 - 23.33E^3$$
$$\frac{dE}{d\mathcal{R}_e} = 10.5 + 1.126 \times 10^3\mathcal{R}_e - 9.251 \times 10^5\mathcal{R}_e^2 + 2.593 \times 10^8\mathcal{R}_e^3 4.964 \times 10^{10}\mathcal{R}_e^4$$

Appendix F

Cellular S values

In this appendix, the S values for tritium are listed in table F.1. S values are, as described in the text (section 2.3.6 on page 15), the imparted dose-rate per unit activity to different compartement of the cell. The values are taken from Goddu et al. (1997).

$S(R_N \leftarrow R_N)$ is the dose impartion rate from the nucleus to itself, per unit activity within the nucleus. $S(R_N \leftarrow R_{Cy})$ is the impartion rate of dose from the cytoplasm to the nucleus, per unit activity in the cytoplasm.

Table F.1: *Cellular S values*

r_C (μm)	r_N (μm)	$S(R_N \leftarrow R_N)$ (Gy/Bq·s)	$S(R_N \leftarrow R_{Cy})$ (Gy/Bq·s)
3	2	1.56×10^{-2}	2.99×10^{-3}
3	1	8.16×10^{-2}	4.25×10^{-3}
4	3	5.58×10^{-3}	1.20×10^{-3}
4	2	1.56×10^{-2}	1.46×10^{-3}
5	4	2.61×10^{-3}	5.84×10^{-4}
5	3	5.58×10^{-3}	6.36×10^{-4}
5	2	1.56×10^{-2}	8.01×10^{-4}
6	5	1.43×10^{-3}	3.25×10^{-4}
6	4	2.61×10^{-3}	3.26×10^{-4}
6	3	5.58×10^{-3}	3.74×10^{-4}
7	6	8.61×10^{-4}	1.99×10^{-4}
7	5	1.43×10^{-3}	1.87×10^{-4}
7	4	2.61×10^{-3}	1.99×10^{-4}
7	3	5.58×10^{-3}	2.35×10^{-4}
8	7	5.58×10^{-4}	1.30×10^{-4}
8	6	8.61×10^{-4}	1.17×10^{-4}
8	5	1.43×10^{-3}	1.18×10^{-4}
8	4	2.61×10^{-3}	1.30×10^{-4}
9	8	3.82×10^{-4}	8.97×10^{-5}
9	7	5.58×10^{-4}	7.77×10^{-5}
9	6	8.61×10^{-4}	7.51×10^{-5}
9	5	1.43×10^{-3}	7.86×10^{-5}
10	9	2.73×10^{-4}	6.44×10^{-5}
10	8	3.82×10^{-4}	5.42×10^{-5}
10	7	5.58×10^{-4}	5.07×10^{-5}
10	6	8.61×10^{-4}	5.10×10^{-5}
10	5	1.43×10^{-3}	5.50×10^{-5}

Appendix G

Recipies

RPMI 1640 medium

Stem solution (1000 ml)

RPMI 1640 powder	10.43 g
$NaHCO_3$	2.00 g
Milli-Q water	1000 ml

RPMI medium with serum (1000 ml)

RPMI 1649 stem solution	880 ml
Foetal celf serum	100 ml
Penicillin streptomycin	10 ml
Insulin (200 units/l)	2 ml
L-glutamine	10 ml

Trypsin

Stem solution (1000 ml)

NaCl	8.00 g
KCl	0.40 g
Glucose	1.00 g
$NaHCO_3$	0.35 g
Phenol red	0.002 g

Trypsin with EDTA (1000 ml)

Trypsin stem solution	1000 ml
EDTA	200 mg
Trypsin powder	500 mg

L-glutamin (35 ml)

L-glutamin	1.0227 g
RPMI stem solution	35 ml

Hepes 1 M (10 ml)

Hepes	2.38 g
Milli-Q water	10 ml

pH is adjusted to 7.9 with pure HCl or 40% NaOH and then sterilized by filtration.

Buffer A (10 ml)

Hepes 1 M (pH 7.9)	0.1 ml
$NaVO_3$	0.0012 g
DTT	0.001 g
Triton X-100	10 μl
$MgCl_2$	0.003 g
KCl	0.0075 g
Glycerolphosphate	0.02 g
Milli-Q water	10 ml

PBS (1 l)

NaCl	8.000 g
KCl	0.201 g
KH_2PO_4	0.204 g
$Na_2HPO_4 \bullet 12H_2O$	2.858 g
Milli-Q water	1.0 l

Appendix H

Chemical list

In this appendix, the chemicals used are listed in table H.1 along with manufacturer and country.

Table H.1: *Chemical list*

Chemical	Manufacturer
DTT	Sigma, USA
EDTA	Fluka, Switzerland
Emulsifier-Safe®	Packard BioScience, Netherland
Ethanol	Kemetyl Norge AS, Norway
Foetal calf serum	Euroclone, Great Britain
Glucose	Sigma, USA
Glycerophosphate	Sigma, USA
Hepes	Sigma, USA
Insulin	Sigma, USA
KCl	Merck, Germany
L-glutamin	Sigma, USA
L-valin ($C_5H_{11}NO_2$)	Sigma, USA
L-[3,4(n)-^{3}H]-valin	Amersham, GE Healthcare, Great Britain
Methylene blue	Merck, Germany
Milli-Q H_2O	Millipore, USA
$MgCl_2$	Merck, Germany
NaCl	Riedel de Haën, Germany
NaDOC ($C_{24}H_{39}O_4Na$)	Sigma, USA
$NaHCO_3$	Norsk Medisinaldepot AS, Norway
NaOH	Merck, Germany
$NaVO_3$	Sigma, USA
PBS	Euroclone, Great Britain
Penicillin-Streptomycin	Euroclone, Great Britain
Phenol red	Merck, Germany
RPMI powder with L-glutamin	JHR Biosciences, USA
RPMI stem solution	Euroclone, Great Britain
Triton X-100	Bio-rad, USA
Trypsin	PAA Laboratories, Austria